Investigation of heavily boron doped diamond thin film for electronic devices

Xian Zhang

University of BRISTOL

A dissertation submitted to the University of Bristol in accordance with the requirements of the degree of Doctor of Philosophy in the Faculty of Science, school of physics

March 2017

Abstract

This thesis presents the investigation of heavily boron-doped diamond (BDD) thin films prepared for potential electronic and power devices. Due to various defects existing within the bulk and surface of the synthetic diamond thin films, the work of this thesis focused on the improvement of electric carrier transport and the quality of CVD diamond by using a post-annealing method. Additional focus was the underlying mechanism by which thermal annealing affects the structural and electrical properties of as-deposited BDD thin films. The work described in this thesis was undertaken using the facilities in CVD Diamond group and Interface Analysis Centre (IAC) at Bristol University. Diamond thin film growth and doping were achieved by using Hot Filament Chemical Vapour Deposition (HFCVD). Surface and bulk characterisations were undertaken by using Scanning Electron Microscopy (SEM) coupled with Electron Backscatter Diffraction (EBSD), Raman Spectroscopy and Secondary Ion Mass Spectroscopy (SIMS) respectively. The home-built 4-probe Hall Effect set up was used to measure the electrical properties of as-deposited BDD thin films.

A series of polycrystalline diamond thin films grown on the polycrystalline diamond (PCD) substrate with different seeding conditions have been prepared with various boron atom concentrations ranging from the magnitude of 10^{20} cm^{-3} to 10^{21} cm^{-3}. A comparison was made between seeded and non-seeded samples to establish changes in the surface morphology, lattice structure and boron incorporation profile through the whole layer. The homoepitaxial (non-seeded) BDD film grown with the minimum diborane flow rate of 0.005 sccm ([B] ~2×10^{20} cm^{-3}) has a better quality and electrical properties, with a resistivity of 0.27 $\Omega\cdot$cm and carrier mobility of 186 cm$^2\cdot$V$^{-1}\cdot$s^{-1} at room temperature. Less than 1% of boron produced an electrically active acceptor.

A comprehensive study to determine the influence of post-annealing on the homoepitaxial BDD thin films showed that thermal treatment under vacuum at 900°C for 1 hour greatly improved the conductivity by over 40% with the carrier mobility increasing from 198 cm$^2\cdot$V$^{-1}\cdot$s^{-1} to 988 cm$^2\cdot$V$^{-1}\cdot$s^{-1}.

For the temperature range of 700°C to 1200°C at the same annealing time, a valley (V) shape behaviour describes the variation in morphology and phase (sp^2/sp^3) composition of the sample surface. Also, the distribution and concentration of dopants, the thin film thickness and its electrical behaviour has shown the same valley shape behaviour with annealing temperature. This structural and electrical behaviour around 900°C provides experimental evidence to support thermodynamic model for the predicted bonding and dissociation processes of boron pairs (B$_2$) at high temperature.

Experimental results have also been undertaken to identify the optimum annealing time at 900°C. It has been found for annealing times between 20 minutes and 120 minutes the same "V" shape behaviour occurs around a 1 hour anneal at 900°C for both the physical and electrical properties.

To my Almighty God and beloved parents

Acknowledgments

I would like to express my greatest gratitude to my God, Jesus Christ, who faithfully guides me go through the past a few years and provides me everything I need to overcome all difficulties I had encountered.

Thanks for everyone who contributes to this thesis as following:

Dr. Neil Fox, the most encouraging and patient supervisor I have ever had, for his supervision, knowledge, incredible enthusiasm about diamond research;

Professor Paul May, a very efficient and easy-going adviser, for his great knowledge on the diamond growth and data interpretation

Dr. James Smith, for his help on building Hall Effect measurement set up, knowledge about Raman spectroscopy and thesis proofreading

Dr.Zamir Othman, Dr. Sarah Halliwell, Hugo Dominguez and Alex Croot, for the valuable academic opinions on the data interpretation and experiment improvement

Ed Mahoney, for bringing entertaining atmosphere in the office.

Thanks for the support from my family and friends!

Author's declaration

I declare that the work in this dissertation was carried out in accordance with the requirements of the University's Regulations and Code of Practice for Research Degree Programmes and that it has not been submitted for any other academic award. Except where indicated by specific reference in the text, the work is the candidate's own work. Work done in collaboration with, or with the assistance of, others, is indicated as such. Any views expressed in the dissertation are those of the author.

SIGNED: .... DATE:...........................

Contents

List of Figures

Chapter 1   Introduction

1.1   Background

1.1.1   Diamond

1.1.1.1   Nature of carbon

Carbon is the fourth most abundant element in the galaxy and solar system by mass after hydrogen, helium and oxygen.[1, 2] Each carbon atom has six electrons around the nucleus, with the ground-state electron configuration of $1s^2 2s^2 2p^2$ (two core and four outer shell electrons), which makes it the sixth element in the periodic table. The four electrons in the outermost shell (valence electrons) split equally between s and p orbitals which provides the availability to form at maximum four covalent chemical bonds. When the carbon is not bonded with other elements, it forms either three-fold (graphite, graphene) or four-fold (diamond) coordinated structures [3]. In the three-fold graphite coordinated structure, three covalent electrons of each carbon are re-assigned into three hybridised sp^2 orbitals, which lie in one single plane, to form σ-covalent bond with the other atoms. The remaining p orbital with one covalent electron of each atom is perpendicular to the sp^2 plane forming the π-covalent bond between sp^2 hybridised layers providing a π-bonded system for the electron to conduct electricity [4]. In the four-fold coordinated structure, four hybridised sp^3 orbitals form four equal lengths of an σ bonded covalent system.

1.1.1.2   Properties of diamond

Diamond is a four-fold coordinated structure of pure carbon in a tetrahedral configuration with each atom co-ordinated to its four nearest neighbour atoms. **Figure 1.1** shows the crystal structure of diamond. Diamond's unit cell consists of two

1

interpenetrating face-centred cubic (FCC) lattices with a lattice constant α_o = 0.357 nm

at room temperature [5]. Eight atoms per unit cell with a strong C-C σ-bond of short

distance (0.154 nm[6]) leads to a very compact material with the atomic number

density of diamond of 1.76×10^{23} cm^{-3} and mass density of 3516 kg·m^{-3}[7]. Such a

strong tetrahedral arrangement of short C-C bonds in the diamond lattice is

responsible for the extreme hardness and many other exceptional properties. Table1.1

lists some of the prominent properties exhibited. In addition to the properties listed in

this table, another exceptional property of diamond is a very wide window of

transparency over a broad range of wavelength from deep ultraviolet to far infrared[8].
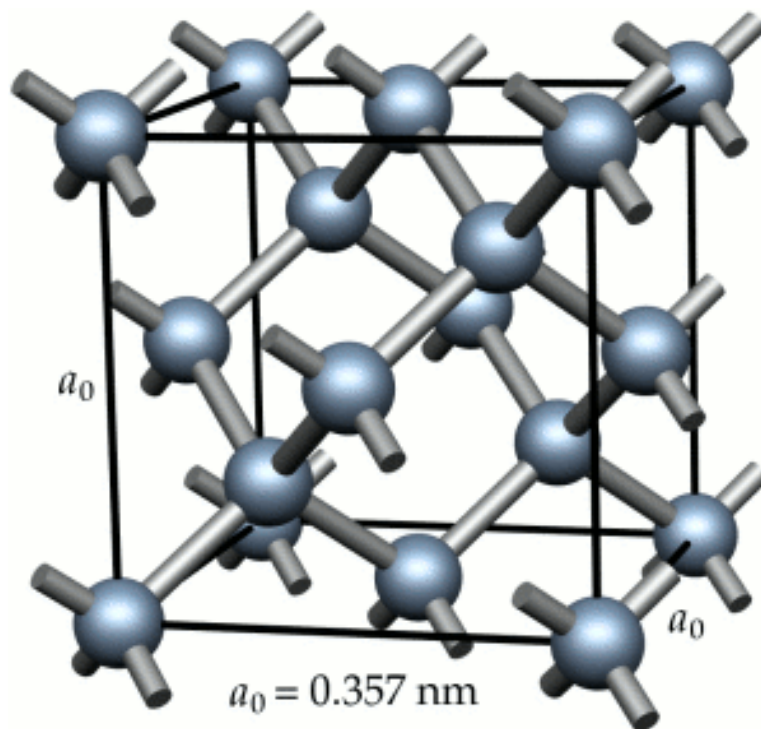
Figure 1.1 *The unit cell of diamond lattice structure where α_o is the cubic lattice parameter* [9].

Table 1.1 *A list of some key properties of diamond* [8]

Property	Value with unit
Hardness	10,000 kg·mm^{-2}
Young's modulus	1.22 Gpa
Thermal expansion coefficient	1.1 × 10^{-6} K^{-1}
Thermal conductivity	20 W·cm^{-1}·K^{-1}
Resistivity	10^{13}-10^{16} Ω·cm
Hole mobility	1600 cm^2·V^{-1}·s^{-1}
Electron mobility	2200 cm^2·V^{-1}·s^{-1}
Band gap	5.4 eV

1.1.1.3 Natural diamond

Natural diamond has always obtained massive favour, especially in the manufacture of jewellery where it is one of most precious stones found in the natural world. Natural diamonds, which have been properly cut and processed, possess huge commercial value as they sparkle, shine and refract light seemingly more than other gems. Another important reason that makes natural diamond so valuable is their rarity. This tends to be as a consequence of the typical extreme growth conditions of diamond in nature being high temperature (>1000°C) and pressure (4-7 GPa), with growth occurring slowly over a period of 1 billion to 3.3 billion years within the upper mantle of around 120-190 km below the Earth's surface[10].

1.1.1.4 Synthetic diamond

Synthetic diamonds are made by artificial techniques, such as chemical vapour deposition (CVD) and high pressure high temperature (HPHT).

1.1.1.4.1 HPHT diamond

The HPHT process has made a well-known success since the early 1950s [11-13] in which diamond in grown under metastable conditions, i.e. in the graphite stable region. Although the difference in enthalpy of forming diamond and graphite is relatively small (2.9 kJ·mol^{-1}[14]), the large energy barrier prevents the spontaneous conversion of diamond into graphite which helps make diamond the favourable product. The HPHT synthesis was successfully developed by General Electric in the early 1950s which was reproducing the growth condition in nature. Metal powders, such as Ni or Co, were used as a catalyst to boost the transition of graphite to diamond in the high pressure and temperature condition [15]. HPHT diamonds with dimensions between nanometres (nm) and millimetres (mm) are often used in industrial abrasive and cutting tools. However, impurities are commonly found in the as-grown crystals thereby limiting its use in electronic and electrochemical applications.

1.1.1.4.2 Chemical Vapour Deposition (CVD) diamond

The CVD method is another alternative process to fabricate thin film diamond layer-by-layer. The process was initiated by Eversole at 1958[16] and developed by Deryagin et al. [17] a decade later. Layers of diamond and graphite were deposited by using the thermal decomposition of a carbon-containing gases on the surface of natural diamond heated at 900°C under a reduced pressure with very low growth rate. Soon after, the work by Angus [18] revealed that atomic hydrogen introduced during growth leads to an etching effect of graphite rather than diamond thereby allowing high

4

quality diamond films to be grown. They also made a p-type diamond by incorporating boron into diamond during the CVD growth [19]. Later work from Deragin [20] found that the chemical vapour technique can be also applied to growth onto non-diamond substrates.

The CVD process involves a complicated gas-phase chemical reaction of carbon-containing active species above the substrate surface which causes the deposition of the diamond. Such a reaction can be achieved by thermal processes such as by a hot filament and by a microwave plasma, these are the most commonly used methods applied in diamond CVD techniques [8].

In the early work of development of CVD reactors in the 1980s, the Japanese National Institute for Research in Inorganic Materials (NIRIM) were among the first to build both hot filament and microwave plasma-enhanced CVD reactors[21]. These two different ways of decomposing carbon-containing precursors are shown in **Figure *1.2***. The hot filament reactor as shown in frame A creates high-temperature thermal decomposition by passing an electrical current through metal filaments positioned above the heated substrate, while the microwave plasma reactor as shown in frame B forms a plasma ball of reactant gases from microwaves[22]. Other plasma methods, such as radio frequency plasma (RF) [23, 24] and D.C. plasma [25-27] may also be used to grow diamond.

By altering the chemical composition of carbon-containing precursor gases, conditions of seeding layer, and substrate material and temperature, it is possible to grow diamond with different orientation surfaces and with grain sizes varying from ultra-nanocrystalline (<10 nm) to single crystal diamond[28].
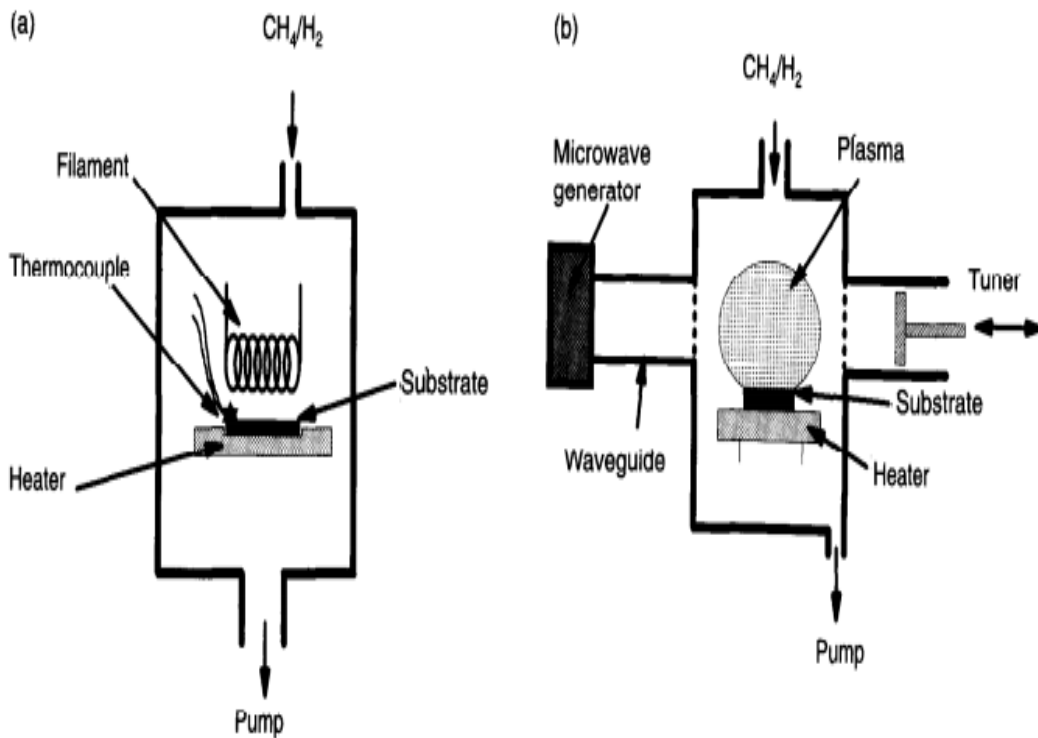
Figure 1.2 *The schematic diamond of (A) a hot filament CVD reactor and (B) a microwave enhanced plasma reactor[21]*

1.1.2   Doping diamond

Major progress has also been made on the doping of CVD diamond. The many studies [29-31] on the synthesis of p-type semiconducting diamond have opened the door for researchers around the world aiming to fabricate practical semiconducting diamond for electronic devices. Introducing impurity atoms into the diamond lattice during CVD growth alters the electrical properties of as-grown diamond which can be transformed from insulator to semiconductor and even semi-metal. Dopants, such as nitrogen and phosphorus make an n-type semiconductor while the addition of boron produces a p-type semiconductor. **Figure *1.3*** illustrates the band gap of intrinsic, n-type and p-type of diamond, respectively.
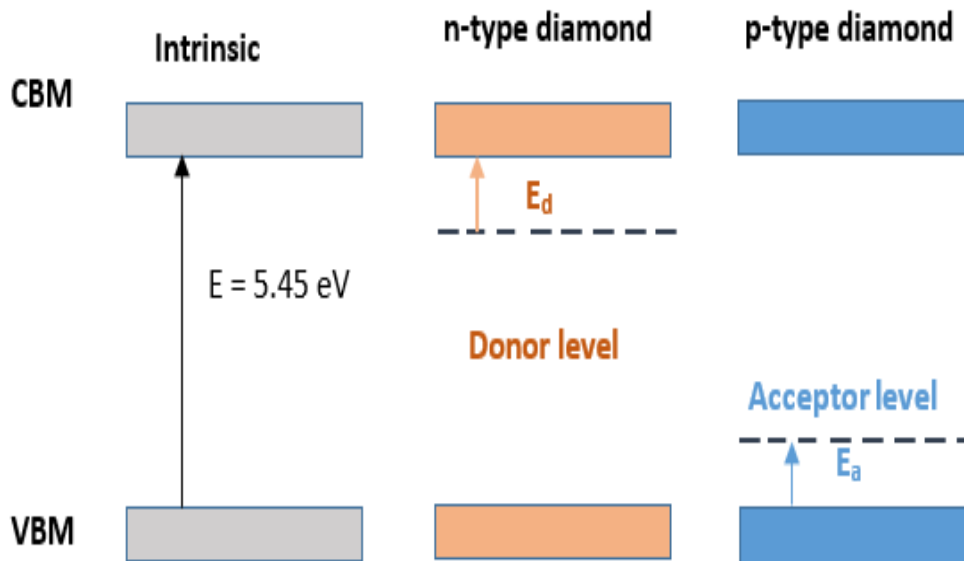
Figure 1.3 *Band diagram of intrinsic, n-type and p-type diamond (E_d: activation energy of donor; E_a: activation energy of acceptor. CBM: conduction band minimum; VBM: valence band maximum)*

As can be seen in **Figure *1.3***, the energy for an electron to be excited from the VBM to the CBM for the intrinsic diamond is around 5.45eV which is larger than most semiconductor materials. Therefore, pure diamond is electrically insulating at room temperature. Adding a donor, such as nitrogen, to form n-type diamond, contributes electrons into the diamond lattice through a substitutional position, and thereby forms a donor level just below the CBM. In contrast, the acceptors operate the opposite way by accepting electrons from carbon via substitutional doping and forms an acceptor energy level just above the VBM. As a result of a missing electron in the host atom, the free positively charged holes will be created which conduct the electrical current by continuously accepting an electron from the neighbouring carbon.

1.1.2.1   N-type doping

There are a few elements that have been studied as potential donors, such as nitrogen [32], phosphorus[33, 34], sulfur[35-37] and lithium[38, 39] . Theoretically, n-type diamond should have superior performance as a material for electronic-based applications due to the freely available electrons able to carry charge throughout the lattice. However, true n-type diamond has not been effectively fabricated and none of these elements have yielded convincing electron related conductivity [40, 41]. One of the main reasons is the deep donor energy level within the band gap which provides a huge barrier for potential impurity atoms to be effectively ionised [41]. Another issue is the short C-C bond length and tight lattice structure which excludes the majority of elements of the periodic table that have a larger ionic radius than a substitutional site in the diamond.

1.1.2.2   P-type doping

P-type diamond has been intensively studied and already widely utilised in the industry and commercial fields [42]. Boron is one of the most common atoms widely used as the dopant, giving a shallow energy level (activation energy = 0.37 eV) just above the VBM which is responsible for its potential low resistivity as a semiconductor. The growth of boron doped CVD diamond (BDD) has been achieved by adding small amounts of boron-containing gases, such as B_2H_6 or B_2O_3, with carbon-containing gases into the MW or HF reactor [42]. The earlier reports on the electrical properties of BDD diamond were made by Fujimori at 1986 who found doping boron (flow rate >1000 ppm) gives rise to the p-type conductivity of diamond with an activation energy of 0.015 eV [30]. Later in 1988, Okane *et al* [13] produce BDD films, doped by 100 ppm, with an activation energy of 0.16 eV. These results suggested that the electrical

8

conductivity maybe controlled by carefully adjusting the boron concentration. Later in the early 1990s, Shiomi *et al* [43] observed the metallic conduction of BDD within the temperature range 300K < *T* < 770K with boron concentration of 3×10^{20} cm^{-3}. They stated that the lowest resistivity of 3 x 10^{-3} Ω ·cm was achieved at room temperature. Soon later, Borst *et al* [44] systematically investigated the electrical properties as a function of temperature with different boron concentrations varying from 1×10^{18} cm^{-3} to 3×10^{20} cm^{-3} [45]. **Figure *1.4*** from Borst group [44] illustrates the temperature-dependent conductivity and mobility. As can be seen in this figure, these BDD films exhibit semiconducting behaviour as the temperature changes but semi-metallic properties once the boron concentration reaches the threshold of insulator-metal transition (3×10^{20} cm^{-3}). In the early 2000's, Ekimov *et.al* [46] showed that heavily boron doped diamond exhibited superconductivity at Tc = 4 K and confirmed later on by Lee *et.al* [47] with a critical temperature of 7 K.
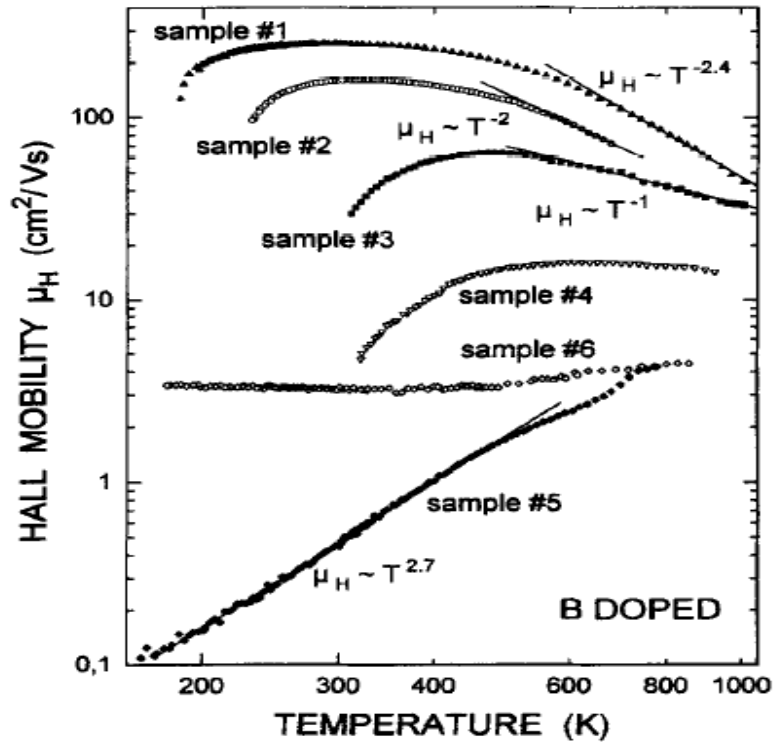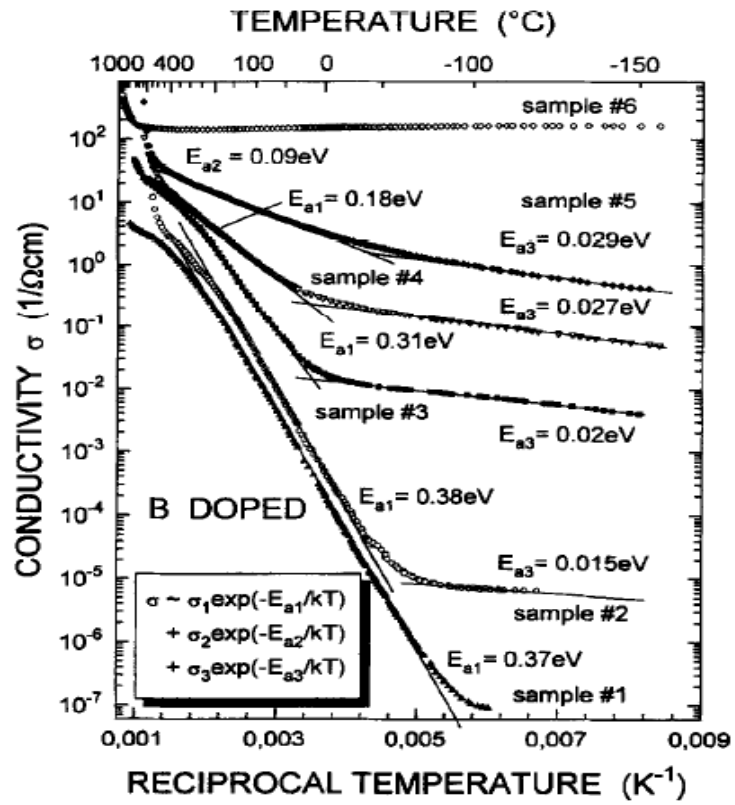
Figure 1.4 *Temperature dependent conductivity and Hall mobility data at different boron concentrations* [44]. *(sample #1: 1×10^{18} cm^{-3}; #2: 2×10^{18} cm^{-3}; #3:2×10^{19} cm^{-3}; #4:5×10^{19} cm^{-3}; #5:8×10^{19} cm^{-3};#6:3×10^{20} cm^{-3};).*

Doping boron into the diamond lattice by an ion implantation method is another popular method to make BDD films [48-50]. However, it also introduces damage to the lattice and gives rise to sp^2 carbon content. Some of this damage can be readily removed by post-annealing at above 1400°C [51, 52]. The maximum boron concentration that can be doped into diamond has been shown to be of the magnitude 10^{21} cm^{-3} [45].

1.1.3 Applications of semiconducting diamond

Since Custers *et al* [29] discovered the natural semiconducting properties in type IIb diamond with the successful manufacture of boron doped diamond, synthetic semiconducting diamond for electronic device has been a hot topic in terms of its applications [53]. Due to the high breakdown voltage (>10^7 V·m^{-1}) and low resistivity, boron doped diamond makes a promising material for high power and high frequency electronics devices [45]. In addition, BDD has the largest electrochemical potential window in aqueous solutions when compared to traditional electrode materials such as gold, platinum and glassy carbon thereby enabling a wide range of commercial electrodes [54].

1.1.3.1 Passive Electronic devices

Early in the 1990s, BDD materials were first tested for use as the active material in temperature and pressure sensors for harsh environments as BDD exhibits a high level of endurance. Aslam *et al* [55] found the response time for thermal measurement of BDD films at a temperature range of 80K – 1270K was 0.29 μs – 25 μs. They also designed and fabricated a first-generation diamond microchip with a minimum feature size of 250 μm which was used to study the sensing properties of BDD materials. Later, Taher *et al* [56] measured the piezoresistive gauge factors at 300 K under various

pressures by using the integrated sensor test chip. Recently, Shintani *et al* [57] developed a pH-sensitive sensor by using an oxygen-terminated BDD surface and comparing this with a hydrogen-terminated one.

1.1.3.2 *Positive electronic devices*

The characteristics of a Schottky diode based on a collector-emitter based junction was first measured by Prins [58], this represented one of the most major milestones in the advancement of diamond devices since Custer [29] reported the discovery of semiconducting properties in natural IIb diamond. The device was made by implanting N into a p-type semiconducting surface layer and a typical emitter-based diode I-V curve was obtained. However, the power gain was very low which indicated the development of geometry fabrication process. Later, Geis *et al* [59] successfully fabricated the first point-contact transistor and Schottky diodes with a power gain at 510°C and operational temperature at 700°C, respectively. Since then, much research

has been focused on the improvements of performance operational temperature and voltage by altering the deposition conditions [60] (such as substrate and boron concentration) and refining the addition of a metal ohmic contact [61] (such as Au or Ti) onto the diamond surface. **Figure *1.5*** shows the influence of boron concentration fabricated with different procedures (Graph A) on the I-V behaviour at a temperature of 300K (Graph B) and 573K (Graph C), respectively.

A

N_A (cm^{-3})

10^{19}

the solid lines represents doping profiles calculated from CV-measurements

10^{18}

sample A
(high doped)

sample B
(low doped)

10^{17}

10^{16}

sample C
(pulse doped)

1   (microns)

Thickness of the Epitaxial Layer

B

10^3

10^2

10^1

10^0

T=300K

J
[A/cm^2]

high doped epitaxial layer
(sample A)

10^{-2}

10^{-3}

pulse doped epitaxial layer
(sample C)

10^{-4}

10^{-5}

low doped epitaxial layer
(sample B)

10^{-6}

10^{-7}

-20   0   20   40   60   80   100

V [V]

Figure 1.5 *Graph A: doping profile on the homoepitaxial diamond; Graph B: I-V characteristic of the Schottky diodes at 300 K; Graph C: I-V characteristic of the Schottky diodes at 573 K* [59].

It can be seen in **Figure *1.5*** the diodes with high concentrations of boron (> 10^{18} cm^{-3}) have higher I-V curves both operating at 300K and 573K. The operational temperature of BDD Schottky diodes has been pushed as high as 1273K by Butler *et al* [62] with low boron concentration between 5×10^{14} to 1×10^{16} cm^{-3}. They also stated that the highest known breakdown voltage (above 6 kV) was also observed. Also, the current leakage was measured at 1000 V from 100 °C to 325 °C which indicated that the Schottky barrier height was 1.05 eV. The reason for the leaking current of BDD

Schottky diode was ascribed to the structural defects and surface roughness which could be improved by post-annealing methods [62, 63].

1.1.3.3   Electrode

Boron doped diamond electrodes have been widely reported and applied in the field of electroanalytical chemistry due to the outstanding properties such as broad potential window, chemical inertness, resistance to passivation, low noise and background current, and particularly biocompatibility[54]. They have been commercialised and used extensively in industrial, environmental and clinical tests. Recently, chemical modification of BDD electrode surfaces became another main direction in the field of biosensors with the aim of improving its electrochemical properties. [54]

Other applications of BDD materials, such as field-effect transistors [57,58], electron emitters [63] and even nuclear radiation detectors [64], are also of major interest within the field of semiconducting diamond.

Although there is a large potential for the use of boron doped diamond in electronic devices, some challenges exist which need to be resolved. Defects, such as dopants, vacancies and grain boundaries, are the main reasons that limit the electrical performance of as-fabricated devices. Surface conditions, such as the roughness and morphology, are other major factors that influence electron emission-based devices [59]. Post-annealing is a common technique primarily used for improving the conductivity of BDD films fabricated by ion implantation. However, the annealing mechanism of as-grown BBD film is still unclear, and needs theoretical and experimental efforts to give us a clearer picture.

1.2 Outline of thesis and objectives

With the aim of improving the electrical properties of heavily BDD thin films for a potential electronic device and completing the understanding of CVD thin film diamond growth and doping mechanism, the work in this thesis is presented as follow:

In Chapter **2**, theoretical background of CVD diamond growth and free carrier dynamics in boron doped diamond is presented. Theoretical modelling of defects in diamond and their thermodynamics properties will also be discussed in this chapter.

In Chapter **3**, experimental methods and materials used in this work will be discussed. Some basic concepts related to the instruments will also briefly be described in order to understand data interpretations.

Chapter **4** is the first results chapter about growing boron-doped diamond thin film on polycrystalline CVD substrate surfaces with and without seeding layer in the heavily doping range from 10^{20} cm^{-3} to 10^{21} cm^{-3}, respectively. The influence of boron concentration and seeding layer on the lattice structure and electrical properties will also be discussed in this chapter.

Chapter **5** is the second results chapter about improving electrical properties by thermal annealing in the temperature range between 700°C to 1200°C. The variations of phase transition and grain size of the surface, distribution and concentration of dopant as well as the electrical properties at room temperature will be explored in this result chapter.

Chapter **6** is the last results chapter about improving electrical properties by thermal annealing at 900°C with various annealing times between 20 minutes to 120 minutes.

The evidence for defect diffusion will be presented and the influence of diffusion on the variations of phase transition and grain size of the surface, distribution and concentration of dopants as well as the electrical properties at room temperature will be discussed.

In Chapter **7**, the results obtained from the three result chapters in this thesis will be summarised and therefore, a series of potential work is presented for future development.

1.3   References

1.   Kwok, S., *Organic matter in space: from star dust to the Solar System.* Astrophysics and Space Science, 2009. **319**(1): p. 5-21.

2.   Sarada, B., T. Rao, D.Tryk, and A. Fujishima, *Electrochemical oxidation of histamine and serotonin at highly boron-doped diamond electrodes.* Analytical Chemistry, 2000. **72**(7): p. 1632-1638.

3.   Mauri, F., B.G. Pfrommer, and S.G. Louie, *Ab initio NMR chemical shift of diamond, chemical-vapor-deposited diamond, and amorphous carbon.* Physical Review Letters, 1997. **79**(12): p. 2340.

4.   Falkovsky, L. and A. Varlamov, *Space-time dispersion of graphene conductivity.* The European Physical Journal B, 2007. **56**(4): p. 281-284.

5.   Jiang, Q., J. Li, and G. Wilde, *The size dependence of the diamond-graphite transition.* Journal of Physics: Condensed Matter, 2000. **12**(26): p. 5623.

6.   Twitchen, D., J. Baker, M. Newton, K. Johnston, *Identification of cobalt on a lattice site in diamond.* Physical Review B, 2000. **61**(1): p. 9.

7.   Stewart, R.F., *Charge density study of diamond.* The Journal of Chemical Physics, 1973. **58**(10): p. 4430-4438.

8.   Spear, K.E. and J.P. Dismukes, *Synthetic diamond: emerging CVD science and technology*. Vol. 25. 1994: John Wiley & Sons.

9.   Sque, S.J., *A first-principles study on bulk and transfer doping of diamond*. 2005: University of Exeter.

10.   Pearson, D., D. Canil, and S. Shirey, *Mantle samples included in volcanic rocks: xenoliths and diamonds.* Treatise on geochemistry, 2003. **2**: p. 171-275.

11.   Chu, C.J., D. Patternson, R.H. Hauge, and J. Margave, *Mechanistic Studies of CVD Diamond Thin Film Growth*. in *Symposium on High Temperature and Materials Chemistry*. 1989.

12.   Akaishi, M., H. Kanda, and S. Yamaoka, *High pressure synthesis of diamond in the systems of grahpite-sulfate and graphite-hydroxide.* Japanese Journal of Applied Physics, 1990. **29**(7A): p. L1172.

13.   Okano, K., H. Naruki, Y. Arkiba, T. Kurosu, M. Lida, and Y. Hirose, *Synthesis of diamond thin films having semiconductive properties.* Japanese Journal of Applied Physics, 1988. **27**(2A): p. L173.

14.   Kleppa, O. and K. Hong, *New applications of high-temperature solution calorimetry 1. Enthalpy of the diamond-to-graphite transformation and enthalpy of formation of Mn 5 C 2 at 1320 K.* The Journal of Chemical Thermodynamics, 1978. **10**(3): p. 243-248.

15.   Bundy, F., H. Hall,H. Strong, and R. Wentorf, *Man-made diamonds.* Nature, 1955. **176**(4471): p. 51-55.

16.   Eversole, W., *Diamond synthesis.* US patents, 1958(3030187): p. 3030188.

17.   Derjaguin, B., D. Fedoseev, V.Lukyanovich, B. Spitzin, V. Ryabov, and A. Lavrentyev *Filamentary diamond crystals.* Journal of Crystal Growth, 1968. **2**(6): p. 380-384.

18.   Angus, J.C., H.A. Will, and W.S. Stanko, *Growth of diamond seed crystals by vapor deposition.* Journal of Applied Physics, 1968. **39**(6): p. 2915-2922.

19.   Poferl, D.J., N.C. Gardner, and J.C. Angus, *Growth of boron-doped diamond seed crystals by vapor deposition.* Journal of Applied Physics, 1973. **44**(4): p. 1428-1434.

20.   Spitsyn, B., L. Bouilov, and B. Derjaguin, *Vapor growth of diamond on diamond and other surfaces.* Journal of Crystal Growth, 1981. **52**: p. 219-226.

21.   May, P.W., *CVD diamond: a new technology for the future?* Endeavour, 1995. **19**(3): p. 101-106.

22.   Kobashi, K., K. Nishimura, Y. Kawate, and T. Horiuchi, *Synthesis of diamonds by use of microwave plasma chemical-vapor deposition: morphology and growth of diamond films.* Physical Review B, 1988. **38**(6): p. 4067.

23.   Meyer, D.E., R.O. Dillon, and J.A. Woollam, *Radio‐frequency plasma chemical vapor deposition growth of diamond.* Journal of Vacuum Science & Technology A, 1989. **7**(3): p. 2325-2327.

24.   Matsumoto, S., M. Hino, and T. Kobayashi, *Synthesis of diamond films in a rf induction thermal plasma.* Applied Physics Letters, 1987. **51**(10): p. 737-739.

25. Suzuki, K., A. Sawabe, and H. Yasuda, *Growth of diamond thin films by dc plasma chemical vapor deposition.* Applied Physics Letters, 1987. **50**(12): p. 728-729.

26. Kurihara, K., K. Sasaki, M. Kawarada, and N. Koshino, *High rate synthesis of diamond by DC plasma jet chemical vapor deposition.* Applied Physics Letters, 1988. **52**(6): p. 437-438.

27. Koizumi, S., T. Murakami, and T. Inuzuka, *Epitaxial growth of diamond thin films on cubic boron nitride {111} surfaces by dc plasma chemical vapor deposition.* Applied Physics Letters, 1990. **57**(6): p. 563-565.

28. Das, D. and R. Singh, *A review of nucleation, growth and low temperature synthesis of diamond thin films.* International Materials Reviews, 2013.

29. Custers, J., *Unusual phosphorescence of a diamond.* Physica, 1952. **18**(8-9): p. 489-496.

30. Fujimori, N., T. Imai, and A. Doi, *Characterization of conducting diamond films.* Vacuum, 1986. **36**(1-3): p. 99-102.

31. Angus, J., N. Gardner, and D. Poferl, *Growth of Semiconductor Diamond at Subatmospheric Pressures, Sint*. 1971, Almazy.

32. Okano, K., S. Koizumi, S. Silva, and G. Amaratunga, *Low-threshold cold cathodes made of nitrogen-doped chemical-vapour-deposited diamond.* Nature, 1996. **381**(6578): p. 140-141.

33. Koizumi, S., M. Kamo, and Y. Sato, *Growth and characterization of phosphorous doped {111} homoepitaxial diamond thin films.* Applied Physics Letters, 1997. **71**: p. 1065-1067.

34. Katagiri, M., J. Isoya, S. Koizumi, and H. Kanda, *Lightly phosphorus-doped homoepitaxial diamond films grown by chemical vapor deposition.* Applied Physics Letters, 2004. **85**(26): p. 6365-6367.

35. Nishitani-Gamo, M., E. Yasu, C. Xiao, and Y. Kikuchi, *Sulfur-doped homoepitaxial (001) diamond with n-type semiconductive properties.* Diamond and Related Materials, 2000. **9**(3): p. 941-947.

36. Saada, D., J. Adler, and R. Kalish, *Sulfur: A potential donor in diamond.* Applied Physics Letters, 2000. **77**(6): p. 878.

20

37.   Nishitani-Gamo, M., C. Xiao, Y. Zhang, E. Yasu, and Y. Kikuchi, *Homoepitaxial diamond growth with sulfur-doping by microwave plasma-assisted chemical vapor deposition.* Thin Solid Films, 2001. **382**(1): p. 113-123.

38.   Geis, M., J. Twichell, and J Macaulay, *Electron field emission from diamond and other carbon materials after H2, O2, and Cs treatment.* Applied Physics Letters, 1995. **67**(9): p. 1328-1330.

39.   Okumura, K., J. Mort, and M. Machonkin, *Lithium doping and photoemission of diamond thin films.* Applied Physics Letters, 1990. **57**(18): p. 1907-1909.

40.   Kalish, R., *The search for donors in diamond.* Diamond and Related Materials, 2001. **10**(9–10): p. 1749-1755.

41.   Kalish, R., *Doping of diamond.* Carbon, 1999. **37**(5): p. 781-785.

42.   Okano, K., et al., *Characterization of boron-doped diamond film.* Japanese Journal of Applied Physics, 1989. **28**(6R): p. 1066.

43.   Shiomi, H., Y. Nishibayashi, and N. Fujimori, *Characterization of boron-doped diamond epitaxial films.* Japanese Journal of Applied Physics, 1991. **30**(7R): p. 1363.

44.   Borst, T. and O. Weis, *Electrical characterization of homoepitaxial diamond films doped with B, P, Li and Na during crystal growth.* Diamond and Related Materials, 1995. **4**(7): p. 948-953.

45.   Volpe, P.-N., et al., *Boron incorporation issues in diamond when TMB is used as precursor: Toward extreme doping levels.* Diamond and Related Materials, 2012. **22**: p. 136-141.

46.   Ekimov, E.A., et al., *Superconductivity in diamond.* Nature, 2004. **428**(6982): p. 542-545.

47.   Lee, K.-W. and W. Pickett, *Superconductivity in boron-doped diamond.* Physical Review Letters, 2004. **93**(23): p. 237003.

48.   Prins, J.F., *Activation of boron-dopant atoms in ion-implanted diamonds.* Physical Review B, 1988. **38**(8): p. 5576.

49.   Zhu, W., G. Kochanski, S. Jin, L. Seibles, D.Jacobson, M. McCormack, and A. Whiteless, *Electron field emission from ion‐implanted diamond.* Applied Physics Letters, 1995. **67**(8): p. 1157-1159.

50. Sandhu, G., M. Swanson, and W. Chu, *Doping of diamond by coimplantation of carbon and boron.* Applied Physics Letters, 1989. **55**(14): p. 1397-1399.

51. Braunstein, G. and R. Kalish, *Effective p‑type doping of diamond by boron ion implantation.* Journal of Applied Physics, 1983. **54**(4): p. 2106-2108.

52. Fontaine, F., C. Uzan-Saguy, B. Philosoph, and R. Kalisha, *Boron implantation/insitu annealing procedure for optimal p‑type properties of diamond.* Applied Physics Letters, 1996. **68**(16): p. 2264-2266.

53. Collins, A., *Diamond electronic devices-a critical appraisal.* Semiconductor Science and Technology, 1989. **4**(8): p. 605.

54. Xu, J., M. Granger, Q. Chen, J. Strojek, T. Lister, and G. Swain, *Peer reviewed: boron-doped diamond thin-film electrodes.* Analytical Chemistry, 1997. **69**(19): p. 591A-597A.

55. Aslam, M., G. Yang, and A. Masood, *Boron-doped vapor-deposited diamond temperature microsensors.* Sensors and Actuators A: Physical, 1994. **45**(2): p. 131-137.

56. Taher, I., M. Aslam, M. Tamor, T. Potter, and R. Elder, *Piezoresistive microsensors using p-type CVD diamond films.* Sensors and Actuators A: Physical, 1994. **45**(1): p. 35-43.

57. Shintani, Y., S. Ibori, K. Igarashi, T. Naramura, M. Inaba, and H. Kawarada, *Polycrystalline boron-doped diamond with an oxygen-terminated surface channel as an electrolyte-solution-gate field-effect transistor for pH sensing.* Electrochimica Acta, 2016. **212**: p. 10-15.

58. Prins, J., *Bipolar transistor action in ion implanted diamond.* Applied Physics Letters, 1982. **41**(10): p. 950-952.

59. Geis, M., D. Rathman, D. Ehrlich, R. Murphy, and W. Lindley, *High-temperature point-contact transistors and Schottky diodes formed on synthetic boron‑doped diamond.* IEEE Electron Device Letters, 1987. **8**(8): p. 341-343.

60. Ebert, W., et al., *High-voltage Schottky diode on epitaxial diamond layer.* Diamond and Related Materials, 1997. **6**(2): p. 329-332.

61. Grot, S., W. Ebert, A. Vescan, P. Gluche, T. Borst, and E. Kohn, *The effect of surface treatment on the electrical properties of metal contacts to boron-doped*

homoepitaxial diamond film. IEEE Electron Device Letters, 1990. **11**(2): p. 100-
102.

62.   Butler, J., M. Geis, K. Krohn, J. Lawless, S. Deneault, T.Lyszczarz, D. Flechtner,
and R. Wright, *Exceptionally high voltage Schottky diamond diodes and low
boron doping.* Semiconductor Science and Technology, 2003. **18**(3): p. S67.

63.   Twitchen, D., A. Whitehead, S. Coe, J. Isberg, J. Hammersberg, T. Wikström, and
E. Johansson, *High-voltage single-crystal diamond diodes.* IEEE Transactions on
Electron Devices, 2004. **51**(5): p. 826-828.

64.   Pleskov, Y.V., *New corrosion-resistant electrodes: Synthetic diamond and
diamond-based materials. The semiconductor and structure aspects—a review.*
Protection of Metals, 2006. **42**(2): p. 103-118.

Chapter 2   The theory of chemical vapour deposition diamond

growth and electrical characteristics of synthetic diamond

2.1   Chemical vapour deposition (CVD) method of growing diamond

The recipe for making diamond is well established and has been discussed in Chapter 1

Section 1.1.1.4. It has been noted that the CVD approach of forming diamond is

characterised by the thermal decomposition of carbon-containing gases such as CH_4 or

CO mixed with a large excess of H_2[65] which plays an extremely important role in

controlling the quality and growth rate of as-grown diamond films. Therefore,

understanding the chemical component and gas phase reactions within the precursor

gases mixture is crucial to understand diamond thin film growth.

2.1.1   Gas phase chemistry of CVD diamond

Since the first breakthrough of depositing diamond on non-diamond substrates in the

late 1990's [20], a large number of reports on CVD diamond of various surface

morphology and thickness emerged within the decade [8]. In order to understand the

gas phase chemistry during growth, the first "C-H-O" phase diagram (**Figure *2.1***) was

formed by Bachmann [66], based on over 70 deposition experiments which provides a

common basis for all CVD diamond grown at low pressure. This diagram reveals that

only a well-restricted relative ratio of C, H and O can produce diamond, which implied

an independence on the nature of the gas phase precursors used.
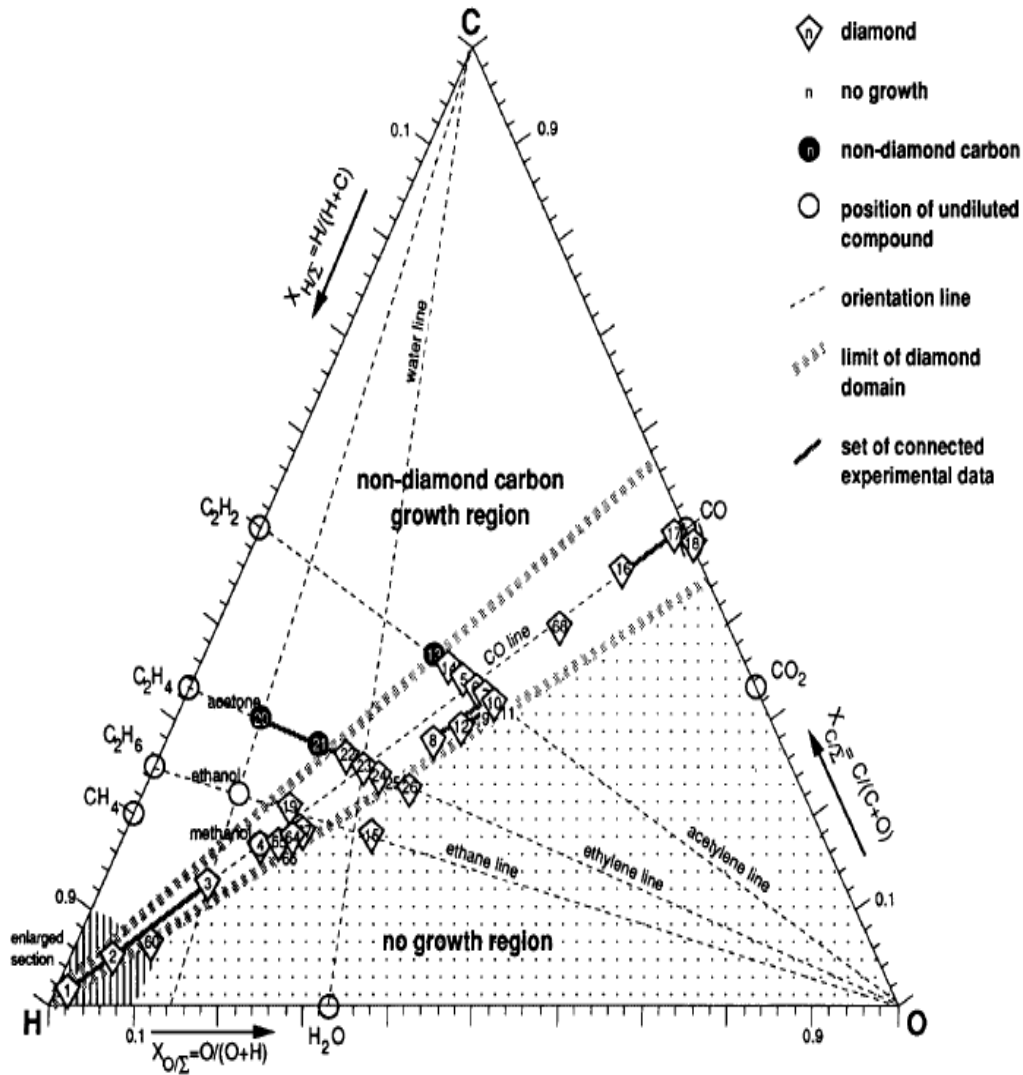
Figure 2.1 *The scheme of C-H-O phase diagram summarising over 70 deposition experiments with various gas mixture by Bachmann* [66]

It is generally believed that atomic hydrogen(·H) is a vital component in the gas phase mixture to keep the growth of the metastable diamond phase while at the same time inhibiting the nucleation of a stable non-carbon phase[67]. The role of atomic hydrogen is to act as an etch reagent which rapidly removes graphitic sp^2 carbon relative to sp^3 carbon on the growing surface, and reacts with neutral species such as CH_4 creating reactive hydrocarbon radicals (·CH_x) which can attach to a suitable active site on the substrate surface[68, 69]. In addition, ·H also retains the stability of the ongoing growth

by breaking long-chained hydrocarbons into smaller pieces to prevent the formation of carbon polymers or large ring structures which might inhibit the diamond growth[68, 70]. Therefore, a large amount of hydrogen must be used in the deposition and the typical C/H relative ratio is normally around 1%- 4%.

2.1.1.1   General CH4/H2 gas phase chemistry

Methane mixed in excess amounts of hydrogen is the most common source gas mixture used. The knowledge of the chemical component and their reaction processes in reactors have been extensively reviewed [69-72] and the general step (with sometimes a bit addition Ar or O_2) of the overall decomposition process is driven by the abstraction of hydrogen (reaction 2.1) at high temperatures,

$$CH_x + H \leftrightarrow CH_{x-1} + H_2 \quad x = 1\sim4 \qquad \text{(Reaction 2.1)}$$
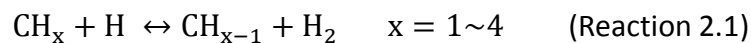
and addition (if there is a third body M) in the cooler region (reaction 2.2).

$$CH_{x-1} + H + M \leftrightarrow CH_x + M \quad x = 1\sim4 \quad \text{(Reaction 2.2)}$$

Other important specious C_2H_y are also formed by the recombination of CH_x

$$CH_x + CH_y + M \leftrightarrow C_2H_{x+y} + M \qquad \text{(Reaction 2.3)}$$

$$CH_x + CH_y + M \leftrightarrow C_2H_{x+y-1} + H \qquad \text{(Reaction 2.4)}$$

$$CH_x + CH_y + M \leftrightarrow C_2H_{x+y-2} + H_2 \qquad \text{(Reaction 2.5)}$$
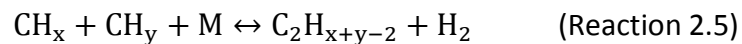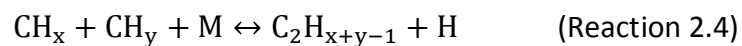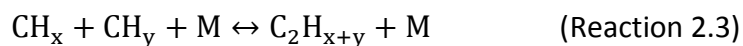
The relative concentration of various CH_x species (x≤4) is dependent on the local H atom concentration and gas temperature (T_{gas}). The concentration of various CH_x, C_2H_y as a function of the distance from the filament in the hot filament reactor (**Figure *2.2***) suggested that the main growth specious in CVD reactor is CH_3[73].
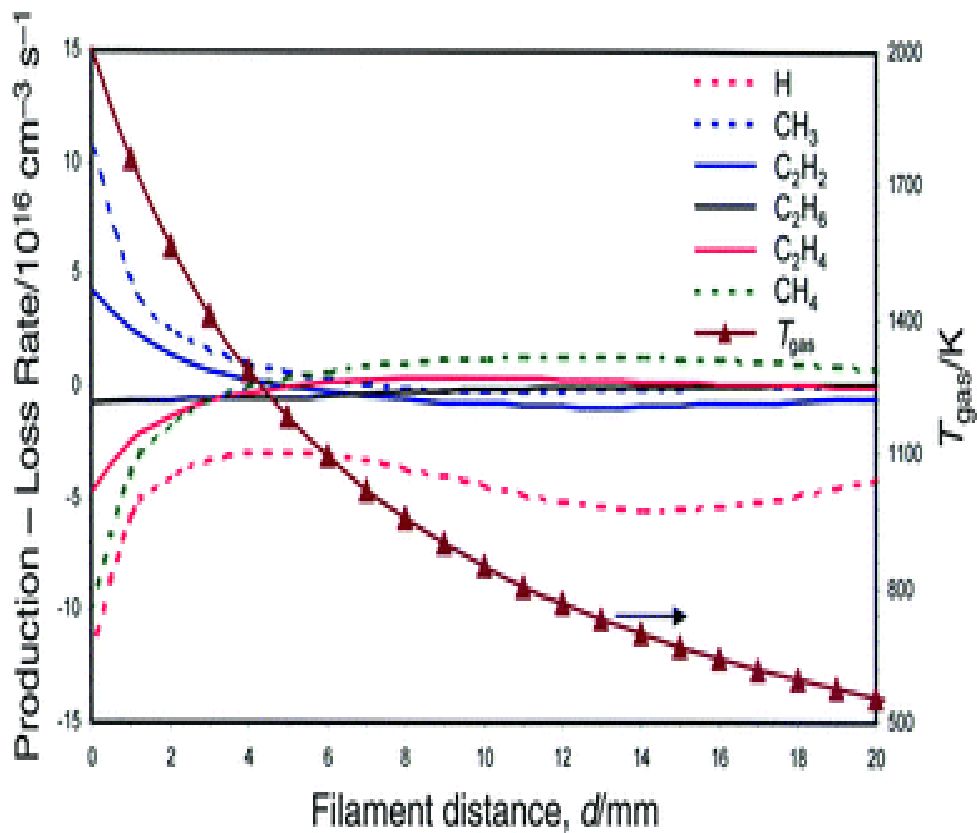
Figure 2.2 *The variation of density and spatial distribution of various CH_x and C_2H_y as a function of gas temperature* [73]

2.1.1.2 $B_2H_6/CH_4/H_2$ gas phase Chemistry

The research of gas-surface chemistry in CVD diamond is of considerable interest, as it fundamentally helps researchers obtaining a better insight into understanding the mechanism of the influence of boron doping on the structural and electrical properties of CVD semiconducting diamond. Experimental and theoretical investigations on the B/H/C gas-phase chemistry of HFCVD reactor in the Bristol Diamond group, which is also used in this thesis, were conducted by Ashfold *et al* [74-76]. In the simple mixture of B_2H_6/H_2, most B_2H_6 molecules are thermally decomposed into BH_3 [74, 76] as a primary product, (Reaction 2.6),

27

$$B_2H_6 \leftrightarrow 2BH_3 \qquad \qquad \text{(Reaction 2.6)}$$

Which then quickly converted into various B-containing active specious (BH_x) by the

"H-shifting" reaction. (Reaction 2.7)

$$BH_x + H \leftrightarrow BH_{x-1} + H_2 \quad x = 1{\sim}3 \quad \text{(Reaction 2.7)}$$

Beside H, BH_3 is the most abundant species within in the B_2H_6/H_2 gas mixture as it is

shown in **Figure 2.3**.
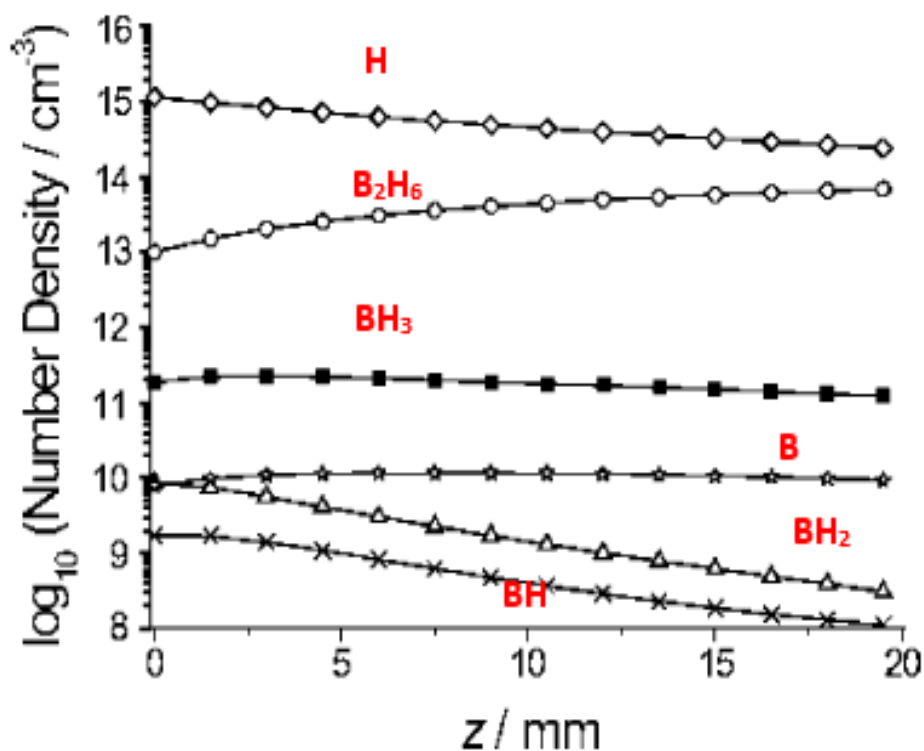
Figure 2.3 *Calculated number densities of H, B_2H_6, BH_3, BH_2, BH and B as a function of the distance between substrate surface and filaments based on the experimental results* [75].

The addition of 1% CH_4 causes the loss of [B] signal by > 30% which might be the

result of the competition reaction of H abstraction/addition between BH_x and CH_3

species [76]. However, there are still very few experimental observations on the

28

reactions between carbon-containing and boron-containing species (such as BH₃ +

C₂H₂).

2.1.2   CVD diamond growth

2.1.2.1   *Diamond growth mechanism from substrate surface*

There are many models that have been used to explain the mechanism of carbon

addition and incorporation into the diamond lattice under CVD growth conditions [77].

Basic and standard growth mechanisms are believed to be based on the process of H

abstraction and methyl (CH₃) addition [78]. The growth path varies on the different

crystalline planes (111), (110), and (100) of the substrate surfaces. The schematic in

Figure 2.4 illustrates one such growth path onto a substrate surface.
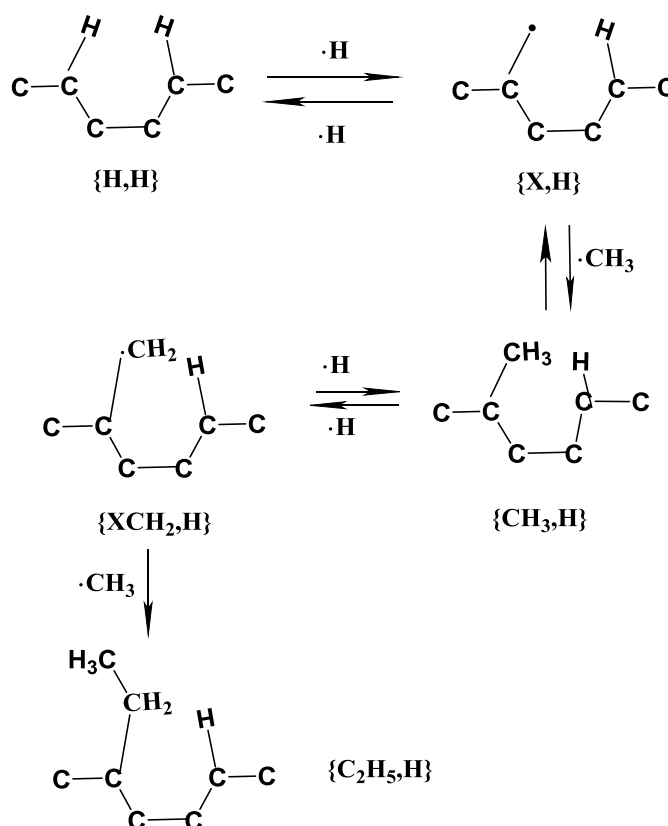
Figure 2.4 *The growth path for hydrocarbon singly bonded to the (110) site by hydrogen*

abstraction and re-termination (Adapted from [79]).

29

As shown in this figure that through abstraction of H, the reactive site on the surface has been provided for the re-attachment methyl species (CH_3) which finally leads to the incorporation of carbon atoms into the diamond lattice. The as-formed ethyl species can either form the sp^3 CH_2-CH_2 bridge structure or an ethylene group singly bonded to the surface [C_2H_3,H][77]. However, this simplified mechanism is not suitable to explain all CVD diamond growth, as it depends on the nature of substrate materials, gas phase chemistry and the reactor used [72].

2.1.2.2   *The substrate materials*

Diamond can both be homoepitaxially grown on a diamond substrate (such as polycrystalline CVD diamond, single crystal diamond) and heteroepitaxially on a non-diamond substrate, such as silicon or Mo [20]. There are some requirements for the substrate materials to meet in order to grow an adherent continuous sp^3 diamond lattice. First requirement is that the melting point of the substrate material must be higher than the temperature for diamond growth which is normally greater than 700°C[72] . This requirement precludes materials like some glasses, aluminium, plastic and some semiconductors (such as GaAs). Another requirement for the substrate material is whether its coefficient of thermal expansion (α) is comparable with that of diamond [68]. During the heating or cooling stage in a CVD reactor, very high stresses are induced in the diamond coating on substrate surfaces when the thermal-expansion coefficients of the films and the substrate vary significantly from each other. These stresses will lead to cracking or even delamination of the as-deposited thin film[80]. Therefore, materials like glass ($\alpha=8.5\times10^{-6}$ K^{-1}) or iron ($\alpha=11.8\times10^{-6}$ K^{-1}) are not desirable substrates to grow adherent diamond films.

Nucleation onto a foreign substrate is very slow due to the lack of a template for the diamond lattice for the carbon atoms to follow, which will be quickly etched back into the gas phase because of the reaction with atomic H. In order to enhance the density of nucleation sites, pre-treatment, normally called seeding, prior to deposition, is often used for CVD diamond grown on a non-diamond substrate. Manual scratching, which is simply abrading a substrate with diamond powder, or Electrospray deposition seeding, which is described in Chapter 3 section 2.1.2.

2.1.2.3   The ratio of [H]/[CH$_x$]

The ratio of atomic hydrogen and hydrocarbon species is an important factor that determines the crystal size of an as-deposited film [72].

Figure 2.5 illustrates the relationship between the [H]/[CH$_x$] ratio and grain size at different temperatures. It can be seen that the higher the [H]/[CH$_x$], the bigger the grain size of the morphology. The reason for this phenomenon is the increased re-nucleation probability provided by the increasing of CH$_x$ (especially CH$_3$) that is incorporated into the diamond lattice. However, if the concentration of CH$_x$ is too high (>10% in H$_2$), there is a large chance of forming graphitic sp^2 structures as relatively less atomic hydrogen is available to etch away the non-diamond carbon.
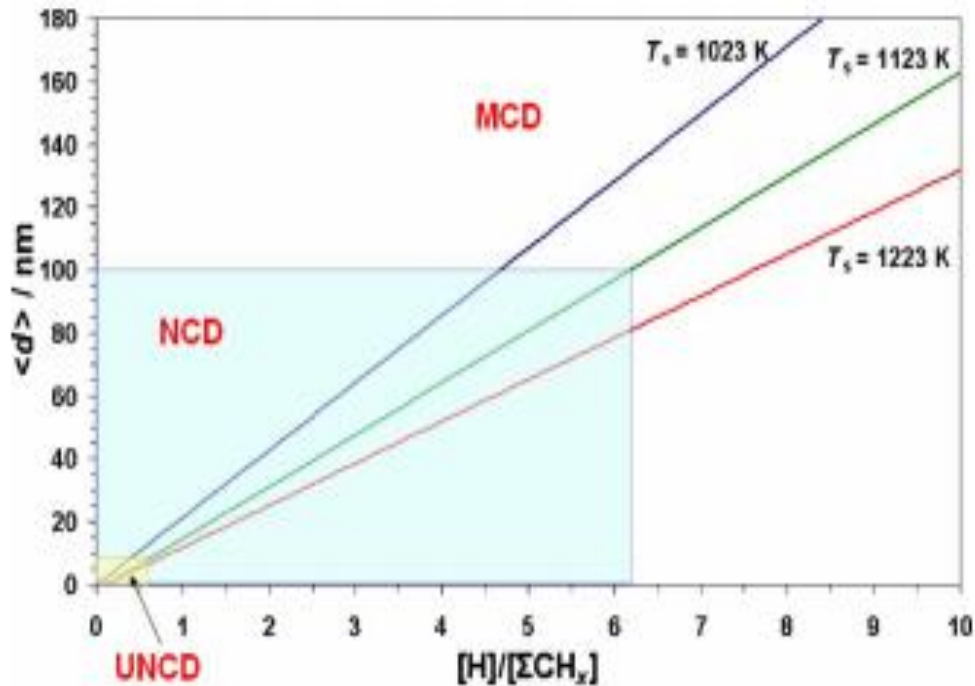
Figure 2.5 Diagram showing the average diamond grain size <d> verses the ratio of atomic

hydrogen concentration and hydrocarbon radical species ([H]/[CH$_x$] x<4) for three substrate

temperatures[81].

2.1.2.4   The α-parameter

In diamond surfaces, three basic important shapes of crystals are often observed

under SEM images: these are square (100), triangle (111) and the less well defined

(110). The α-parameter, which is also called the growth parameter, established by Wils

et al [82] to describes the orientation of diamond crystals. Modelling the kinetics of

growing rate on these three different surfaces results in equation (2.1) defined below:

$$a = \sqrt{3}\, \frac{\vartheta_{100}}{\vartheta_{111}} \qquad \qquad \text{Equation (2.1)}$$

where v_{100} and v_{111} are the growth rates along the (100) and (111) directions,

respectively.

The evolution of crystal shapes grown for different α is shown in **Figure *2.6***
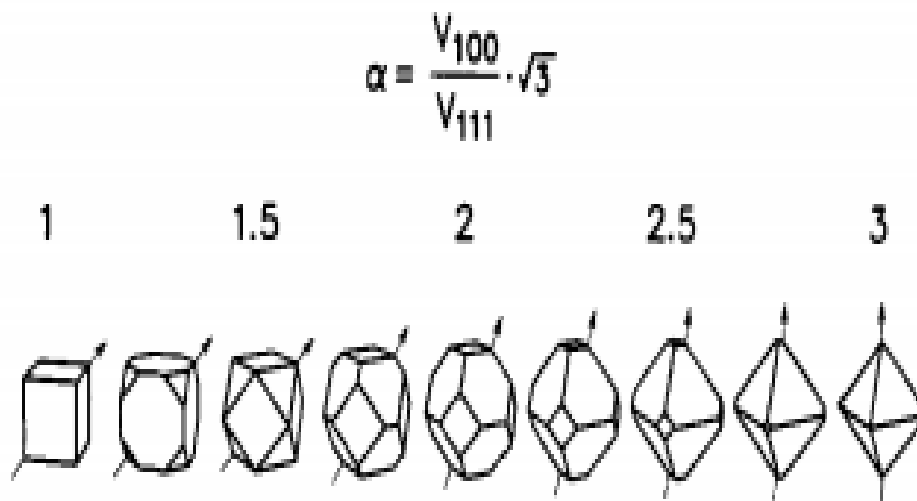
Figure 2.6 *Crystal shapes for different values of α. Arrows represent the fastest growth direction* [83].

The shape and growth direction is influenced by the substrate temperature (T_s) and the concentration of carbon-containing gas during growth. It can be seen in Equation 2.1 that the relative growth velocities of <111> and <100> play an important part in the formation of surface texture on the polycrystalline diamond. **Figure *2.7*** summarises the relationship between T_s, methane concentration and facets that form the thin film surface by using Microwave Enhanced Plasma CVD reactor (MWCVD). In this figure, at temperatures above 500°C, the majority of crystals formed are (111) facets at CH_4 concentrations above 1%. Temperatures below 500°C result in spherical balls of as-grown films.
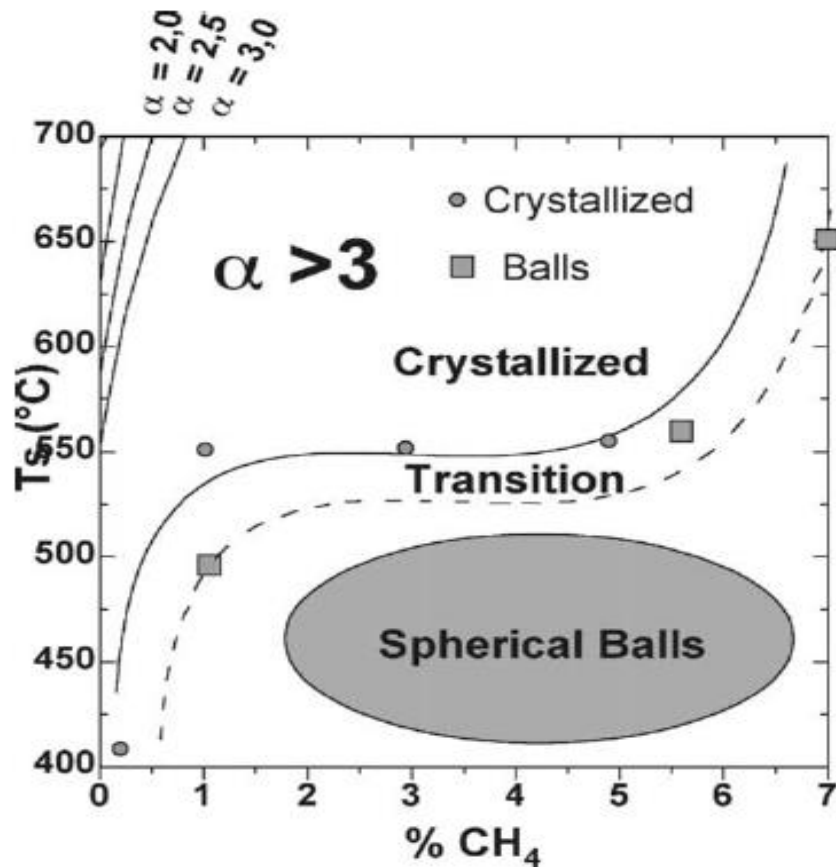
Figure 2.7 *Evolution of CVD diamond surface morphology as a function of %CH₄ and substrate temperature grown by MWCVD[84].*

2.1.3 Characterisation of defects in CVD diamond

In the previous sections discussing crystal structure and growth of CVD diamond, it has been assumed, for simplicity, that the entire diamond lattice is defect-free. However, in reality no perfect crystal exists. The existence of defects in synthetic diamond grown from a CVD process significantly influences the mechanical, physical, optical and electrical properties of as-fabricated materials. There are many different structural and compositional types of defects within the films. In this section, grain boundaries, point defects and non-diamond carbon phases are the focus in this work as they will be integral to the discussion in the result Chapters.

2.1.3.1   Grain boundaries (GBs)

Grain boundaries separate two grains with different orientation and can be usually seen in SEM images. They are two-dimensional defects within a polycrystalline CVD diamond which are usually the result of uneven growth when the material is crystallising [85]. Based on the previous discussion on CVD diamond growth in section 2.1.2, the growth of a polycrystalline diamond thin film on a seeding layer begins with the nucleation site which is scattered on the substrate. The grains then grow three-dimensionally from these "island" nucleation sites until each individual grain touches another (coalescence event) where grain boundaries form [86]. During the crystal growth stage, the microstructure of the thin film is continuously evolving according to the particular growth velocity and direction of α-parameter (**Figure 2.6**) of individual nucleation sites which result in either highly or randomly oriented surface morphology on the PCD films. Consequently, high or low angle grain boundaries can be formed.

It has been widely investigated that impurities, defects or non-diamond carbon energetically tend to gather at GBs. Experimental evidence of graphite, amorphous carbon and preferential doping of dopants within a GB area is abundant [87-92]. Therefore, GBs are expected to significantly influence the thermal and electrical transport within the as-deposited PCD thin films. Carrier[93, 94] and phonon scattering [95, 96] within the GBs has been intensively explored as it is believe that the scattering effect is one of the key parameters that control the electrical and thermal properties of PCD thin films.

2.1.3.2 Incorporation of impurities in homoepitaxial films

2.1.3.2.1 Structural and chemical analysis of point defects

Point defects are zero-dimensional defects with characteristics of thermodynamic equilibrium [97]. **Figure 2.8** briefly summarises various type of 0D defects within the lattice which includes intrinsic point defects of vacancies (V), self-interstitials (I) and extrinsic point defects of dopants or impurities occupying either substitutional or interstitial lattice sites. Electrical and thermal properties depend on the concentration of these point defects. However, the schematic shown below is a simplified feature as there are many existence forms and configuration of point defects in CVD diamond. Furthermore, point defects often cluster themselves, such as boron aggregates and vacancies clusters, or interact with each other forming defect complexes, such as (H, B), (H, vacancies). Unlike planar defects, such as grain boundaries, which can be directly observed under microscopy, point defects are difficult to observe directly. Therefore, the analysis is often carried out through some physical or optical property that these defects affect [97].

Foreign Substitutional atoms e.g., N,

Foreign interstitial atoms e.g., H, Li

Self- interstitial (I)

Vacancy (V)
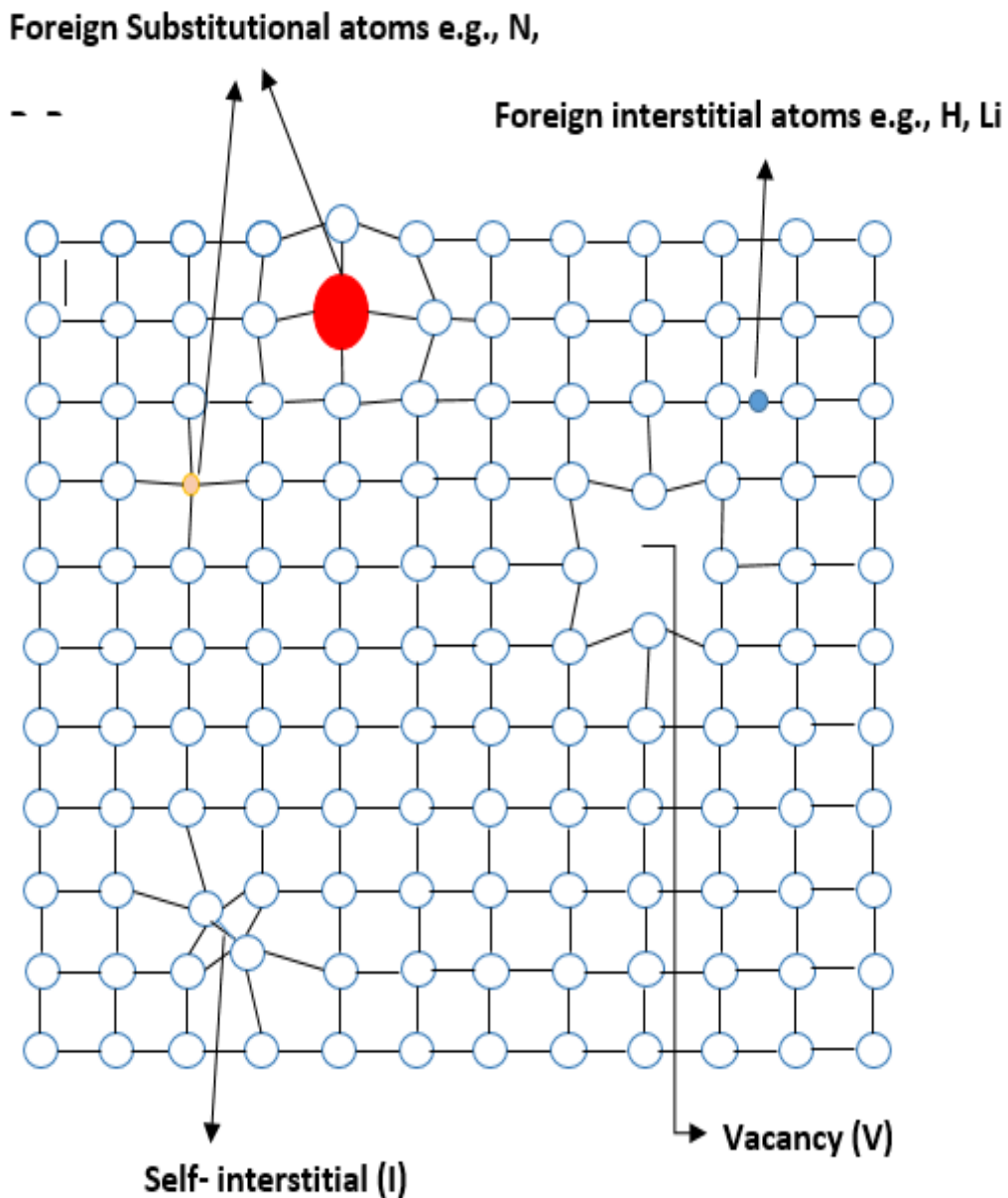
Figure 2.8 *Schematic of some point defects in CVD diamond* [97].

2.1.3.2.2   Hydrogen (H)

Hydrogen (H) is one of most common impurities contained in the CVD diamond thin

film because of the H-rich growth environment. In CVD diamond films, it has been

theoretically found that the bond-centred hydrogen (C-H-C) is more stable than the

isolated H at a tetrahedral or hexagonal interstitial site [98, 99]. This hydrogen pairing, a

H_2^* defect, is also revealed to be the most stable for a pure diamond with an activation

energy around 4.1 eV [98]. Hydrogen is often inhomogeneously distributed on the

planar defects such as grain boundaries and dislocations as well as terminating carbon

dangling bonds [97]. Furthermore, hydrogen also plays an important role in the

electrical conductivity of CVD diamond. Experimentally, CVD diamond has a surface

electrical conductivity 4-5 orders of magnitude larger than the oxidised boron doped

diamond [100, 101]. Exposing natural crystal diamond to a hydrogen plasma causes a

remarkable reduction in resistivity from $\sim 10^{16}$ $\Omega \cdot cm$ to 10^5 $\Omega \cdot cm$ [102].

  In boron-doped diamond thin films, experimental evidence shows that hydrogen can

passivate the boron acceptor electrically from p-type films into insulators [103, 104].

Theoretical calculations indicate that the formation of bond centred (B-H-C) or (B-H-B)

structures which are more stable than isolated H at the interstitial site [105] is

responsible for this passivation effect. The thermal release of H from various

substitutional boron-hydrogen complexes (B_sH_m), can recover the conductivity of

boron-doped diamond films which require annealing well above room temperature.

The calculated activation energy of B_sH_m pairs for dissociation varies widely from 0.23

eV to 2.5 eV which depends on the hydrogen numbers attached and the charge state

of these complexes [105, 106]. For instance, an experimental study found that B_sH_2 is

thermally unstable and dissociated at a temperature of 550°C [106]. Positive H^+ is a

highly mobilised species within CVD diamond with a very low migration barrier energy

(<0.2 eV), and thereby can be diffused by thermal annealing even at temperatures

below 550°C. In contrast, the neutral and negative bond-centred hydrogen have

higher migration barriers for diffusion of 1.6 eV and 2 eV, respectively [107].

Experimental data show the hydrogen diffusion coefficient in a BDD thin film is 8 −11

$\times 10^{-13}$ cm$^2 \cdot$s^{-1} at 711 °C ([B] = 1×10^{20} cm^{-3})[105]. However, the diffusion profile is very dependent on the dopant concentration, crystallographic structure and other defects state in this specific sample.

2.1.3.2.3 Boron

Due to the negative formation energy and relatively small radius of boron, it can be easily incorporated into substitutional sites in the diamond lattice [97]. Ideally, the dopant should be incorporated into the substitutional site homogenously without distorting the diamond lattice. However, experimental results reveal that over 90% of impurities are electrically inactive [108]. This is thought to be due to either boron acting as a deeper acceptor passivated by the massive amount of H within the film or boron segregating into highly defective regions. It has been widely accepted that the majority of boron atoms are taken up interstitially [109] and that pairs of interstitial neighbour boron (B$_2$) sites in the "dumbells" structure were purposed to be the reason for the superconducting properties of boron doped diamond [110]. Theoretical calculations on various (B, defect) configurations (such as B-B, B-vacancy (V) and B-self-interstitial (I)) and binding energies, indicated the possible existence of boron aggregates within BDD films [111]. Of particular interest, the calculated binding energy of self-interstitial neighbouring and substitutional boron paring (B$_2$) is around 0.2 eV and 0.7 eV respectively, which may account for deep hydrogen trap centres forming B$_2$H$_m$ complexes [111]. Thermodynamic modelling reveals that the bonding/dissociation equilibrium process is not only temperature dependent but also defect concentration dependent [112]. **Figure *2.9*** illustrates the variation of activation energy of boron as the function of boron concentration. It is very clear to see that the higher the boron concentration, the lower activation energy. **Figure *2.10*** shows the evolution of critical

temperature (T_0) at zero-binding energy as a function of boron concentration. The boron pair favours in dissociation (blue dashed line) when the temperature (T) is higher than T_0 or bonding when the $T < T_0$.
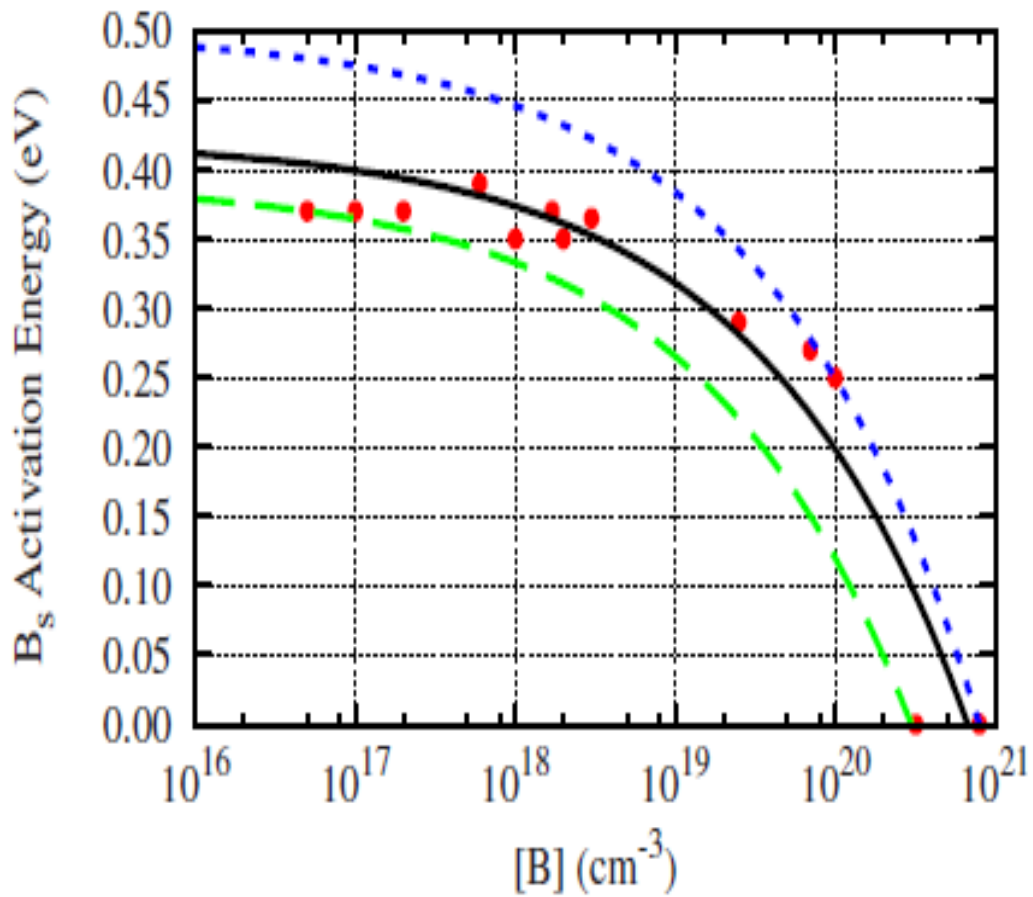
Figure 2.9 *Fitted Boron acceptor energy level (solid line) as a function of its concentration. (Dash line: lower energy bonds; Dot line: upper energy bonds; Red dot: experiment data)*[112]
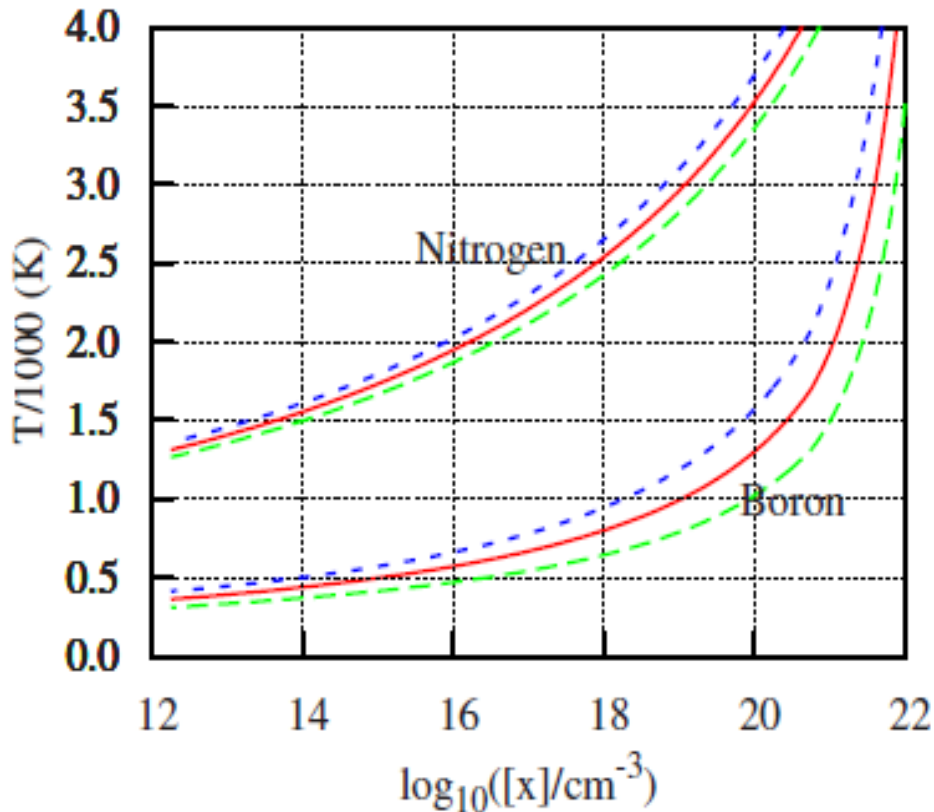
Figure 2.10 *Summary of calculated zero-binding energy critical temperature (Red solid line),$T_0(K)$, as a function of [B] and [N] concentration. (Blue dash line: positive "+" free binding energy; Green dash line: negative "-"free binding energy)* [112]

2.1.3.2.4   Non-diamond carbon phases

Graphitic sp^2 phases and amorphous carbon are the common defects existing in a diamond lattice grown by the CVD method. As discussed in section 2.1, CVD diamond growth is a kinetically competitive process of different forms of carbon radicals (CH_x,*x* <4) resulting in the film ranging from diamond (sp^3 bonding) to diamond-like carbon (DLC, mixed sp^3 and sp^2 bonding networking) and to graphite (sp^2 bonding). No CVD diamond thin film consists of only pure sp^3 tetrahedral bonding. Experimental evidence shows the direct emission from grain boundaries of the surface of un-doped CVD diamond thin films suggesting graphitic impurities are responsible for this emission [113]. Graphitisation caused by ion implantation degrades the electrical properties of p-

type semiconducting diamond thin film used for electronic device by reducing the carrier mobility as a scattering channel [51]. Post-annealing at temperatures not higher the graphitisation temperature (>1200°C) under vacuum can remove the graphitic layer within ion implantation CVD diamond thus enhancing the conductivity of as-deposited films [51, 114].

2.2 Hall Effect electrical properties of p-type semiconducting CVD diamond

2.2.1 The formation of p-type diamond

The addition of a small amount of foreign atoms into the host lattice changes the electrical properties of a material. In intrinsic diamond, four valence electrons from each carbon are shared with 4 other neighbouring carbons forming four covalent bonds. Each valence electron from carbon is fully used for bonding with other four carbons, therefore there are no excess electrons or holes in the pure diamond which means the concentration of electrons and holes will be approximately equal. With a boron atom doped into a substitutional site of a host diamond lattice, three valence electrons of boron are used to form covalent bonds with neighbouring carbon atoms leaving the 4th bond uncompleted. Boron then attracts one electron from a neighbouring atom to form the 4th bond which creates a hole left in an adjacent atom. Due to the loss of an electron from a neighbouring atom and its transfer to boron, the hole is positively charged and boron is negatively charged. Doping with boron results in excess holes present in the semiconductor material which can transport electric current when an electrical field is applied. This doped diamond material is a p-type semiconductor with a bonding represented in **Figure *2.11***. Since the concentration of boron in a BDD can be of the magnitude 10^{21} cm^{-3}, the majority charge carriers are

holes in p-type semiconducting diamond. Boron is also referred to as an acceptor as it needs to obtain one electron to complete the 4th bond.
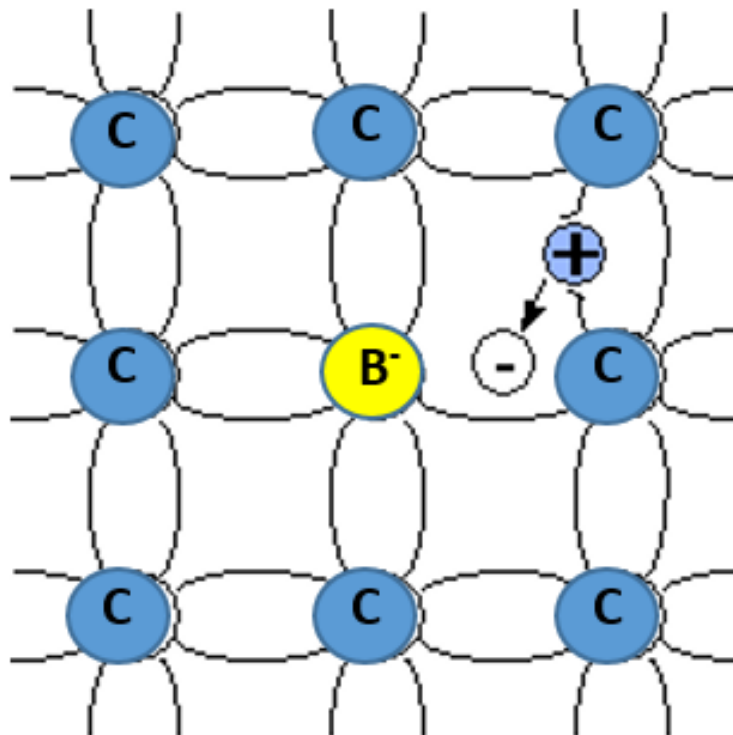
Figure 2.11 *Schematic diagram of a p-type semiconducting diamond lattice structure.*

N-type diamond, on the other hand, is formed by doping atoms with more valence electrons than C atoms, typically N or P. In the case of N with five valence electrons, one extra electron is free because other four electrons are used to fully satisfy the four covalent bonds with the neighbouring atoms, leaving the N atom positively charged. Therefore, the majority of carriers in n-type diamond are electrons. As the N gives an extra electron to the materials, it is also called a donor as it is donating an electron to the lattice.

2.2.2 Carrier transport in electrical field

2.2.2.1 The theory of Hall Effect phenomenon

The Hall Effect phenomenon is used to describe the motion of electrical carriers under a magnetic field which was first shown by Edwin Hall in 1879[115]. The basic principle of the Hall Effect is the Lorentz force which is the driving force to guide the motion of charge carriers. The basic theory is shown in **Figure *2.12***. When an electric current flows along the x-direction of the conductor while in a magnetic field perpendicular (z-direction) to the current direction, the charged carriers experience a resulting force named as Lorentz force and are deflected in the y-direction. Positively charged carriers travel in the same direction as the magnetic force and vice versa for the negatively charged carriers. These negative and positive charges are deflected on the opposite side respectively, and will build up a potential difference between the two sides of the sample along the y-direction thereby producing an electric field (E_H). The resulting electric and applied magnetic forces will eventually reach a balance, forming a constant and measurable voltage between the two sides of the conductor. The presence of this transverse voltage along z direction is called the Hall voltage (V_H).
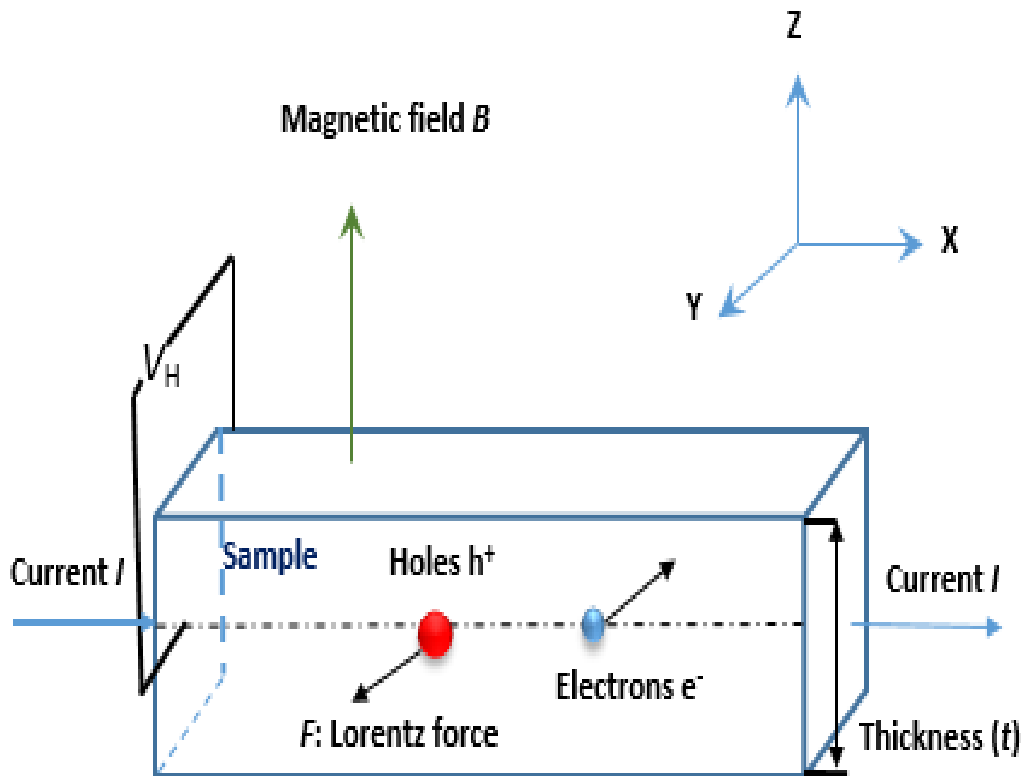
Figure 2.12 *The physical principle of Hall Effect measurement.*

2.2.2.2   Simple mathematics of carrier transport related to Hall Effect phenomenon

2.2.2.2.1   The derivation of Hall voltage (V_H) and carrier density (p)

The Lorentz force on the holes (h^+) along the y-direction based on **Figure *2.12*** is described in equation 2.1:

$$F_L = q\vartheta_y B_y \qquad \text{Equation 2.1}$$

where F_L: Lorentz force; *q*: elementary charge; ϑ_y: the velocity of a hole; B_y, the magnetic field.

As the holes gradually accumulate on the front side (y-direction) of the material, the potential difference increases between the two sides. The resulting electric field (-y direction) exerts a force on the holes defined in equation 2.2:

$$F_E = qE_{-y} \qquad \text{Equation 2.2}$$

where F_E: electric force; E_{-y}: Electrical field. The electrical field equation is defined as:

$$E_H = \frac{V_H}{t} \qquad \text{Equation 2.3}$$

where E_H: electric field; V_H: Hall voltage; t: sample thickness. When these two forces are balanced, i.e. when $F_L = F_E$, the result equation by combining Equation 2.1,2.2 and 2.3 results in:

$$q\vartheta B = qE_H = q\frac{V_H}{t} \qquad \text{Equation 2.4}$$

$$\vartheta B = \frac{V_H}{t} \qquad \text{Equation 2.5}$$

By defining the current density (J) of applied current (I) in equation 2.6

$$J = qpB = \frac{I}{wt} \qquad \text{Equation 2.6}$$

where J: current density; p: the density of hole; B: electrical field; wt: the cross-section area of the materials that current goes through. Combining Equation 2.5 and 2.6 together produces equation 2.7:

$$V_H = \frac{IB}{qpw} \qquad \text{Equation 2.7}$$

As shown in Equation 2.7, the Hall voltage can be measured by the Hall Effect for a known current, magnetic field and sample dimension the carrier density can be measured.

2.2.2.2.2 *The derivation of carrier mobility (μ)*

The conductivity (σ) of a p-type semiconductor maybe expressed as in equation 2.8

$$\sigma = \frac{1}{\rho} = \frac{1}{R_s t} = qp\mu \quad \text{Equation 2.8}$$

where ρ: resistivity of the sample; R_s: resistance of a sheet; μ: carrier mobility. Equation 2.8 can be re-written into:

$$\mu = \frac{1}{qpR_s t} \qquad \text{Equation 2.9}$$

Therefore, the carrier mobility can be calculated by measuring the Hall voltage and carrier concentration. The Hall Effect measurement is set up based on Equation 2.7 and 2.9 which will be discussed in Chapter 3 section 3.5.

2.2.2.3 Free carrier dynamics in CVD diamond

Based on the mathematics discussed, it can be seen that the diamond material contains a finite amount of free charge carrier. The electrical conductivity of semiconducting diamond is determined by the concentration and motion of free carriers [116]. The mobility describes the ability of the carriers to move within the material when influenced by an electric field and is limited by the scattering effect of defects within in the film [117]. In CVD diamond, acoustic phonons and ionised impurities are the dominant sources of scattering [118]. Specifically, acoustic phonon scattering is dominant in pure diamond especially at high temperature as phonon vibration increases with increasing thermal energy. In the case of doped diamond, the impurities such as dopants are the dominant scattering source, assuming the impurities are shallow enough to be ionised[118]. Considering the case of boron doped homoepitaxial diamond, the Hall hole mobility of boron doped polycrystalline CVD diamond varies from 0.1 $cm^2 \cdot V^{-1} \cdot s^{-1}$ to 150 $cm^2 \cdot V^{-1} \cdot s^{-1}$(Figure 1.4) which is considerably lower than that of undoped or natural diamond (>1000 $cm^2 \cdot V^{-1} \cdot s^{-1}$). From figure 1.4,

the higher the boron concentration, the stronger the ionised atom scattering effect, therefore, the lower the carrier mobility. One of the most effective ways to enhance the mobility is by reducing the dopant concentration. However, the electrical conductivity will also decrease as the cost of reduced boron concentration.

Other scattering centres, such as the structural defects and microstructure of crystals also contribute to the low carrier mobility in polycrystalline diamond. Due to the high density of grain boundaries in PCD or even NCD diamond, the as-measured carrier mobility could reduce to as low as around of 1 -3 $cm^2 \cdot V^{-1} \cdot s^{-1}$ for the same amount of boron concentration (4×10^{17} cm^{-3}) in the homoepitaxial film which is around 100 $cm^2 \cdot V^{-1} \cdot s^{-1}$[119, 120]. PCD films with aligned (100) grains also show the improved carrier mobility but still lower than the single crystal diamond[121]. Vacancies typically created by ion implantation are another scattering or trapping centre that exists within the BDD films[122]. Thermal annealing after deposition is often used to reduce the defects in order to enhance the carrier mobility of p-type diamond.

2.3   Summary

The growth mechanism of CVD diamond and electrical properties of p-type semiconducting diamond have been discussed in this Chapter for the purpose of explaining results in Chapters 4, 5 and 6. Diamond thin film growth depends on its gas phase component, the nature of the substrate material and growth conditions, such as the reactor and substrate temperature, resulting in a diamond thin film with various surface morphologies which may be utilised in different applications. In other words, diamond crystallisation and growth can be considered as a combination of physical aspects (surface transformations and diffusion) and chemical aspects (thermodynamics

and kinetics of gas phase reaction) [67]. The research progress of understanding the growth mechanism and the defects existing in CVD diamond can be a strong force that pushes forward the development of diamond-based devices. The performance of p-type diamond thin films in electronic devices is significantly influenced by defects presented during the growth. Therefore, different kinds of main defects and their characteristics in diamond have been summarised in order to understand the electrical behaviour. Finally, a homoepitaxial boron doped diamond thin film was fabricated in this thesis to explore the optical, physical and electrical behaviour under thermal annealing procedure.

2.4 References

65.   Bachmann, P.K. and W. van Enckevort, *Diamond deposition technologies.* Diamond and Related Materials, 1992. 1(10-11): p. 1021-1034.

66.   Bachmann, P.K., D. Leers, and H. Lydtin, *Towards a general concept of diamond chemical vapour deposition.* Diamond and Related Materials, 1991. 1(1): p. 1-12.

67.   Badzian, A.R. and R.C. DeVries, *Crystallization of diamond from the gas phase; Part 1.* Materials Research Bulletin, 1988. 23(3): p. 385-400.

68.   May, P.W., *Chemical vapour deposition–A route to microcrystalline, nanocrystalline, ultrananocrystalline and single crystal diamond films.* Chapter, 2007. 6: p. 145-176.

69.   Railkar, T.A., W. Kang, H. Windischmann, A. Malshe, H. Naseem, J. Davidson, W.Brown, *A critical review of chemical vapor-deposited (CVD) diamond for electronic applications.* Critical Reviews in Solid State and Materials Sciences, 2000. 25(3): p. 163-277.

70.   Gruen, D.M., *Nanocrystalline diamond films 1.* Annual Review of Materials Science, 1999. 29(1): p. 211-259.

71.   Butler, J.E. and H. Windischmann, *Developments in CVD-diamond synthesis during the past decade.* MRS Bulletin, 1998. 23(09): p. 22-27.

72.   May, P.W., *Diamond thin films: a 21st-century material.* Philosophical Transactions of the Royal Society of London A: Mathematical, Physical and Engineering Sciences, 2000. 358(1766): p. 473-495.

73.   Ashfold, M.N., et al., *Unravelling aspects of the gas phase chemistry involved in diamond chemical vapour deposition.* Physical Chemistry Chemical Physics, 2001. 3(17): p. 3471-3485.

74.   Cheesman, A., J.N. Harvey, and M.N. Ashfold, *Computational studies of elementary steps relating to boron doping during diamond chemical vapour deposition.* Physical Chemistry Chemical Physics, 2005. 7(6): p. 1121-1126.

75.   Comerford, D.W., et al., *Experimental and modeling studies of B atom number density distributions in hot filament activated B_2H_6/H_2 and $B_2H_6/CH_4/H_2$ gas mixtures.* The Journal of Physical Chemistry A, 2006. 110(9): p. 2868-2875.

76.   Mankelevich, Y.A., M. Ashfold, D. Comerford, J. Ma, and J. Richley, *Boron doping: B/H/C/O gas-phase chemistry; H atom density dependences on pressure and wire temperature; puzzles regarding the gas-surface mechanism.* Thin Solid Films, 2011. 519(14): p. 4421-4425.

77.   Butler, J., Y.Mankelevich, A. Cheesman, J. Ma, and M.Ashfold, *Understanding the chemical vapor deposition of diamond: recent progress.* Journal of Physics: Condensed Matter, 2009. 21(36): p. 364201.

78.   Harris, S.J., *Mechanism for diamond growth from methyl radicals.* Applied Physics Letters, 1990. 56(23): p. 2298-2300.

79.   Butler, J.E., L.Richard, L.Woodin, M. Brown, and P. Fallon, *Thin Film Diamond Growth Mechanisms [and Comment].* Philosophical Transactions of the Royal Society of London. Series A: Physical and Engineering Sciences, 1993. 342(1664): p. 209-224.

80. Singh, R.K., K. Singh, D. Gilbert, J. Fitz-Gerald, S. Harkness, and D. Lee, *Engineered interfaces for adherent diamond coatings on large thermal-expansion coefficient mismatched substrates.* Science, 1996. 272(5260): p. 396.

81. May, P., M. Ashfold, and Y.A. Mankelevich, *Microcrystalline, nanocrystalline, and ultrananocrystalline diamond chemical vapor deposition: Experiment and modeling of the factors controlling growth rate, nucleation, and crystal size.* Journal of Applied Physics, 2007. 101(5): p. 053115.

82. Wild, C., R. Kohl, N. Herres, W. Miiller-Sebert and P. Koidl, *Oriented CVD diamond films: twin formation, structure and morphology.* Diamond and Related Materials, 1994. 3(4-6): p. 373-381.

83. Wild, C., P.Koidl, W.Müller-Sebert, H.Walcher, R.Kohl, N.Herres, and R.Locher *Chemical vapour deposition and characterization of smooth {100}-faceted diamond films.* Diamond and Related Materials, 1993. 2(2-4): p. 158-168.

84. Gicquel, A., K. Hassouni, F. Silva, and J. Achard, *CVD diamond films: from growth to applications.* Current Applied Physics, 2001. 1(6): p. 479-496.

85. Steeds, J., A. Gilmore, K. Bussmann, *On the nature of grain boundary defects in high quality CVD diamond films and their influence on physical properties.* Diamond and Related Materials, 1999. 8(6): p. 996-1005.

86. Graebner, J., S. Jin, G. Kammlott, J. Herb, and *C. Gardinier, Unusually high thermal conductivity in diamond films.* Applied Physics Letters, 1992. 60(13): p. 1576-1578.

87. Knight, D.S. and W.B. White, *Characterization of diamond films by Raman spectroscopy.* Journal of Materials Research, 1989. 4(2): p. 385-393.

88. Windischmann H., and C. Epps, *Intrinsic stress in diamond films prepared by microwave plasma CVD.* Journal of Applied Physics, 1991. 69(4): p. 2231-2237.

89. Turner, S., H. Idrissi, A. F. Sartori, S. Korneychuck, Y.-G. Lu, J. Verbeeck, M. Schreck, and G. Van Tendeloo, *Direct imaging of boron segregation at dislocations in B: diamond heteroepitaxial films.* Nanoscale, 2016. 8(4): p. 2212-2218.

90. Sato, Y. and M. Kamo, *Texture and some properties of vapor-deposited diamond films.* Surface and Coatings Technology, 1989. 39: p. 183-198.

91. Schauer, S., J. Flemish, and R. Wittstruck, *Phosphorus incorporation in plasma deposited diamond films.* Applied Physics Letters, 1994. 64(9): p. 1094-1096.

92. Zhu, W., C. A. Randall, A. R. Badzian, and R. Messier, *Graphite formation in diamond film deposition.* Journal of Vacuum Science & Technology A: Vacuum, Surfaces, and Films, 1989. 7(3): p. 2315-2324.

93. Liu, W., M. Shamsa, I. Calizo, and A. A. Balandina, *Thermal conduction in nanocrystalline diamond films: Effects of the grain boundary scattering and nitrogen doping.* Applied Physics Letters, 2006. 89(17): p. 171915.

94. Steinhauser, J., S. Faÿ, N. Oliveira, E. Vallat-Sauvain, and C. Ballif, *Transition between grain boundary and intragrain scattering transport mechanisms in boron-doped zinc oxide thin films.* Applied Physics Letters, 2007. 90(14): p. 142107.

95. Rowe, D. and V. Shukla, *The effect of phonon‐grain boundary scattering on the lattice thermal conductivity and thermoelectric conversion efficiency of heavily doped fine‐grained, hot‐pressed silicon germanium alloy.* Journal of Applied Physics, 1981. 52(12): p. 7421-7426.

96. Graebner, J., M. E. Reiss, L. Seibles, T. M. Hartnett, R. P. Miller, and C. J. Robinson, *Phonon scattering in chemical-vapor-deposited diamond.* Physical Review B, 1994. 50(6): p. 3702.

97. Pan, L.S. and D.R. Kania, *Diamond: electronic properties and applications*. 2013: Springer Science & Business Media.

98. Upadhyay, A., A.K. Singh, and A. Kumar, *Electronic structure and stability of hydrogen defects in diamond and boron doped diamond: A density functional theory study.* Computational Materials Science, 2014. 89: p. 257-263.

99. Briddon, P., R. Jones, and G. Lister, *Hydrogen in diamond.* Journal of Physics C: Solid State Physics, 1988. 21(30): p. L1027.

100. Hayashi, K., S.Yamanaka, H. Okushi, and K. Kajimura, *Study of the effect of hydrogen on transport properties in chemical vapor deposited diamond films by Hall measurements.* Applied Physics Letters, 1996. 68(3): p. 376-378.

101. Hayashi, K., S.Yamanaka, and H.Watanabe, *Investigation of the effect of hydrogen on electrical and optical properties in chemical vapor deposited on homoepitaxial diamond films.* Journal of Applied Physics, 1997. 81(2): p. 744-753.

102. Landstrass, M. and K. Ravi, *Hydrogen passivation of electrically active defects in diamond.* Applied Physics Letters, 1989. 55(14): p. 1391-1393.

103. Ogura, M., N. Mizuochi, S. Yamasaki, and H. Okushi, *Passivation effects of deuterium exposure on boron-doped CVD homoepitaxial diamond.* Diamond and Related Materials, 2005. 14(11): p. 2023-2026.

104. Barjon, J., J. Chevallier, F. Jomard, and C. Baronet, *Electron-beam-induced dissociation of B–D complexes in diamond.* Applied Physics Letters, 2006. 89(23): p. 232111.

105. Goss, J., P. Briddon, R. Jones, Z Teukam, and D. Ballutaud, *Deep hydrogen traps in heavily B-doped diamond.* Physical Review B, 2003. 68(23): p. 235209.

106. Goss, J. and P. Briddon, *Dissociation of B–H pairs in diamond as enhanced by electronic excitation and electron capture: Computational modeling.* Physical Review B, 2008. 77(3): p. 035211.

107. Goss, J.P., P. Briddon, S. Sque, and R. Jones, *Boron-hydrogen complexes in diamond.* Physical Review B, 2004. 69(16): p. 165215.

108. Chen, Y.-H., C.-T. Hu, and I.-N. Lin, *Defect structure and electron field-emission properties of boron-doped diamond films.* Applied Physics Letters, 1999. 75(18): p. 2857-2859.

109. Utyuzh, A., Y.A. Timofeev, and A. Rakhmanina, *Effect of boron impurity on the Raman spectrum of synthetic diamond.* Inorganic materials, 2004. 40(9): p. 926-931.

110. Pogorelov, Y.G. and V. Loktev, *Metallization in the boron-doped diamond C B x.* Physical Review B, 2005. 72(7): p. 075213.

111. Goss, J. and P. Briddon, *Theory of boron aggregates in diamond: First-principles calculations.* Physical Review B, 2006. 73(8): p. 085204.

112. MacLeod, R.M., S. W. Murray, J. P. Goss, P. R. Briddon, and R. J. Eyre, *Model thermodynamics and the role of free-carrier energy at high temperatures: Nitrogen and boron pairing in diamond.* Physical Review B, 2009. 80(5): p. 054106.

113.   Chatterjee, V., R. Harniman, P. W. May, and P. K. Barhai, *Direct observation of electron emission from the grain boundaries of chemical vapour deposition diamond films by tunneling atomic force microscopy.* Applied Physics Letters, 2014. 104(17): p. 171907.

114.   Fontaine, F., C. Uzan‑Saguy, and R. Kalish, *Boron implantation/in situ annealing procedure for optimal p‑type properties of diamond.* Applied Physics Letters, 1996. 68(16): p. 2264-2266.

115.   Hall, E.H., *On a new action of the magnet on electric currents.* American Journal of Mathematics, 1879. 2(3): p. 287-292.

116.   Denisenko, A. and E. Kohn, *Diamond power devices. Concepts and limits.* Diamond and Related Materials, 2005. 14(3–7): p. 491-498.

117.   Pernot, J., P. N. Volpe, F. Omnès, and P. Muret, *Hall hole mobility in boron-doped homoepitaxial diamond.* Physical Review B, 2010. 81(20): p. 205203.

118.   Nebel, C.E., *Electronic properties of CVD diamond.* Semiconductor Science and Technology, 2003. 18(3): p. S1.

119.   Mori, Y., et al., *Characterization of homoepitaxial diamond films grown from carbon monoxide.* Japanese Journal of Applied Physics, 1993. 32(10R): p. 4661.

120.   Looi, H.J., R.B. Jackman, and J.S. Foord, *High carrier mobility in polycrystalline thin film diamond.* Applied Physics Letters, 1998. 72(3): p. 353-355.

121.   Stoner, B., C. Kao, D.M. Malta, and R.C. Glass, *Hall effect measurements on boron‑doped, highly oriented diamond films grown on silicon via microwave plasma chemical vapor deposition.* Applied physics letters, 1993. 62(19): p. 2347-2349.

122.   Thonke, K., *The boron acceptor in diamond.* Semiconductor Science and Technology, 2003. 18(3): p. S20.

Chapter 3 Experimental methods

3.1 Sample treatments

3.1.1 Acid cleaning

Acid cleaning is a traditional and effective way to provide a clean surface for further thin film deposition. By heating up a mixture solution of 100 ml sulfuric acid and 6.5g potassium nitrate at 200 °C for 30 minutes, non-diamond species, such as metallic combinations and graphite is removed from the surface of the substrate. The substrate is then rinsed with deionized water and dried under argon. The surface of the diamond substrate is oxygen-terminated this stabilises any unstable "dangling-bonds".

3.1.2 Electrospray seeding

To grow diamond on a non-diamond substrate, seeding methods are commonly used to assist the initiation of diamond growth. To investigate the influence of seeding on the boron incorporation and distribution throughout the diamond layer, ionised nanodiamond droplets (3.89×10^{14} g·ml^{-1}) were seeded on the smooth nucleation side of polycrystalline diamond (PCD) substrates by applying a high voltage in an electrospray setup (**Figure *3.1***).
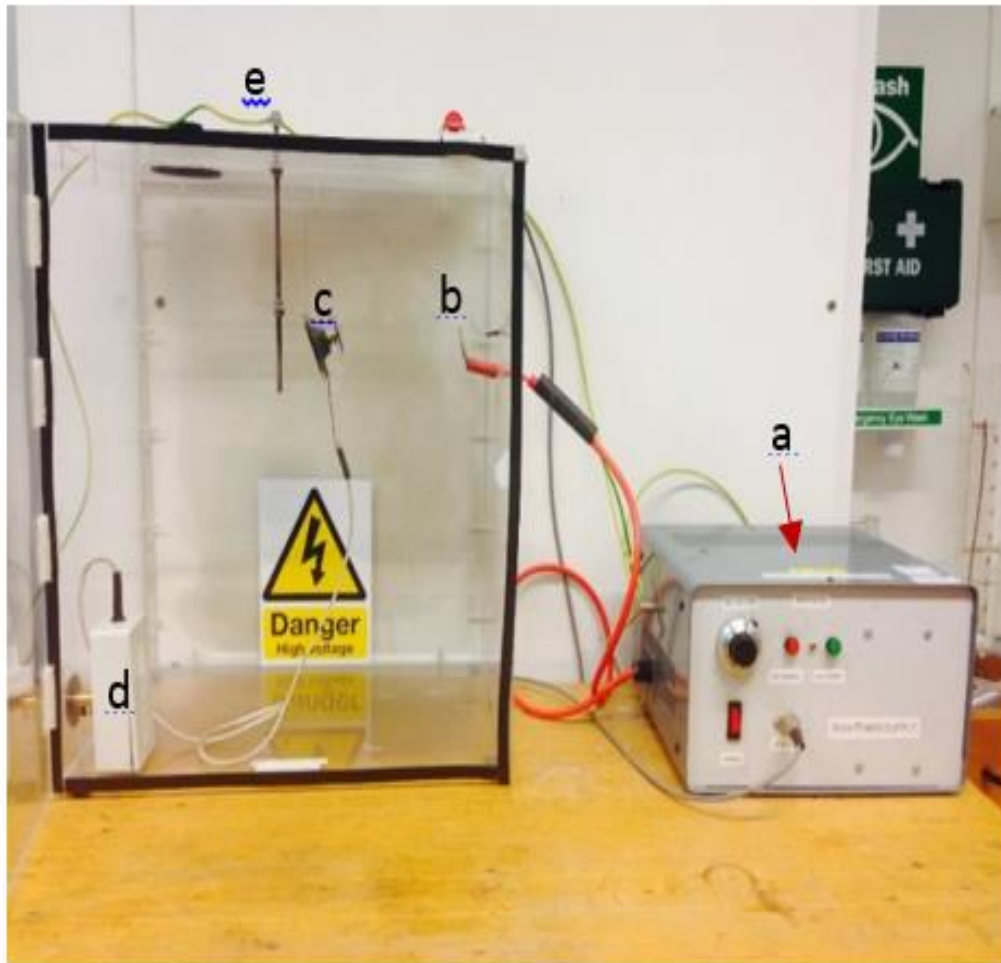
Figure 3.1*: Photograph of the electrospray equipment: a. High voltage power supply b. Capillary nozzle c. Sample mounted on motorised wheel d. Motor control e. Grounding point*

Firstly, 3.3 ± 0.6 nm detonation nanodiamond is uniformly dispersed into 25 ml methanol by sonicating for one hour to avoid particle aggregation. Then, the as-prepared solution (1ml) is injected into the syringe connected to a capillary nozzle (b in **Figure 3.1**), this supplies a constant flow of solution which is ionised by applying 35 kV to the metal syringe needle relative to the grounded substrate surface. Rotating the substrate mount at up to 1500 r.p.m. makes the seeds uniformly dispersed on the substrate surface.

3.1.3 Annealing

Samples were sealed in evacuated quartz tubes (1.0×10^{-6} torr) which were degassed at 200°C for 3 hours prior to sealing.
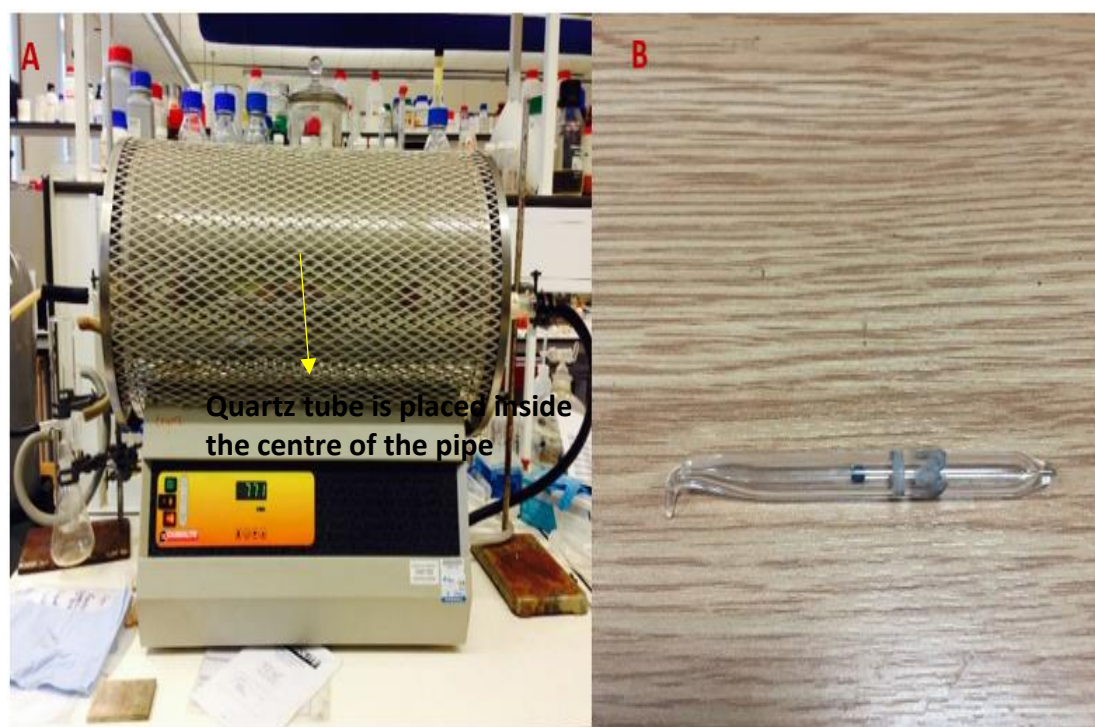
Figure 3.2. *The photograph of annealing set up (A) and quartz tube contained one sample (B).* The sealed quartz tube with the sample inside was placed in the centre of the furnace where a constant temperature was maintained over the whole sample surface. Two parameters are changed (time and temperature) in order to investigate the influence of thermal annealing on the electrical properties of as-grown samples. The annealing temperature used in this work was varied from 700°C to 1200°C and the time changed from 20 minutes to 120 minutes. All samples were annealed at the temperature ramp rate set to 10°C·min^{-1}. All tubes were allowed to cool naturally within the furnace which took 8 hours to reach room temperature.

3.2 Hot Filament Chemical Vapour Deposition (HFCVD)

Chemical vapour deposition (CVD) is a commonly-used method to fabricate solid thin diamond films commercially. By decomposing a mixture of precursor gases into an active gaseous species, the target film is deposited on a heated substrate surface through a dynamic gas-phase chemical reaction. Several decomposition methods can be used to activate the precursor gases such as thermal techniques, electric discharge and combustion flame. Although these methods differ from each other, they all share a similar reactant gas. A small amount of methane (CH_4) (around 1%-5%) blended into pure hydrogen (H_2) is normally used to grow diamond with various dopant-containing gas (such as boron and nitrogen). Altering the concentration of CH_4 will result in a different surface morphology with a range of various grain sizes from ultra-nanocrystalline to microcrystalline and will also influence the growth quality. The substrate material is another key parameter to influence the morphology and crystal structure of as-grown films. They can be classified into two sets: diamond and non-diamond substrates. Diamond films deposited onto a diamond substrate tend to grow homoepitaxially where the substrate lattice structure and crystal orientation are followed through to the grown diamond film.
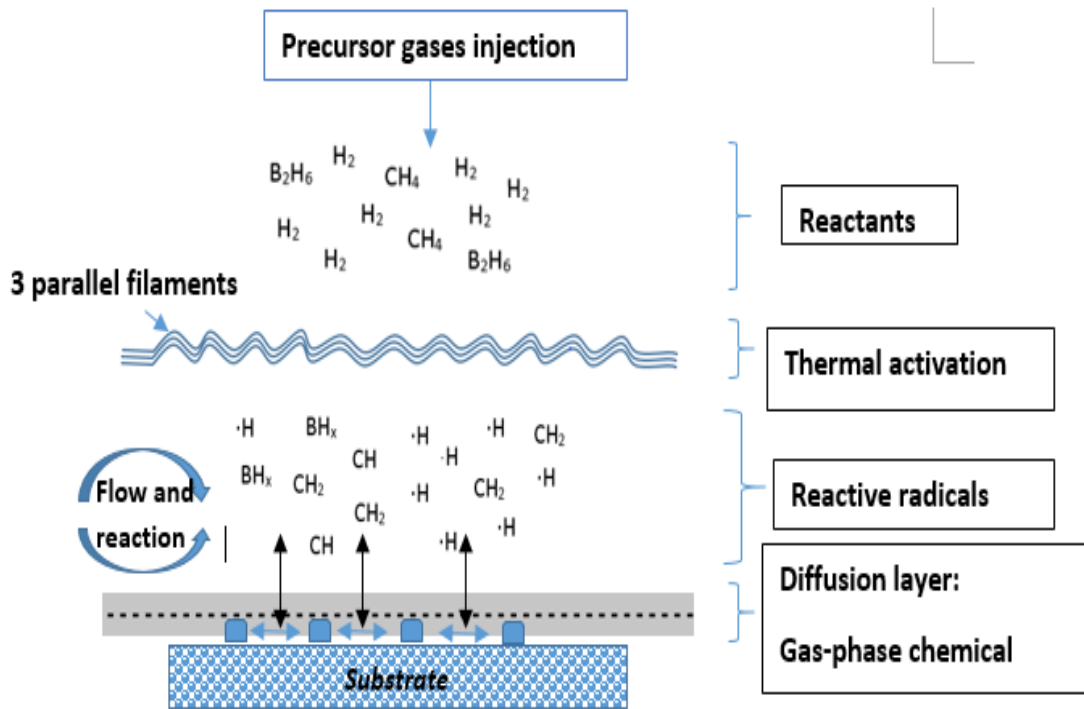
Figure 3.3. *A simple schematic diagram of the chemical mechanism of CVD reactor. (Adapted from [68])*

As shown in **Figure 3.3**, a mixture of gases of CH_4, H_2 and B_2H_6 is injected into the reactor at known flow rates and compositions. Three tantalum filaments are resistively heated to generate a high-temperature gas (2100°C). Both the high gas temperature and the catalytic effect of the filament surface act to break chemical bonds in the gases into the relatively smaller but highly reactive radicals (CH_x and BH_x), ions and atomic hydrogen (·H). These species diffuse to the heated substrate surface and participate in chemical reactions which lead to the deposition of a boron doped diamond film.
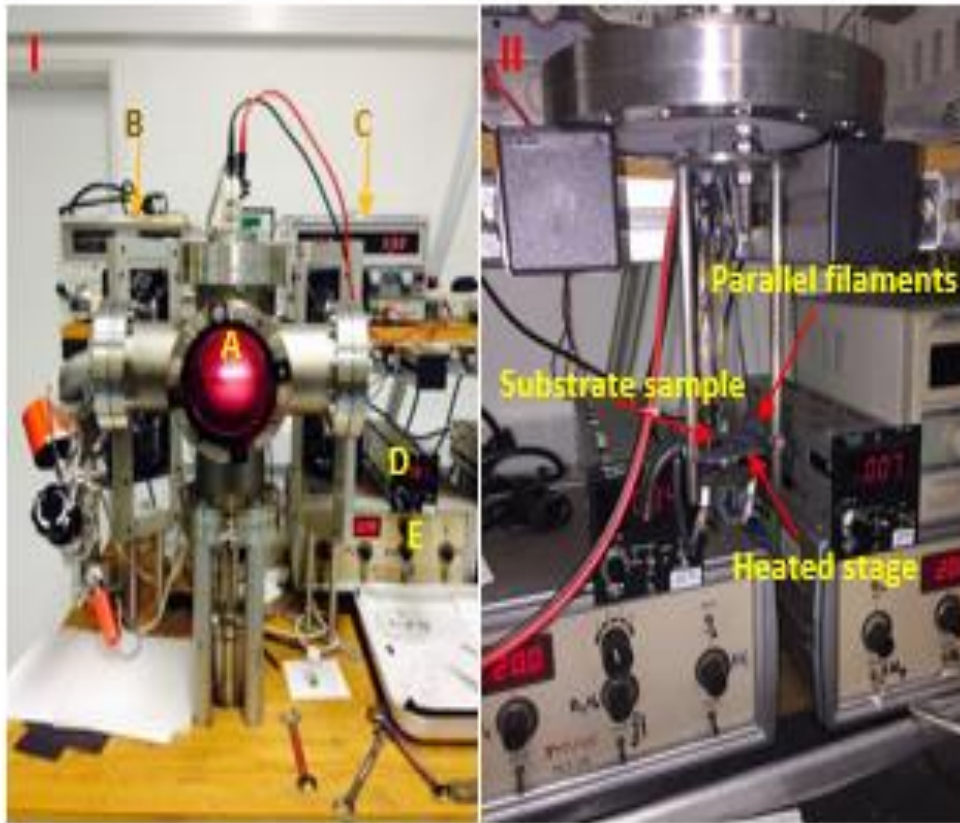
Figure 3.4 *Photograph of the home-built CVD reactor II (A: CVD reactor chamber; B: Stage power supply; C: filament power supply; D: B_2H_6 mass flow controller; E: H_2,CH_4 mass flow controller) and sample stage (II)*

The CVD chamber is made from a stainless steel six-way cross. Specifically, the y-direction flange holds a window to monitor the CVD growth process. The top of the z-direction flange is connected to a power supply (118W) and the base of the chamber is connected to a throttled vacuum pump. All the gas lines are linked to the left side of x-direction flange with a pressure gauge used to measure the pressure in the chamber. The needle valve on the gas inlet tube is used to make minor adjustments to the chamber pressure and thereby keeping a constant value of 20 Torr during growth runs. The sample stage (B) is composed of three parallel tantalum wires which are resistively heated to produce gas temperatures of around 2100°C close to the filament surface.

The sample stage is held 3 mm away from the filaments and resistively heated to around 850°C, this activates the growth surface by promoting migration of species on the surface and providing reaction sites for the thermally decomposed gas species. The growth rate of HFCVD diamond in this reactor is around $0.5\mu m \cdot h^{-1}$.

3.3 Raman spectroscopy

Raman spectroscopy is widely used in material science to investigate molecular vibrations that can be used for sample identification [123]. When a monochromatic laser beam falls on a sample surface, a number of processes may take place during the interactions between the incident electromagnetic wave and the sample, such as light absorption, reflection and scattering. The scattered light caused by elastic scattering or Rayleigh scattering is of the same frequency as the excitation source which normally is blocked off with a filter in a Raman system. The inelastically scattered Raman (Stokes and anti-Stokes) light represents only a small amount of the total light collected for analysing. The difference in the energy between the Raman scattered light and incident photons is called the "Raman shift" which is typically plotted versus wavenumber shift relative to the incident laser, resulting in a Raman spectra of the sample[124].

Raman spectroscopy is an effective tool to measure the quality of carbon films and provides insights into the properties of the material [123]. The intensity of the Raman peak is proportional to the amount of species within the scanned area that can be used as a quantitative technique for measuring the target bonding structure. Generally speaking, diamond fabricated by CVD is carbon with predominantly sp^3 hybridised bonding and small amounts of defects such as graphite or disordered carbon (sp^2),

metals and dopants. The pure diamond has four-fold coordinated sp^3 bonding between the carbons producing a sharp Raman line at 1332 cm^{-1} with a full-width at half-maximum (FWHM) of about 2 cm^{-1}[125]. Carbon with hybridised sp^2 chemical bonding is regarded as graphite or amorphous carbon, it appears as a broad band ("G" band) centred at 1558 cm^{-1}. The relative ratio of sp^2/sp^3 determines the quality of as-grown film as the value is proportional to the presence of non-diamond and diamond carbon respectively. Due to the differences in the sensitivity of the scattering effect of sp^2 and sp^3 bonding, different wavelengths of excitation energy are used to characterise films. Short-wavelength lasers that produce UV radiation are normally used to detect sp^3 bonding while the longer wavelengths produced by NIR or visible lasers are adopted for non-diamond (sp^2) analysis. Doping other elements into diamond results in the change of peak shape and wavenumber shift. When a level of foreign atoms are doped into the host crystal lattice an impurity energy band may form which causes interference to the Raman scattering process, this is referred to as the "Fano effect"[126]. The result of this interference produces an asymmetric and broadened Raman line shape of as-grown diamond films. Secondly, small shifts in the band wavenumber have been related to internal stress in deposited films [127] and the agglomeration of crystal grains and defects present in the films [128]. The Raman line shifting to lower wavenumbers indicates a compressive strain of the film and to higher wavenumber shifts indicate tensile stress. Dopant-related peaks can be observed in the Raman spectra when its concentration is over the threshold of insulator–metal transition. In the case of boron doped diamond, the experimental value is around 3 × 10^{20} cm^{-3} [129].

In this work, a Renishaw 2000 instrument is used to obtain the Raman spectra at room temperature. Three laser excitation wavelengths were used: 325 nm (UV, He:Cd), 514 nm (green, Ar$^+$) and 785 nm (NIR, diode laser). For non-diamond sp^2-related impurity studies, the green laser was adopted in this work. The size of the collection area is around 7µm in diameter.

3.4 Scanning electron microscopy (SEM)

Scanning electron microscopy (SEM) is the most versatile tool used in the characterization of surface morphology. Surface images are formed from the secondary electron emission from the sample surface caused by the interaction between an incident electron beam and the material surface. The following simple schematic describes the how the secondary electrons form. (**Figure *3.5***)
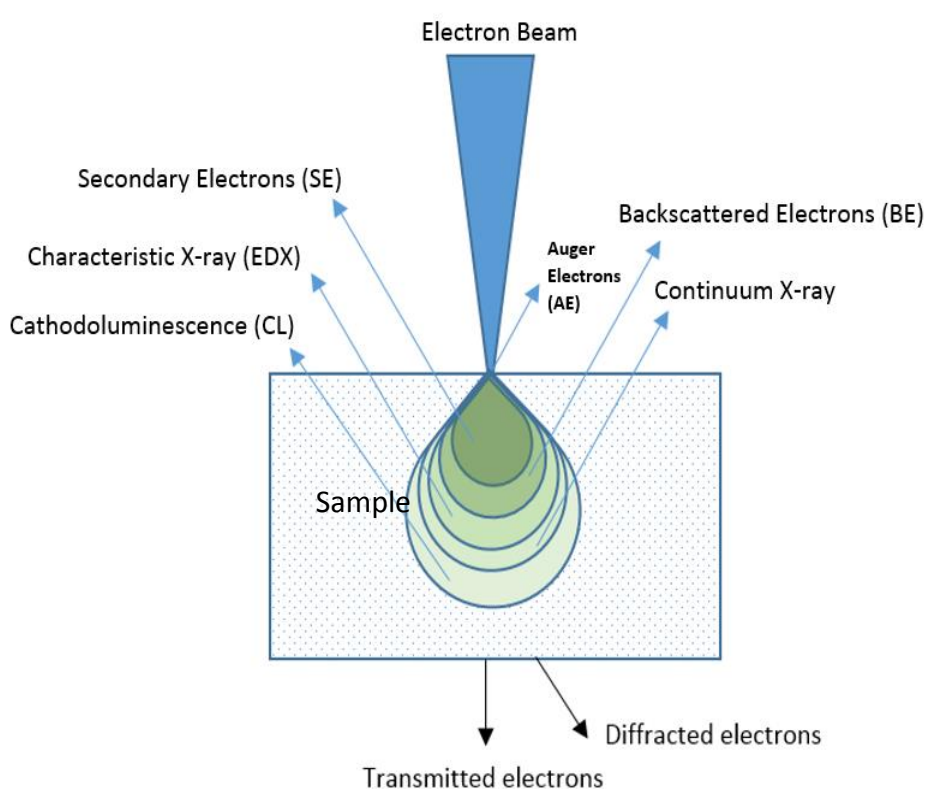
Figure 3.5 *The interactions between electron beam and the sample.*

When an accelerated electron beam (Primary beam) bombards a sample surface, it interacts in mainly two ways: either scattered or transmitted. Both inelastic and elastic scattering can produce various signals for imaging and analysing. As shown in **Figure 3.5**, altering the energy of the incident electron beam can produce various types of signals. The secondary electrons originate through the interactions with the primary electron beam and backscattered electrons. Specifically, the loosely bonded outer electrons of the atoms are collided by the incident or backscattered electrons and obtain enough energy to leave the original orbitals. As a result, these secondary electrons are emitted by the incident electron beam out of the sample's surface and are collected to form the morphology image.

The instrument used for imaging is a Zeiss Stigma field emission SEM in the Interface Analysis Centre. **Figure 3.6** gives a general description of the major components of the instrument.
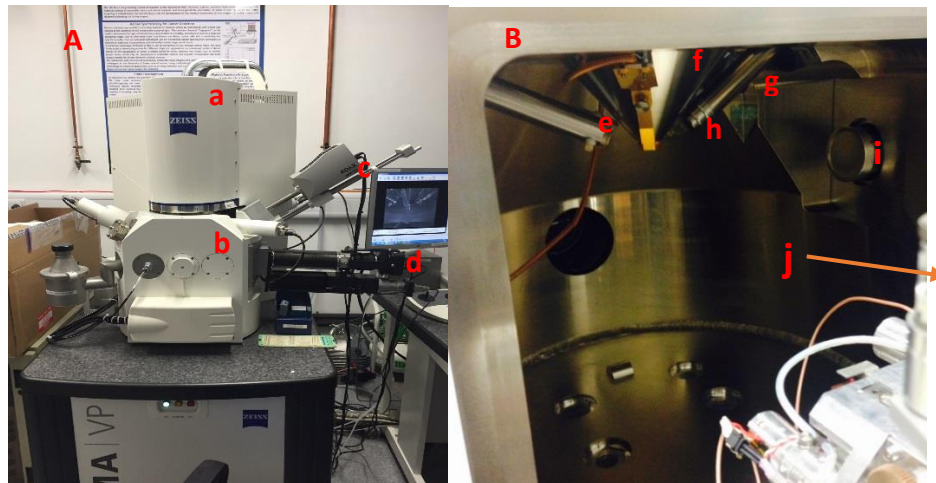
Figure 3.6 *Photograph of Zeiss Stigma (A) and inside view of analysis chamber (B). a. Field emission gun; b. Analysis chamber; c. Energy Dispersion X-ray (EDX) equipment; d. Electron Backscattered Diffraction (EBSD) equipment; e. Variable pressure (VP) detector; f. Objective lens; g.EDS detector; h. Secondary electron (SE) detector; i. EBSD detector; j. Sample stage.*

In this work, 10 KeV accelerating voltage was used for surface imaging with a working distance of 10 cm. Images were taken in the range of 500x to 20,000x magnification on each spot for further grain size comparison.

3.4.1 Electron backscattering diffraction (EBSD)

EBSD is an analysis technique equipped on the SEM instrument and widely used for the microstructure characterization of crystals. Information such as crystal orientation, phase composition and grain size can be obtained through this method.

3.4.1.1 The EBSD technique

Electron backscatter diffraction pattern (EBSP) is the key concept of this technique which offers all crystallographic information of a target material. **Figure *3.7*** briefly explains the formation of EBSP and analysis process.
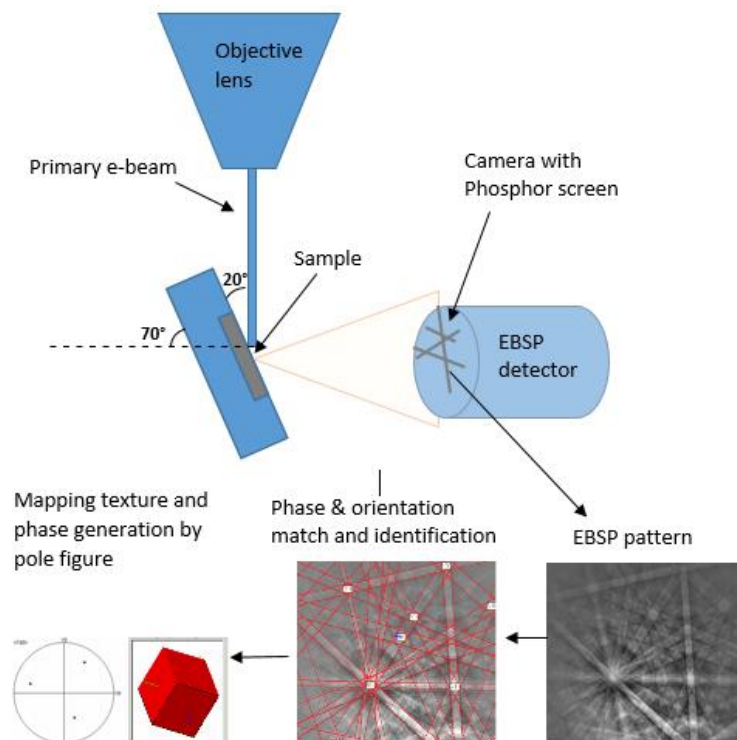
Figure 3.7 *The schematic diagram of the formation of an EBSP pattern and the procedure of EBSD analysis.(Adapted from[130])*

As shown in **Figure 3.7**, an electron beam strikes a tilted sample surface (70°) to

produce backscattered electrons in a small volume. Some of these electrons are

diffracted by the crystal planes of the sample's surface. If the diffraction meets the

condition of the Bragg equation: $2d\sin\theta = n\lambda$, (where d is the spacing of the diffracting

planes, n is the order of reflection, λ is the wavelength of the electron beam, θ is the

angle of incidence of the electrons on the diffracting planes), these electrons interact

with the phosphor screen to form the electron backscattered pattern (EBSP). A typical

EBSP shown in **Figure 3.7** consists of a number of bands whose configuration is

dependent on the various lattice properties [131]. The as-obtained EBSP image is

captured by a CCD camera with evaluation and analysis carried out by computer. This

process is called "band identification" as the band geometry and width can be seen as

a projection of a crystal lattice. The EBSP generated from the sample surface then will

be matched and indexed against reference patterns to identify the phase and crystal

orientation. Through point-scanning mode, the whole set of EBSD data is collected for

further analysis [132]. In this work, the reference pattern used for the band matching

and identification is the standard diffraction data of crystalline diamond and graphite

obtained from X-ray photoelectron spectroscopy (XPS).

3.4.1.2 EBSD mapping

By stepping the electron beam across the specific area, a complete EBSD data set can

be obtained. Each scanning point, which typically represents a single grain, is

converted by the pole figure into a EBSD map which is used to reconstruct grains and

identify grain boundaries. The software: OIM™ on Zeiss FEG instruments, is

programmed to produce analysis results based on the EBSD map, such as a phase and orientation map, grain size statistics and other crystallographic data.

3.4.1.3   The representation of texture in EBSD

Two forms of texture data are normally used to display different orientations of a sample surface: a pole figure and inverse pole figures. In EBSD, the various crystal orientations on the sample surface are presented as a collection of individual points in the pole or inverse pole figure [133]. The formation of these orientation points in the pole figure can be seen in Graph A **Figure 3.8** which shows the 3D crystal directions ([001],[100],[010]) projected as an individual black dot on the 2D projection plane.

In the case of diamond, only certain directions ([001],[100],[010]) are of interest. Therefore, an inverse pole figure, which is the result of crystal symmetry operations, is a better way to show the distribution of crystal directions and visualise the texture. Graph B shows a typical stereographic projection of the cubic system which is comprised of 24 equivalent triangle regions[133]. An example of an inverse pole figure (IPF) component used in this thesis (Graph C) shows an overall result of each orientation measurement over the whole area of the sample surface which reveals the texture of the diamond surface. The orientation point close to a particular crystal direction component will appear as a cluster of points on the pole figure. The IPF in this thesis uses a basic 64 RGB colour scheme to classify the as-measured orientation points. Using this scheme means orientations that are equal will be of the same colour and so aids visualisation.

A

B

C
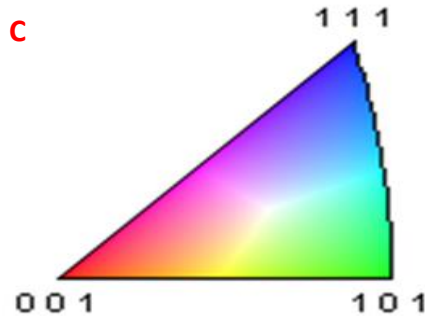
Figure 3.8 *(A) The principle of pole figure and the formation of different orientation points on the 2D projection plane [134] (B) The principle of inverse pole figure (IPF) and typical triangle portion showing the three main directions in the cubic system[134]; (C) An IPF component used in the EBSD orientation mapping comprised of a collective individual orientation points (colour revealing the texture of the sample surface)*

3.4.1.4 Grain size measurement by EBSD

In EBSD, a grain is a collection of scanning points which have similarities in lattice properties through EBSP band analysis. Unlike traditional optical methods in determining and measuring the grain shape and size, the EBSD software has the advantage of offering more accurate and reliable quantitative results [135]. There are a few options which can be used from the OIM™ software according to the shape of grains and calculation methods required. The analysis software provides information on grain size statistics for both circular-like and square grains, areas of grains and intercept length by using ASTM standard methods[136] for random shapes of grains.

3.5 Secondary Electron Mass Spectroscopy (SIMS)

3.5.1 Secondary ion sputtering

Secondary electron mass spectroscopy (SIMS) is an analytical technique that provides quantitative and elemental information of solid materials. It is based on the fact that charged atomic and molecular particles are sputtered from the sample

surface by bombardment with heavy particles, such as Ga or Ar. This leads to complex

energy transfer processes in the surface zone of the material which results in the

charged secondary species being ejected from the surface zone. The emitted charged

particles are transmitted into a Mass Spectrometer for further analysis. The principle

of ion sputtering is similar to that of secondary electron formation: instead of using an

electron beam as a primary source, SIMS uses an ion beam to strike the target. **Figure**

3.9 gives a simple describe of ion-solid interactions.
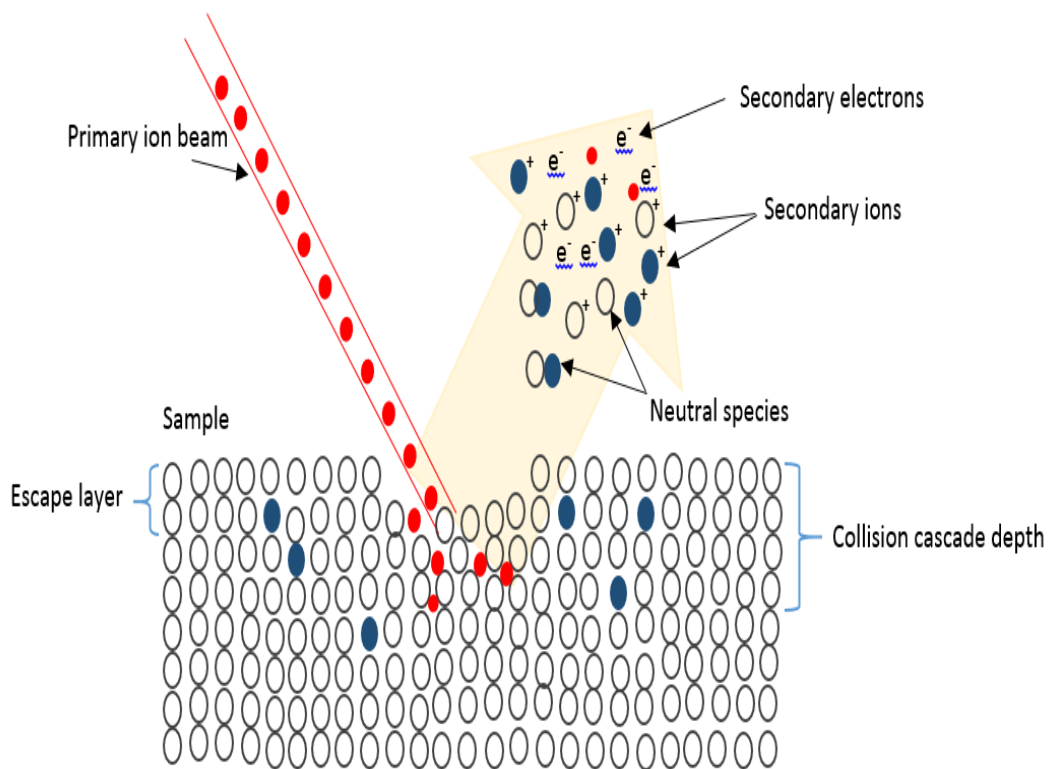
Figure 3.9 *The principle of ion sputtering. (Adapted from [137])*

  When a primary ion beam bombards a sample surface in a particular volume, the

target atoms interact strongly with it. This causes energy and momentum transfer to a

very small area around the point of particle impact [138]. Ions being heavier than

electrons and having much higher momentum than an electron beam, cause bond

breaking and ionisation of the substrate atoms. The sputtered particles may be

69

positive or negative ions, neutron molecules and electrons. The particles are collected

and measured based on their mass-to-charge ratio.

3.5.2 Primary ion beam generation

  The primary ion beam is normally generated from a liquid metal ion source (LMIS)[139, 140]. In this work, a gallium source was used to produce a Ga^+ beam. **Figure *3.10*** gives a

simple schematic diagram of the LMIS container. The liquid metal is stored in a

reservoir which is heated up from Ga metal to wet the tungsten needle. An external

extractor is placed near the tip of the needle and used to create a high electric field

(above 108 V.m) to form a Taylor cone[141]. The applied high voltage (around 7600V)

extracts the Ga^+ ions to form an ion beam through field emission and ionisation

processes. The emitted ions enter the ion column and focused further before being

guided to the sample surface.

Insulating Mount

Power Lines

Coil Heater Ga Source

Tungsten Tip

Suppressor

Extractor
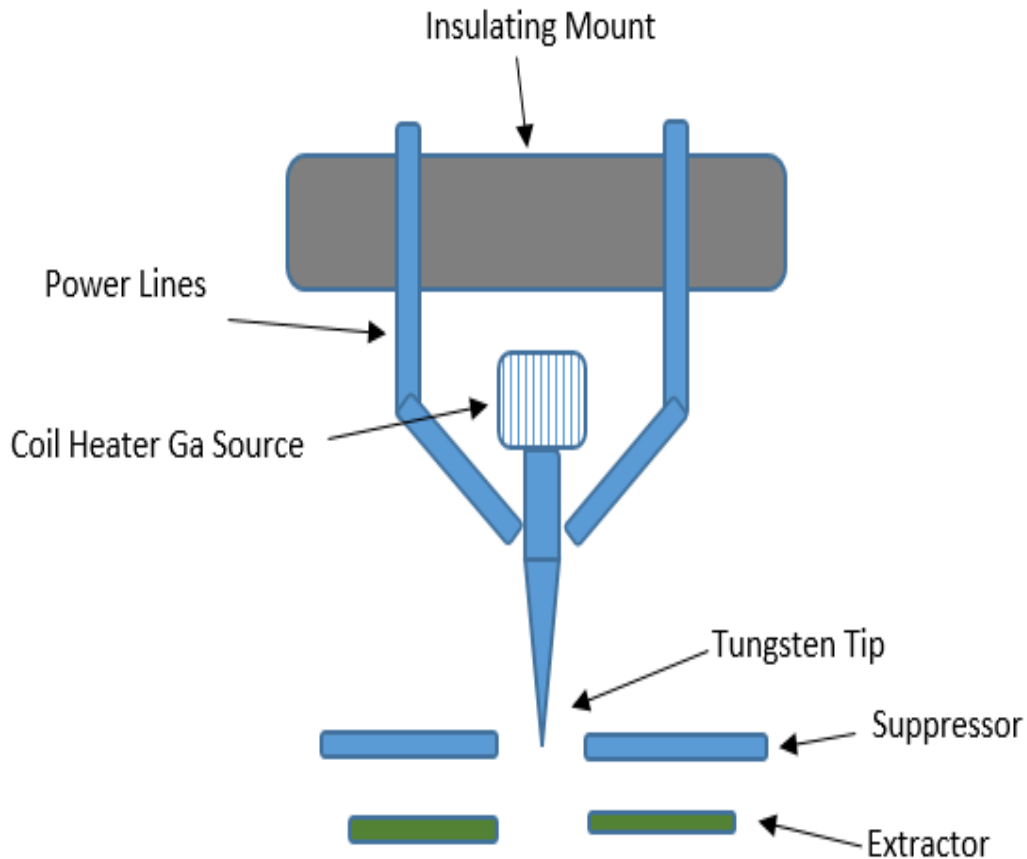
Figure 3.10 *Schematic of the gallium liquid-metal source. (Adapted from* [141]*)*

3.5.3 SIMS instruments

3.5.3.1 Basic concepts

Figure *3.11* shows an overall schematic diagram of how SIMS operates. It can be

broadly divided into two working modes: static and dynamic. Static SIMS uses a very

low energy ion flux to obtain sufficient signal to provide a compositional analysis of a

surface [142, 143]. The aim is to keep the surface undamaged and is normally suitable for

monolayer characterization. Dynamic SIMS uses a strong current beam to continuously

sputter ions from the sample into the bulk which results in a depth profile by plotting

elemental concentration verses depth of the sputtered matter[144, 145]. Dynamic mode

SIMS is used throughout this work to study the distribution of dopants and impurity metals throughout films.
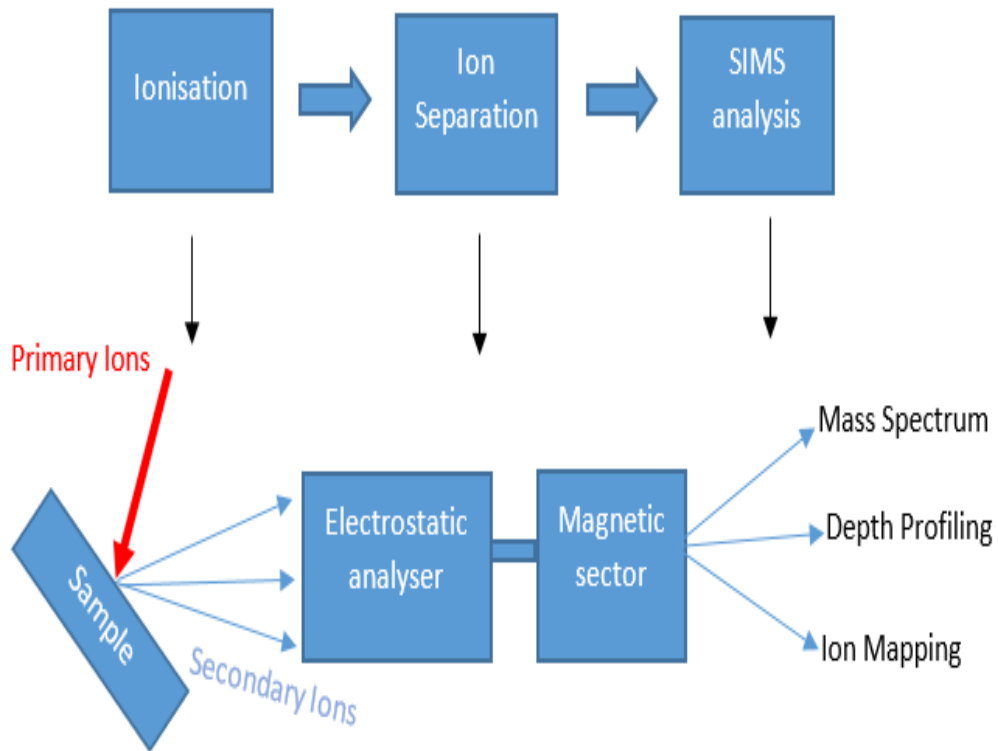
Figure 3.11 *Principle of SIMS analysis showing the three main parts.*

According to **Figure *3.11***, some basic components and concepts are described below:

Vacuum system: To ensure both primary and secondary ions move freely and accurately in the right direction, SIMS operates under a regime of high or ultra-high vacuum to remove residual molecules so that high sensitivity and reproducibility can be achieved.

Sample stage: the sample stage is equipped with x,y,z and tilt manipulation system in order to optimise position-to-yield signal.

 Ion beam optics: Sets of electromagnetic optics are used to extract, focus, direct and accelerate the ions onto the sample surface. The system is built inside the ion column.

Secondary ion extraction and transfer: the sputtered secondary ions (SI) are extracted and transferred into the ion detection section once out of the sample surface. The SI are immediately extracted in an electric field created by applying a voltage bias on the sample stage. Collected SI from a well-defined sputtering area are then transferred through an immersion lens to the mass spectrometer for further analysis.

Mass resolving power (MRP): the term is used to describe the ability of SIMS to separate similar masses. MRP can be defined by Equation 3.1, where Δm is the peak width for separating masses.

$$MRP = \frac{m}{\Delta m} \quad \text{(Equation 3.1)}$$

Energy filter: There is a wide range of ion energies generated during the sputtering process[146]. The energy filter is designed to select the desired secondary ion energy range for analysis and eliminate the scattered primary ions. This increases the mass resolving power of the system[147].

Ion separation: A double focussed analyser was used throughout this work for higher resolution. It consists of an electrostatic analyser and a magnetic sector (**Figure 3.13**, e and f) and used to separate and deflect the sputtered secondary ions for analysis [148].

Detector: collects the sputtered secondary ions arising from the mass spectrometer with a pulse counting system able to detect single ions. The detector type is dependent on the mode of SIMS and the requirement of the collected data. Microchannel image plate [149], Faraday cups[150] and most commonly electron multipliers[151] are used as detectors.

Data acquisition and analysis system: A PC running in-house written software by Dayta

System Ltd was used. It is used to monitor and manipulate the operating conditions

and process the collected data generating mass spectra, depth profile spectra and

secondary ion images.

3.5.3.2   Instrumentation

The SIMS instrument used in this work is a customer-built instrument based at the

Interface Analysis Centre in the University of Bristol designed by Professor Peter

Heard. **Figure *3.12*** shows a schematic diagram of how this instrument works with the

arrangement of each component for SIMS shown in **Figure 3.13**.
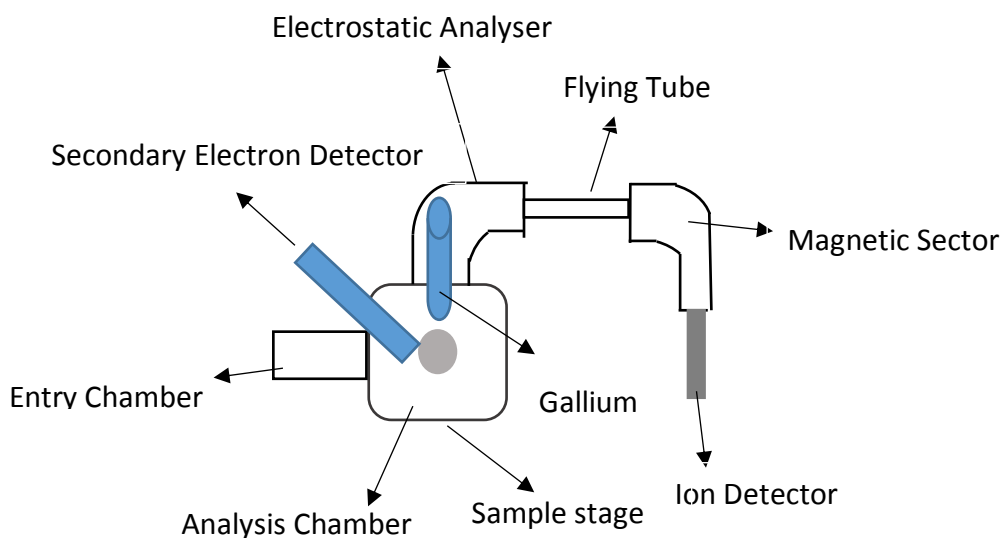
Figure 3.12 *The schematic diagram of SIMS instruments.*

Figure 3.13. *Photograph of the SIMS instrument. a) sample stage manipulator; b) analysis chamber; c) entry chamber; d) Ga$^+$ ion gun; e)electrostatic analyser; f) magnetic sector; g) detector*

The instrument uses an FEI Ga$^+$ ion gun to produce a primary ion beam under the condition of an accelerating voltage of 25keV. The sample stage is set to be 45° off normal to the ion gun so that the emitted secondary ions can be collected by the mass separation system and eventually detected by the collector. Beam current is controlled by a variable electronic aperture, 3.27nA was typically used. Polarity bias voltage is connected to the sample stub in order to collect desirable ions. Positive ions are collected throughout this work, therefore the sample bias voltage applied is positive (around +4eV).
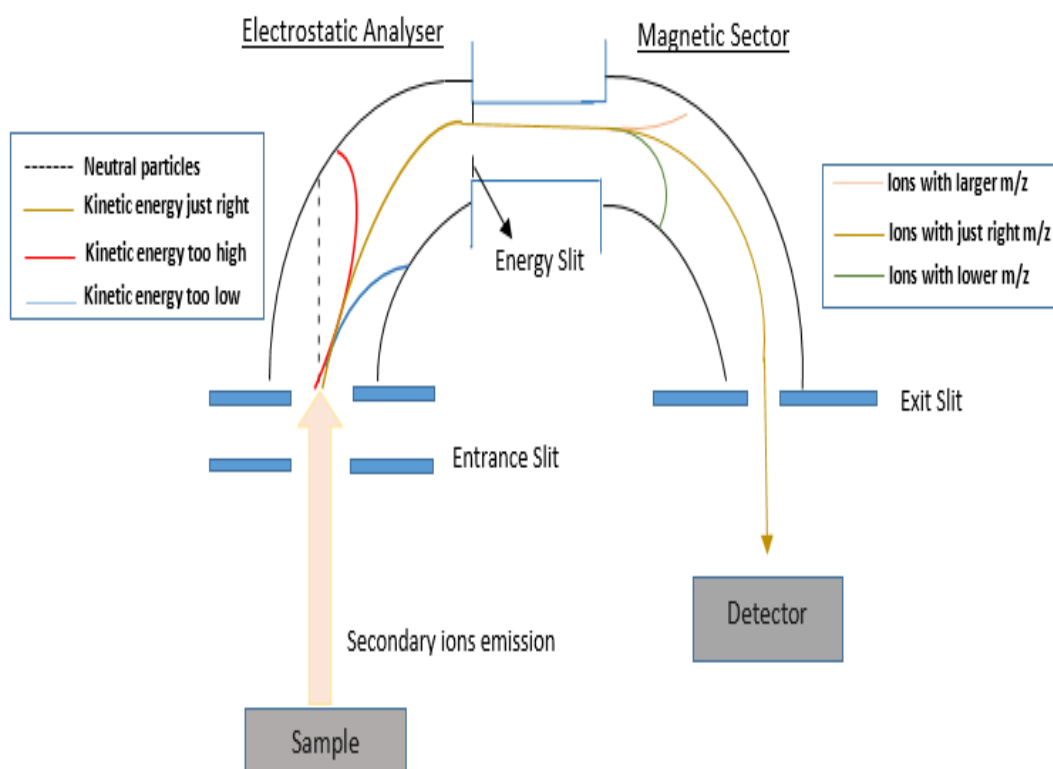
Figure *3.14*. Schematic diagram of ion separation by the double-focusing magnetic sector spectrometer.(Adapted from [152])

gives more detailed information about how the mass separation sector works. Once secondary ions have been sputtered out of the sample surface, they are focused and filtered before entering into the Mass Sector. The electrostatic analyser acts as the energy filter to focus secondary ions only allowing ions with a nominal energy of +4eV to pass through the energy silt. The remaining ions enter into the magnetic sector and are deflected by the magnetic force inside the flight tube due to their mass/charge ratio (m/z). The strength of the magnetic field is measured by a Hall probe situated within the jaws of the magnet. Only ions with a certain m/z can exit through the exit silt to reach the detector. The detector operating in pulse counting mode then records the ion count.

3.5.4 SIMS analysis

3.5.3.3 Mass spectrum

By scanning over a range of masses of interest, a mass spectrum can be obtained. The light elements and metals are the key targets to investigate in this work, therefore a range of 0 to 100 Daltons (Da) was used. The mass spectrum is primarily used for the peak identification for the mass of interest and in order to calibrate the system and eliminate any mass drifting effects. Furthermore, the mass peaks should be assigned to ions or molecular fragments which need the chemical knowledge of the sample to attribute the peaks.

3.5.3.4 Depth profiling

Unlike the mass spectrum which provides information on only the outer most surface of the sample, the aim of depth profiling is to obtain the information of variation of the composition below the initial surface [153]. Recording the intensity of the selected m/z ions' signal with the sputtering time as the primary ion beam is rastered over a selected area results in a depth profile. Due to the dynamic range of SIMS, which normally extends from < 1 ppm to > 1% for most elements, it is a useful tool to detect trace elements and especially dopants in the semiconductor industry [153]. The "depth resolution" is a term used to describe a measured width of an interface between two layers [154]. An example of how to determine the width is given in **Figure *3.15***.
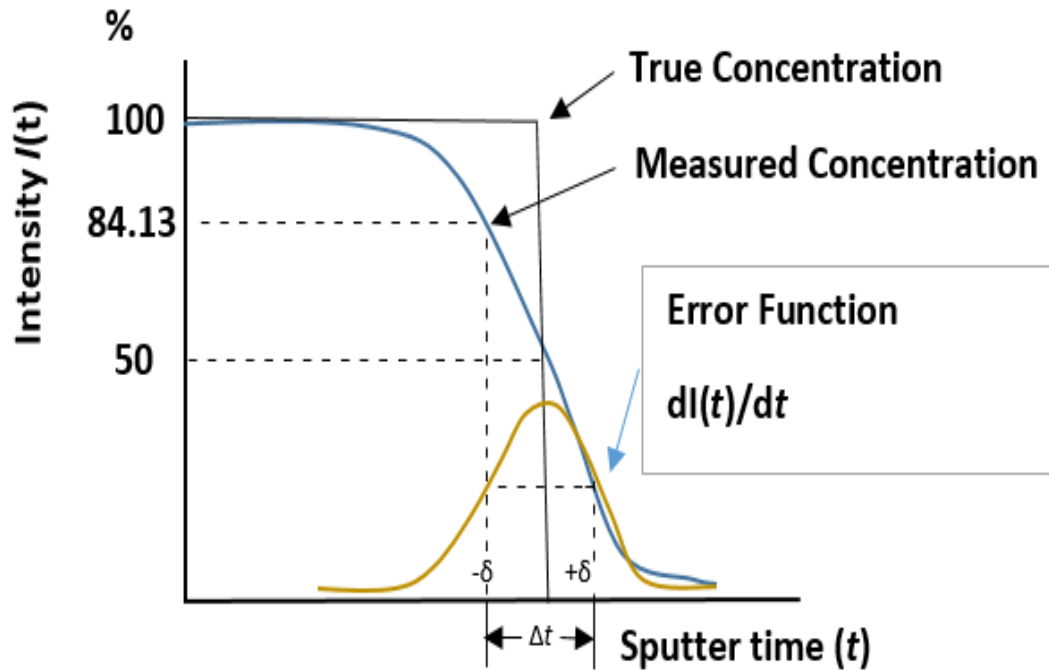
Figure 3.15 *Parameters of depth resolution. (adapted from [154])*

As can be seen from **Figure *3.15***, the true ion concentration distribution should be a rectangular function. As the primary ion beam bombards the sample, some ions of the target materials will be "knocked" into the deeper bulk which results in this "recoil tail" shape. The interface width Δt (refers to sputtering time: t) or Δz (refers to depth: z) are defined as the interval where the intensity of the collected signal drops from 84% to 16% of the maximum signal [154]. As the primary beam continues etching the surface, the thickness of the thin film can be obtained by multiplying the sputtering time with the sputter rate. The value of sputter rate is estimated using the software SRIM (Stopping and Range of Ion in Matter) which models the interactions between the ion beam and the matter [155]. The estimated value of boron doped diamond under the condition of a Ga^+ ion beam at the incident angle of 45° was 4.9 molecules per ion. Etching over long periods can, however, introduce ion mixing and implantation [156],

which may cause inaccuracies in the measured values. Therefore, a boron-doped

diamond thin film with a measured thickness, from the cross-sectional view via SEM,

was used to compare against the calculated value.

3.6 Hall Effect measurement

3.6.1 Van der Pauw resistivity and Hall voltage measurement

Four-point probe configuration was used in this work to obtain sheet resistances and

carrier densities of measured films. Triangular shaped layers of gold were deposited by

metal evaporation onto the corners of the samples in order to make ohmic contacts.

3.6.2 Van der Pauw resistivity measurement

By driving a set of current flows along adjacent points of samples and measuring the voltage on the other side of

voltage on the other side of adjacent points, one may obtain the sheet resistance from the gradient of the current-

the gradient of the current-voltage (I-V) data based on Ohm's law (

Figure *3.16*)
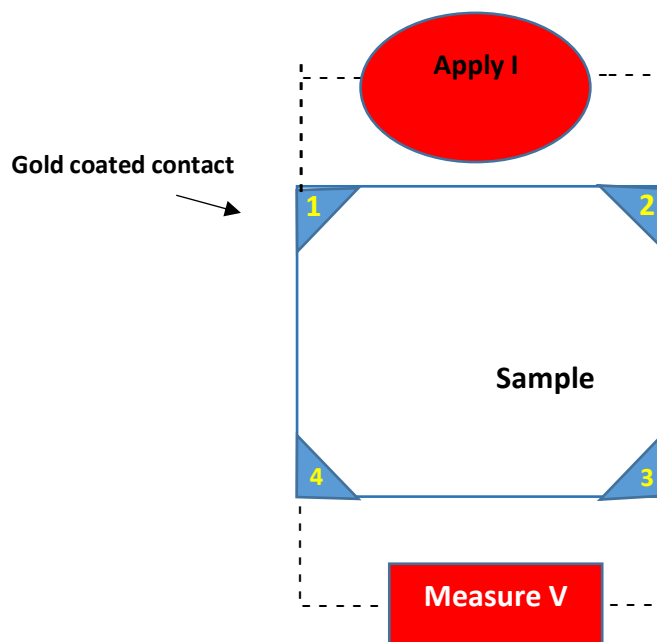
Figure 3.16 *Schematic diagram of Van der Pauw resistivity measurement configuration.*

During this study, sheet resistances were determined using two different measurement configurations: along the vertical edge of the sample ($R_{12,43}$) and along the horizontal edge ($R_{23,14}$)[157]. The actual sheet resistance can be calculated using Van der Pauw formula[157] as described below.

$$e^{-\frac{\pi R_{12,43}}{R_s}} + e^{-\frac{\pi R_{23,14}}{R_s}} = 1 \ \text{(Equation 3.2)}$$

In order to remove the thermocouple effect which introduces thermal electric voltage (V_{TE}) into the Hall voltage value, bipolar current measurements were used ($R_{21,34}$ and $R_{32,41}$). To improve accuracy of the measured resistance value for $R_{12,43}$, $R_{23,14}$, $R_{21,34}$ and $R_{32,41}$, four reciprocal measurements were taken and averaged ($R_{43,12}$, $R_{14,23}$, $R_{34,21}$, and $R_{41,32}$). **Figure 3.17** gives more detailed conventions.
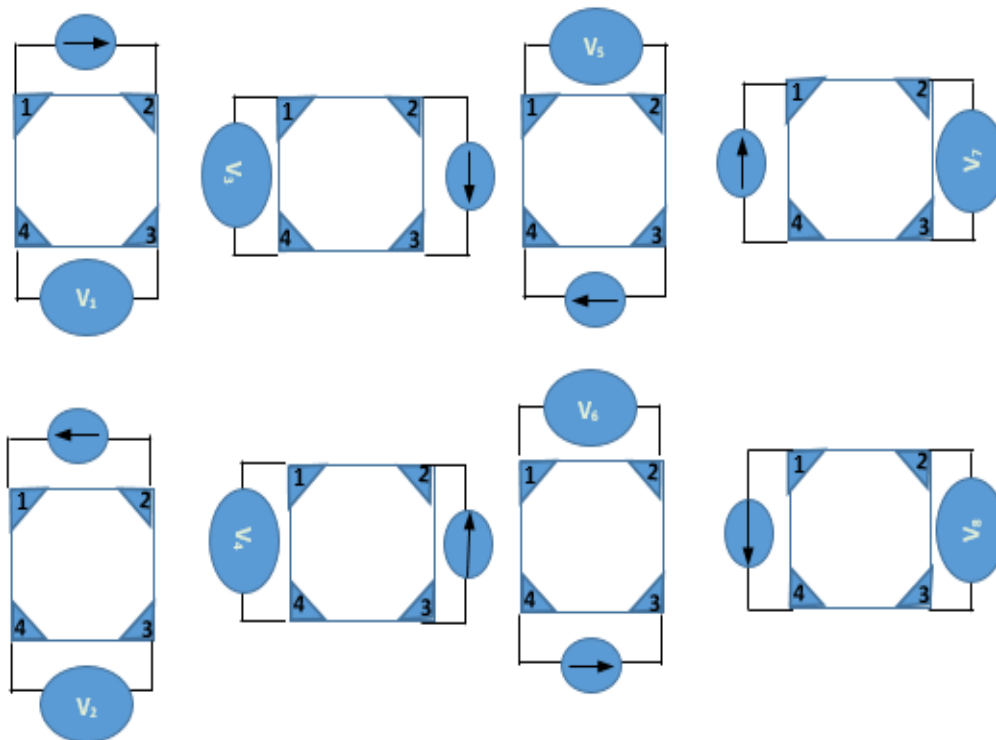
Figure 3.17 *Van der Pauw measurement configurations*

The equations used in these studies based on **Figure *3.17*** are described below:

$$R_{vertical} = \frac{R_{12,43} + R_{21,34} + R_{43,12} + R_{34,21}}{4} \qquad \text{Equation 3.3}$$

$$R_{horizontal} = \frac{R_{23,14} + R_{32,41} + R_{14,23} + R_{41,32}}{4} \qquad \text{Equation 3.4}$$

Then the sheet resistance[157] is the same as equation 3.5.

$$e^{-\pi R_{vertical}/R_s} + e^{-\pi R_{horizontal}/R_s} = 1 \qquad \text{Equation 3.5}$$

The resistivity of as-grown thin film can be obtained by equation 3.6.

$$\rho = R_s \times t \qquad \text{Equation 3.6}$$

3.6.2.1 Hall measurements

In contrast to the resistivity measurement, the configuration of the Hall measurement is to drive the current flow through the opposite points of the sample (**Figure *3.18***)
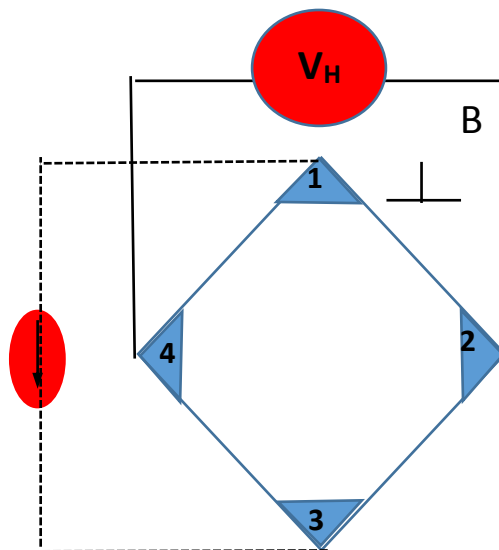
Figure 3.18 *Configurations of Hall measurement in a positive magnetic field*

The voltage measured in a practical experiment (V_H) also includes a misalignment voltage (V_o), offset voltage (V_{off}) and a thermal electric voltage (V_{TE})[158]. V_o can be removed by reversing the magnetic field and V_{off} can be removed by connecting a ground guard probe and further data processing. Current is applied between corners 1 and 3 in a positive magnetic field and the voltage drop V_{24+} measured, followed by reversing the current and measuring the V_{42+}. The same method is then employed to obtain the value of V_{24+}, V_{13+} and V_{31+}. By reversing the magnetic field the Hall voltage is obtained for the same configuration. The final step is to average all the values according to equation 3.

$$V_H = \frac{(V_{24+} - V_{24-}) + (V_{42+} - V_{42-}) + (V_{13+} - V_{13-}) + (V_{31+} - V_{13-})}{8} \quad \text{Equation 3.7}$$

The carrier concentration can be calculated by equation 3.8 and 3.9 below:

$$P_s = \frac{IB}{eV_H} \quad \text{Equation 3.8}$$

$$P_{bulk} = \frac{P_s}{t} \quad \text{Equation 3.9}$$

where, P_s – sheet carrier density for P-type semiconductor (cm^{-2})

P_{bulk} – carrier concentration for P-type semiconductor (cm^{-3})

I – Applied current (A)

B - Intensity of magnetic field (G)

e - electron charge (1.602×10^{-19}C)

V_H – Hall voltage (V)

t – thickness of the thin film (cm)

Finally, the carrier mobility of as measured thin films can be obtained by equation 3.10

$$\mu = \frac{1}{eR_s P_s} \qquad \text{Equation 3.10}$$

3.6.3 Hall Effect measurement set up

Room temperature Hall effect measurement was used in this work. The photograph on the left in **Figure *3.19*** shows the set-up of this method.
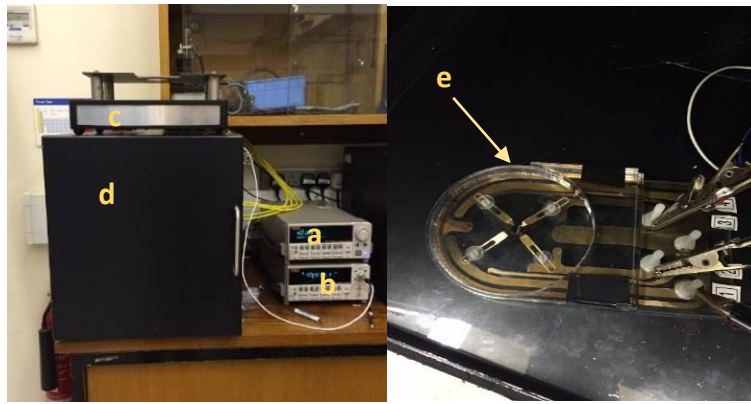
Figure 3.19 *Photograph of the Hall measurement set up. a. DC current source; b. Nanovoltmeter; c. Switch box; d. Faraday box; e. Sample stage*

The Keithley 2128A Nanovoltmeter is designed for low resistance measurements with build-in thermocouple linearization and cold junction compensation [159]. Combined with a Keithley 6220DC current source, the set up can be used in the measurements of resistance range from 10 nΩ to 100 MΩ. The sample stage was made in the in-house workshops with tracks fabricated from 0.1 mm copper strips coated with a layer of gold (20 nm thick). **Figure *3.20*** shows the measurement profile by plotting the voltage as the function of time.
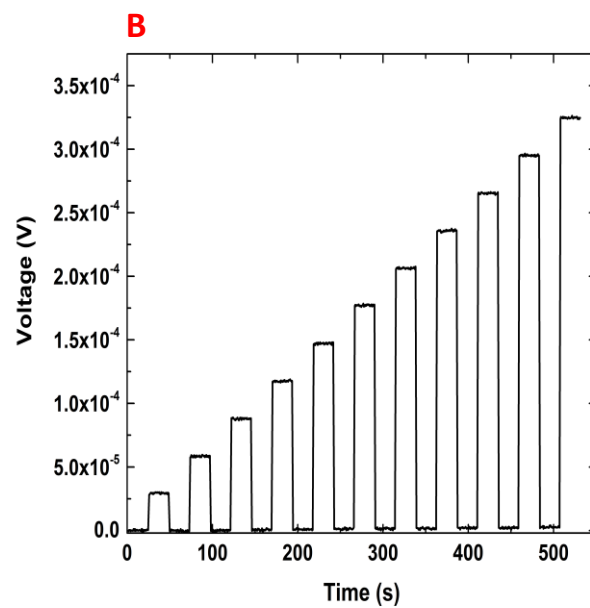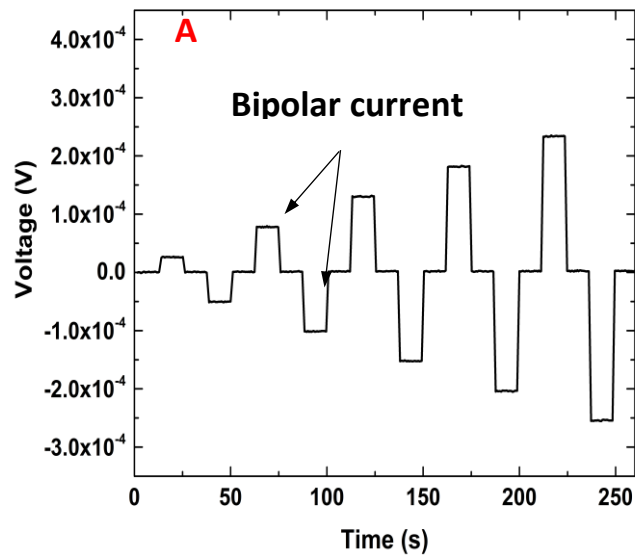
Figure 3.20 *Voltage versus time graphs of Van der Pauw (A) and Hall measurement (B) with the current range from 1× 10⁻⁷ to 1.1×10⁻⁶ A for resistivity measurements and 1× 10⁻⁷ to 1.1×10⁻⁶ A for the Hall measurement.*

In this work, a bipolar current was applied to the Van der Pauw method to eliminate any thermocouple effect. Each current step is set to collect the data 20 times for the

resistivity method and 40 times for the Hall measurement in order to achieve a low

value of standard deviation (SD) and high accuracy of as-measured data at each

current step. Errors can be introduced by a number of sources namely: formation of a

Schottky contact, the shape and materials of contacts, sample geometry, the position

of the tip on the sample and the current range applied (due to undesired sample

heating)[160].

As heavily boron-doped diamond films are the focus of research in this work, standard

boron-doped diamond (BDD) purchased from Element Six (E6) and resistors with

known values were used to calibrate the system (Table 3.1).

Table 3.1 The result of Hall Effect measure of BDD thin films

Sample to be tested	Applied current range (A)	As measured voltage range (V)	Standard deviation (SD) Range	coefficient of determination (R^2)
E6 BDD smooth side	1×10^{-4} ~ 2.1×10^{-3}	3.03×10^{-5} ~ 5.67×10^{-4}	4.21×10^{-8} ~ 7.8×10^{-8}	1
E6 BDD Rough side	1×10^{-4} ~ 1.1×10^{-3}	2.72×10^{-5} ~ 3.04×10^{-4}	4.17×10^{-8} ~ 8.1×10^{-8}	1

3.7 Reference

123.   Ferrari, A.C., Determination of bonding in diamond-like carbon by Raman spectroscopy. Diamond and Related Materials, 2002. 11(3): p. 1053-1061.

124.   Somerville, W., E. C. Ru, P. T. Northcote, and P. G. Etchegoin, High performance Raman spectroscopy with simple optical components. American Journal of Physics, 2010. 78(7): p. 671-677.

125.   Knight, D.S. and W.B. White, Characterization of diamond films by Raman spectroscopy. Journal of Materials Research, 1989. 4(02): p. 385-393.

126.   Deneuville, A., C. Baron, S. Ghodbane, and C. Agnès, Highly and heavily boron doped diamond films. Diamond and Related Materials, 2007. 16(4): p. 915-920.

127.   Bustarret, E., J. Kaˇcmarˇcik, C. Marcenat, E. Gheeraert, C. Cytermann, J.Marcus and T. Klein, Dependence of the superconducting transition temperature on the doping level in single-crystalline diamond films. Physical Review Letters, 2004. 93(23): p. 237005.

128.   Ager III, J.W., W. Walukiewicz, and M. McCluskey, Fano interference of the Raman phonon in heavily boron‐doped diamond films grown by chemical vapor deposition. Applied Physics Letters, 1995. 66(5): p. 616-618.

129.   Klein, T., et al., Metal-insulator transition and superconductivity in boron-doped diamond. Physical Review B, 2007. 75(16): p. 165313.

130.   Venables, J. and C. Harland, Electron back-scattering patterns—a new technique for obtaining crystallographic information in the scanning electron microscope. Philosophical Magazine, 1973. 27(5): p. 1193-1200.

131.   Maitland, T. and S. Sitzman, Electron backscatter diffraction (EBSD) technique and materials characterization examples. Vol. 14. 2007: Springer Berlin.

132.   Chapman, M., P. Callahan, and M. De Graef, Determination of sample surface topography using electron back-scatter diffraction patterns. Scripta Materialia, 2016. 120: p. 23-26.

133. Roe, R.J., Description of crystallite orientation in polycrystalline materials. III. General solution to pole figure inversion. Journal of Applied Physics, 1965. 36(6): p. 2024-2031.

134. Márquez, M. and A.s. Eloy, TEM characterization of B-doped polycrystalline CVD diamond films correlated with micro PL studies. 2003, University of Bristol.

135. Gao, N., S.C. Wang, H.S. Ubhi, M.J. Starink, A comparison of grain size determination by light microscopy and EBSD analysis. Journal of Materials Science, 2005. 40(18): p. 4971-4974.

136. Standard, A., E112: Standard Test Methods for Determining Average Grain Size. West Conshocken, 1996.

137. Yao, N., Focused ion beam system—a multifunctional tool for nanotechnology, in Handbook of Microscopy for Nanotechnology. 2005, Springer. p. 247-286.

138. Benninghoven, A., et al., Secondary ion mass spectrometry SIMS V: proceedings of the fifth international conference, Washington, DC, September 30–October 4, 1985. Vol. 44. 2012: Springer Science & Business Media.

139. Kollmer, F. and P. Hoerster, Mass spectrometer and liquid-metal ion source for a mass spectrometer of this type. 2016, Google Patents.

140. Vickerman, J.C. and N. Winograd, SIMS—A precursor and partner to contemporary mass spectrometry. International Journal of Mass Spectrometry, 2015. 377: p. 568-579.

141. Lindquist, N.C., P. Nagpal, K. M. McPeak, D. J. Norris, and S.Oh, Engineering metallic nanostructures for plasmonics and nanophotonics. Reports on Progress in Physics, 2012. 75(3): p. 036501.

142. Affrossman, S., P. Bertrand, M. Hartshorne, T. Kiff , D. Leonard ,R. A. Pethrick, and R. W. Richards, Surface segregation in blends of polystyrene and perfluorohexane double end capped polystyrene studied by static SIMS, ISS, and XPS. Macromolecules, 1996. 29(16): p. 5432-5437.

143.   Wong, S., R. Hill, P. Blenkinsopp, N.P. Lockyer, D.E. Weibel, and J.C. Vickerman Development of a C^{60+} ion gun for static SIMS and chemical imaging. Applied Surface Science, 2003. 203: p. 219-222.

144.   Jones, E.A., N.P. Lockyer, and J.C. Vickerman, Depth profiling brain tissue sections with a 40 keV C60+ primary ion beam. Analytical Chemistry, 2008. 80(6): p. 2125-2132.

145.   Hofmann, S., Compositional depth profiling by sputtering. Progress in Surface Science, 1991. 36(1): p. 35-87.

146.   Benninghoven, A., Surface investigation of solids by the statical method of secondary ion mass spectroscopy (SIMS). Surface Science, 1973. 35: p. 427-457.

147.   Purser, K., A. Litherland, and J. Rucklidge, Secondary ion mass spectrometry at close to single‐atom concentration using DC accelerators. Surface and Interface Analysis, 1979. 1(1): p. 12-19.

148.   Benninghoven, A., F. Rudenauer, and H.W. Werner, Secondary ion mass spectrometry: basic concepts, instrumental aspects, applications and trends. 1987.

149.   Wiza, J.L., Microchannel plate detectors. Nuclear Instruments and Methods, 1979. 162(1-3): p. 587-601.

150.   Wyss, J., D. Bisello, and D. Pantano, SIRAD: an irradiation facility at the LNL Tandem accelerator for radiation damage studies on semiconductor detectors and electronic devices and systems. Nuclear Instruments and Methods in Physics Research Section A: Accelerators, Spectrometers, Detectors and Associated Equipment, 2001. 462(3): p. 426-434.

151.   Daly, N., Scintillation type mass spectrometer ion detector. Review of Scientific Instruments, 1960. 31(3): p. 264-267.

152.   De Laeter, J.R. and A.K. Kennedy, A double focusing mass spectrometer for geochronology. International Journal of Mass Spectrometry, 1998. 178(1): p. 43-50.

153.   Wittmaack, K., Depth profiling by means of SIMS: Recent progress and current problems. Radiation Effects, 1982. 63(1-4): p. 205-218.

154.   Magee, C. and R. Honig, Depth profiling by SIMS—depth resolution, dynamic range and sensitivity. Surface and Interface Analysis, 1982. 4(2): p. 35-41.

155.   Li, Y.L.Y., et al. SIMS depth profiling and SRIM simulation to lower energy antimony implantation into silicon. in Ion Implantation Technology. 2002. Proceedings of the 14th International Conference on. 2002. IEEE.

156.   Benninghoven, A., Surface analysis by secondary ion mass spectrometry (SIMS). Surface Science, 1994. 299: p. 246-260.

157.   van der PAUYV, L., A method of measuring specific resistivity and Hall effect of discs of arbitrary shape. Philips Res. Rep, 1958. 13: p. 1-9.

158.   Bahk, J.-H., T. Favaloro, and A. Shakouri, Thin film thermoelectric characterization techniques. Annual Review of Heat Transfer, 2013. 16(1).

159.   Model 2128 Nanovoltmeter User's Manual, fifth ed., Keithley Instruments, Inc., Cleveland, 2002

160.   Chien, C., The Hall effect and its applications. 2013: Springer Science & Business Media.

Chapter 4   Investigations of the influence of dopant on the physical, structural and electrical properties of heavily boron doped diamond

4.1   Introduction

Boron-Doped Diamond (BDD) thin film attracts much attention of many research groups and has been extensively studied on Single-Crystal Diamond (SCD) using homoepitaxial[161-163], as well as polycrystalline diamond (PCD) materials[164, 165] for high-frequency and high-power devices applications, such as diamond electrode, field-effect transistors and energy converters[166-169]. In the case of heavily boron-doped samples, superconductivity has been reported [46, 170, 171] which evokes intensive studies of the influence of the boron acceptor upon the structural[165, 172], electrical[173-176], and optoelectronic [177, 178]properties of the diamond films.

There are two main methods to fabricate BDD films: micro-wave plasma chemical vapour deposition (MWCVD) and Hot Filament CVD (HFCVD) and both of them produce films with unique surface morphology of various grain size [179-183]. It is vital to control the doping process in order to achieve a better device performance. Therefore, understanding the doping mechanism is the key to unlocking the door for a more expansive application of BDD films in active electronic devices such as high mobility transistors and beta-voltaics. As it has been discussed previously in Chapter 1 section 1.1.2, the results from experimental studies shows some insights into the influence of boron concentration (10^{19} cm^{-3} -10^{21} cm^{-3})on the electrical[175, 184-187], physical and structural properties[108, 188-191] of the BDD films . However, a comprehensive understanding of its material properties such as the spatial distribution and chemical form of impurity atoms, the mechanism of impurity incorporation and diffusion, which determine the properties and performance of as-fabricated BDD films still remains a challenge [192, 193]. Furthermore, some of the published data contain contradictory

results, for example, several papers [188, 194, 195] found the defects and surface

morphology of boron doped PCD films improved with the increasing boron

concentration , while others [185, 188, 196-198] found that the properties of these PCD films

deteriorated with increasing amounts of boron. There are a few possible explanations

for these ambiguities. Firstly, the condition of substrate surface, such as the chemical

composition, surface morphology, grain size and orientation, can plays an important

role in determining the structure and morphology of as-grown films and there is

insufficient evidence that they have been properly characterised or well-defined by

quantitative surface techniques [54, 84, 199]. Secondly, there are some limitations

associated with existing surface techniques, i.e., EDX is not sensitive enough for

analysing light elements such as B and C, which creates difficulties when trying to

obtain the spatial distribution of dopants. Thirdly the surface roughness of PCD films

barely meet the requirement for certain measurements such as EBSD, EELS, XPS which

require a very flat and smooth sample surface, to provide rich information about the

phase composition, grain size and orientation of as-grown samples.

   Based on the challenges discussed above, this chapter focused on the influence of

the boron concentration on the surface morphology, structural and electrical

properties of PCD thin films grown on the two different diamond substrate surfaces.

Each group of samples was produced with the same set of boron concentrations, but

one set was grown directly onto PCD substrates (Homoepitaxial growth) while the

other was grown onto diamond-seeded PCD substrates (Polycrystalline growth), all

fabricated using Hot Filament Chemical Vapour Deposition (HFCVD). For each cycle of

deposition, samples of both seeded and non-seeded substrates were mounted in order

to compare the influence of different growth mechanism on the boron incorporation.

Surface techniques (such as SEM and Raman) were used to characterise the surface

morphology. Electron Backscatter diffraction (EBSD) was employed for the studies of

crystal orientation, phase composition, grain size and orientation of the homoepitaxial

(non-seeded) BDD films. Electrical properties were measured using a home-built Hall

Effect set up and Secondary Ion Mass Spectroscopy (SIMS) were used to investigate

the bulk properties (such as elementary composition, defect concentration and

distribution thought out the whole layers).

4.2   Materials and method

4.2.1   Fabrication of heavily boron doped diamond (BDD) films

Polycrystalline diamond (PCD, TM100) substrates (10 ×10 mm^2) were purchased
from Element Six Company and cut into 2.5 × 2.5 mm2 square by laser. All the
substrates were cleaned a hot solution (200°C) of sulfuric and potassium nitrate for 30
minutes before growing in order to remove any graphite and metallic contaminations.
Homoepitaxial layers were grown on the smooth side (non-seeded) of free-standing
polycrystalline CVD (PCD) and doped with boron from 0.005 sccm flow rate to 0.025
sccm with increasing step of 0.005 sccm. The seeded PCD substrates were prepared
using an electrospray (E.S.) method [200]. The homoepitaxial group of samples were
labelled with a prefix code beginning with "NS" and for the seeded samples with "ES".
All the BDD thin films were deposited under the same conditions: filament
temperature 2100 °C, substrate temperature 800-900 °C, total gas pressure 19.0-20.1
Torr. The amount of Methane (BOC, 99.995% purity), Hydrogen (Air Liquid, 99.999%
purity) and Diborane (5% in H$_2$) in the feedstock gas mixture are detailed in the Table
4.0.1.

Table 4.1. *Growth condition of BDD thin film with various B_2H_6 flow rate*

Growth time/hr	Substrate	CH_4 flow rate/sccm	H_2 flow rate/sccm	B_2H_6 flow rate/sccm
4	PCD	2	200	0.005
4	PCD	2	200	0.01
4	PCD	2	200	0.015
4	PCD	2	200	0.02
4	PCD	2	200	0.025

4.2.2   Surface characterization

The surface morphology was studied by Scanning Electron Microscopy (SEM, Zeiss Sigma HD VP Field Emission) at an accelerating voltage of 10 kV and with different magnification ranges. Electron Backscattered Diffraction (EBSD) was used to study the grain size, phase composition and crystal orientation of as-grown layers. Because the roughness of PCD films grown on the seeded substrate is beyond the limitation of EBSD technique, only samples grown on the non-seeded substrate are suitable for the EBSD imaging.

As the theory of EBSD has been discussed in section 3.4.1, this section will focus on the parameters used in this work. 30 keV electron beam with 120 μm aperture was used for generating electron backscattering diffraction pattern. The stage was tilted to 70 °C and a square area (100 × 50 μm) selected at a magnification of 2000 for all samples in order to compare the impurity amount and changes in the grain size. Graphite and diamond diffraction patterns stored in the EBSD data folder were chosen as references for indexing the diffraction pattern. All the results need to be further

processed through TSL OIM Analysis 7. Software to produce images or charts for target

information. Three types of data: grain size spread chart, grain orientation and phase

images are plotted in this work.

Thin film quality and composition was measured by Raman spectroscopy using a 512

nm wavelength green laser to excite a resonant phonon response. In order to avoid

over-penetration of a laser into the substrate layer, the power of the green laser was

set to be 1%.

4.2.3 Bulk properties using Secondary Ion mass spectroscopy (SIMS)

The distribution of the dopants and other species were studied from depth profile by

using SIMS. 3.27nA Ga^+ beam was applied for etching throughout the whole doped

layer and all measurements were operated under the positive SIMS mode due to the

sensitivity of the system to positive charged ions. Mass spectra were obtained to

collect information on the elemental composition of the sample surface and identify

how the individual elemental species change with depth profile. A 5000 times

magnification was maintained for all measurements which ensured the same

dimension of etch area on each sample.

The concentration of boron has been calibrated previously (Appendix B) and can be

calculated using equation as described in Appendix B. For other elemental species for

which a calibration is not available, the ratio of the counts collected to the carbon

count is used to determine their trace percentage within the sample. However, this is

only a qualitative determination and can only be used to compare different samples

with roughly the same composition.

Interface identification: can be relatively easily determined by tracking the peak

location of elements in a foreign substrate. However, it is impossible to operate in the

same way for the homoepitaxial layers. Therefore, the location of cross point (Point A

94

in **Figure *4.1***) between the rise of sodium peak and the drop of boron concentration was used in this work **Figure *4.1*** is one of examples to show the location and identification of interface layer. As discussed in section 3.5.4.2, there is no sharp drop in the boron depth profile curve when it reaches to the interface due to the mixing effect caused by the primary ion beam. The sputtering /etch time at the cross point (A) of Na and B depth curve is used to calculate the etch rate of as-grown samples at different B-doping level.
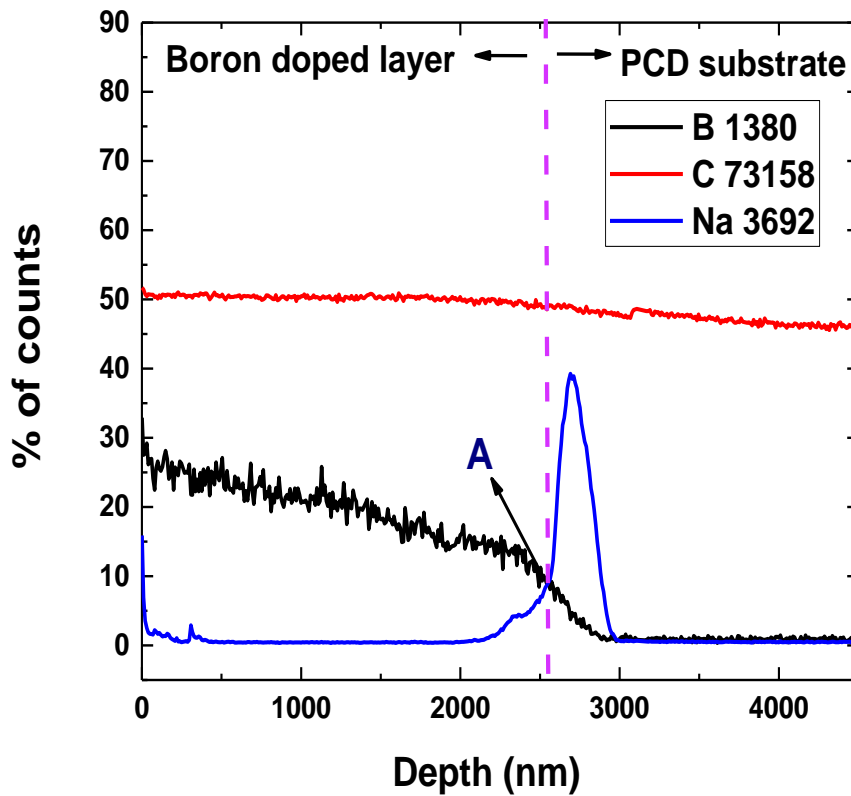
Figure 4.1 *Depth profile of boron (^{11}B), carbon (^{12}C) and sodium (^{23}Na) recorded with the percentage of counts obtained from Mass spectra against the etching depth of sample with 0.005 sccm of B_2H_6.*

Thickness measurements: As there is a seeding layer between the B-doped layer and the substrate for the (ES) group samples, the thickness can be measured by looking at

the cross-sectional SEM images. For the homoepitaxial group of samples, the interface

is not visible on SEM images. Therefore, measuring the thickness of these

homoepitaxial doped layers in this work is achieved through equation 4.1 by using

SIMS depth profile.

$$T_{Homo} = r \times t \ \text{(Equation 4.1)}$$

where T_{HOMO} is the thickness (nm) of homoepitaxial films, r is the etch rate (nm·s^{-1})

and t is the etch time(s) at the cross point between sodium and boron depth profile.

It is obviously that the etch rate is the key parameter for the accuracy of the results

since the etch time can be directly obtained from depth profile (**Figure 4.1**). As the

comparing group was grown under the same condition of each deposition round with

the homoepitaxial group at every B-doping flow rate, the assumption has been made

that the etch rate between NS and ES sample sets is almost the same. Further evidence

to support this assumption is found by looking at the linear relationship between the

etch rate obtained from SIMS depth profile and the sample thickness measured by

SEM from each of the sample sets. **Figure 4.2** shows that there is a steady reduction in

the sample thickness as the boron content increases which indicated that the etch rate

is independent of the concentration of boron dopant. In other words, the etch rate of

ES group can be used for the Equation 4.1.

Equation	y = a + b*x
Plot	Etch rate
Weight	No Weighting
Intercept	0.03649
Slope	3.84632E-4
Residual Sum of Squares	4.78097E-4
Pearson's r	0.99824
R-Square(COD)	0.99649
Adj. R-Square	0.99532
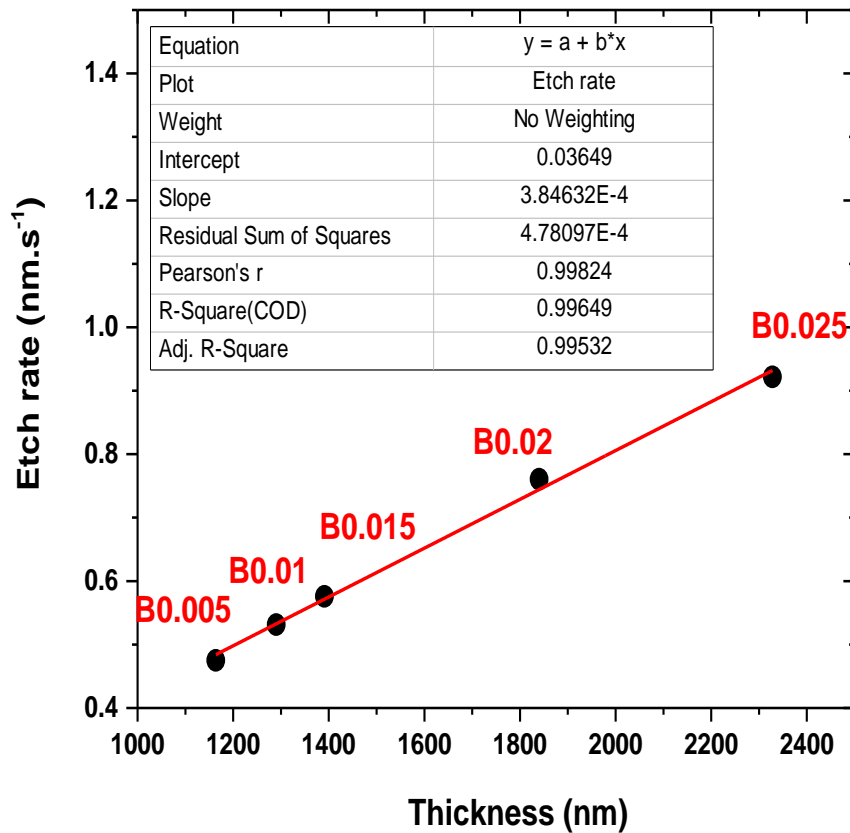
Figure 4.2 *The etch rate obtained at different boron doping flow rate from SIMS depth profile verses the real thickness measurement from cross-sectional SEM images.(Red line is fitted linear line)*

4.2.4   Hall Effect measurement

A 4-point probe Hall Effect set up is used to investigate the electrical properties of heavily boron doped thin films. As previously discussed in Chapter three section 3.6, the is measurement divided into two parts: the Van der Pauw method was performed without magnetic field to obtain the sheet resistance through the slope of I-V curve; the Hall measurement was made with both positive and negative magnetic field to obtain the average Hall voltage which was then put into equation 3.8 and 3.10 to finally get the value of carrier concentration and mobility. Each sample was measured 3 times to get the average value and error. All the measurements were performed at room temperature.

4.3 Results and discussion

4.3.1 Macrostructure surface characterization

Two groups of heavily boron-doped diamond films were successfully fabricated on seeded and non-seeded PCD substrates using HFCVD with various boron doping level achieved by varying the diborane concentration in the feedstock gas between 0.1 sccm and 0.5 sccm flow rate. This section discusses the influence of boron incorporation on the surface morphology, grain boundaries and lattice structure using SEM and Raman spectroscopy.

4.3.1.1 Microcrystalline CVD films on the Electrospray-Seeded (ES) diamond substrate.

Figure 4.3 shows the morphology of boron-doped diamond thin films grown on the seeded substrate with various B-flow rates. The surface morphology with the lower magnification value of x1000 is comprised of irregular blocks with a grainy texture at all doping levels (left column of **Figure 4.3**). It is very clear to see that at the higher magnification value of x20,000 (right column of **Figure 4.3**), the boron doped films consist of a mixture of faceted grains with the average grain size around 712 – 1100 nm according to the result calculated from Image J. Specifically, the sample surface is comprised of mainly triangular-shaped grains, which are related to the formation of C (111) facets [201], and the lamellar-shaped twin characteristic due to the re-nucleation effect introduced by boron doping [202, 203]. The cross-sectional SEM images (**Figure 4.4**) show that the whole doped layer contains disordered orientations of crystal growth. It is also observed that the substrate surface is comprised of large crystals with different growth directions. Furthermore, the thickness measurement (Figure 4.6) from the cross-sectional SEM images (Figure 4.5) shows that the rate of growth decreases with increasing boron concentration indicating the enhanced re-nucleation effect that

occurs when more diborane is added into the feedstock gas mixture for growth on the

seeded substrate[204-206].
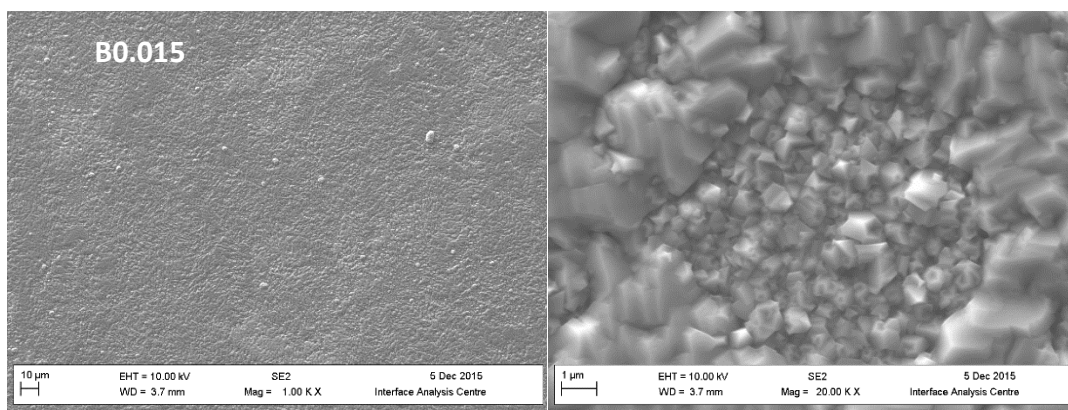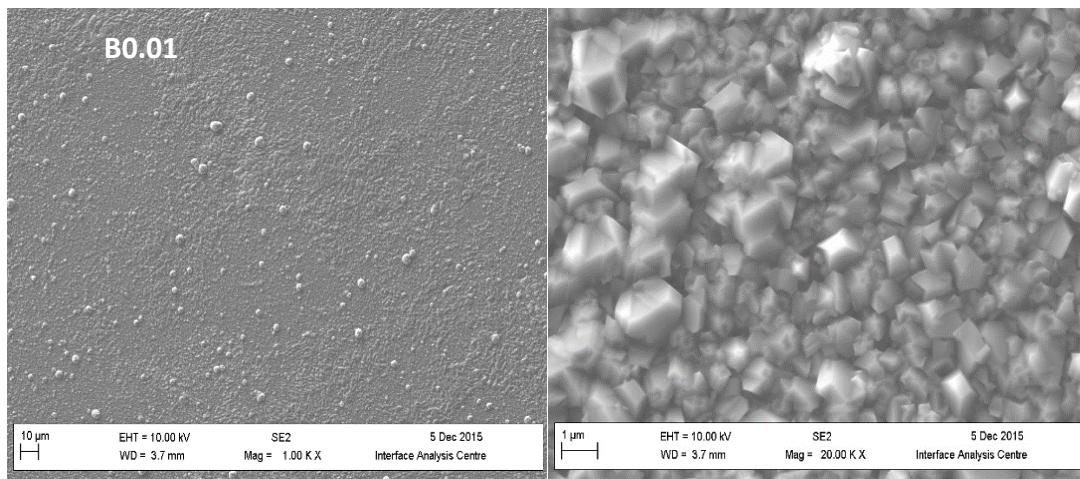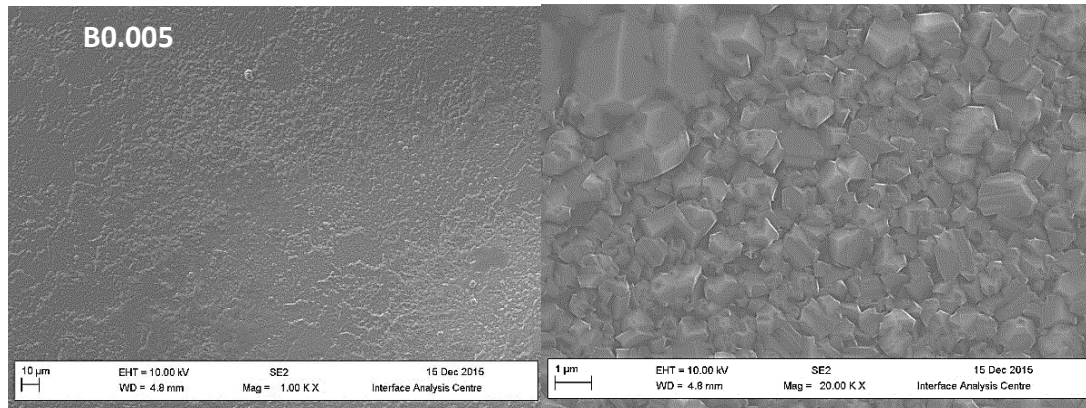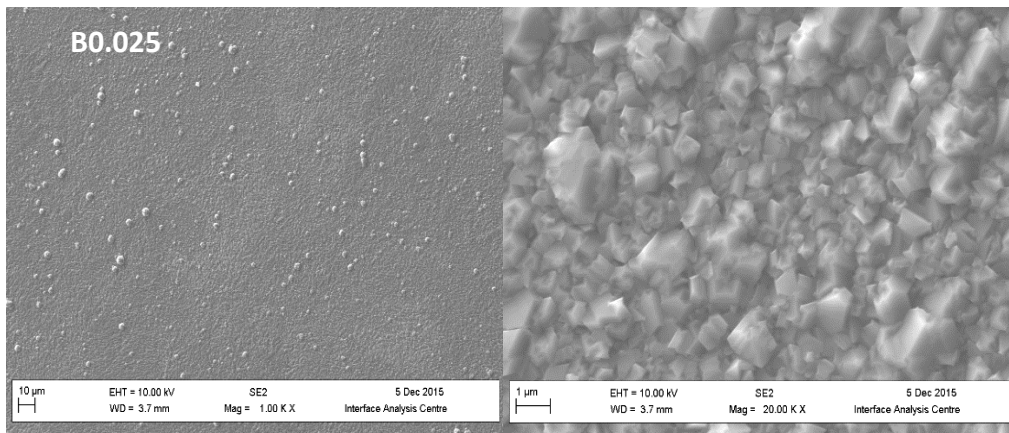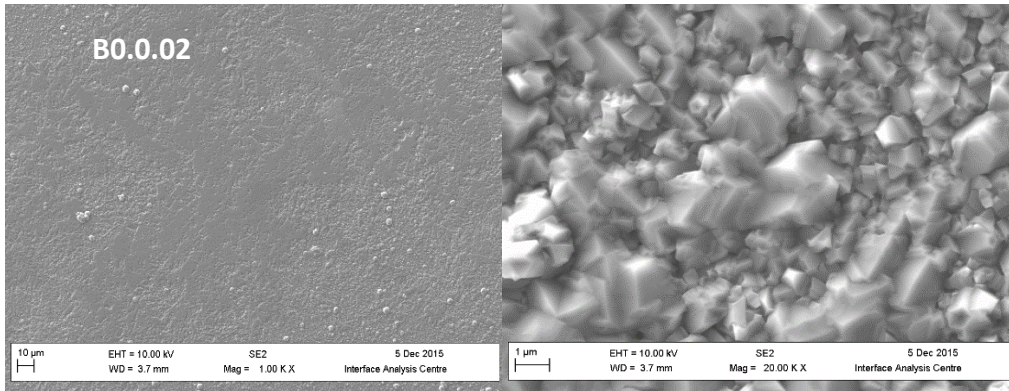
Figure 4.3. *The SEM images of boron-doped diamond thin films grown on the seeded layer.(x1000 magnification on the left column; x20,000 magnification on the right column)*
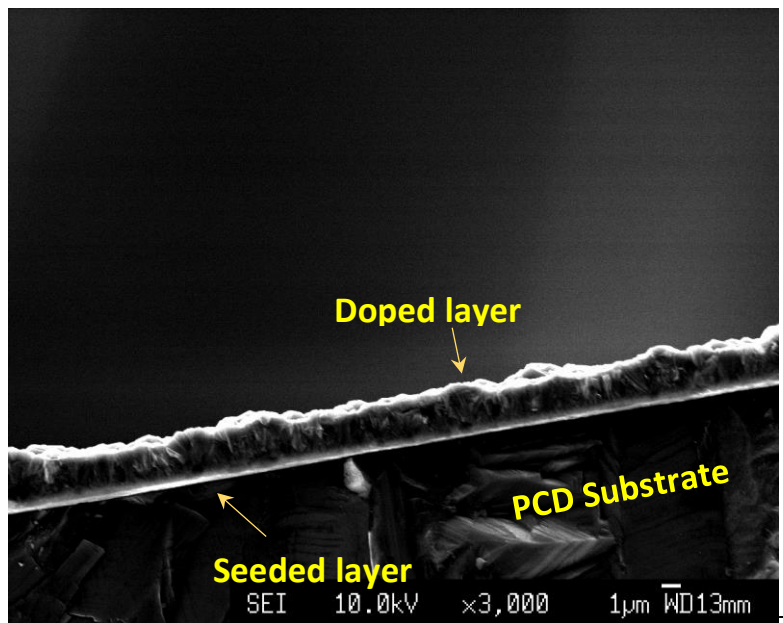
Figure 4.4 *The cross-sectional SEM image of PCD substrate and boron doped thin films.*

Equation	y = a + b*x
Plot	Tickness
Weight	Instrumental
Intercept	2523.64521
Slope	-54873.07959
Residual Sum of Squar	1.56253
Pearson's r	-0.99332
R-Square(COD)	0.98669
Adj. R-Square	0.98225
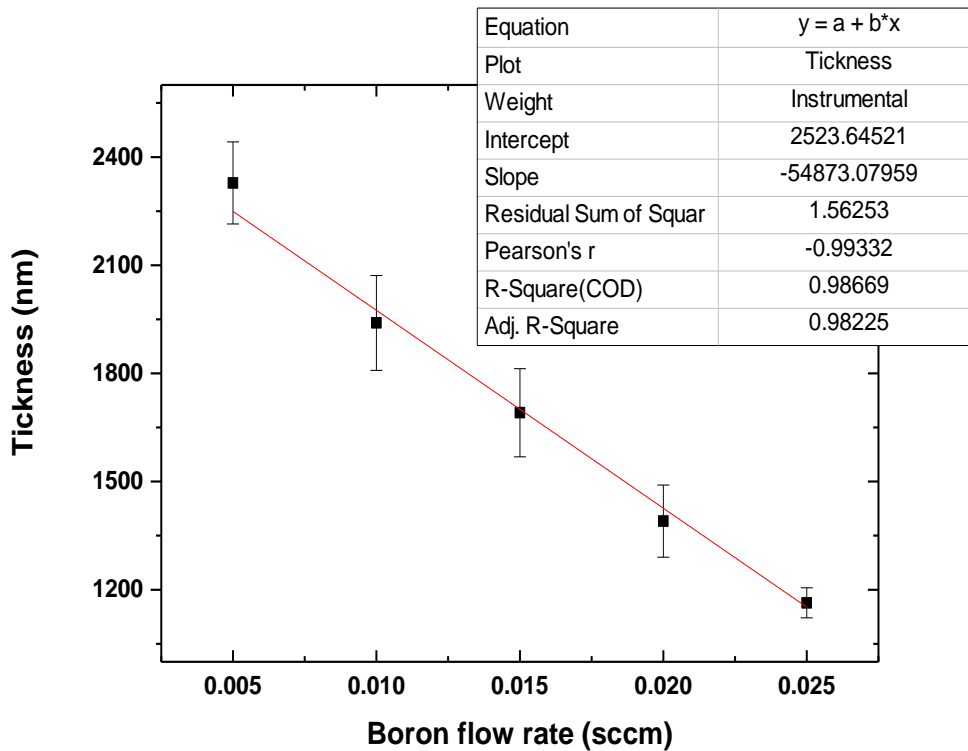
Figure 4.5 *The result of thickness measurement from cross-sectional SEM images of BDD films grown on the seeded PCD substrate as a function of diborane flow rate 1% CH_4 in H_2 under 20 Torr pressure for 4 hours growth (red line is the fitted linear line,)*

4.3.1.2 Homoepitaxial boron doped layer

Figure 4.6 shows the surface morphology of homoepitaxial boron doped diamond film grown on the polycrystalline CVD diamond substrate. It can be seen that the morphology of the surface at the lower magnification is composed of giant leaf-shaped grains of different grain sizes with the step-terrace texture and planar defects can be observed at the higher magnification due to renucleation and mis-angle homoepitaxial growth [207, 208]. It can be seen in Figure 4.6 that these texture and planar defects shown in the B0.005 sample gradually disappear together with a smoother surface as the doping level increases. This phenomena is well documented in the literature and

ascribed to the enhanced surface diffusion of carbon with a high concentration of

boron which leads to the minimised structural defects [197]. The cross-sectional image

of ES samples in Figure 4.7 shows that the substrate surface is the result of

homoepitaxial growth in different directions which leads to the morphology of the as-

doped layer. It can be observed from Figure 4.6 that the increase in boron dopant level

leads to the enlarged grain sizes, which is supported by Electron Backscattered

Diffraction(EBSD) measurements of grain size. The same result has also been found for

the boron-doped heteroepitaxial films, and it is believed that the extra boron atoms

influence the lateral growth of homoepitaxial films [194, 197].
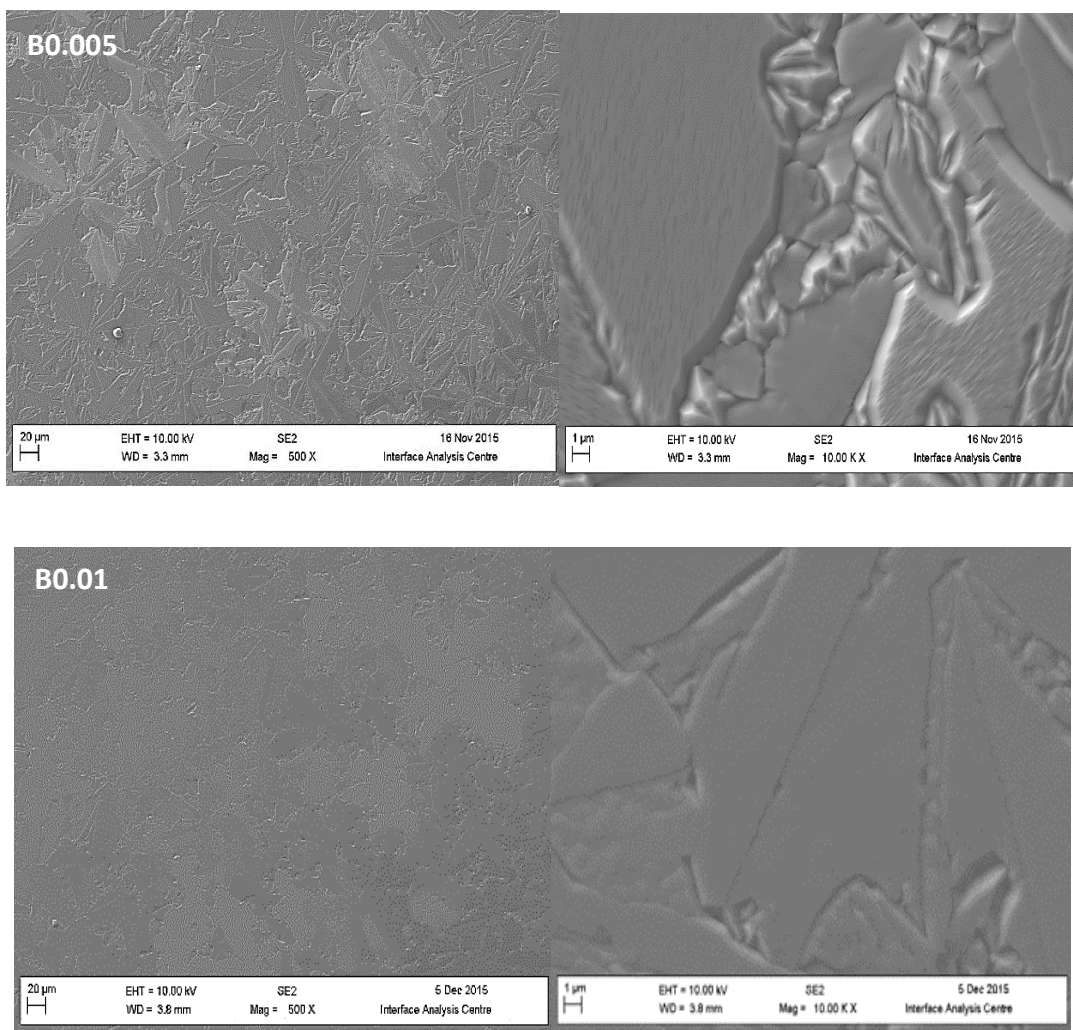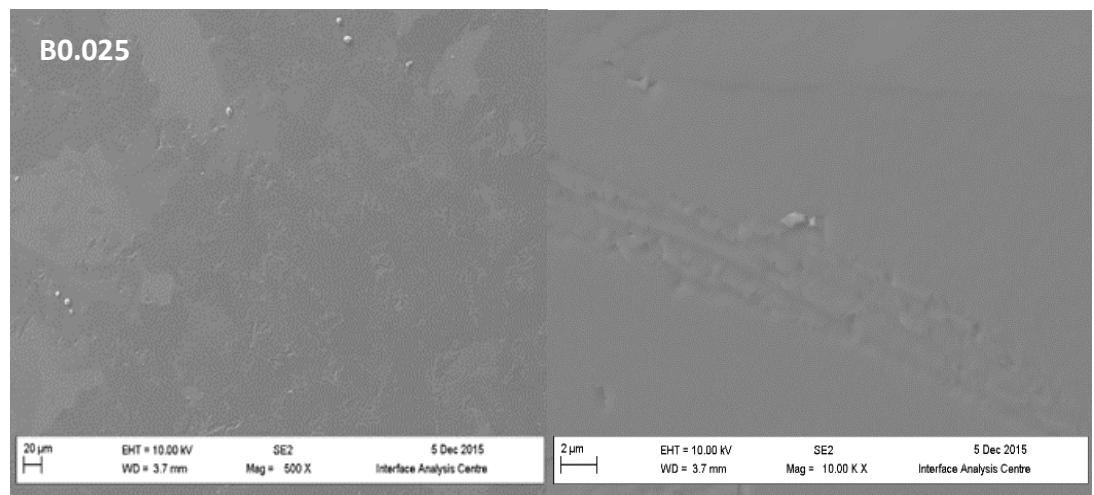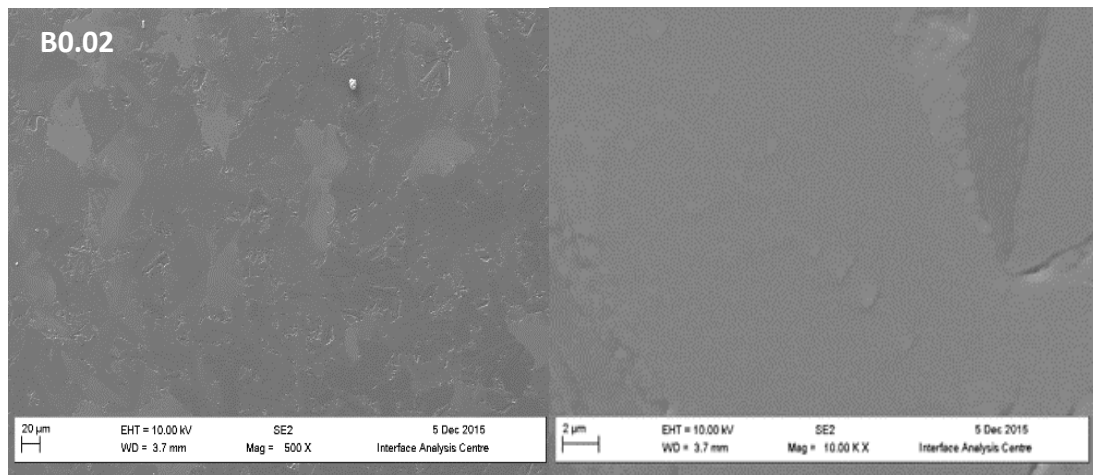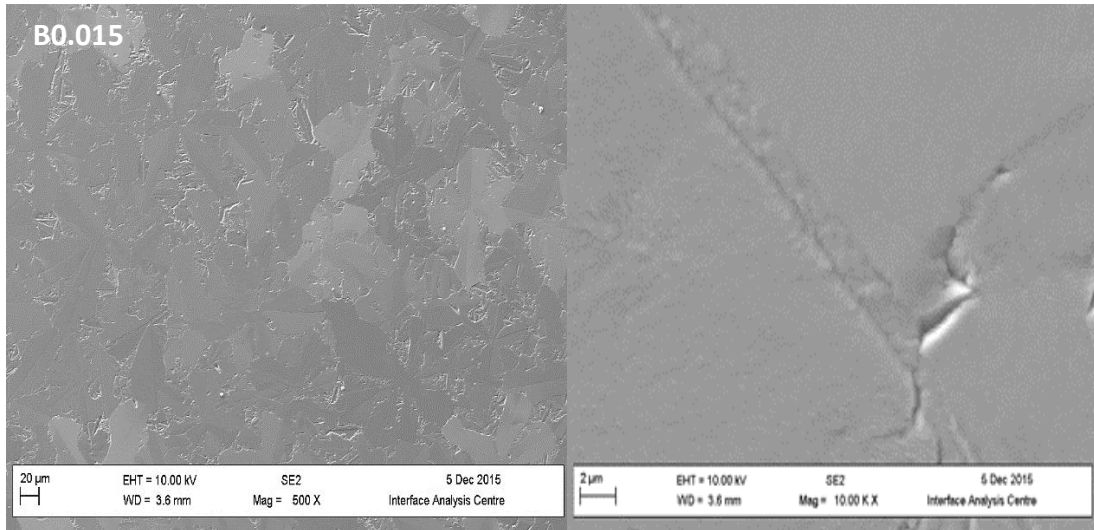
Figure 4.6 *The SEM images of boron doped homoepitaxial films grown on the non-seeded PCD substrate*

(The figure in the left top box is the doping flow rate of boron)

The lattice structure and orientation of the substrate material is one of the key parameters that determines the morphology of the growth layer for homoepitaxial films [79, 209, 210]. Figure 4.8 is the cross-sectional SEM image of the seeded sample which provides the bulk information of crystal growth direction of the PCD substrate. Each large grain on the surface is the result of columnar growth with different texture patterns which results in the differences of grain orientations and growth rate on the sample surface.
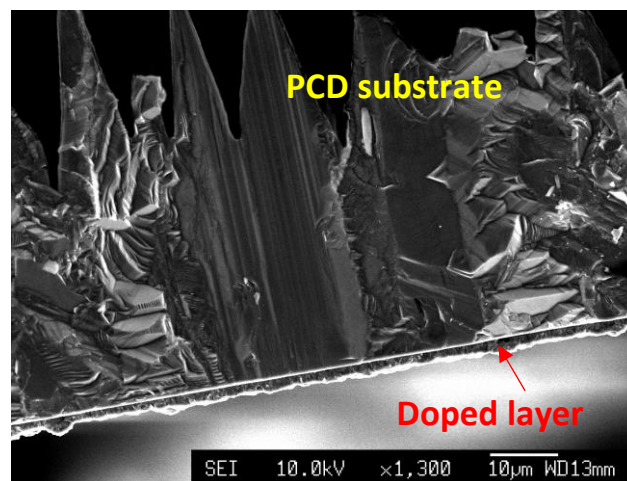
Figure 4.7. *The cross-sectional SEM of homoepitaxial samples with boron doping level at 0.005 sccm*

Figure 4.8,4.9 and 4.10 shows different types of EBSD images (crystal orientation, grain size and phase) coloured inverse pole figure according to the target parameters. Scanning the same area for all samples gives a complete picture of how the boron concentration influences the surface morphology. Figure 4.8 shows the orientation image of BDD film surface at doping flow rate of 0.01 sccm. It can be seen that the majority of crystals exhibit [001] facets with mixture textures of [111] and [101] facet. Each different orientation indicates a different growth direction which is the extension of the surface texture of underlying substrate layer that can be observed from the

cross-sectional image (Figure 4.7). The whole set EBSD images on the flow rate at 0.005,0.01, 0.015,0.02 and 0.025 sccm can be seen in Appendix A.
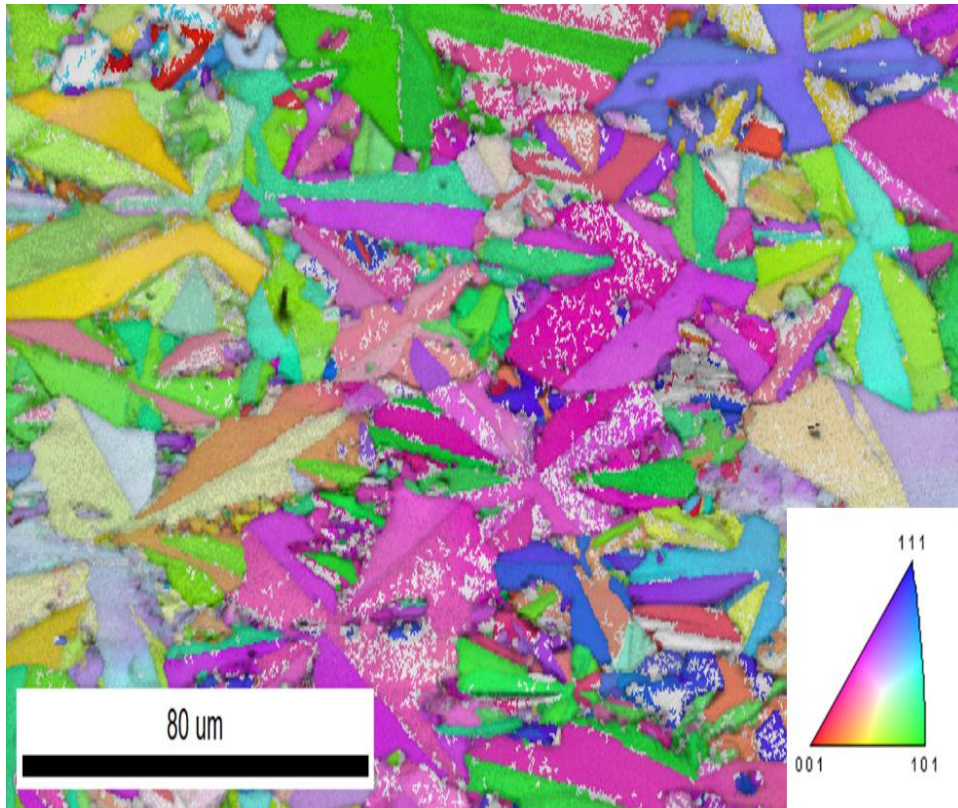
Figure 4.8*. EBSD orientation images of as-grown BDD film (1%CH$_4$) surface coloured with crystal orientation for boron doping level at 0.01 sccm grown on the non-seeded substrate*

Figure 4.9 gives the quantitative information of the grain size distribution over the whole 'as-scanned' area as a function of the boron doping level. It is found that the grain size of the sample with the lowest doping level (B0.005) varies in a wide range and the majority of the grains lie in the range between 5 µm to 19 µm displayed by the variation height of the bar. As the boron doping level increases, the maximum grain size increases from 20 µm at 0.0015 sccm, 26 µm at 0.02 sccm and 34 µm at 0.025 sccm, respectively. This chart shows the relationship between the enlarged size of crystals of BDD films and the level of boron doping flow rate which is mutually supported by the SEM images in Figure 4.6.

105
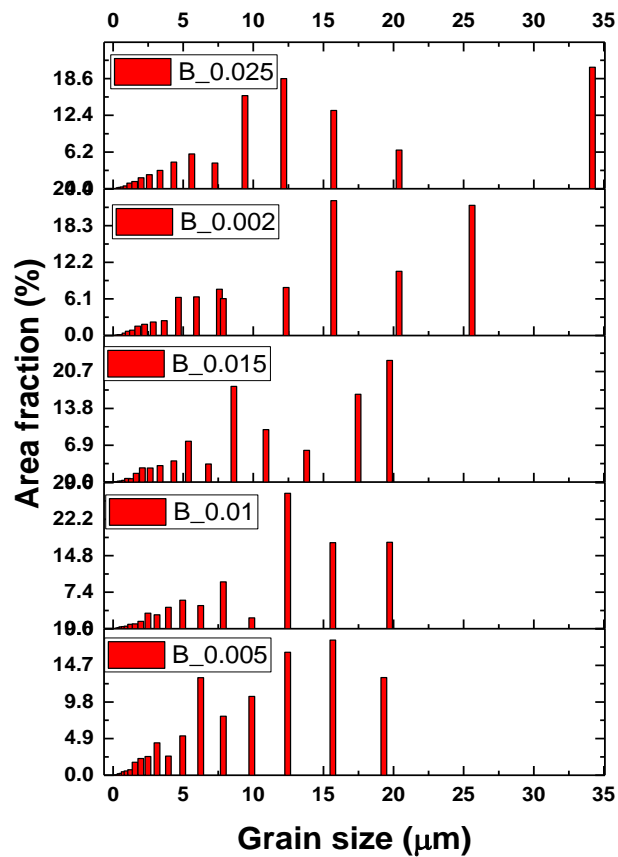
Figure 4.9. *EBSD grain size distribution chart of boron-doped diamond thin films. (Colour ranged by the different boron doping flow rate in the range from 0.005 to0.025 sccm. The height of coloured column represents the amount of percentage of certain grain size accounted for the overall scanned area at particular boron doping flow rate)*

The diamond and graphite phase images (**Figure 4.10**) provide both visual and quantitative information about sp^2/sp^3 composition of the as-grown homoepitaxial films. It can be observed that the graphite impurities are mainly distributed between the diamond grains with a few scattered within the grains. The scale bar on the right-hand side of the image shows that the scanned area contains 11.1 % of carbon in the graphite phase and 88.9 % of the carbon in the sp^3 phase when the doping level of boron at the surface is 0.005 sccm.

Table 4.2 is the summary of phase images of homoepitaxial thin films for doping level from 0.005 sccm to 0.025 sccm. It can be seen that the percentage of carbon in the graphite phase is gradually decreasing with increasing boron concentration which is

the result of the enlarged diamond phase shown in the phase images. The increased percentage of the diamond phase can be used as further evidence to support the EBSD grain size charts and SEM data.
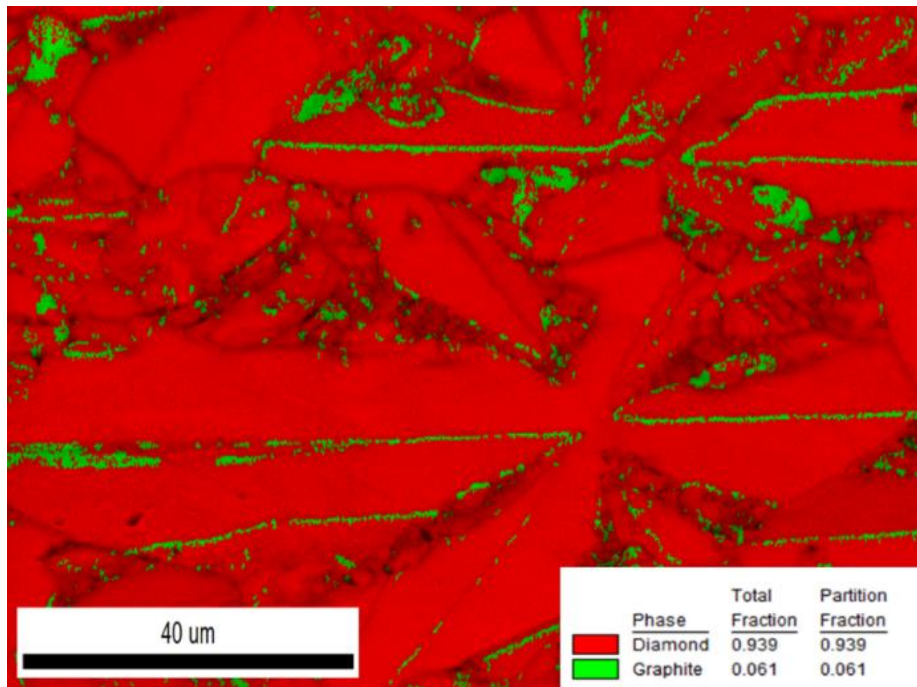
Figure 4.10 *The EBSD phase image of the as-scanned area for a boron doping level of 0.01 sccm (Red and green colour represents diamond and graphite phase respectively. The figure in the total/partition means the amount of each phase accounted for in the as-scanned area).*

Table 4.2 *The summary result of fraction percentage of diamond and graphite based on EBSD phase images as a function of boron doping level.*

B_2H_6 flow rate (sccm)	Graphite percentage (%)	Diamond percentage (%)
0.005	11.1	88.9
0.01	6.1	93.5
0.015	6.5	93.9
0.0.02	5.2	94.8
0.025	5.1	94.9

4.3.1.3 Seeded boron doped film vs Homoepitaxial film

CVD diamond growth on the seeded substrate is different with a non-seeded

substrate which leads to the huge difference in the surface morphology of as-grown

samples.   Both seeded and non-seeded samples were grown under the same

condition in order to be able to make accurate comparisons between them. SEM

images from **Figure 4.11** illustrate the difference in the surface morphology when

diamond seeds are introduced to initial nucleation prior to the thin film growth. It can

be seen that increasing boron concentration smoothed the surface morphology of

homoepitaxial BDD films while it had no significant influence on the samples grown on

the seeded substrate. Furthermore, the grain boundary density of BDD films on the

seeded substrate is much higher than the non-seeded samples at every level of boron

doping. **Table *4.3*** obtained from grain boundary calculations using Image J (Appendix D)

under a magnification x5000 offers approximate information on the influence of boron

concentration upon a number of grain boundaries on the sample surface. There is a

slight reduction in grain size in the seeded samples with the average grain boundary

percentage value of 38%. However, a gradually reduced grain boundary percentage

(from 23% to 4.85%) can be found with increasing boron doping level which is in the

agreement with results found in the literature[194, 197]. It has been suggested that the

boron doping strengthens the lateral growth which leads to the smoothness of the

homoepitaxial films [194].
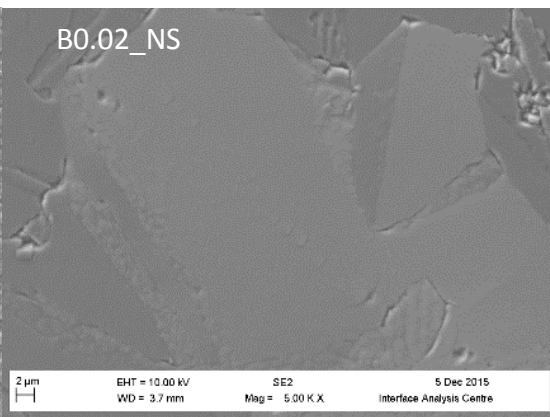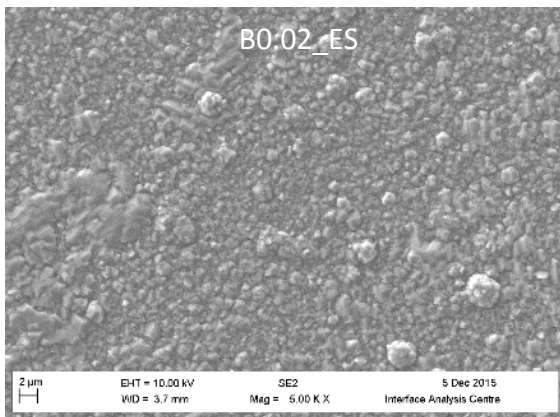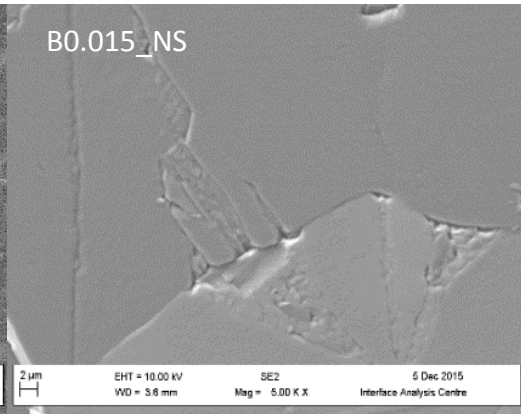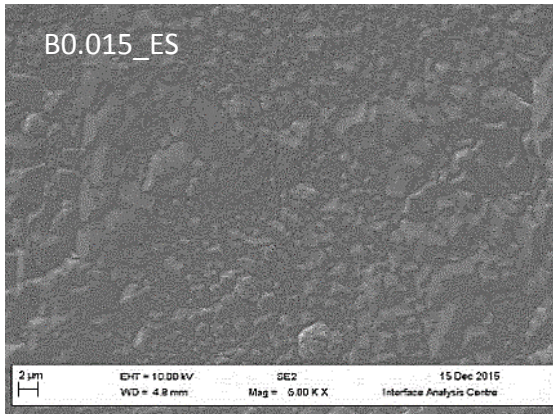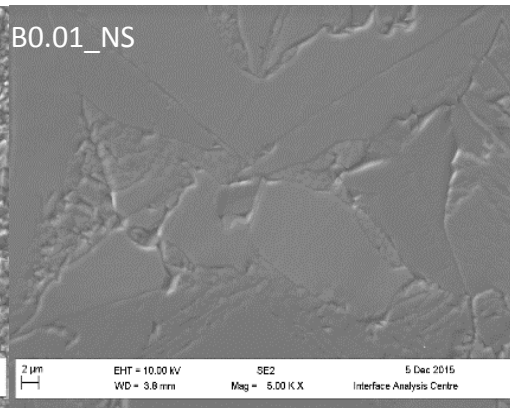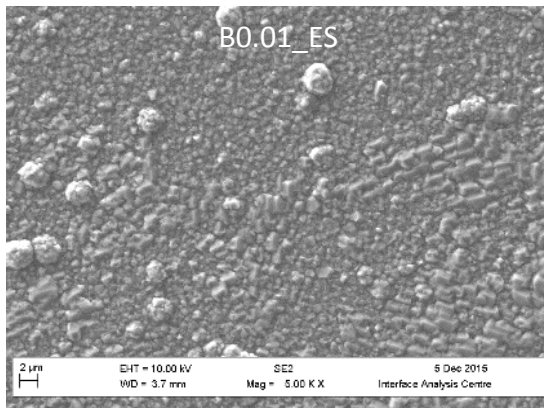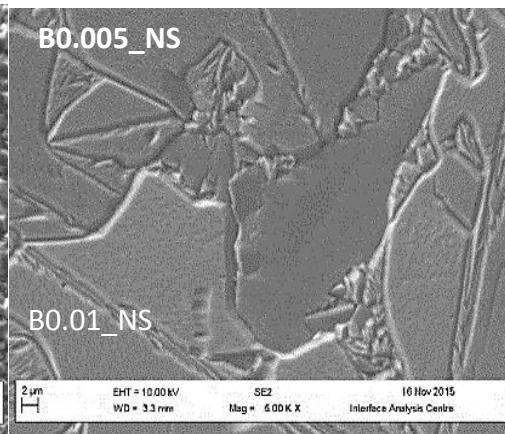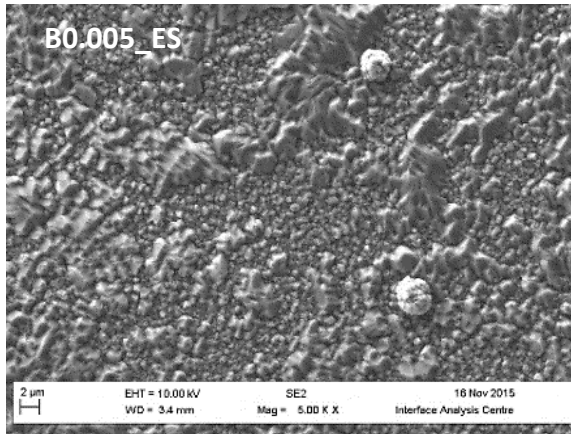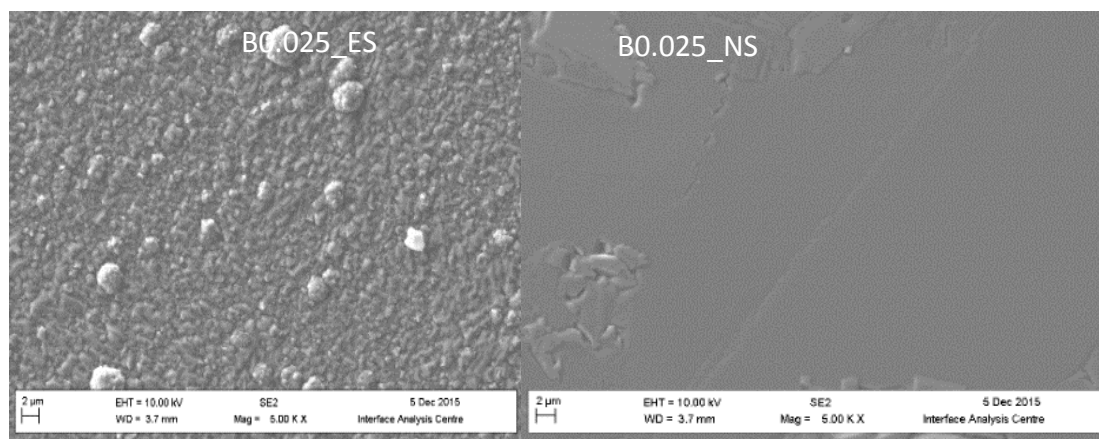
Figure 4.11 *The SEM images of boron doped diamond samples grown on the seeded (left column) and non-seeded (right column) substrate at diborane doping flow rates from 0.005 sccm to 0.025 sccm; ES represents electrospray seeding, NS represents non-seeded substrate*

As the growth mechanism has been discussed in Chapter 2 section 2.1, diamond growth is the result of competition between etching and deposition of carbon as well as the conditions of the substrate surface. Under the same deposition procedure, columnar growth on the individual small seed "islands" produced numerous facets resulting in the rough surface and larger density of grain boundaries than the homoepitaxial growth on the polished non-seeded substrate. With the addition of boron which is much harder to etch away by the atomic hydrogen, the chance for the carbon to co-ordinate from the site where the boron has impinged on. Therefore, the re-nucleation effect is strengthened with increasing boron content on the surface which leads to the smaller crystal size on the thin films grown on the seeded substrate. In the case of homoepitaxial growth, the additional boron will enhance lateral growth which leads to the formation of larger sized crystal grains.

Table 4.3. *The calculation results of both grain and grain boundary density for the comparing group samples and homoepitaxial ones.*

Seeded substrate	Doping level/sccm	Grain area percent /μm^2	Grain boundary percent/μm^2
	0.005	62.58	37.42
	0.01	62.05	37.95
	0.015	61.8	38.2
	0.02	61.5	38.5
	0.025	60.5	39.05
Non-seeded substrate	0.005	76.352	23.65
	0.01	85.396	14.605
	0.015	86.96	13.04
	0.02	92.95	7.5
	0.025	95.15	4.85

4.3.1.4 Lattice structure and impurity of boron doped film on seeded substrate

Green laser (λ = 514nm) in this work is used to check the quality and the non-diamond impurities within the samples. Diamond is characterised by four fold-coordinated sp^3 bonding of O_h symmetry [211]. The first-order Raman mode of natural diamond, which can be only observed from the zone-centre phonon modes, is located

at 1332 cm^{-1} [212]. As shown in Figure 4.12, the sharp and narrow peak (FWHM: 9.1 cm^{-1}) was obtained at the location of 1332.08 cm^{-1} in sample A with a graphitic peak positioned at 1554.69 cm^{-1} which shows the good quality of the as-grown BDD thin film. The asymmetric diamond peak observed from the spectra indicates a "Fano interference effect" due to the quantum interference between diamond lattice and the large amount of doped boron[213, 214]. It can be observed that this sp^3 peak is gradually downshifted from 1332.08 cm^{-1} to 1305.94 cm^{-1} with decreasing intensity as the boron doping range is varied from 0.01 sccm to 0.025 sccm (B,C,D,E figure 4.13). Meanwhile, broad peak at 1234.24 cm^{-1} appears in graph B and increases in intensity to become the main features in graphs C, D and E, which is believed to be related to the formation of the boron impurity band[184] is in agreement with previous reports[188, 196, 215-217]. The experimental and modelling results detailed in these reports found that this phenomenon was attributed to the relaxation of the momentum conservation caused by the disruption of symmetry of crystal lattice due to the very high boron concentration present in the diamond lattice. In this work, as the concentration of boron was increased, the symmetry of diamond lattice progressively disrupted and disappeared at a very high level of boron leading to a breakdown in the selection rules of Raman scattering [218]. Therefore, the disappearance of the sp^3 peak and the presence of the boron-related impurity band can be explained by the complete relaxation of selection rules owing to the presence of a very high boron content in the diamond lattice [179, 219].

The Raman peak intensity ratio (I_G/I_D) of graphic peak (I_G) over diamond peak (I_D) and full width half maximum (FWHM) are usually used as a check of the crystal perfection of semiconductor materials [220]. After normalisation of the spectra, the higher value of

112

I_D/I_G ratio leads to a lower concentration of graphitic impurities. In comparison, the lower the value of FWHM, the better quality of diamond lattice [220]. The G-band peak located at 1554.69 cm^{-1} in Figure 4.13, Graph A gradually reduced in graph B, C with a broader tail on the higher wavenumber, and disappeared in graph D,E which could be the result of being covered by the strong photoluminescence (PL) emission arising from increasing impurities within the film. As it can be observed from Figure 4.13, the value of I_D/I_G ratio gradually decreased in graph A, B and C with the increasing FWHM value of sp^3 diamond peak which indicated the severe interference and degree of imperfection introduced by adding more boron into the diamond lattice. The position of the G-peak was also downshifted to lower wavenumber which is believed to be the result of bond angle distortions in graphitic planes, reportedly caused by the high boron concentration [219].
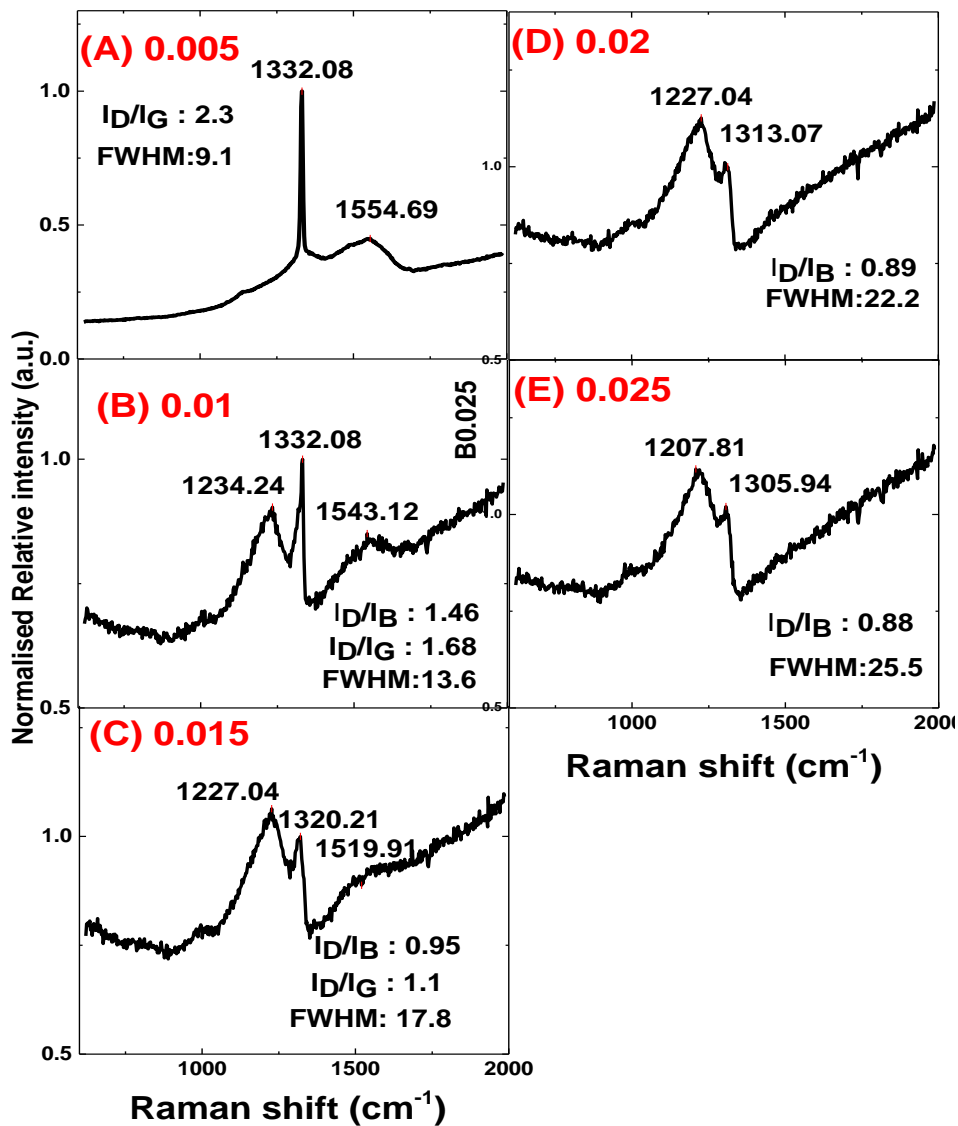
Figure 4.12 *The Raman spectra of boron-doped diamond thin films grown on the seeded substrate from 0.005 sccm to 0.025 sccm boron flow rate. (Red figure on the left top of image represent boron flow rate)*

Figure 4.13 shows the Raman spectra of homoepitaxial films grown on the PCD substrate. This result shows that there is a large downshift of the diamond peak in the control group under the same experimental conditions (section 4.3.1.4), the contribution of the sp^3 signal from the diamond substrate material can be excluded from this case. As has been discussed in section (4.3.1.4) about the D-peak dramatic

downshift for the group of samples (seeded substrate), the complete breakdown of the selection rules leads to such a significant change in Raman position. It seems like this explanation doesn't apply to the homoepitaxial films in this work. The main reason for this is the spot size of Raman laser (around 7 µm in diameter) used in this work is "small" enough to just focus on the single orientated-grain on the homoepitaxial surface (Figure 4.7) while it could cover multiple grains and grain boundaries on the seeded sample surface (Figure 4.12). This could be another evidence to support the influence of size effect on the Raman spectra. Furthermore, based on the SEM and EBSD results discussed above (section 4.3.1.2), the surface morphology (grain size and smoothness) is improved by doping more boron into the growth which might relax the stress of the as-deposited thin film and hence no significant shift can be observed from Raman spectra. Meanwhile, the boron-related broad band appears in graph C and become the dominant feature in graphs D and E. On the other hand, the gradually reducing FWHM value (wider peak) and I_D/I_G ratio indicated the worse quality of as-grown B-doped layer with high boron content.
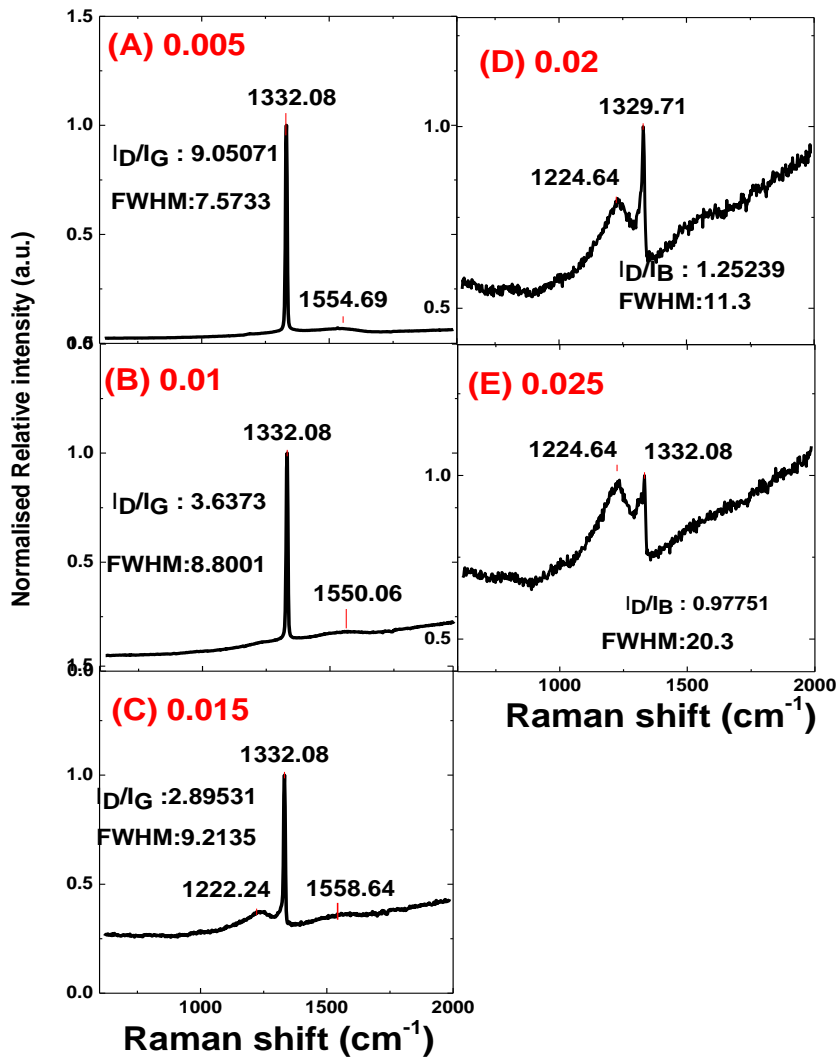
Figure 4.13 *The Raman spectra of boron-doped diamond thin films grown on the non-seeded substrate from 0.005 sccm to 0.025 sccm boron flow rate.(Red figure on the left top of image represent boron flow rate)*

4.3.1.5   The comparison of Raman spectra between homoepitaxial and comparing group

Based on the previous discussion about Raman spectra of seeded and non-seeded (homoepitaxial) samples separately, it can be easily found that the influence of boron concentration on the graphitization degree and crystallinity presented a similar trend for both of them. The sp^3 diamond peak widening and I_D/I_G ratio decreasing all show

that the increasing impurity content degraded the quality of as-grown diamond thin films. At the higher doping level (B-flow rate over 0.3 sccm), a broad band located around 1225 cm^{-1} is significant in the spectra of both types indicative of the impurity band formation and severe Fano interference which results in an asymmetric diamond peak. Furthermore, this impurity band changes electrical carrier transport at room temperature at a giving magnetic and electrical field which will be discussed in the later section of Hall Effect measurement as further evidence to explain the influence of these extra boron atoms on the conductivity performance. By comparison, the value of I_D/I_G ratio for the homoepitaxial film is higher than for the seeded samples and FWHM is lower than the control group at every doping level under the same procedure. Hence, the BDD films grown on the non-seeded substrate have better quality than the ones on the seeded substrate.

In summary, introducing high concentrations of boron atoms into diamond lattice caused a significant change in the lattice structure and thin film stress based on the Raman spectra, and surface morphology based on the SEM/EBSD results. The impact of impurity content on the seeded samples was more severe than on the non-seeded samples demonstrating the advantage of homoepitaxial growth.

4.3.2   Distribution of defects in BDD thin films

Secondary Ion Mass Spectroscopy (SIMS) was used to obtain information on the distribution and concentration of defects (Boron and CH_x) throughout the entire film. As all samples are grown on PCD substrates, the determination of the interface layer is based on the depth resolution which is the width of interface between two layers [221]. Figure 4.14 provides the qualitative and elementary information about the surface composition of B-doped films fabricated by HFCVD method. Mass 11, 12,15 and 16 can be assigned to -B,-C, –CH$_3$ and –O while mass 13 can comes from the combination of –

CH and ^{13}C and mass 14 from $-CH_2$ or-N. As the precursor gases used in this work is N4.5 purity CH_4 and N5 H_2, the majority signal of mass 13 and 14 come from $-CH$ and $-CH_2$. Oxygen and Sodium are common contamination elements which could come from the air and SIMS chamber. One thing that needs to be borne in mind is that the intensity of the signal has no directly link to the amount of the species because of the different sensitivity in response to the SIMS system. For example, the sodium signal is very sensitive in positive SIMS mode and it often used to locate and calibrate the secondary ion images, while the CH_x species is more sensitive under negative SIMS mode. Therefore, the count value of Na is much higher than CH_x which means the mass spectra can only provide qualitative rather than quantitative analysis.
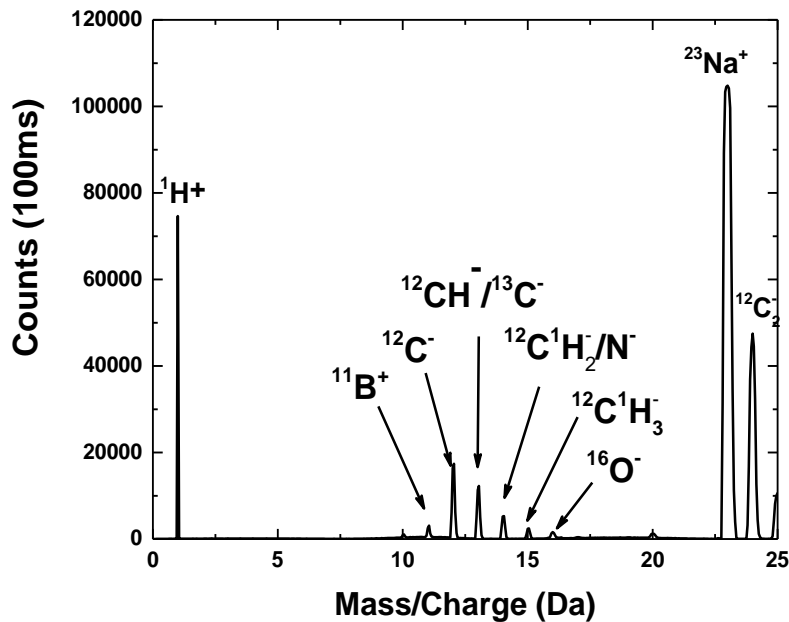
Figure 4.14 *The mass spectra of BDD thin film surface grown on PCD substrate under positive SIMS mode.*

Based on the information given by the mass spectra (Figure 4.14), a depth profile is used to study the variation of those species throughout the whole layer. Figure 4.15 gives two graphs plotted under negative and positive SIMS over the same sample, the depth is used as a function of the percentage of the count. The Y-axis value is not the

actual count of each species, it is the ratio of the counts at a particular depth over the counts recorded on the surface (value in the upper right box) for each element or group. Therefore, these graphs only present the distribution of each species rather than the percentage of each element within the layer. It can be seen from graph A that -CH_x and -O are species present in the sample which are the common defects that are known to exist in CVD diamond [222, 223]. The actual count of –CH_2 and -CH_3 is below the detection limit (account number lower than 50 in a mass spectra) indicating that there is bare –CH_2 and –CH_3 in the bulk in this sample at the boron doping level of 0.005 sccm. There is a peak in the –O depth profile that shows that there is a thin layer on the growth substrate which mainly comes from the acid cleaning treatment. The depth profile (Graph B Figure 4.15) under positive SIMS mode shows that in the top few nanometres a localised sodium layer is present on the substrate, which is in the same location as –O. The location of Na or O peak indicated the interface between the boron doped layer and substrate.
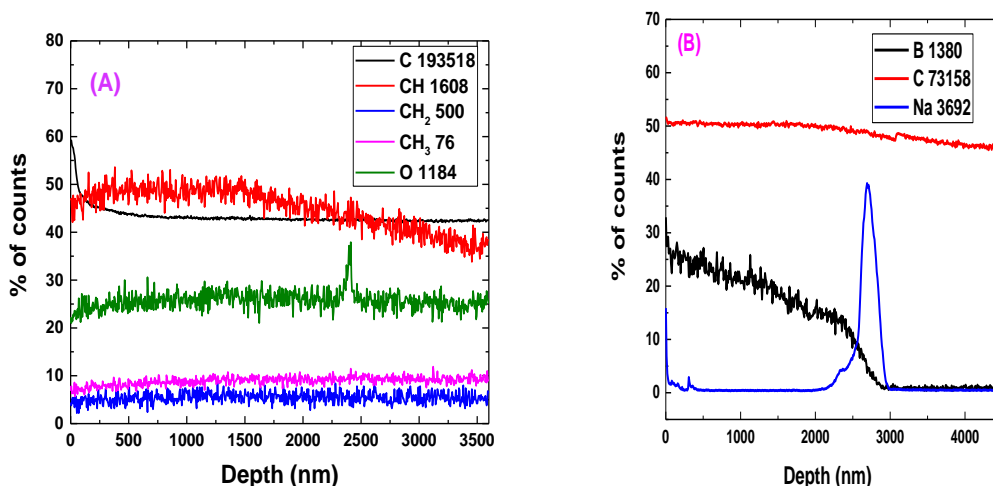
Figure 4.15 *The depth profile of -CH_x and –^{16}O under negative SIMS mode (A) and –^{11}B,-^{12}C, -^{23}Na under positive SIMS mode over the depth of the samples with boron doping level at 0.005*

sccm. The percentage of each element is obtained from the counts ratio (count at certain depth over the count at the surface)

4.3.2.1 Boron distribution and incorporation concentration of seeded samples (ES)

Figure 4.16 shows the depth profile of boron doping calculated using equation 4.1 at different depths into the seeded substrate surface. It can be observed that boron is evenly distributed from the substrate all the way to around 3/4 of the film and then slightly increases near the sample surface. The doping process at flow rate of 0.005 sccm displays flat and uniform profile shows no segregation procedure which is in agreement with previous reports [224, 225]. Furthermore, the decreasing in the penetration depth as the boron concentration increasing found in Figure 4.16 is in a well agreement with the thickness measurement found in Table 4.2 which confirm the fact that the growth rate decreases with the content increasing. This evidence also has been supported by inspecting SEM images of the cross-sectional view of the doped layers (**Figure *4.5***) and SIMS analysis of the depth profile of Na in the doped layer. Figure 4.17 is the depth profile of Na which arranged according to the different doping levels. It can be observed that the location of the peak shifted towards to the surface with increasing boron content. As it has been discussed previously (section 4.1), the increasing boron content enhances re-nucleation which leads to the decreasing growth rate during thin film deposition.
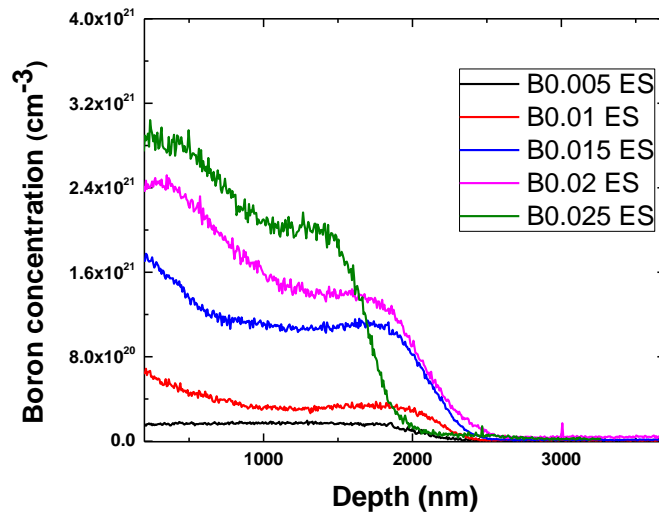
Figure 4.16. *The depth profile of boron (^{11}B) recorded with the boron concentration against the etching depth of BDD thin films grown on the seeded substrate (ES group) in the doping range from 0.005 sccm to 0.025 sccm*
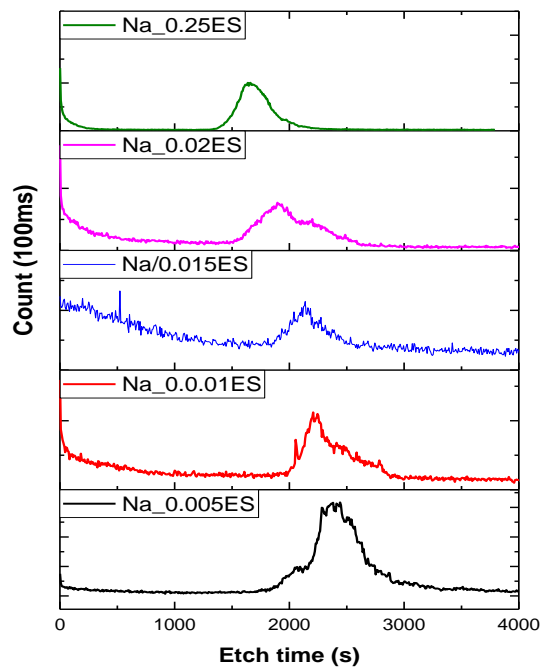
Figure 4.17. *The depth profile of Na (^{23}Na) count ratio ($^{23}Na/^{12}C$) recorded with the boron concentration against the etching time of BDD thin films grown on the seeded substrate (ES group) in the doping range from 0.005 sccm to 0.025 sccm*

121

4.3.2.2   Boron distribution and incorporation of the homoepitaxial/non-seeded films (NS)

Figure 4.18 shows the depth profile of boron throughout the thin films at B-doping flow rates from 0.005sccm to 0.025 sccm. It can be seen that the boron atoms are evenly distributed from the substrate all the way to the surface at the minimum doping level (black line: 0.005 sccm) which shows a good controllable dynamics of boron incorporation. However, there is no flat [11]B profile occurs in the sample with a doping level of 0.01 sccm (red line) and the boron concentration differs from the substrate to the sample surface.

The remaining boron depth profile at higher doping level shows even larger difference in dopant distribution from the substrate to the surface which shows that be the boron aggregates or clusters prevent the incorporation efficiency. The results from the SEM and EBSD images show the improvement in the surface quality and enlarged crystals further support the enhanced lateral crystal growth at very high level of boron concentration [189]. Another influence of boron on homoepitaxial thin film growth is the reduced thickness of the layers with increasing dopant content which can be seen in Figure 4.20. The Na peak gradually becomes shifted towards to the shorter ion etch time at the increasing levels of flow rate which further confirms that the growth rate reduction by incorporating more boron content into diamond lattice.
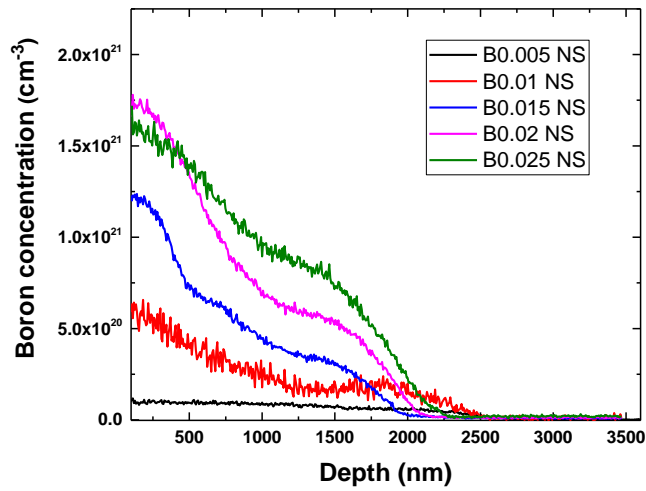
Figure 4.18. *The depth profile of boron (^{11}B) recorded with the boron concentration against the etching depth of BDD thin films grown on the non-seeded substrate (NS group) in the doping range from 0.005 sccm to 0.025 sccm*
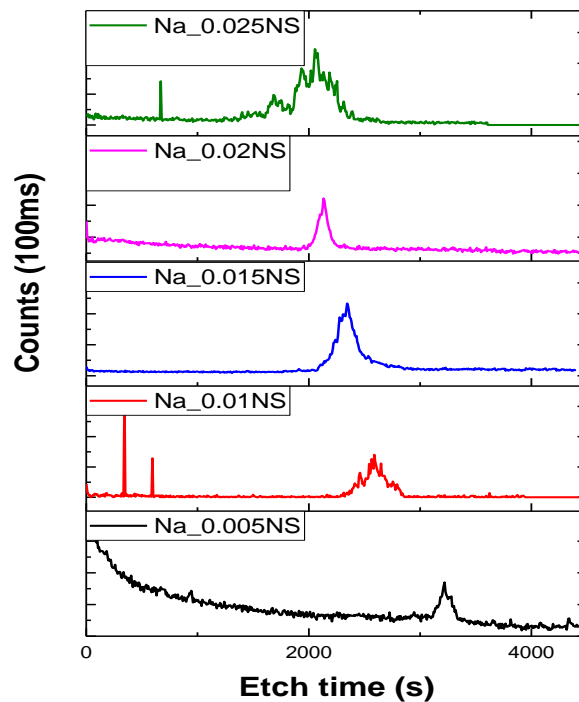
Figure 4.19 *The depth profile of Na (^{23}Na) count ratio (^{23}Na/^{12}C) recorded with the boron concentration against the etching depth of BDD thin films grown on the non-seeded substrate (NS group) in the doping range from 0.005 sccm to 0.025 sccm*

Under the same growth condition, the concentration of doped boron on the seeded substrate is around double that of an equivalent sample from the non-seeded substrate set, which offers further evidence that it is energetically favoured for the boron to sit at the grain boundaries where the concentration is larger than in the homoepitaxial films (Graph A, Figure 4.20)[120, 220, 226]. It can be also found that the Ga$^+$ beam takes the shorter time to reach the non-seeded substrate samples than the seeded substrate sample at all doping level which can be seen by the Na peak location in Graph B. As discussed in Section 4.2.3 before, the boron concentration has no significant influence on the etch rate. Therefore, this result indicated that the seeded samples have the thinner films than the non-seeded ones at every doping level under the same deposition conditions. The reason behind this is linked to the re-nucleation effect on the different conditions of substrate surfaces.
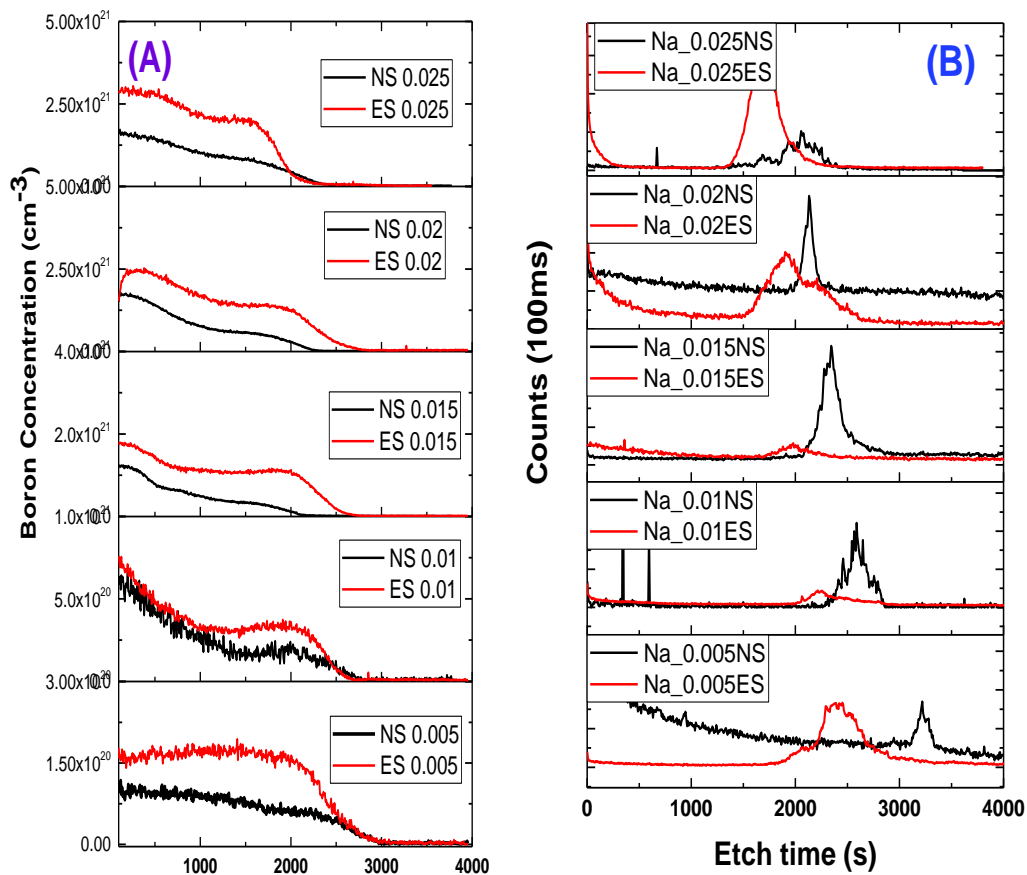
Figure 4.20 *The comparisons of boron(^{11}B) concentration between two group of samples (A)*

and sodium (^{23}Na) distribution (B)

4.3.3 Electrical properties of heavily boron doped diamond thin films

There are many studies and reports [227-231] on the electrical properties of doped diamond layers. Hall Effect measurement conducted in this work provides the key parameters (conductivity, carrier concentration and mobility) that are important for electronic applications. By comparing electrical properties between seeded and homoepitaxial samples, it is possible to gain a deeper insight, and together with previous results, to explain the influence of boron and the lattice structure on the electrical performance.

4.3.3.1 Electrical properties of seeded samples

It is found in Figure 4.21 that the resistivity of as-grown samples gradually decreases with increasing doping flow rate (1%CH_4 in H_2) which shows the thin film became more conductive with increasing boron content. The behaviour of carrier concentration and mobility is divided by the threshold boron concentration (3×10^{20} cm^{-3}) for the metal-insulator transition. It can be seen in Graph B (Figure 4.21) that the carrier mobility decreases with increasing hole concentration before 0.015sccm which suggest a strong defect-scattering effect upon the carriers' ability to move. However, the as-measured carrier concentration decreases with increasing mobility while the doping level keeps increasing. This shows the metallic conductivity of the as-grown BDD layer. In connection with SIMS data (Figure 4.20), the rise in the hole concentration (h^+) follows from the increasing boron concentration within the doping range of 0.005 to 0.015 sccm. However, the as-measured hole concentration (h^+) reduced despite the boron concentration increasing (Figure 4.20) between the doping level of 0.02 and 0.025 sccm which shows less of the incorporated boron is electronically active. Referring to the Raman spectra (Figure 4.12), the appearance of a broad peak at around 1234.24 cm^{-1} with a large downshift of the D band from 1332 cm^{-1} to 1313.07 cm^{-1} (Graph D) and 1305.94 cm^{-1} (Graph E), respectively, gives firm evidence for the formation of a boron impurity band and highly defective diamond films. This could mean that there are much fewer substitutional boron atoms taking up substitutional positions the in diamond lattice. From the viewpoint of conductivity, the as-measured boron concentration of 0.015 sccm is above the metal-like threshold of $3 \sim 5 \times 10^{20}$ cm^{-3} [224]and the opposite electrical behaviour before and after this point (Figure 4.21) shows a transition point from the semi-conductivity to metal-like conductivity.
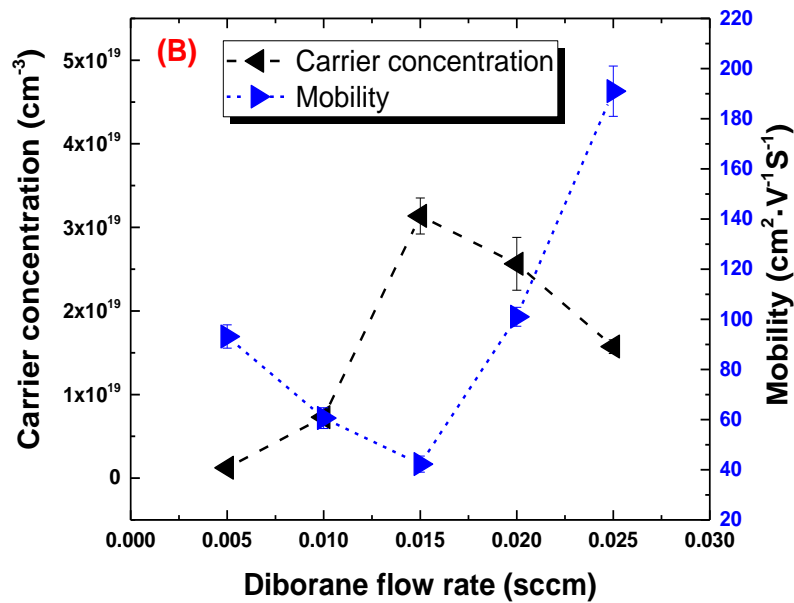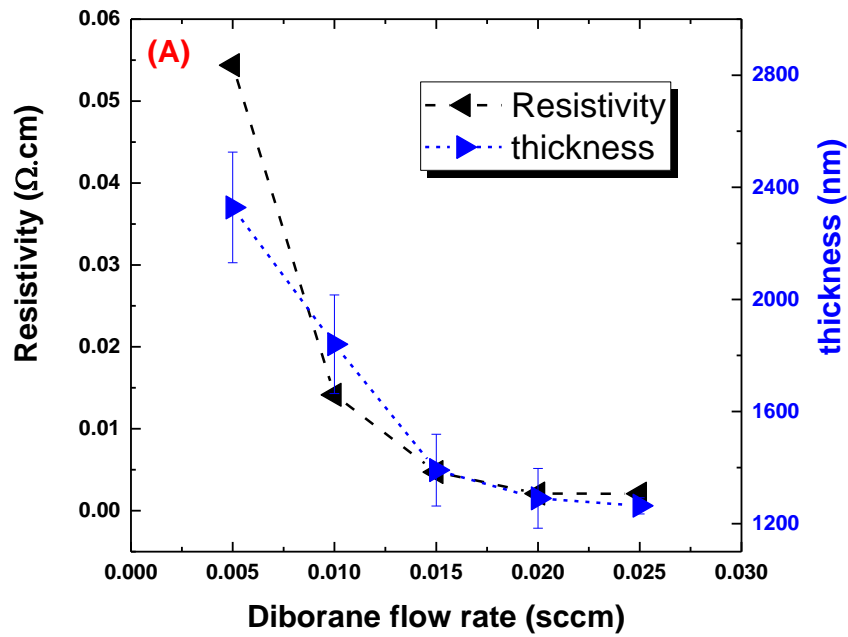
Figure 4.21 *The Hall Effect result of resistivity, carrier concentration and mobility of BDD films grown on the seeded substrate as a function of boron flow rate with 1%CH$_4$ in H$_2$ under 20 torr pressure. All the measurements have been done at the room temperature. Graph (A) plots resistivity (black data point) with thickness (blue data point) of the BDD films and Graph (B) shows the relationship between carrier concentration (black) and mobility (blue) with increasing boron doping level.c*

4.3.3.2 Carrier transport of Homoepitaxial film

  Similar electrical properties to the seeded sample set were found in Figure 4.22 for

the resistivity of the as-grown homoepitaxial films, which reduced with increasing

boron doping level (Figure 4.22). The carrier concentration rises while the hole

mobility falls up to a flow rate of 0.015 sccm, and then the behaviour reverses at

higher dopant levels. Using the SIMS depth profile data for boron (Figure 4.20), the as-

measured charged carriers keep increasing with the boron concentration until a value

of 0.015 sccm is reached and then falls with the higher boron content. Although the D

peak in Graph D and E of Raman spectra (Figure 4.13) barely shifted, the large boron-

related broad band appears at the location of 1224 cm^{-1} indicates the formation of an

impurity band.
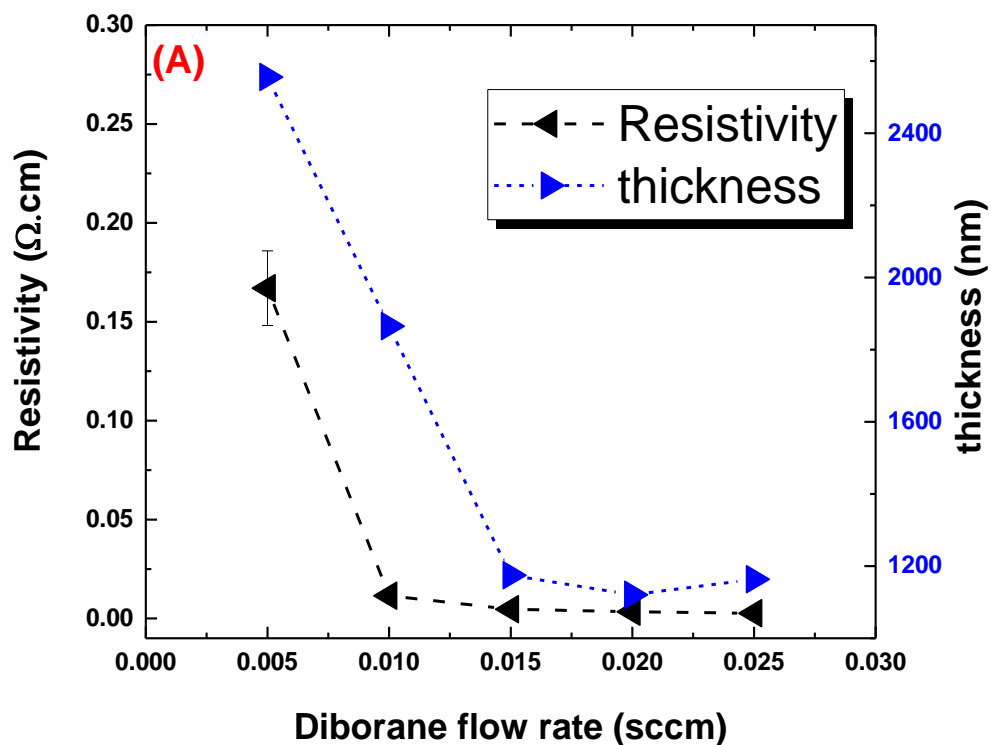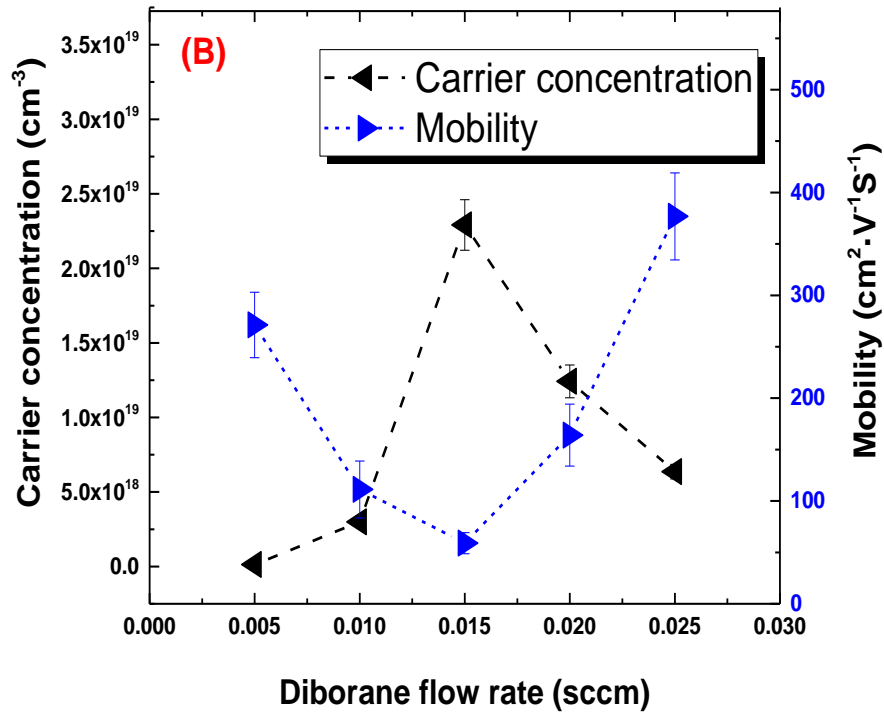
Figure 4.22 *The Hall Effect result of resistivity, carrier concentration and mobility of BDD homoepitaxial films were grown on the non-seeded substrate as a function of boron flow rate. Graph (A) plots resistivity (black data point) with thickness (blue data point) of the BDD films and Graph (B) shows the relationship between carrier concentration (black) and mobility (blue) with increasing boron doping level.*

4.3.3.3   Comparison between seeded polycrystalline and homoepitaxial films

Figure 4.23 (Graphs A, B and C) presents a comparison between the electrical properties of seeded crystalline samples and homoepitaxial samples for each of the chosen boron doping levels. Generally, the overall resistivity (Graph A) of both sets of samples decreases with diborane flow rate until reaching a saturation level. It is apparent that the boron dopant has much less influence on the room temperature conductivity in the range of extremely high concentrations. Also, based on the SIMS results (Figure 4.20), it can be speculated that there is a saturation concentration for the boron function as hole carriers for electrical transport. The carrier concentration of seeded samples is around double the value of homoepitaxial ones which is in

129

agreement with the difference in the boron concentration measured by SIMS (Figure 4.20). SEM comparisons of the two sample sets grown at each doping level (figure 4.11) confirm that the proportion of grain boundaries in the seeded sample is consistently higher than the homoepitaxial ones, which provide more places for boron clusters/aggregates. Furthermore, from Hall measurements, no more than 3% of boron atoms, ([B⁻]/[B], values obtained from carrier concentration and boron concentration in Hall measurements SIMS depth profile, respectively), are electronically active. This indicates a low efficiency for boron incorporation and a large amount of defects within the as-grown films which is one of main factors that greatly influences the mobility values of the samples (graph C figure 4.23).

In comparison, despite the resistivity of seeded samples being lower than non-seeded ones, the mobility of homoepitaxial films is higher overall than seeded CVD films due to their higher quality which make them better materials for electronic applications.

131
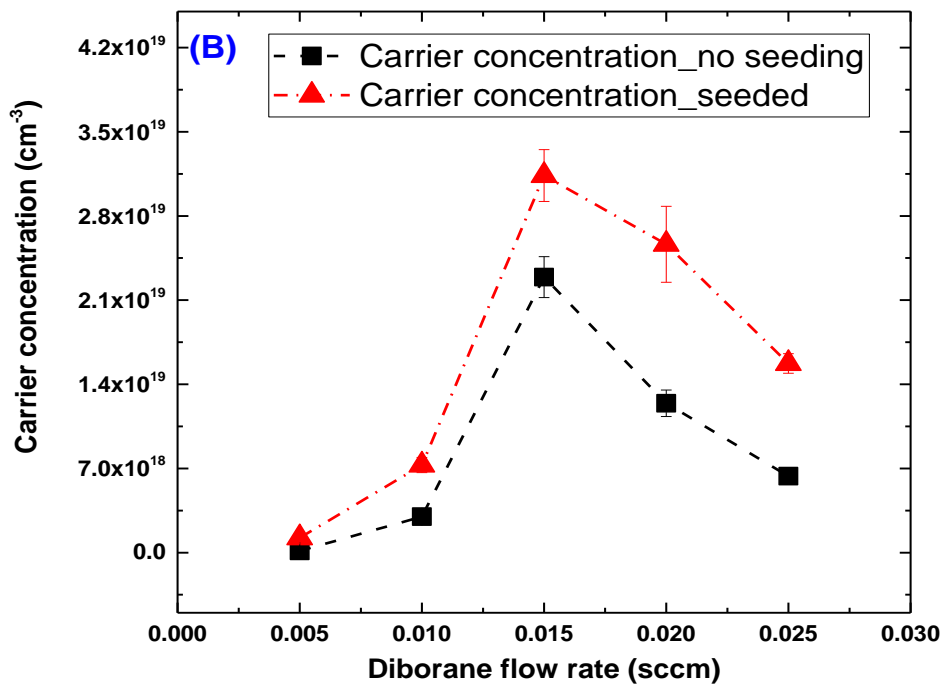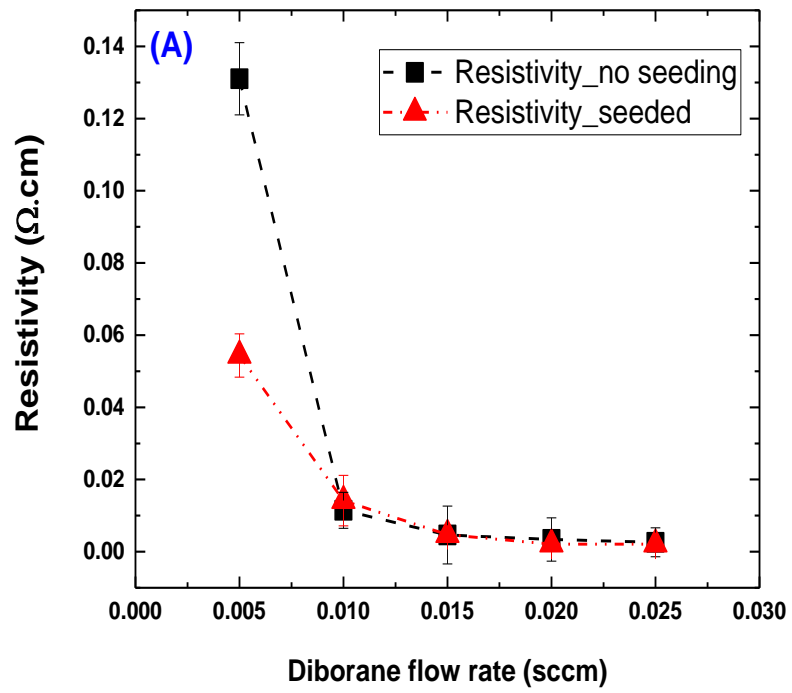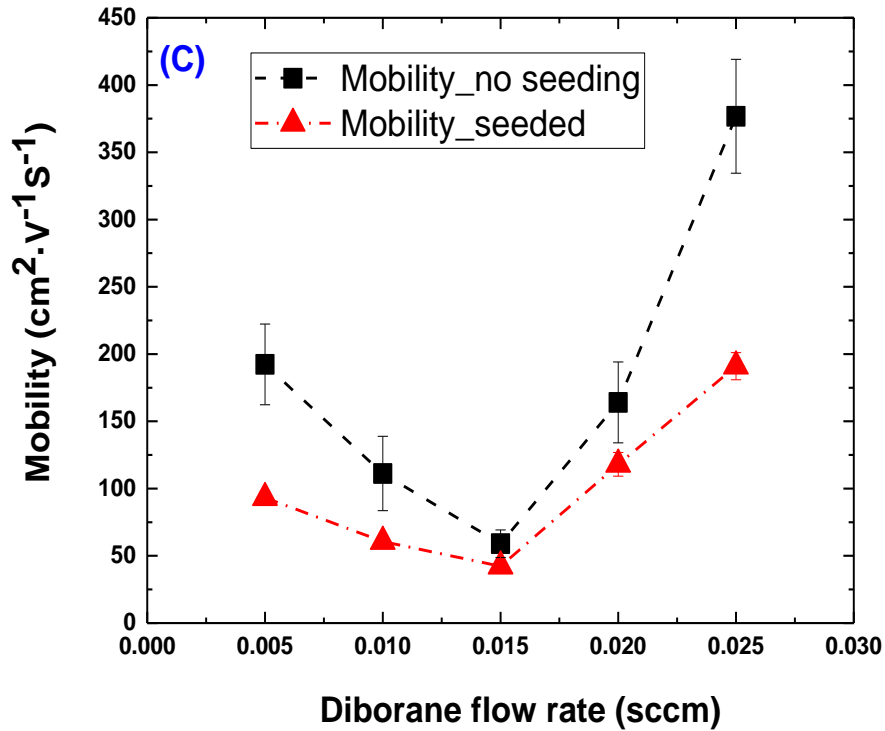
Figure 4.23 *The comparison of resistivity (A), carrier concentration (B) and mobility (C) between seeded (red triangle data point) and non-seeded (black square data point) BDD films as a function of boron doping level from 0.005 sccm to 0.025 sccm.*

4.4   Conclusions

Two sets of polycrystalline diamond thin films grown on the seeded and non-seeded PCD substrate were fabricated by using the HFCVD method and were synthesised at different diborane flow rates. The influence of substrate seeding and high doses of boron on the surface morphology, lattice structure and electrical properties have been systematically investigated in this work. The result from SEM and EBSD data indicated that seeding on the diamond substrate prior to the growth significantly changed the morphology of as-grown thin films in comparison with non-seeded ones. This was found to lead to smaller crystals with a larger density of grain boundaries than homoepitaxial layers which greatly affected how boron becomes

incorporated into the diamond film and its electrical properties. The changes in grain size and surface morphology with increasing boron dopant level for seeded and homoepitaxial samples are significantly different which is the result of the higher levels of defects introduced during growth for the former. Results from SIMS depth profiling show different boron incorporation behaviour between these two sets of samples and changes in the thickness of the film.

It can be found that there was higher amount of boron doped into the bulk of seeded samples than non-seeded samples which could be the evidence to support the fact that excess boron atoms are clustered at grain boundaries, causing significant stress to exist within the films at very high level boron concentrations in the diamond. This is supported by the fact that the D band shifted and widened in Raman spectra between seeded and non-seeded samples. Interestingly, the electrical behaviour of these samples may be divided by the boron concentration. Both the polycrystalline and homoepitaxial films exhibit semi-conductivity typical of a non-degenerate semiconductor up to 3×10^{20} cm^{-3}, but degenerate, metal-like conductivity above this level. It is found that at very high doping level, the hole concentration reduced in spite of the increasing boron concentration which might indicate that there are less positively charged entities (such as B$^+$ and H$^+$) and more boron clusters/complexes formed within the films.

In summary, the homoepitaxial group of samples has better electrical and structural properties making this material attractive for device applications. However, different kinds of defects, such as substitutional dopants and vacancies, cause the low mobility

133

of these homoepitaxial films. Post-annealing may be used to improve the electrical

properties of these homoepitaxial samples which will be discussed in the next Chapter.

4.5 References

161.   Wei, L., P. K. Kuo, R. L. Thomas, T. R. Anthony, and W. F. Banholzer, Thermal conductivity of isotopically modified single crystal diamond. Physical Review Letters, 1993. 70(24): p. 3764-3767.

162.   Isberg, J., et al., High Carrier Mobility in Single-Crystal Plasma-Deposited Diamond. Science, 2002. 297(5587): p. 1670.

163.   Schreck, M., F. Hörmann, H. Roll, J. K. N. Lindner, and B. Stritzker, Diamond nucleation on iridium buffer layers and subsequent textured growth: A route for the realization of single-crystal diamond films. Applied Physics Letters, 2001. 78(2): p. 192-194.

164.   Pleskov, Y.V., Y.E. Evstefeeva, and M.D. Krotova, Effect of crystal structure on the electrochemical behaviour of synthetic semiconductor diamond: Comparison of growth and a nucleation surfaces of a coarse-grained polycrystalline film. Journal of Applied Electrochemistry, 2003. 33(10): p. 909-915.

165.   Paul, R.C., J. Colin, and W. Matthias, Physical properties of diamond for thermistors and pressure transducers. Semiconductor Science and Technology, 2003. 18(3): p. S113.

166.   Fujishima, A., T.N. Rao, and D.A. Tryk, TiO2 photocatalysts and diamond electrodes. Electrochimica Acta, 2000. 45(28): p. 4683-4690.

167.   Geng, R., et al., A sandwich structured SiO2/cytochrome c/SiO2 on a boron-doped diamond film electrode as an electrochemical nitrite biosensor. Biomaterials, 2008. 29(18): p. 2794-2801.

168.   Hiromu, S., N. Yoshiki, and F. Naoji, Field-Effect Transistors using Boron-Doped Diamond Epitaxial Films. Japanese Journal of Applied Physics, 1989. 28(12A): p. L2153.

169.   Zhou, Y. and J. Zhi, The application of boron-doped diamond electrodes in amperometric biosensors. Talanta, 2009. 79(5): p. 1189-1196.

170.   Lee, K.W. and W.E. Pickett, Superconductivity in Boron-Doped Diamond. Physical Review Letters, 2004. 93(23): p. 237003.

171.   Shirakawa, T., S. Horiuchi, Y. Ohta, and H. Fukuyama, Theoretical Study on Superconductivity in Boron-Doped Diamond. Journal of the Physical Society of Japan, 2007. 76(1): p. 014711.

172.   P, B.H. and W.J.R. H, Method for the introduction of boron atoms into diamond crystals. 1964, Google Patents.

173.   Yano, T., D. A. Tryk, K. Hashimoto and A. Fujishima, Electrochemical Behavior of Highly Conductive Boron‐Doped Diamond Electrodes for Oxygen Reduction in Alkaline Solution. Journal of The Electrochemical Society, 1998. 145(6): p. 1870-1876.

174.   Xiang, H.J., Z. Li, J. Yang, J.G. Hou, and Q. Zhu, Electron-phonon coupling in a boron-doped diamond superconductor. Physical Review B, 2004. 70(21): p. 212504.

175.   Nishimura, K., K. Das, and J.T. Glass, Material and electrical characterization of polycrystalline boron‐doped diamond films grown by microwave plasma chemical vapor deposition. Journal of Applied Physics, 1991. 69(5): p. 3142-3148.

176.   Grot, S.A., et al., The effect of surface treatment on the electrical properties of metal contacts to boron-doped homoepitaxial diamond film. IEEE Electron Device Letters, 1990. 11(2): p. 100-102.

177.   Gajewski, W., P. Achatz, O.A. Williams, K. Haenen, E. Bustarret, M. Stutzmann, and J.A. Garrido, Electronic and optical properties of boron-doped nanocrystalline diamond films. Physical Review B, 2009. 79(4): p. 045206.

178.   Kawarada, H., H. Matsuyama, Y. Yokota, T. Sogi, A. Yamaguchi, and A. Hiraki, Excitonic recombination radiation in undoped and boron-doped chemical-vapor-deposited diamonds. Physical Review B, 1993. 47(7): p. 3633-3637.

179.   Gheeraert, E., P. Gonon, A. Deneuville, L. Abello Effect of boron incorporation on the "quality" of MPCVD diamond films. Diamond and Related Materials, 1993. 2(5): p. 742-745.

180.   Raiko, V., R. Spitzl, J. Engemann, and V. Borisenko, MPCVD diamond deposition on porous silicon pretreated with the bias method. Diamond and Related Materials, 1996. 5(10): p. 1063-1069.

181.   Fernandes, A.J.S., V.A. Silva, J.M. Carrapichano, G.R. Dias, R.F. Silvab, and F.M. Costa, MPCVD diamond tool cutting-edge coverage: dependence on the side wedge angle. Diamond and Related Materials, 2001. 10(3–7): p. 803-808.

182.   Afzal, A., C.A. Rego, W. Ahmed, R.I. Cherry, HFCVD diamond grown with added nitrogen: film characterization and gas-phase composition studies. Diamond and Related Materials, 1998. 7(7): p. 1033-1038.

183.   Sarangi, S.K., A. Chattopadhyay, and A.K. Chattopadhyay, Effect of pretreatment, seeding and interlayer on nucleation and growth of HFCVD diamond films on cemented carbide tools. International Journal of Refractory Metals and Hard Materials, 2008. 26(3): p. 220-231.

184.   Bernard, M., C. Baron, and A. Deneuville, About the origin of the low wave number structures of the Raman spectra of heavily boron doped diamond films. Diamond and Related Materials, 2004. 13(4–8): p. 896-899.

185.   Zhang, R.J., S.T. Lee, and Y.W. Lam, Characterization of heavily boron-doped diamond films. Diamond and Related Materials, 1996. 5(11): p. 1288-1294.

186.   Lagrange, J.P., A. Deneuville, and E. Gheeraert, Activation energy in low compensated homoepitaxial boron-doped diamond films1. Diamond and Related Materials, 1998. 7(9): p. 1390-1393.

187.   Stoner, B.R., C. Kao, D.M. Malta, and R.C. Glass, Hall effect measurements on boron‐doped, highly oriented diamond films grown on silicon via microwave plasma chemical vapor deposition. Applied Physics Letters, 1993. 62(19): p. 2347-2349.

188.   Liao, X.Z., R.J. Zhang, C.S. Lee, S.T. Lee, and Y.W. Lam, The influence of boron doping on the structure and characteristics of diamond thin films. Diamond and Related Materials, 1997. 6(2): p. 521-525.

189.   Brunet, F., P. Germi, M. Pernet, and A. Deneuville, The effect of boron doping on the lattice parameter of homoepitaxial diamond films. Diamond and Related Materials, 1998. 7(6): p. 869-873.

190.   Bovenkerk, H.P., Compact of boron-doped diamond and method for making same. 1981, Google Patents.

191.   Wang, W.L., M. C. Polo, G. Sa´nchez, J. Cifre, and J. Esteve, Internal stress and strain in heavily boron‐doped diamond films grown by microwave plasma and hot filament chemical vapor deposition. Journal of Applied Physics, 1996. 80(3): p. 1846-1850.

192.   Kohn, E. and A. Denisenko, Concepts for diamond electronics. Thin Solid Films, 2007. 515(10): p. 4333-4339.

193.   Sun, S., W. Cui, X. Jia, H. Ma, and J. Lv, The synthesis of "BCN" diamond materials with different B/N additives under high pressure and high temperature. International Journal of Refractory Metals and Hard Materials, 2016. 59: p. 56-60.

194.   Jiang, X., et al., Coalescence and overgrowth of diamond grains for improved heteroepitaxy on silicon (001). Journal of Applied Physics, 1998. 83(5): p. 2511-2518.

195.   Nemanich, R.J., Growth and Characterization of Diamond Thin Films. Annual Review of Materials Science, 1991. 21(1): p. 535-558.

196.   Ferreira, N.G., N.G. Ferreira , E. Abramo, E.J. Corat, and V.J. Trava-Airoldi, Residual stresses and crystalline quality of heavily boron-doped diamond films analysed by micro-Raman spectroscopy and X-ray diffraction. Carbon, 2003. 41(6): p. 1301-1308.

197.   Wang, X.H., G.-H. M. Ma, W. Zhu and J. T. Glass, Effects of boron doping on the surface morphology and structural imperfections of diamond films. Diamond and Related Materials, 1992. 1(7): p. 828-835.

198.   Wei, J.J., C.M. Li, X.H. Gao, L.F. Hei, and F.X. Lvun, The influence of boron doping level on quality and stability of diamond film on Ti substrate. Applied Surface Science, 2012. 258(18): p. 6909-6913.

199.   Lee, S.T., Z. Lin, and X. Jiang, CVD diamond films: nucleation and growth. Materials Science and Engineering: R: Reports, 1999. 25(4): p. 123-154.

200.   Fox, O.J.L., J. Holloway, G.M. Fuge, P.W. May and M. Ashfold, Electrospray Deposition of Diamond Nanoparticle Nucleation Layers for Subsequent CVD Diamond Growth. MRS Proceedings, 2009. 1203.

201.   Li, H., T. Zhang, L. Li, X. Lü, B. Li, Z. Jin, and G. Zou, Investigation on crystalline structure, boron distribution, and residual stresses in freestanding boron-doped CVD diamond films. Journal of Crystal Growth, 2010. 312(12–13): p. 1986-1991.

202.   Ramamurti, R., et al., Boron doped diamond deposited by microwave plasma-assisted CVD at low and high pressures. Diamond and Related Materials, 2008. 17(4–5): p. 481-485.

203.   Tsugawa, K., M. Ishihara, J. Kim, Y. Koga, M. Hasegawa, Nanocrystalline diamond film growth on plastic substrates at temperatures below 100°C from low-temperature plasma. Physical Review B, 2010. 82(12): p. 125460.

204.   Iniesta, J., P.A. Michaud, M. Panizza, G. Cerisola, and A. Aldaz, Electrochemical oxidation of phenol at boron-doped diamond electrode. Electrochimica Acta, 2001. 46(23): p. 3573-3578.

205.   Lévy-Clément, C., et al., Boron doped diamond electrodes for nitrate elimination in concentrated wastewater. Diamond and Related Materials, 2003. 12(3–7): p. 606-612.

206.   May, P.W., W.J. Ludlow, M. Hannaway, P.J. Heard, J.A. Smith, and K.N. Rosser, a Raman and conductivity studies of boron-doped microcrystalline diamond, facetted nanocrystalline diamond and cauliflower diamond films. Diamond and Related Materials, 2008. 17(2): p. 105-117.

207.   Yanagisawa, M., L. Jiang, D.A. Tryk, K. Hashimoto, Surface morphology and electrochemical properties of highly boron-doped homoepitaxial diamond films. Diamond and Related Materials, 1999. 8(11): p. 2059-2063.

208.   Tokuda, N., H. Umezawa, T. Saito, and K. Yamabe, Surface roughening of diamond (001) films during homoepitaxial growth in heavy boron doping. Diamond and Related Materials, 2007. 16(4–7): p. 767-770.

209.   Stringfellow, G.B., The importance of lattice mismatch in the growth of GaxIn1–xP epitaxial crystals. Journal of Applied Physics, 1972. 43(8): p. 3455-3460.

210.   Das, D. and R.N. Singh, A review of nucleation, growth and low temperature synthesis of diamond thin films. International Materials Reviews, 2007. 52(1): p. 29-64.

211.   Shenderova, O.A., D. Areshkin, and D.W. Brenner, Bonding and Stability of Hybrid Diamond/Nanotube Structures. Molecular Simulation, 2003. 29(4): p. 259-268.

212.   Lucazeau, G., Effect of pressure and temperature on Raman spectra of solids: anharmonicity. Journal of Raman Spectroscopy, 2003. 34(7-8): p. 478-496.

213.   Ager, J.W., W. Walukiewicz, and M. McCluskey, Fano interference of the Raman phonon in heavily boron‐doped diamond films grown by chemical vapor deposition. Applied Physics Letters, 1995. 66(5): p. 616-618.

214.   Ushizawa, K., et al., Boron concentration dependence of Raman spectra on {100} and {111} facets of B-doped CVD diamond. Diamond and Related Materials, 1998. 7(11–12): p. 1719-1722.

215.   Locher, R., J. Wagner, F. Fuchs, M. Maier, P. Gonon, and P.Koidl, Optical and electrical characterization of boron-doped diamond films. Diamond and Related Materials, 1995. 4(5): p. 678-683.

216.   Locher, R., J. Wagner, F. Fuchs, M. Maier, P. Gonon, and P.Koidl, Boron doped diamond films: Electrical and optical characterization and the effect of compensating nitrogen. Materials Science and Engineering: B, 1995. 29(1): p. 211-215.

217.   Ohtani, N. and K. Kawamura, Theoretical investigation of Raman scattering from microcrystallites. Solid State Communications, 1990. 75(9): p. 711-715.

218.   Martin, R.M. and T. Damen, Breakdown of selection rules in resonance Raman scattering. Physical Review Letters, 1971. 26(2): p. 86.

219.   Brunet, F., P. Germi, M. Pernet, and A. Deneuville, Microstructure evolution of boron doped homoepitaxial diamond films. Journal of Applied Physics, 1998. 83(1): p. 181-186.

220.   Prawer, S. and R.J. Nemanich, Raman spectroscopy of diamond and doped diamond. Philosophical Transactions of the Royal Society of London. Series A: Mathematical, Physical and Engineering Sciences, 2004. 362(1824): p. 2537-2565.

221.   Magee, C.W. and R.E. Honig, Depth profiling by SIMS—depth resolution, dynamic range and sensitivity. Surface and Interface Analysis, 1982. 4(2): p. 35-41.

222.   Tutein, A.B., S.J. Stuart, and J.A. Harrison, Role of Defects in Compression and Friction of Anchored Hydrocarbon Chains on Diamond. Langmuir, 2000. 16(2): p. 291-296.

223.   Filik, J., et al., Raman spectroscopy of nanocrystalline diamond: An \textit{ab initio} approach. Physical Review B, 2006. 74(3): p. 035423.

224.   Klein, T., et al., Metal-insulator transition and superconductivity in boron-doped diamond. Physical Review B, 2007. 75(16): p. 165313.

225.   Tallaire, A., et al., Growth of thick and heavily boron-doped (113)-oriented CVD diamond films. Diamond and Related Materials, 2016. 66: p. 61-66.

226.   May, P.W., W.J. Ludlow, J. Smith, K.N. Rosser, and P.J. Heard, M HannawayBoron Doping of Microcrystalline and Nanocrystalline Diamond Films: Where is the Boron Going? MRS Proceedings, 2007. 1039.

227.   Gildenblat, G.S., S. A. Grot, C. R. Wronski, A. R. Badzian, T. Badzian, and R. Messierless, Electrical characteristics of Schottky diodes fabricated using plasma assisted chemical vapor deposited diamond films. Applied Physics Letters, 1988. 53(7): p. 586-588.

228.   Wilson, W.B., Evidence for Hopping Transport in Boron-Doped Diamond. Physical Review, 1962. 127(5): p. 1549-1550.

229.   Garcia-Segura, S., E. Vieira dos Santos, and C.A. Martínez-Huitle, Role of sp^3/sp^2 ratio on the electrocatalytic properties of boron-doped diamond electrodes: A mini review. Electrochemistry Communications, 2015. 59: p. 52-55.

230.   Bentley, C.L., A.M. Bond, A.F. Hollenkamp, and P.J. Mahon, Concentration and electrode material dependence of the voltammetric response of iodide on platinum, glassy carbon and boron-doped diamond in the room temperature ionic liquid 1-ethyl-3-methylimidazolium bis(trifluoromethanesulfonyl)imide. Electrochimica Acta, 2013. 109: p. 554-561.

231.   Bormashov, V.S., S.A. Tarelkin, S.G. Buga, M.S. Kuznetsov, S.A. Terentiev, A.N.Semenov, and V.D. Blank, a Electrical properties of the high quality boron-doped synthetic single-crystal diamonds grown by the temperature gradient method. Diamond and Related Materials, 2013. 35: p. 19-23.

Chapter 5   An investigation of the influence of thermal annealing on the structural and electrical properties of heavily boron doped diamond

5.1   Introduction

Thermal annealing is one of the most common post-growth techniques used to produce changes in the properties of materials. It is often used to improve optical quality [232, 233], structural performance [234, 235], or electrical transport properties [236, 237] often modifying the surface morphology [238]. In commercial applications of diamond, annealing treatments are used to "repair" the lattice damage caused by ion implantation/irradiation. Such treatments can also be used to activate impurity dopants to function more efficiently as an acceptor or donor level in in active electronic device applications that use semiconducting diamond [239-242]. Since defects, such as vacancies, impurity dopants and non-diamond carbon located at grain boundaries, play a significant role in the electrical carrier transport, thermal annealing is an important area of fundamental research for the purpose of enhancing the electronic properties of heavily doped diamond. There are a few experimental studies that study the changes in the electrical properties upon annealing: Gu *et al.*[243] found that the Hall mobility of B-doped NCD films increased to 53.3 $cm^2V^{-1}s^{-1}$ after annealing in vacuum at 1000°C. Sahi[244] annealed a BDD film for 10minutes in N_2 at 600°C which caused an increase in the resistivity of the as-grown material. Chen [245] observed that the activation energy of heavily BDD films significantly decreased from 0.38 eV to 0.014 eV after annealing. Furthermore, it has been found that the annealing effect on diamond containing a high concentration of dopant is much greater than for lightly doped samples which suggests that dopant clusters and interstitial defects may be

present [246]. However, the explanation for the observed annealing effect remains unclear for the following reasons: firstly, the annealing effect arises from the interplay between a number of material factors including structure, phase and bonding; Secondly, the mechanism is also associated with the thermodynamics of the interaction and diffusion of impurity defects, such as dopants/hydrogen, of vacancies and the presence of grain boundaries within the surface and bulk of the materials; lastly, there are technological limitations that hinder the collection of consistent experimental evidence to explain the results. Based on the challenges above, modelling and theoretical calculations provide an effective way to explain and predict the behaviour in specific annealing scenarios.

One of the key aspects that greatly influences the annealing results is the diffusion of H through diamond and its interaction with defects present within the thin films. There have been a number of reports that present experimental evidence [247-249] for hydrogen diffusion within diamond thin films at low temperatures (0-600°C) that incorporate deuterium in place of hydrogen to allow a SIMS depth profile to reveal its distribution. Another important aspect is the thermodynamic behaviour of the boron-hydrogen (H, B) complex and stability of boron pairs (B_2) at different temperatures. This has been the focus of recent theoretical studies by Goss and coworkers [106, 107, 111, 112]. They successfully accounted for the stability of boron pairs in boron doped diamond by using a thermodynamic model and statistical mechanics combined with ab-initio calculations. They predicted that there is a boron-concentration dependency on the critical temperature that governs the dissociation/bonding of boron pairs. To date, there has been no systematic experimental data to support this prediction in the

143

higher temperature range for heavily BDD thin films. In this chapter, the effect of annealing on the surface morphology, the phase, the structural composition, dopant distribution and electrical properties of heavily BDD films is systematically investigated for the high temperature range of 700°C to 1200°C. The aims of this work are to demonstrate high mobility p-type semiconducting diamond thin films with improved conductivity and to provide new experimental evidence to support theoretical results.

5.2   Material and method

5.2.1   Boron-doped diamond thin film growth

5.2.1.1   Acid cleaning

Polycrystalline diamond substrates (TM100) were purchased from Element Six and cleaned in a hot solution (200°C) of fuming nitric acid for 30 minutes before growth in order to remove any graphitic or metallic contamination.

5.2.1.2   Hot Filament Chemical Vapour Deposition (HFCVD)

The boron doped thin films were grown on the smooth side of pre-cut PCD substrates comprising 27 samples placed together in the hot filament reactor. This ensured that the sample set was grown under the same conditions. The growth was performed with a Ta filament temperature of 2000°C (filament current of 25A), a total gas pressure of 20 torr, and a feedstock gas mixture containing 1% CH_4 and 0.005% B_2H_6 in H_2 for a total growth time of 4 hours. Under these conditions, a homoepitaxial diamond layer was produced without the use of a seed layer.

5.2.2   Thermal Annealing

The annealing experiments were conducted using an annealing set up (Eeyore,2x012) that could heat samples to 1200°C. As shown in **Figure 5.1** (A), each sample was sealed

into a quartz tube and placed under high vacuum (p = 1×10^{-6} torr). The quartz tube was

placed in the centre of ceramic tube furnace in order to keep the uniformity of heat

conduction (Graph B). Each sample was annealed at a specific temperature in the

range of 700°C to 1200°C for 1hour. A temperature ramp rate of 10°C·min^{-1} was used

for all annealing experiments. The samples were left in the tube furnace to naturally

cool down to room temperature in order to provide enough time for the species within

the diamond lattice reach thermodynamic equilibrium.
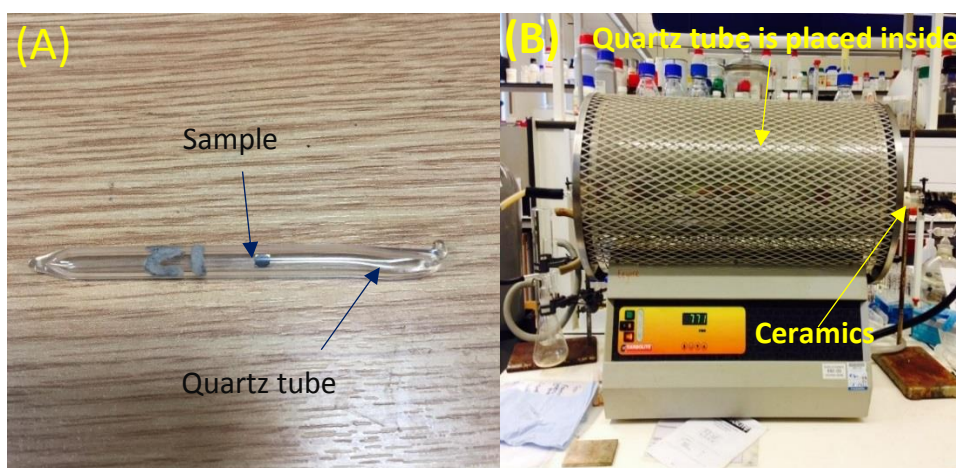
Figure 5.1 *(A) Sample sealed in quartz,(B) Tube furnace used for annealing experiments.*

5.2.3   Characterization of BDD thin films

The surface morphology was studied by Scanning Electron Microscopy (SEM, Zeiss

Sigma HD VP Field Emission) at an accelerating voltage of 10 kV and with different

fields of view (operation and instrument detail has been discussed at section 3.4

Chapter 3) . Thin film quality and composition was measured by Raman spectroscopy

using a 514 nm green laser to excite a resonant photon response. Each sample was

analysed using the accumulation mode to record a signal spectrum for periods of up to

one hour. Measurements were repeated 5 times on the different areas for each

sample to ensure the representative quality of the Raman data.

5.2.4   Bulk properties of BDD films

5.2.4.1   *Impurity distribution within the whole layer*

Secondary Ion Mass Spectroscopy (SIMS) is used in this work to investigate the variation of dopants within the samples as a function of annealing temperature. The experiment condition and method of SIMS is the same as discussed in Chapter 4 section 4.2.3.

5.2.4.2   *Electrical carrier transport*

The electrical properties of BDD films were measured by using a 4-probe system Hall Effect set up at room temperature. The setup is comprised of DC current system, which provided a high quality and low-noise signal, with a wide range of resistivity values. A Van der Pauw configuration is used for resistivity and Hall voltage measurement in a 1T magnetic field

The surfaces of all of the samples were O-terminated for 30 minutes by using acid cleaning in order to insulate the surface and avoid surface conductivity which might be induced by hydrogen terminating the growth surface. A range of dipolar currents (1×10^{-7}A to 1×10^{-6}A) were applied using the Van der Pauw method to record resistivity measurements. This method is used so as to remove thermal couple effect. The Hall voltage was measured in a 1T magnetic field with a range of monopolar current (1×10^{-6}A to 1×10^{-5}A) and further calculations were made to get the value of the carrier concentration and mobility through Equation 3.5 and Equation 3.10 in Chapter 3, respectively. A total of 20 measurement cycles were made for each current using the Van der Pauw method and 50 measurement cycles for the Hall measurement in order to get consistent experimental data.

5.3   Results and Discussion

5.3.1   Surface and phase change as a function of annealing temperature

5.3.1.1   Influence of annealing temperature on the surface morphology

5.3.1.1.1   SEM study of surface morphology as a function of annealing temperature

Figure 5.2 illustrates the changes in surface morphology obtained at different

annealing temperatures. It can be seen in **Figure 5.2** that the surface morphology of as-

grown BDD films is improved from 700°C to 900°C and then deteriorated after 900°C.

Specifically, the surface roughness is improved in the temperature range between

700°C to 900°C with an increase in crystal size (which has been supported by EBSD

grain size analysis), while above 900°C the surface roughness increases, which is an

interesting discovery. In order to further confirm this result, EBSD is employed to look

at the grain size and phase transformation of these BDD films at the different

annealing temperatures.
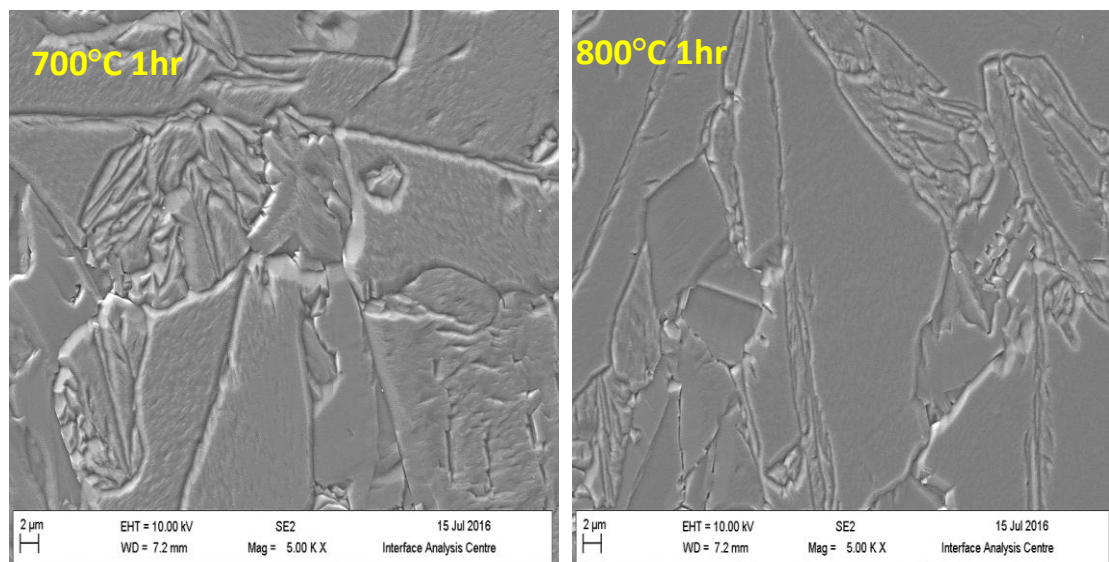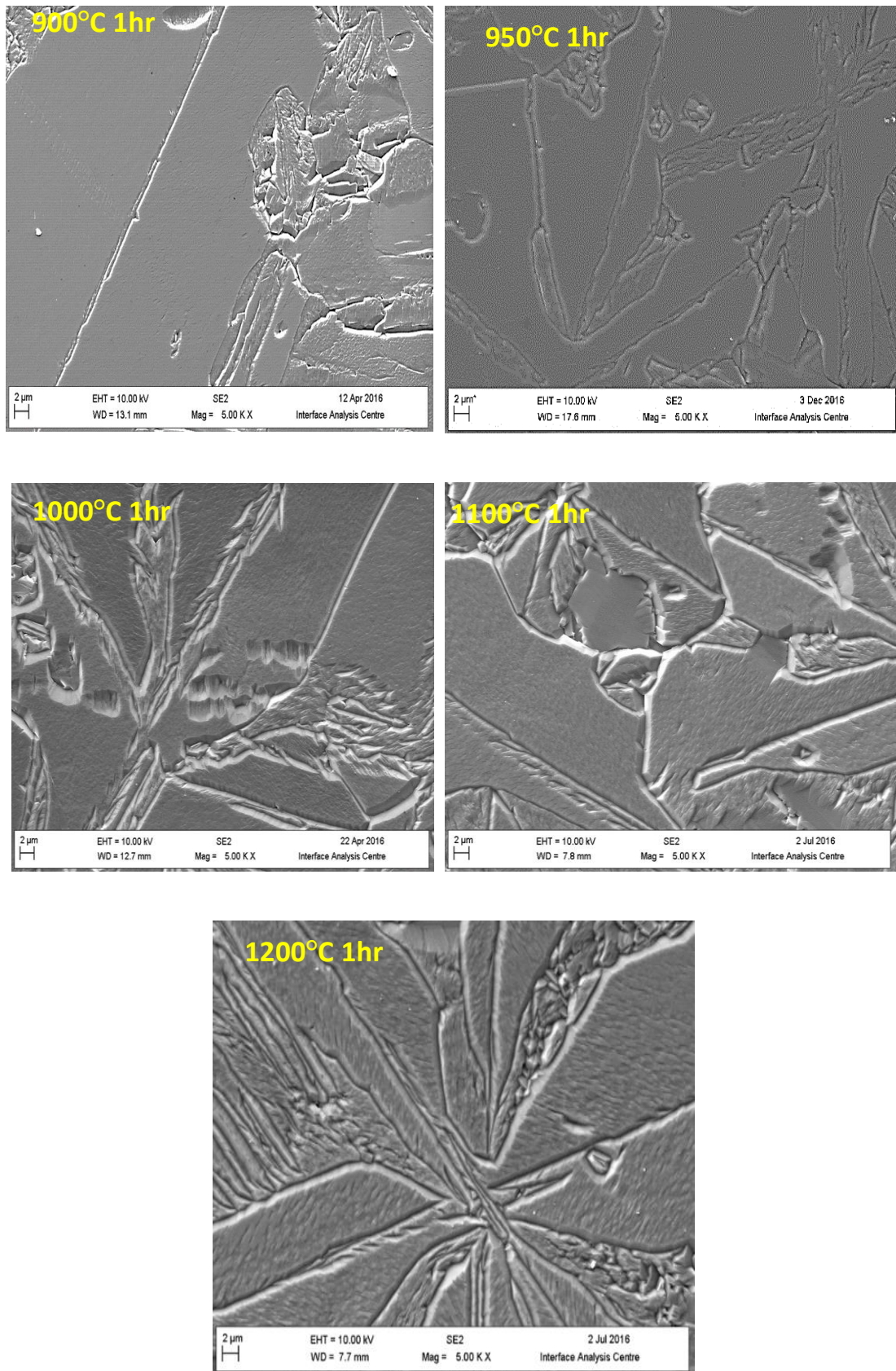
Figure 5.2 *The SEM images of boron-doped diamond (BDD) thin films annealed for 1 hour from*

700 ℃ to 1100 ℃ under 1×10^{-6} torr vacuum

5.3.1.1.2   EBSD study on phase and grain size variation as a function of annealing temperature

EBSD phase images in **Figure 5.3** show the distribution of graphite and diamond in the annealed films. It can be seen that the percentage (total fraction in the right corner of images) of graphite decreases from 9.9% to 3.3% in the temperature range 700°C to 900°C, but increases up to 11.2% in the range 900°C - 1200°C. As it has been discussed based on Figure 4.10 in Chapter 4 section 4.3.1 the majority of the crystalline graphite is located on the grain boundaries. This suggests the variation in the phase change between graphite and diamond shown in **Figure 5.3** mainly happened at grain boundaries. The graphite and diamond percentage reaches the lowest (3.3%) and the highest level (96.7%) at 900°C, respectively. This explains one of the reasons why the average polycrystalline grain size reaches a maximum at 900°C which is supported by the EBSD grain size chart shown in **Figure 5.4**.
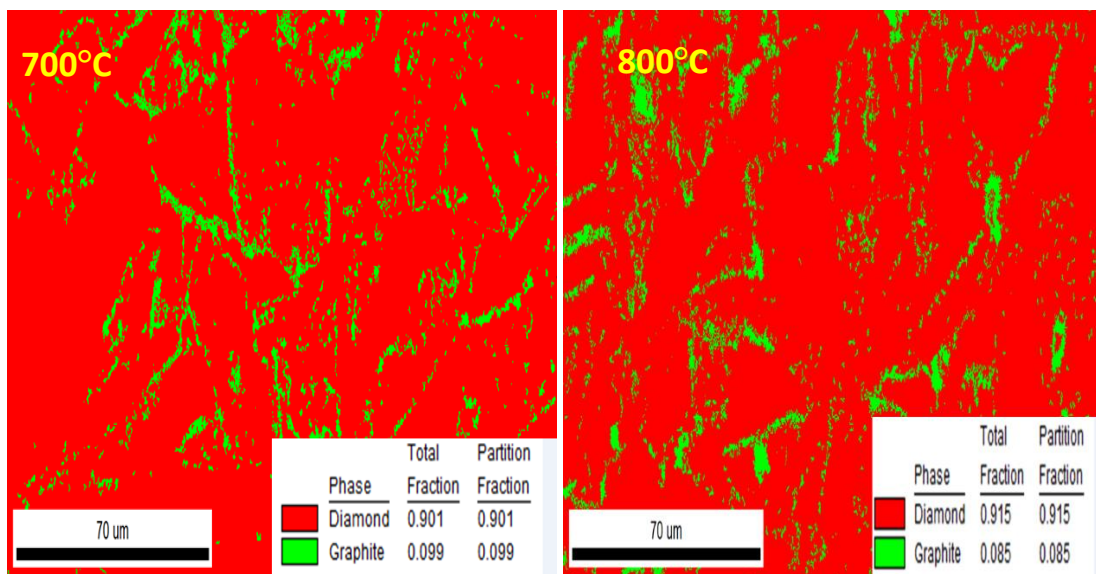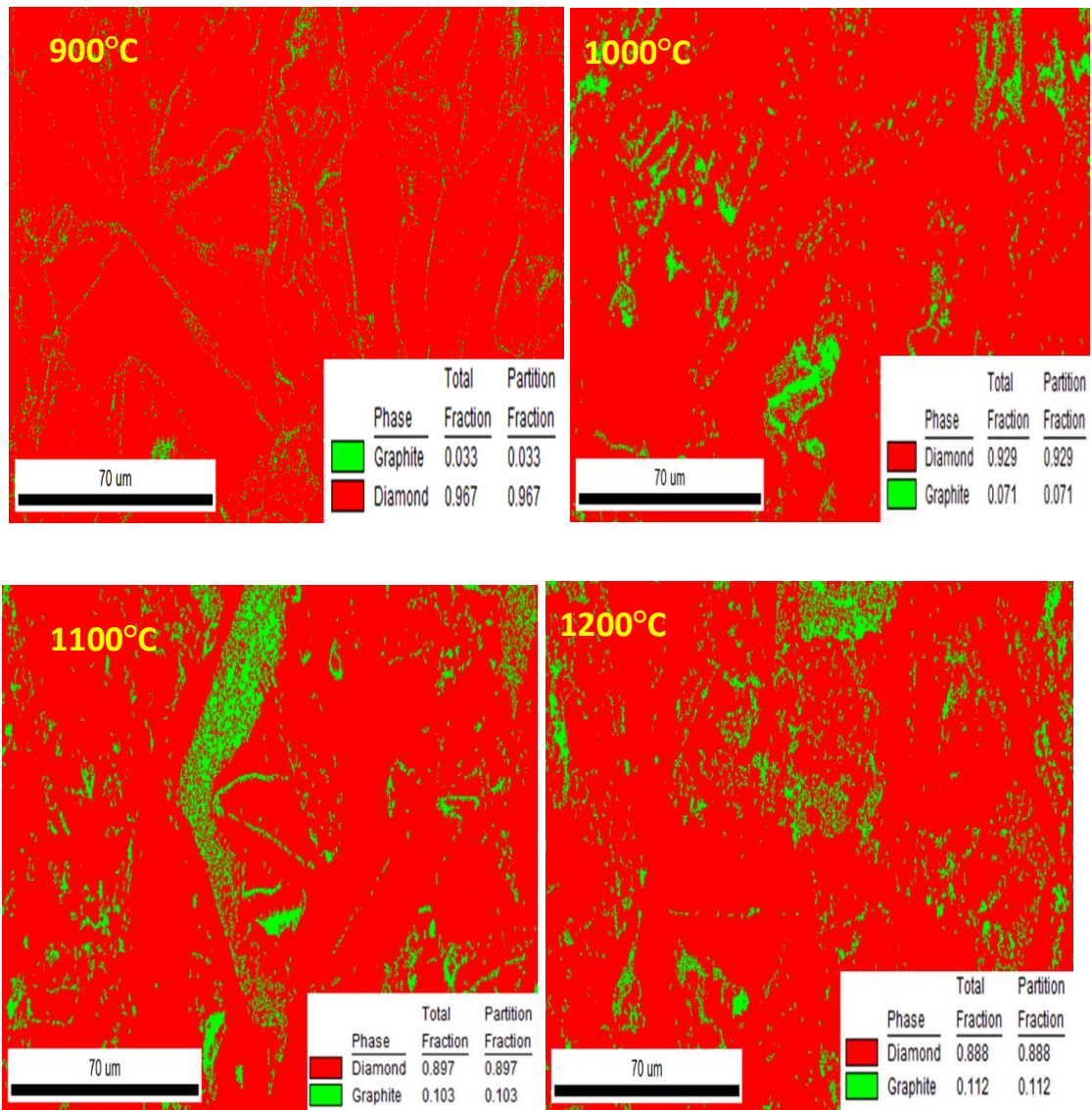
Figure 5.3 *EBSD phase images of the distribution and percentages of crystalline graphite and diamond on the surface as a function of annealing temperature.*

The EBSD data of the surface area can be converted into a grain size chart that shows the grain size distribution over the sample surface. **Figure 5.4** shows the distribution and variation of grain size as a function of annealing temperature. The variation in the height of black, red and cyan bars demonstrates the evolution of the increasing grain size in the temperature range below 900°C. It can be seen in **Figure 5.4** that the majority of grains following an anneal at 700°C are largely confined to a size range

between 1- 20 μm, but a significant percentage of the annealed-grains are much larger with a maximum grain size of 45 μm, accounting for nearly 12% of the as-scanned area (Y-axis) which is represented by the height of the black bar. The size range occupied by the majority of grains shifts to a larger crystal size as the annealing temperature is stepped up to 900°C. For 800°C the range is from 15 μm – 40 μm (red bar), while at 900°C the majority of grains are in the 20 μm-43 μm range (cyan bar) with a maximum value of 55 μm. However, this trend reverses once an annealing temperature above 900°C is selected. As it can be found in this figure that the percentage of the PCD area with a large grain size (> 30 μm) gradually decreases with the majority of grains shifting to smaller size ranges. It is seen that the average grain size reduces as the temperature increases, from 25.73 μm at 1000°C, 23.07 μm at 1100°C and 21.22 μm at 1200°C.

 Another distinct change is that the maximum grain size of 900°C sample (55 μm) gradually decreases to 41 μm at 1200°C. The results presented in **Figure *5.4*** are in good agreement with SEM images found in **Figure *5.2***. In connection with the EBSD phase image (***Figure 5.3***) which shows an increasing or decreasing percentage of diamond phase before and after 900°C respectively. This could be the result of the joining together of relatively smaller grains due to the variation of graphite in grain boundaries.
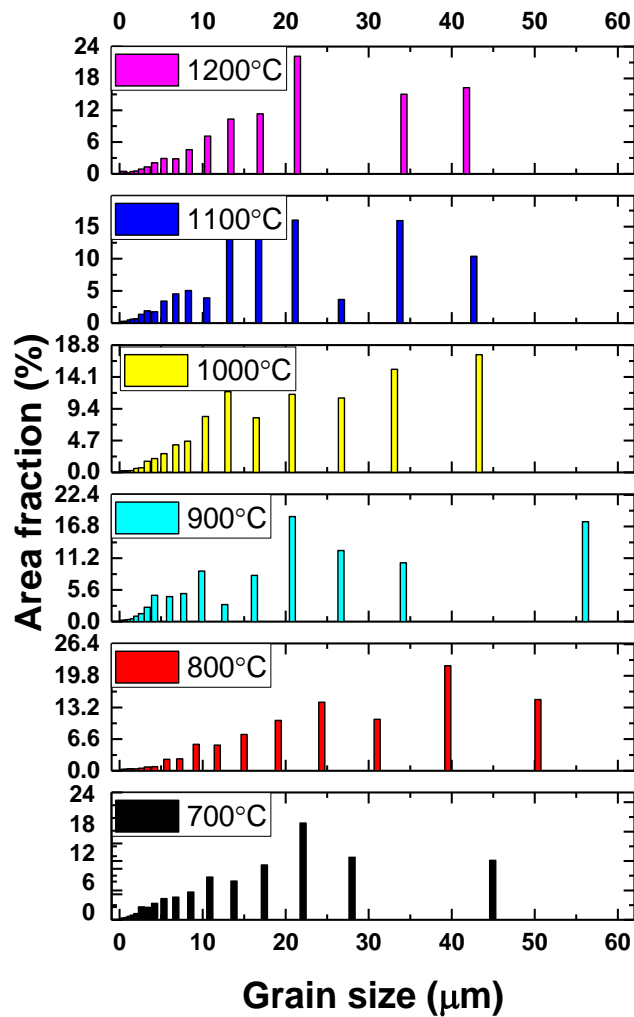
Figure 5.4 *EBSD grain size distribution chart of as-annealed sample surfaces coloured by temperature in the range from 700 ℃ to 1200 ℃. The height of coloured column represents the percentage of certain grain size over the whole scanned area at the particular annealing temperature.*

Based on the SEM and EBSD results, it is evident that the vacuum annealing performed at 900°C for 1 hour has a strong influence on the transformation direction of surface morphology of as-grown BDD films. These results suggested that the mechanism behind this phenomenon is linked to the defects (such as graphite, hydrogen and boron) variation along the grain boundaries which is influenced by their thermodynamic behaviour at different annealing conditions[237]. In order to gain a

152

deeper insight into the mechanism behind this transformation, Raman spectra were used to investigate the influence of annealing on the structural properties of BDD films under the different annealing temperatures.

5.3.1.2 *Raman spectra of lattice structure and impurity of BDD films*

Figure 5.5 (A and B) are the normalised Raman spectra of BDD films produced under the same deposition conditions but annealed at different temperatures. Graph A shows the strong and dominant signal at around 1331 cm^{-1} (zone centre phonon diamond line) with the asymmetric shape in the temperature range between 700°C to 900°C which indicates the good quality and stability of the diamond sp^3 structure. The slight asymmetric shape of the diamond peak shows a "Fano-effect" due to the interference due to a large amount of boron incorporation [250]. There are two broad bands which appear at 1548 cm^{-1} and 800°C cm^{-1}, respectively, for the 700°C samples (Graph A) and gradually diminish when the temperature increases up to 900°C.

However, the opposite trend for these two features is found in Graph B. The broad band (G-band) at 1548^{-1} cm is assigned to sp^2-hybridized carbon and attributed to the nonhomogeneous broadened graphite Raman line [251, 252]. The relatively weak and broad Gaussian-shaped band located at 800 cm^{-1} is a common feature that normally can be observed in carbon films and CVD diamond films [206]. Some papers [253-255] assigned it to the hydrogen-free amorphous carbon (α-C) structure but others papers [256, 257] tentatively attributed it to Si-C vibrational modes in silicon-containing materials. Based on the depositions condition of the HFCVD method used for this films, the amount of silicon present in these boron doped homoepitaxial films is very low. Therefore, a hydrogen-free amorphous carbon structure is assigned to this feature at

153

800 cm^{-1}. There is a very weak and broad peak located at around 1200 cm^{-1} which is a common feature for very heavily boron doped films due to the formation of an impurity band. As it has been discussed in Chapter 4 section 4.3.1.4, this band becomes dominant when the boron concentration exceeds the threshold of the semiconductor-metal transition concentration (3×10^{20} cm^{-3}). The boron doping level used in the experiments reported in this chapter is the minimum amount that our mass flow controller can achieve. Therefore, the 1200 cm^{-1} is very weak as the boron concentration is not high enough to form a consistent impurity band, as it is invisible in *Figure 5.5* in this work.
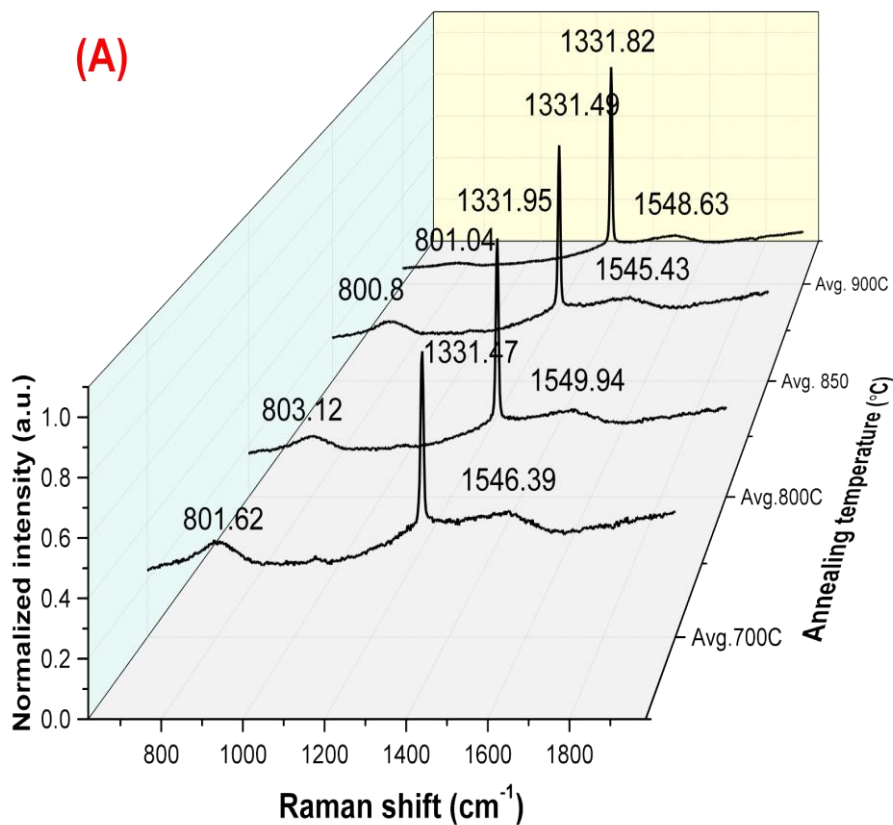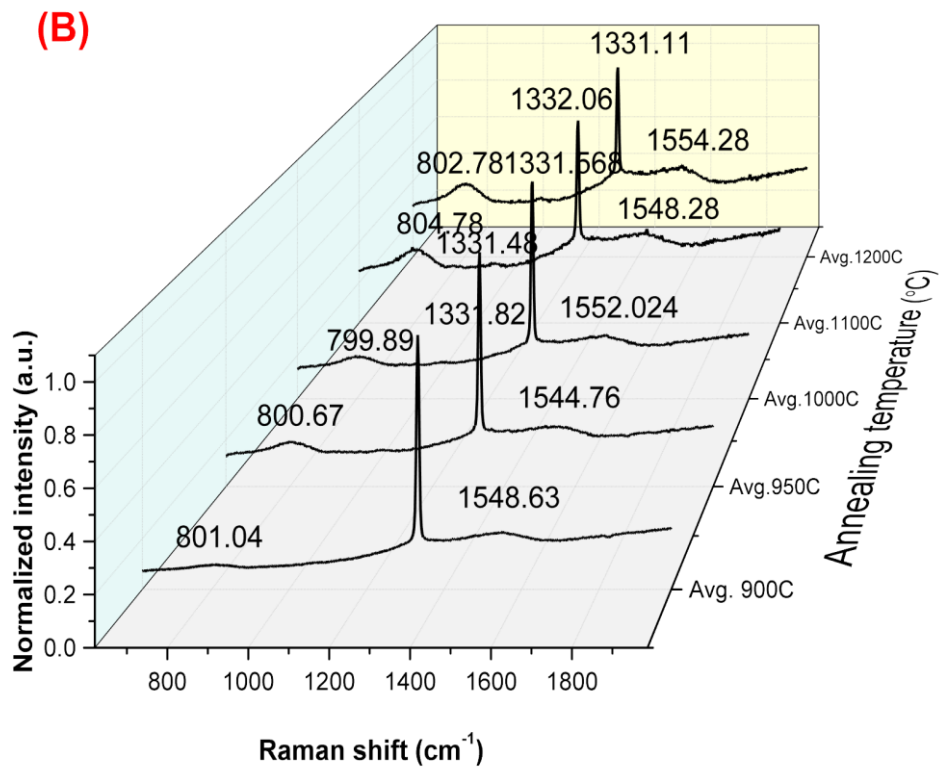
Figure 5.5 *Normalized Raman spectra of as-annealed BDD film surface as a function of annealing temperature*

The ratio (I_G/I_D) of the graphic peak (I_G) to the diamond peak (I_D) and the ratio (I_{a-C}/I_D) of the amorphous peak (I_{a-C}) over the diamond peak (I_D) are used to trace the evolution of the phase conversion of the non-diamond carbon structure as a function of the annealing temperature. The two graphs in **Figure 5.6** show how the annealing temperature effects the ratio of I_G/I_D and I_{a-C}/I_D. The data with black-hollow and red-solid data points in Graph A and Graph B are measured individually before and after annealing, respectively. In **Figure 5.6**.A, annealing generally caused more graphitisation within the samples in comparison to the non-annealed ones, except for samples treated in the range 900°C to 950°C. Also it is apparent that annealing at 900°C results in diamond material properties that are quite distinct from those obtained at other annealing temperatures. This observation is based on the SEM analysis and EBSD data

155

discussed in the previous section. The ratio of I_G/I_D decreased from 0.46 to 0.2 in the

temperature range below 900°C and then started to increase significantly to 0.6. This

trend is supported by the EBSD phase images and where this trend is reproduced in

the increasing/decreasing diamond phase images in EBSD data (**Figure *5.3***). This

phenomenon is related to the hydrogen effusion/diffusion near the sample surface

and the reconstruction of C-C bonding [258, 259]. As has been discussed in Section 2.1.3.2

Chapter 2, hydrogenated carbon is are one of the main defects that is known to exist

within the CVD diamond films. Experimental studies [260] show that the desorption of

hydrogen terminated on the sample surface occurs at temperatures above 500°C in

vacuum. The "dehydrated" carbon in the near surface area preferentially

reconstructed into sp^2 graphite rather than sp^3 due to the high stability of the sp^2 C-C

bond. However, these experimental results are not enough to explain the valley shape

of the sp^2/sp^3 conversion around the temperature range of 900°C. Another major

factor is boron pairing (B_2) is believed to be a deep trap for hydrogen forming

hydrogen-boron complexes [107]. This means that boron pairs/aggregates behave as

bonding-dissociation centres for hydrogen in the diamond lattice according to the

different thermal energy it has. Theoretical studies [112] from Goss *et al* found that

there is a critical temperature (T_0) for the dissociation/bonding equilibrium of these

boron pairing (B_2) where the binding energy is zero as a function of doping

concentration. Below or above this T_0 leads to paired configuration or dissociation

respectively. It is intriguing to note that the critical temperature (around 1200 K)

obtained from the theoretical calculations of Goss are in good agreement with the

experimental annealing temperature (900°C) found in this work. Furthermore, there

are many other types of (H, defects) complexes, such as (H, vacancies) and (H,N), which exist and react thermodynamically at different temperatures[105, 247, 261]. Based on the above, the decreasing ratio of sp^2/sp^3 (in **Figure 5.5**.A) below 900°C could be due to the overall compensation effect of multiple hydrogen trapping by carbon according to the thermodynamic behaviour of various trapping centres which, in this case, is believed to be mainly boron complex centres. The similar trend of gradually reduced signal of hydrogen free α-C before 900°C is one of the pieces of evidence to suggest this multiple hydrogen trapping behaviour. This effect disappears once the temperature rises above 900°C where boron pairing (B_2) are favoured in the dissociation which means the reducing of hydrogen-trapping centres. The "dehydrated" carbon then energetically prefers to form sp^2 rather than sp^3 structures.

The same trend can be found in **Figure 5.6**.B which presents the change of I_{a-C}/I_D ratio over the temperature range studied. It can be seen that, besides the 900°C annealing condition, the ratio of hydrogen-free α-C is generally higher than for the non-annealed samples at each given temperature which is evidence that supports the results found in Figure 5.A indicating that the carbon is gradually losing H. The changes in the I_{a-C}/I_D seen for temperatures above and below 900°C are the result of a combination effects including hydrogen effusion out of hydrated amorphous carbon (C-H) and the compensation of hydrogen arising from the dissociation/trap process of thermodynamic equilibrium of hydrogen-defect complexes [11].

In summary, the I_{a-C}/I_D and I_G/I_D ratio is an effective indicator of the change in proportions of non-diamond and diamond species as a function of annealing

157

temperature for the BDD sample sets that were studied. The results from **Figure *5.6***

support the interpretation of EBSD phase images (**Figure *5.3***) and SEM data (**Figure *5.2***)

which indicate that at annealing temperatures close to 900°C BDD films have their

optimum sp^2/sp^3 composition.
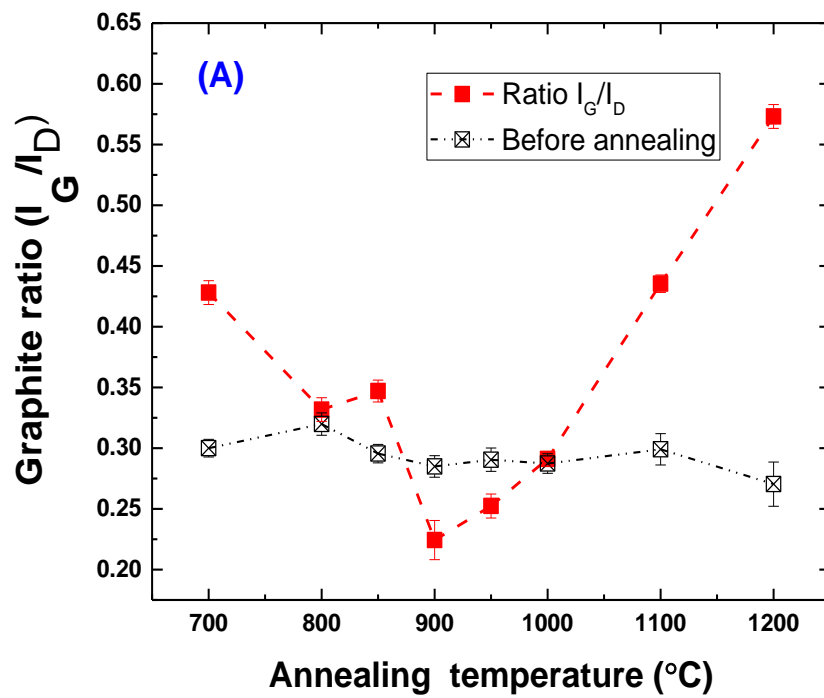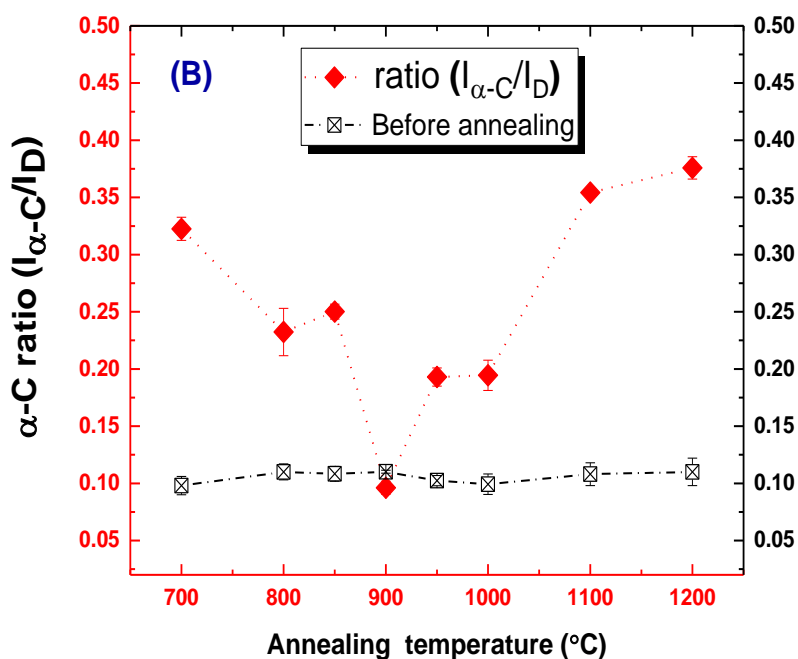
Figure 5.6.*The sp²/sp³ (A) and a-C/sp³ (B) ratio of BDD thin films grown on the PCD substrate as a function of temperature based on the normalised Raman spectra.(Black-hollow data points are the results obtained before annealing for each sample)*

The full width at half maximum (FWHM) of the sp^3 peak is a rough indicator of the overall defect densities present within the diamond lattice. It can be seen in **Figure *5.7*** that there are slightly less defects within the films than the non-annealed samples before 900°C which increases greatly when the temperature is above 950°C. This is a further result that supports the suggestion that the recombination of the H-defect complex may temporarily "improve" the quality of the BDD diamond, while high-temperature annealing (*T*>950°C) produces more defects within the diamond lattice as the result of the formation of non-diamond carbon (graphite and amorphous-C), in the agreement with Raman data (***Figure 5.6***).

159

The location of the peak positions of sp^3 and sp^2 bonded carbon is shown in **Figure *5.8***

and records the stress present in the diamond film. Due to the smaller size (-6 μm) of

the Raman laser spot compared to the grain size, the effect of grain boundary material

on the Raman spectra is not considered in this figure. The main result conveyed by the

data in **Figure *5.8*** is that there is no significant shift in both peaks which suggests a

relaxed state for the BDD after annealing.
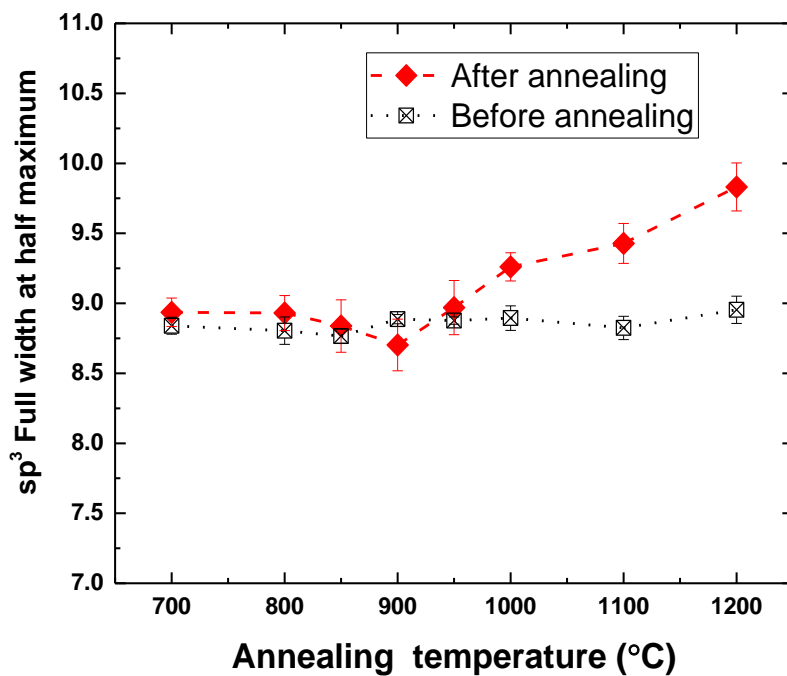
Figure 5.7. *Full width at half maximum (FWHM) value of diamond (sp^3) peak as a function of annealing temperature based on the Raman spectra of individual samples.*
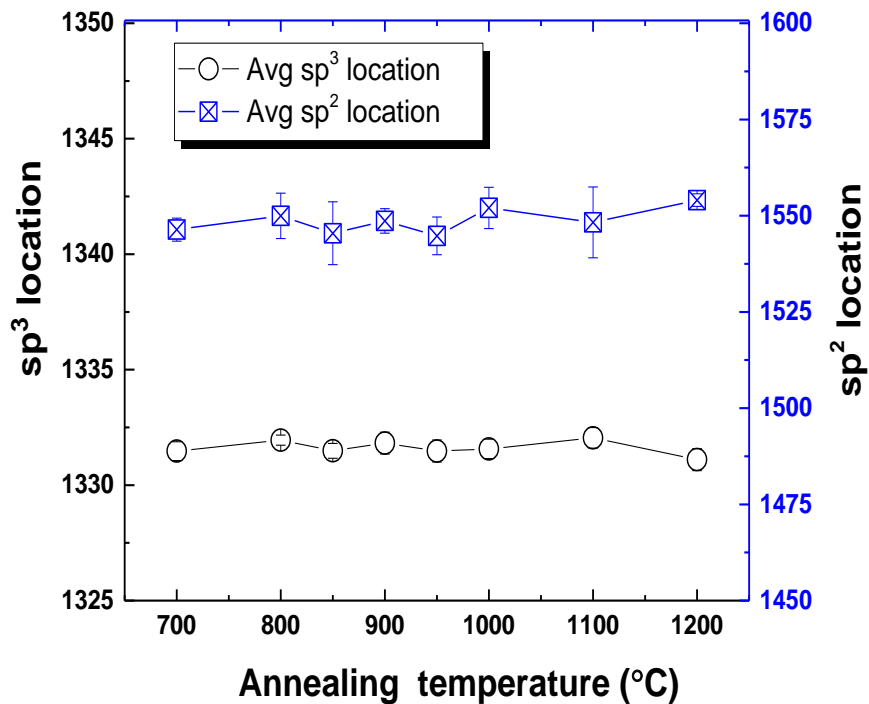
Figure 5.8 *The location of sp^3 and sp^2 peak as a function of annealing temperature based on the Raman spectra of individual samples.(Avg. means the average value from 5 times Raman measurements)*

In summary, the influence of thermal annealing on the surface morphology and composition of BDD thin films have been characterised by using SEM, EBSD and Raman. There is a critical temperature which is 900°C in this work that has been found in all data which changes the surface morphology and structural defects of as-annealed BDD films. This phenomenon is related to the thermodynamics of the association and bonding of hydrogen-defect complexes at the different annealing temperatures. In the next section, the variation of the distribution and concentration of boron upon thermal annealing will be discussed, and one of the key defects and also the hydrogen-trapping centre existing within the bulk, will be investigated by using Secondary Ion Mass Spectroscopy (SIMS).

5.3.2   Bulk properties as a function of thermal annealing

5.3.2.1   Mass spectra interface identification of as-annealed BDD thin films under SIMS operation

Secondary Ion Mass Spectroscopy (SIMS) is used in this work to study how the thermal annealing affects the distribution and concentration of boron throughout the whole layer as a function of the temperature. **Figure *5.9*** is the mass spectrum of the sample obtained under positive SIMS mode before annealing and shows the elementary composition of the surface. As discussed in Chapter 4 section 4.3, the signal sensitivity of these species by SIMS is different, therefore the mass spectra can only provide qualitative rather than quantitative information. However, once the species have been properly calibrated, the calculation of their concentration is possible through depth profile analysis. As seen in **Figure *5.10***, beside boron and sodium, the surface of the film is composed of different kinds of hydrocarbon species which are common defects existing within the CVD diamond film. A depth profile that samples these hydrocarbon species in Figure 4.15 Chapter 4 shows that they are always present within the films. Due to the presence of residual water molecules in the SIMS chamber, it is not possible to compare the concentrations of different forms of $-CH_x$ through depth profile with any accuracy. Therefore, positive ions, such as B^+ and Na^+, are used instead to assist in interpreting the doping profile. Sodium, in particular, is used to identify the interface between the substrate and doped layer as shown in **Figure *5.10***.
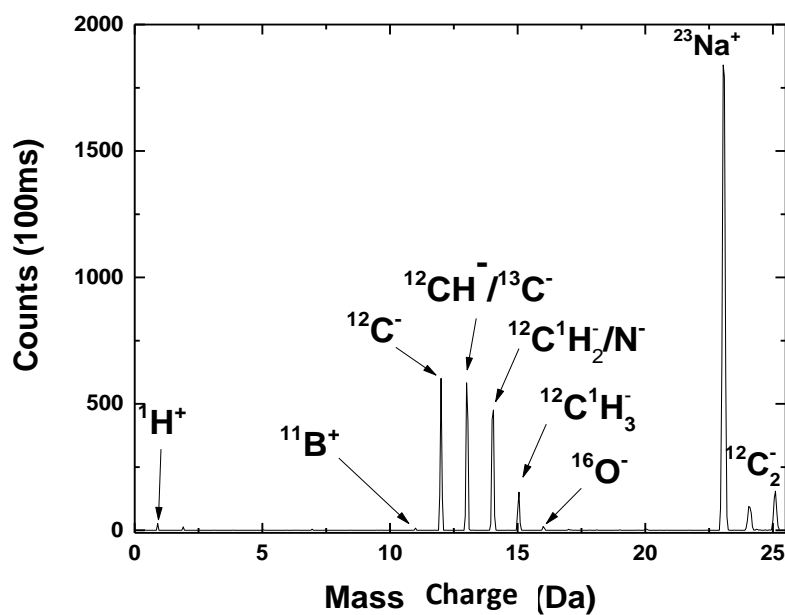
Figure 5.9. *The mass spectra of an as-annealed BDD thin film surface grown on a PCD substrate under positive SIMS mode (annealing condition 700 °C for 1 hour).*
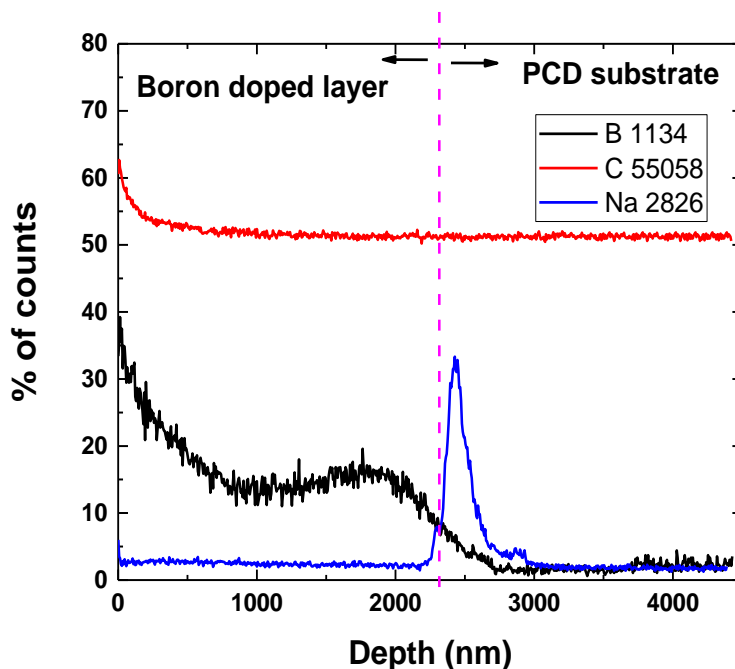
Figure 5.10 *Depth profile of boron (^{11}B), carbon(^{12}C) and sodium (^{23}Na) recorded with the percentage of counts obtained from mass spectra against the etching depth of samples.*

5.3.2.2 Boron concentration and distribution as a function of annealing temperature

Figure 5.11 shows the depth profile of boron under SIMS positive mode. The boron concentration is plotted against the depth of the films in the temperature range below 900°C. It can be seen that the depth for the boron distribution is getting smaller with increasing annealing temperature which can be confirmed by tracing the Na depth profile in **Figure 5.12**. Furthermore, there is a slightly increasing boron concentration in the near-surface region and a large decrease in the bulk of the doped layer. It can be seen that the peak location of Na in **Figure 5.12** which gradually shifts to a shallower depth indicating that the thickness of the film is decreasing with increasing temperature in the range investigated below 900°C. This result is supported by the thickness measurements from the cross-sectional SEM images of BDD films grown on the seeded layer (Appendix C). Previous experimental results revealed that the diffusion coefficient of boron is extremely low at temperatures below 1000°C, for example, 10^{-19} $cm^2{\cdot}s^{-1}$ at 800°C [262]. Therefore, the in-diffusion of boron is not the key parameter that influences the change in thickness of the films but functions as an indicator to track the dimensional changes in this temperature range. The large reduction in depth seen at 900°C could be the result of the transition of non-diamond carbon (such as graphite and a-C) to sp^3 bonded carbon especially in the grain boundaries leading to shrinkage in volume of the films, which is supported by EBSD data (**Figure 5.3**) and Raman spectra (**Figure 5.6**). Additionally, the thermodynamic interactions between hydrogen and its trapping centres which involve pairs of boron atoms and boron aggregates in the case of heavily boron doped diamond sample also support by the observed reduction in boron concentration seen in SIMS depth profile

164

data (*Figure 5.11*). Other suggestions, such as vacancy filling by hydrogen or deep trapping from various impurity complexes has been previously reported. [107, 247, 248]

The significant change in *Figure 5.11* that can be observed is the large reduction in boron concentration in the bulk area, especially for the boron profile line at 900°C (purple line), as the overall boron concentration of as-annealed samples has no significant increase add to compensate for the shrinkage in volume of the film with increasing temperature (700C-900°C). This phenomenon is related to the thermodynamic equilibrium shifting from bonded boron (B_2) to substitutional boron (B_s) before and after the critical temperature of 900°C. As discussed previously, the B_2 pairs are the thermodynamically favoured bonding configuration for defects below 900°C which also functions as a deep hydrogen trap centre forming a B_2H_x complex (mass number > 11). This is the main reason that has been proposed to explain the loss of signal for [11]B which could be the experimental evidence to support the published modelling results [112].

Therefore, together with the results discussed previously (Section 5.3.1), the overall effect of thermal annealing below 900°C on the boron-doped diamond films appears to be repairing the defects within the bulk layer leading to a decreased thickness in which the boron is "compressed" into a smaller volume in the near-surface region.
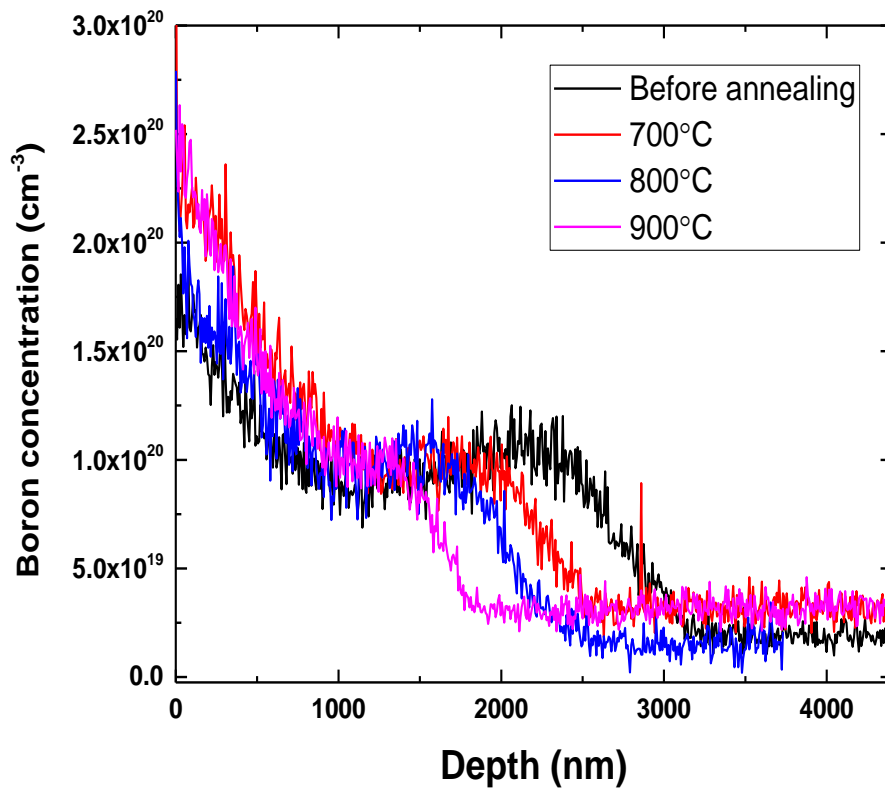
Figure 5.11 *The depth profile of boron (^{11}B), recorded as boron concentration against the etching depth of annealed BDD thin films in the temperature range between 700 ℃ to 900 ℃.*
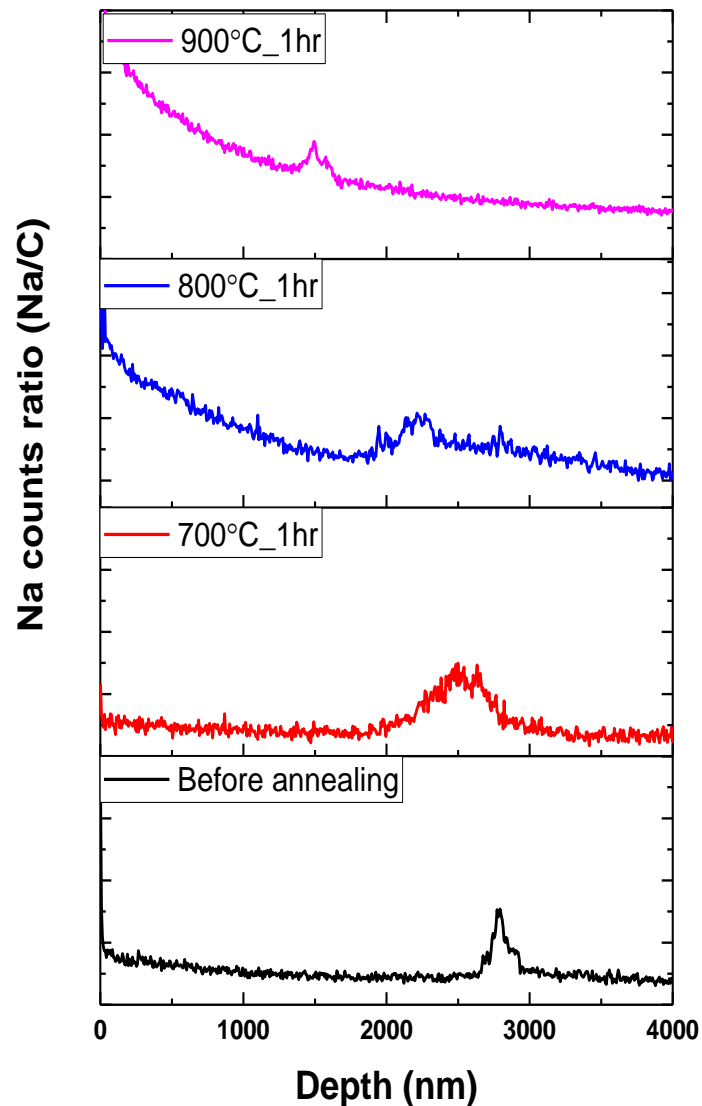
Figure 5.12 *The depth profile of sodium (^{23}Na), recorded with the ratio of ^{23}Na count over ^{12}C count against the etching depth. The graph is arranged from bottom to top with the annealing temperature range between 700℃ to 900℃*

Figure *5.13* is the SIMS depth profile of the boron concentration plotted as a function of annealing temperature above 900°C. One of main features observed from this figure is that there is no significant change in the depth with the temperature up to 1000°C which can be tracked by following the change in the peak location of Na in

Figure *5.14*. Furthermore, the boron concentration over the whole depth, ie film thickness, of the doped layer increases slowly at temperatures higher than 1000°C , which is supported by the thermodynamics modelling of boron pairing complexes which is favoured to dissociate into substitutional boron (B_s) at temperatures above 900°C[112] and the increased carrier concentration measured by Hall Effect set up which will be discussed in the next section. The increase in the concentration of boron arises from various multi-atom boron complexes, boron-interstitials, and complexes of B with vacancies [21].

On the other hand, it can be seen in **Figure *5.15*** that the change in depth is much smaller at temperatures above 1000°C than below 900°C in comparison with the non-annealed samples which might indicate the important role of hydrogen diffusion and their interaction with defects, especially boron pairs (B_2), below 900°C resulting in the change in the volume of the films. The increasing ^{11}B signal over the whole layer at temperatures above 1000°C is further evidence to show experimentally that the transition of the deep hydrogen trapping centre of B_2 into substitutional B which leads to the hydrogen effusion and, hence a high level of graphitisation on the surface which is supported by Raman (***Figure 5.5***) and EBSD data (***Figure 5.3***) discussed previously (Section 5.3.1) in this work. Due to the very slow diffusion coefficient (10^{-15} $cm^2 \cdot s^{-1}$ at 1200°C [263]) of boron, it is very difficult to detect boron deeper than is measured in non-annealed samples following one hour of annealing. This gives the overall depth variation over the temperature range between 700°C to 1100°C which is the result of sp^2/sp^3 conversion and hydrogen diffusion at the temperature range below and above 900°C.

168

In summary, annealing BDD films leads to the variation in the configuration of boron within in the diamond lattice which is supported by the SIMS depth profile data for [11]B. Therefore, the hydrogen diffusion/effusion and its interactions with other defects is a result of changes in the configuration of dopants and other defects in the lattice. This leads to the phenomena which have been observed previously, the change in the surface morphology, phase composition and thin film thickness. It is very important to verify that whether the electrical properties, such as carrier concentration, resistivity and mobility are in accordance with the results that have been found in this work. The next section will discuss in detail the influence of annealing temperature upon the electrical behaviour of these boron doped samples.
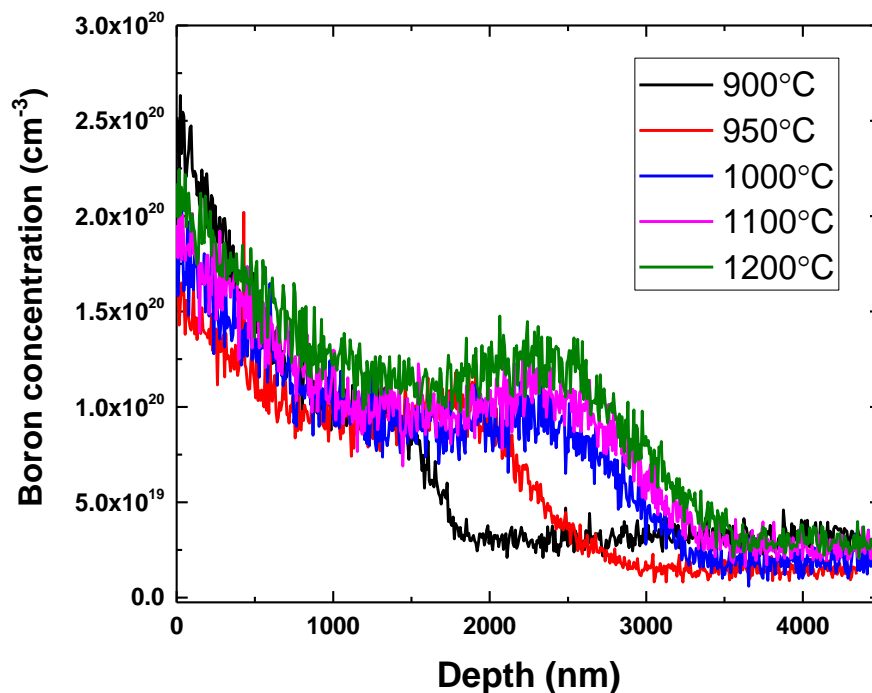
Figure 5.13 *Depth profile of boron ([11]B), recorded with the boron concentration against the etching depth of as-annealed BDD thin films in the temperature range between 900°C to 1200°C.*
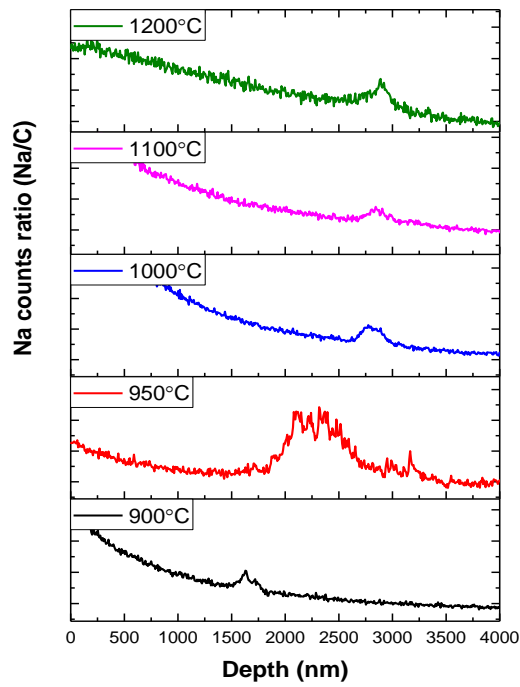
Figure 5.14 *Depth profile of Sodium (^{23}Na), recorded with the ratio of ^{23}Na count over ^{12}C count against the etching depth of as-annealed BDD thin films. The graph is arranged from bottom to top with the annealing temperature range between 900 ℃ to 1200 ℃*
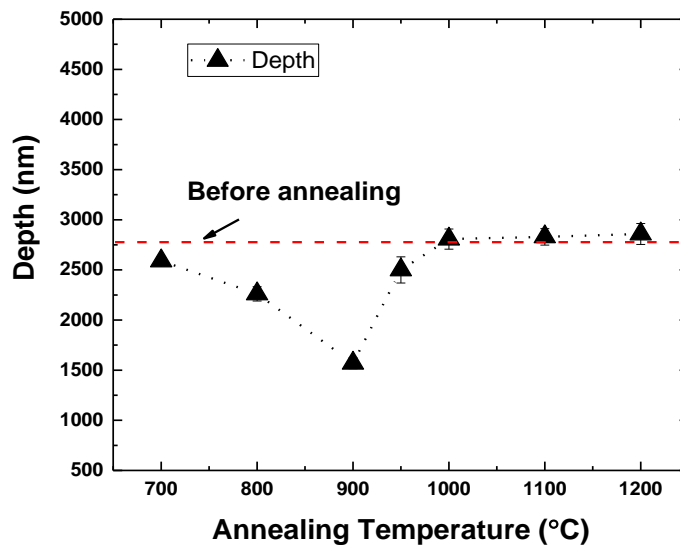
Figure 5.15 *The variation of depth (film thickness) of as-annealed BDD thin films (black solid data points) as a function of annealing temperature.*

5.3.3 The influence of thermal annealing on the electrical carriers in boron doped thin films.

Hall Effect measurement was used in this work to measure the electronic properties: carrier concentration, mobility and resistivity of the as-grown BDD films at room temperature as a function of thermal annealing. In the literature, the electronic properties of CVD diamond are governed by intrinsic defects, extrinsic contaminates (dopants and dopants complex), grain boundary and surface effects [118, 264-266] which exhibit activation energies significantly smaller than 2.5eV [267]. Boron as an acceptor in P-type diamond creates free holes (B$^-$) are the CVD diamond which is believed to be electrically passivated by hydrogen forming hydrogen-boron complexes [268]. Thermal annealing changes the content and structure of defects in diamond which significantly influences the electrical behaviour of BDD films. This section focuses on the influence of annealing temperature on the electrical properties of BDD samples.

5.3.3.1 *The influence of annealing temperature on the carrier concentration and mobility of BDD thin films*

Figure *5.16* is the measured carrier concentration plotted versus temperature. It can be seen that the amount of carriers in annealed samples is generally lower than the non-annealed samples in the temperature range below 950°C, and then higher when the annealing temperature rises above 1000°C. This is due to the combination effect of hydrogen effusion/diffusion, sp^2/sp^3 phase transition and trapping/dissociation thermodynamics of hydrogen-boron complexes. Specifically, there are a few reasons for the reduced value of carrier concentration: one is the decreasing amount of highly mobilised H$^+$, which is experimentally and theoretically acknowledged to be a diffusing species and contributes to the conductivity in p-type diamond due to it being trapped by defect centres within the bulk and lost on the surface [248, 255]. A second reason is the that paired B$_2$ or boron aggregates exist in the diamond lattice at temperatures

below 900°C and function as deep H$^+$ trapping centres forming the neutralised –BH complex which is believed to be electrically inactive[107].

A third reason is the recombination of mobilised defects, such as H$^+$ and vacancies, which could be another reason that causes the measured carrier concentration to decrease. Once the temperature increases above 950°C the boron pairs are more likely to be subject to dissociation and hence greatly weaken the passivation effect of hydrogen-boron complexes which increase the amount of activated substitutional boron acceptors. This change in carrier concentration is in good agreement with SIMS depth profile information for boron (**Figure *5.11*** and **Figure *5.13***). However, the ratio of [B$^-$]/[B],functioning as an effective acceptor, is no more than 0.2% even at the 1200°C suggesting that large amounts of boron form atom clusters and the number density of (B,H) defects that still exist in the films would need a much higher temperature to activate all of the incorporated boron.
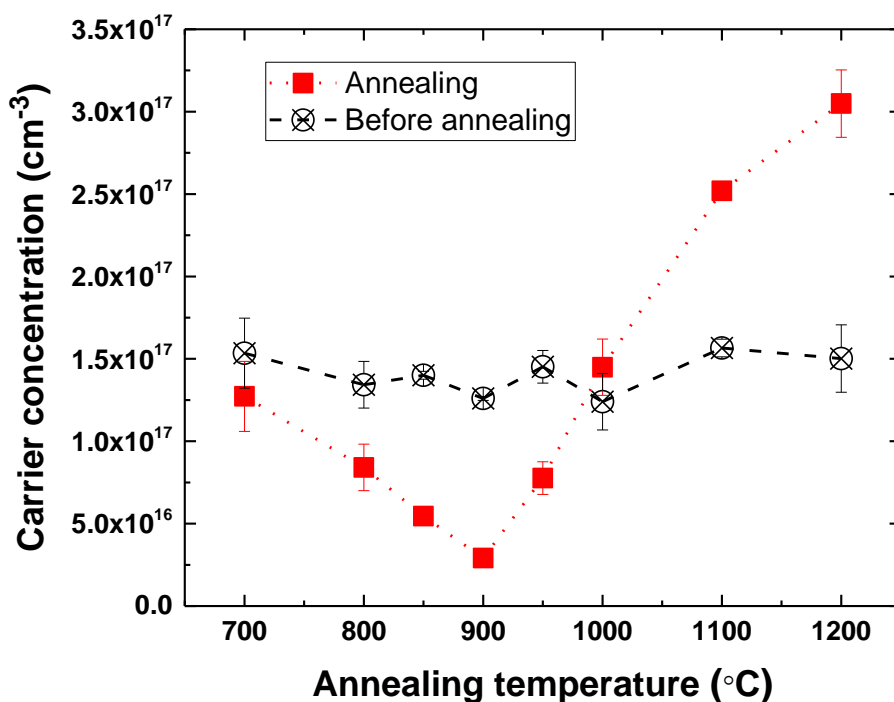
Figure 5.16 *Graph of carrier concentration as a function of annealing temperature. (Black-hollow circle and red-solid square points represent before and after annealing, respectively)*

The mobility of the free carriers is limited by the defect-scattering mechanism which means that the higher the defect concentration, the lower the value of carrier mobility. **Figure *5.17*** is the measured mobility plotted against the annealing temperature. It can be found that the mobility increases from around 200 $cm^2V^{-1}s^{-1}$ to nearly 1000 $cm^2V^{-1}s^{-1}$ and then drops back to less than 60 $cm^2v^{-1}s^{-1}$ which is even lower than the non-annealed sample. There are several possible factors that may be contributing to this variation: firstly, based on the EBSD phase images (**Figure *5.3***) and Raman spectra (**Figure *5.5***) for sub- 900°C annealing temperatures, the reduction of non-diamond impurities and the strengthening of the diamond phase leads to a lowering of the density of grain boundaries which strongly influences the hole mobility. Secondly, the formation of neutralised $-B_2H_x$ complexes reduces the ionised impurity concentration which leads to the passivation of boron acceptors as evidenced by the results found from Hall measurements (**Figure *5.16***); Lastly, the mean path for carrier transport is reduced as the thickness of the films decreases based on the SIMS depth profile (**Figure *5.11***) which would strongly influence the ability of carriers to move. As the annealing temperature rises above 900°C, the concentration of defects, including grain boundaries, ionised boron acceptors and non-diamond carbon, increases enhancing the defect-scattering effect that lowers measured mobility.

A plot of carrier concentration and mobility together as a function of annealing temperature is shown in **Figure *5.18***, can conclude that the main factor that influences the carrier mobility is the ionised acceptor, a defect-scattering effect.

173
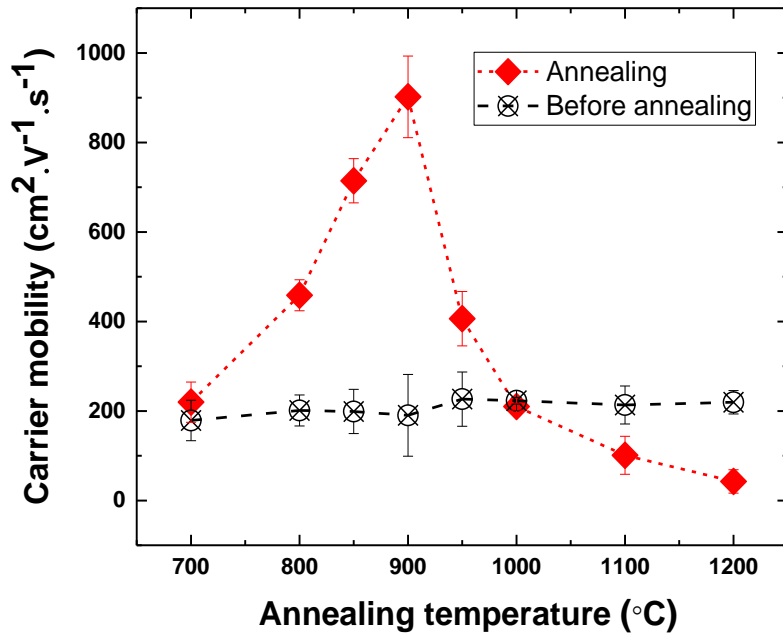
Figure 5.17 *Carrier mobility as a function of annealing temperature for annealed and the non-annealed samples. (Black-hollow circle and red-solid square points represent before and after annealing, respectively)*
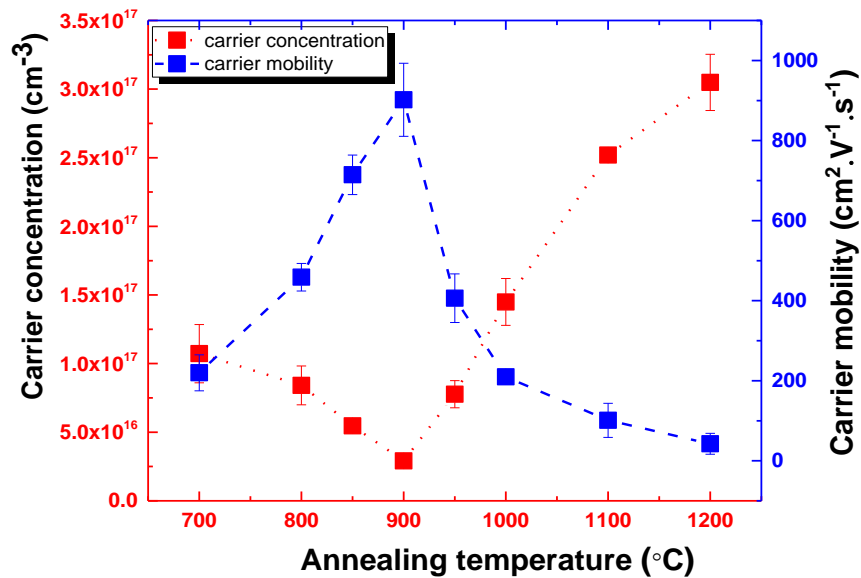
Figure 5.18 *Carrier concentration and mobility plotted as a function of annealing temperature. (Red solid and blue solid points represent carrier concentration and mobility, respectively)*

5.3.3.2 The influence of annealing temperature on the resistivity of BDD thin films

Figure *5.19* presents the overall effect of annealing temperature on the resistivity of as-grown thin films. The negative/positive value in the figure represents the variation in the resistivity. In comparison with non-annealed ones, the BDD film is over 40% more conductive in the temperature range below 950°C and more resistive at temperatures higher than 1000°C. Specifically, the sheet resistivity decreases by 40% with increasing temperature up to a critical temperature and then increases at the higher temperature level. The reason for the variation of thin film resistivity is linked to the state of the defects existing within the annealed thin films. The conductivity of a p-type semiconductor material is proportional to the carrier concentration and mobility as described in equation 5.1 below:

$$\sigma = p\mu_h e \quad \text{Equation 5.1}$$

where p is the hole concentration, μ_h is the hole mobility and e is the electron charge.

Therefore, the large increase in the value of carrier mobility below 900°C despite the reduced value in carrier concentration (***Figure 5.17***), is the driving force for the improvement in the conductivity of BDD films. Experimental evidence found from Raman ***Figure 5.6*** and EBSD data ***Figure 5.3*** show that the reduction in non-diamond carbon and also the grain boundary density observed below 900°C is another major reason for the better electrical conductivity. At the higher range above 900°C, the increased amount of ionised substitutional boron (B$_s$) based on SIMS ***Figure 5.13*** and Hall measurement data ***Figure 5.16***) as well as impurities such as non-diamond carbon

175

and grain boundaries based on Raman *Figure 5.6* and EBSD data *Figure 5.3* enhance

the scattering-effect of hole carriers, which significantly limits the ability of carriers to

move within the bulk of the films leading to an increase in the resistivity of the BDD

films.
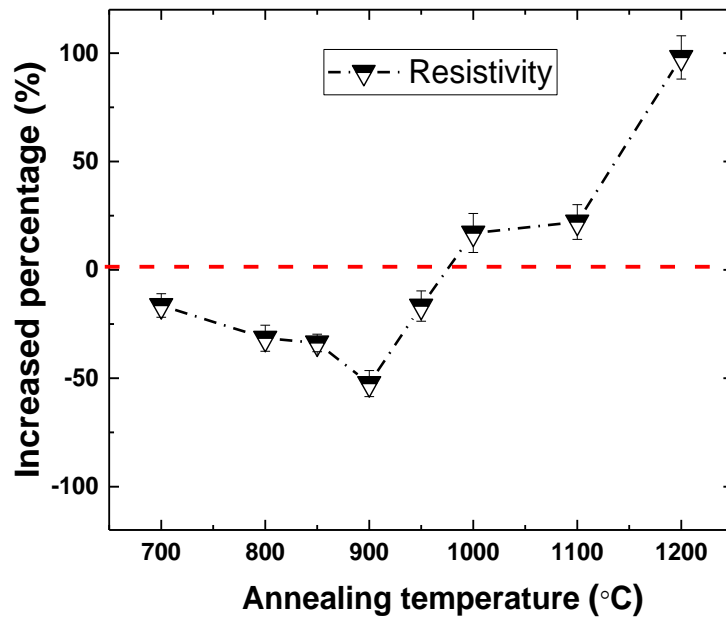
Figure 5.19 *Percentage change in resistivity before and after annealing ($\frac{\rho_{after} - \rho_{before}}{\rho_{before}}$) as a function of annealing temperature (The red-solid line divides negative and positive values which represents increasing and decreasing resistivity, respectively)*

5.4   Conclusions

A set of heavily boron-doped diamond thin films grown on the non-seeded PCD

substrate have been fabricated by using HFCVD under the same deposition conditions.

These samples were annealed under vacuum for one hour in the temperature range

from 700°C to 1200°C. Surface techniques including SEM, EBSD and Raman, were

combined with SIMS and Hall Effect measurement to investigate the influence of

thermal annealing on the structural and electrical properties of BDD films. This chapter

demonstrates that 900°C is the critical post-annealing temperature which divides the

electrical behaviour of BDD film as a result of hydrogen diffusion, diamond/non-

diamond conversion and the thermodynamic process of boron pairs.   It has been

found that increasing annealing temperature < 900°C causes several effects

1) A number of defects, such as graphite, non-diamond carbon and GBs reduced within the surface area.

2) The morphology of the surface is smoother and the crystal sizes enlarge.

3) The thickness of the films decreases with increasing temperature.

4) The films are more conductive as a result of reduced carrier concentration and high value of mobility.

In the comparison, annealing samples at temperatures above 900°C causes the

opposite effect on these films. One of the main reasons is related to the

thermodynamics of dissociation/bonding of (B_2, H) complexes around the critical

temperature.

In summary, the overall structural, physical and electrical behaviour of BDD films

under different temperatures is controlled by the thermodynamics of the

bonding/dissociation of boron pairs (B_2) and hence B_2H_m complexes, which is

accompanied by the defect diffusion, such as highly mobilised hydrogen. The next

chapter will demonstrate the evidence and influence of defect diffusion at 900°C as a

function of annealing time which is another result to mutually support the results

reported in this Chapter.

5.5   References

232.   Zakery, A. and S.R. Elliott, Optical properties and applications of chalcogenide glasses: a review. Journal of Non-Crystalline Solids, 2003. 330(1–3): p. 1-12.

233.   Kitatani, T., K. Nakahara, M. Kondow, K. Uomi, T. Tanaka, Mechanism analysis of improved GaInNAs optical properties through thermal annealing. Journal of Crystal Growth, 2000. 209(2–3): p. 345-349.

234.   Hultman, L., Thermal stability of nitride thin films. Vacuum, 2000. 57(1): p. 1-30.

235.   Minoru, F., H. Shinji, and Y. Keiichi, Growth of Ge Microcrystals in SiO_2 Thin Film Matrices: A Raman and Electron Microscopic Study. Japanese Journal of Applied Physics, 1991. 30(4R): p. 687.

236.   Shuji, N., T. Mukai, M. Senoh and N. Iwasa, Thermal Annealing Effects on P-Type Mg-Doped GaN Films. Japanese Journal of Applied Physics, 1992. 31(2B): p. L139.

237.   Aghamalyan, N.R., et al., Influence of thermal annealing on optical and electrical properties of ZnO films prepared by electron beam evaporation. Semiconductor Science and Technology, 2003. 18(6): p. 525.

238.   Alonzo-Medina, G.M., et al., Understanding the thermal annealing process on metallic thin films. IOP Conference Series: Materials Science and Engineering, 2013. 45(1): p. 012013.

239.   Uzan‑Saguy, C., C. Cytermann, R. Brener, V. Richter, M. Shaanan, and R. Kalish, Damage threshold for ion‑beam induced graphitization of diamond. Applied Physics Letters, 1995. 67(9): p. 1194-1196.

240. Parikh, N.R., J. D. Hunn, E. McGucken, and M. L. Swanson, Single‐crystal diamond plate lift off achieved by ion implantation and subsequent annealing. Applied Physics Letters, 1992. 61(26): p. 3124-3126.

241. Zhu, W., G. P. Kochanski, S. Jin, L. Seibles, D. C. Jacobson, M. McCormack, and A. E. White, Electron field emission from ion‐implanted diamond. Applied Physics Letters, 1995. 67(8): p. 1157-1159.

242. Prins, J.F., Activation of boron-dopant atoms in ion-implanted diamonds. Physical Review B, 1988. 38(8): p. 5576-5584.

243. Gu, S.S. and X.J. Hu, Enhanced p-type conduction of B-doped nanocrystalline diamond films by high temperature annealing. Journal of Applied Physics, 2013. 114(2): p. 023506.

244. Sahli, S. and D.M. Aslam, Effect of postdeposition anneal on the resistivitity of p‐type polycrystalline diamond films. Applied Physics Letters, 1996. 69(14): p. 2051-2052.

245. Chen, S.H., S.L. Chen, M.H. Tsai, J. J. Shyu, and C.F. Chen, a Electrical Characteristics and Annealing Study of Boron‐Doped Polycrystalline Diamond Films. Journal of the Electrochemical Society, 1995. 142(12): p. L223-L225.

246. Werner, M., O. Dorsch, H. U. Baerwind, and E. Obermeier, Charge transport in heavily B‐doped polycrystalline diamond films. Applied physics letters, 1994. 64(5): p. 595-597.

247. Chevallier, J., et al., Hydrogen-acceptor interactions in diamond. Diamond and Related Materials, 2001. 10(3–7): p. 399-404.

248.   Uzan-Saguy, C., et al., Hydrogen diffusion in B-ion-implanted and B-doped homo-epitaxial diamond: passivation of defects vs. passivation of B acceptors. Diamond and related materials, 2001. 10(3): p. 453-458.

249.   Zeisel, R., C. Nebel, and M. Stutzmann, Passivation of boron in diamond by deuterium. Applied physics letters, 1999. 74(13): p. 1875-1876.

250.   Wang, Y.G., S.P. Lau, B.K. Tay, X.H. Zhang, Resonant Raman scattering studies of Fano-type interference in boron doped diamond. Journal of Applied Physics, 2002. 92(12): p. 7253-7256.

251.   Tuinstra, F. and J.L. Koenig, Raman Spectrum of Graphite. The Journal of Chemical Physics, 1970. 53(3): p. 1126-1130.

252.   Nemanich, R.J., J.T. Glass, G. Lucovsky, and R.E. Shrorder, Raman scattering characterization of carbon bonding in diamond and diamondlike thin films. Journal of Vacuum Science & Technology A, 1988. 6(3): p. 1783-1787.

253.   Li, F. and J.S. Lannin, Disorder induced Raman scattering of nanocrystalline carbon. Applied Physics Letters, 1992. 61(17): p. 2116-2118.

254.   Bacsa, W.S., J.S. Lannin, D.L. Pappas, J.J. Cuomo, Raman scattering of laser-deposited amorphous carbon. Physical Review B, 1993. 47(16): p. 10931-10934.

255.   Schwan, J., S. Ulrich, V. Batori, and H. Ehrhardt, Raman spectroscopy on amorphous carbon films. Journal of Applied Physics, 1996. 80(1): p. 440-447.

256.   Zhang, X., W. H. Weber, W. C. Vassell, T. J. Potter, and M. A. Tamor, Optical study of silicon-containing amorphous hydrogenated carbon. Journal of Applied Physics, 1998. 83(5): p. 2820-2825.

257.	Rejowski, E.D., M.C.L. de Oliveira, and R.A. Antunes, Structural Characterization and Corrosion Stability of a Si-Doped DLC Coating Applied on Cylinder Liner. Journal of Materials Engineering and Performance, 2014. 23(11): p. 3926-3933.

258.	Sung, J., Graphite → diamond transition under high pressure: A kinetics approach. Journal of Materials Science, 2000. 35(23): p. 6041-6054.

259.	Dmitriev, V.P., S. B. Rochal, Yu. M. Gufan, and P. Tolédano, Reconstructive transitions between ordered phases: The martensitic fcc-hcp and the graphite-diamond transitions. Physical Review Letters, 1989. 62(21): p. 2495-2498.

260.	Robinson, V.S., Y. Show, G. M. Swain, R. G. Reifenberger, and T. S. Fisher, Thermionic emission from surface-terminated nanocrystalline diamond. Diamond and Related Materials, 2006. 15(10): p. 1601-1608.

261.	Rutledge, K.M. and K.K. Gleason, Hydrogen in CVD diamond films. Chemical Vapor Deposition, 1996. 2(2): p. 37-43.

262.	Narducci, D., J. J. Cuomo, C. R. Guarnieri, and S. J. Whitehair, Electrical characterization of metal contacts on diamond thin films. in MRS Proceedings. 1989. Cambridge Univ Press.

263.	Vavilov, V., Ion implantation into diamond. Radiation Effects, 1978. 37(3-4): p. 229-236.

264.	Thibault, J., J.-L. Rouviere, and A. Bourret, Grain Boundaries in Semiconductors, in Materials Science and Technology. 2006, Wiley-VCH Verlag GmbH & Co. KGaA.

265.   Morelli, D.T., T.M. Hartnett, and C.J. Robinson, Phonon‐defect scattering in high thermal conductivity diamond films. Applied Physics Letters, 1991. 59(17): p. 2112-2114.

266.   Olson, J.R., R. O. Pohl, J. W. Vandersande, A. Zoltan, T. R. Anthony, and W. F. Banholzer, Thermal conductivity of diamond between 170 and 1200 K and the isotope effect. Physical Review B, 1993. 47(22): p. 14850-14856.

267.   Elshabini, A., A.A. Elshabini-Riad, and F.D. Barlow, Thin film technology handbook. 1998: McGraw-Hill Professional.

268.   Teukam, Z., et al., Shallow donors with high n-type electrical conductivity in homoepitaxial deuterated boron-doped diamond layers. Nat Mater, 2003. 2(7): p. 482-486.

Chapter 6   The investigation of the influence of annealing time on heavily boron-doped diamond thin films

6.1   Introduction

The importance of choosing the correct temperature at which to anneal thin layers of heavily boron-doped Diamond (BDD) has been experimentally demonstrated and discussed in the previous chapter. Based on those results it has been found that a thermodynamic equilibrium exists between the structural and electrical properties of heavily BDD thin film after annealing at 900°C for a duration of one hour. Subsequent measurements have shown that the quality and electrical behaviour of as-grown BDD films was significantly improved. The entire structural, physical and electrical behaviour is controlled by the thermodynamics of the bonding-dissociation process of the boron pair complex. Previous investigations into the annealing time have found that it plays an important role in terms of thermodynamics diffusion[269, 270]. The diffusion of defects, such as dopant impurities (boron and nitrogen), vacancies, and defect complexes, in diamond, has been a subject of intensive study for years[270-272] and can significantly alter the structural, physical, optical and electrical properties of as-grown diamond[273]. The common methods described in the literature for studying the diffusivity of these defects are either microwave plasma heating [274] or laser irradiation[275]. The diffusion of hydrogen and boron in BDD is an important topic that has been studied in order to improve the optical[101] and electrical [276, 277]properties. The majority of reports are based on the diffusion of boron[278] or deuterium[279] from the surface into the bulk of a BDD layer and their analysis using SIMS depth profile. There are very few experimental reports about the in-diffusion of deuterium or boron using a post-annealing method and especially in relation to a thermodynamic

trapping/de-trapping process of (B, H) complexes at high temperature and for different annealing times. Therefore, the structural and electrical behaviour of heavily BDD thin films as a function of the annealing time at the critical temperature of 900°C has been investigated in this chapter in order to provide experimental evidence of time-dependent hydrogen self-diffusion in relation to the thermodynamics of boron pairing within the diamond lattice.

6.2   Material and Methods

6.2.1   The Fabrication of BDD

All the samples used in the study were grown on the smooth side of polycrystalline diamond (PCD) substrate (TM100) purchased from Element Six, cleaned in a hot solution (200°C) of concentrated sulfuric acid (100 ml) and potassium nitrate (Aldridge 6.5 g) for 30 minutes before growth in order to remove any graphitic and metallic contaminations.

Hot Filament Chemical Vapour Deposition (HFCVD) was used to grow heavily BDD thin films. All seven samples were fabricated together under the same conditions in the same cycle of deposition to eliminate any sample-to-sample variability that might arise from sequential growth cycles. A tantalum filament drawing a current of 25 A was used to generate a filament temperature 2000°C for the thermal dissociation of precursor gases under a total gas pressure in the reactor of 20 torr. The ratio of feedstock gases in the growth mixture was 1% CH_4 in H_2 and total growth time was 4 hours. The B_2H_6 flow rate used in this work was 0.003 sccm which is the minimum flow rate the mass flow controller could regulate. All of the thin film growth on the diamond samples was achieved without a seeding layer and was found to be homoepitaxial in nature.

184

6.2.2 Thermal Annealing

The annealing experiments were conducted by an annealing set up (Eeyore,2x012) with a temperature range up to 1200°C. Each sample was inserted into a quartz tube that was sealed and evacuated to 1×10^{-6} torr prior to the start of the annealing treatment. Table 6.1 is the summary of annealing conditions carried out with each of the BDD films.

Table 6.1 *The summary of annealing condition used in this work*

Sample No.	Annealing temperature (°C)	Temperature increase rate (°C·min^{-1})	Annealing time (minutes)	Cooling time (h)
1	900	10	20	12
2	900	10	40	12
3	900	10	50	12
4	900	10	60	12
5	900	10	70	12
6	900	10	90	12
7	900	10	120	12

185

6.2.3   Surface Characterisation

6.2.3.1   Surface Morphology and Composition

The surface morphology was studied by Scanning Electron Microscopy (SEM) at an accelerating voltage of 10 kV and with different magnification ranges. Electron Back-scattering Diffraction (EBSD) was used to study the influence of different annealing times on the phase composition and crystal size of the as-grown BDD films. A high electron beam current at an accelerating voltage of 30 kV, using a 120 μm aperture and a sample tilt of 70° was used to obtain the distinct diffraction pattern of the diamond lattice. The scanning area was kept constant (200μm ×100μm) in order to quantitatively compare each sample annealed for different annealing times.

6.2.3.2   Lattice Structure and Defects

Thin film quality and composition was measured by Raman spectroscopy using 514 nm green laser to excite a resonant phonon response. Each sample was analysed using the accumulation mode to record a signal spectrum for periods of 15 minutes. Measurements were repeated 5 times on the different areas for each sample to obtain the validation and ensure the representative quality of the Raman data.

6.2.4   Bulk properties of BDD films

6.2.4.1   Boron distribution and concentration within the whole layer

Secondary Ion Mass Spectroscopy (SIMS) is used in this work to investigate the variation of dopants within the samples as a function of annealing time. The experimental conditions and method of SIMS are the same as it has been described in Chapter 4 section 4.3.2.1.

6.2.4.2 Electrical Carrier Transport

The electrical properties of BDD films were measured using a 4-point probe system configured to perform Hall Effect measurements at room temperature. The setup consists of a current source (Keithley model 2128A), which provided a high quality and low-noise DC signal, with a wide range of resistivity values. A Van der Pauw contact configuration was used for resistivity measurements. Hall voltage measurements were made by inserting the contacted sample into a 1 T magnetic field.

The surfaces of all of the samples were O-terminated for 30 minutes by using an Ozone cleaner in order to insulate the surface and avoid surface conductivity which might be induced by hydrogen termination acquired during CVD growth. A range of dipolar currents were applied using the Van der Pauw method to record resistivity measurements. This method is used so as to remove thermal couple effect. The Hall voltage was measured in a 1T magnetic field with a range of monopolar currents and further calculations were made to obtain values of the carrier concentration and mobility. 20 measurement cycles were made for each current using the Van der Pauw method and 50 measurement cycles for the Hall measurement in order to get accurate experimental data. Each measurement was repeated 3 times in order to obtain the validation.

6.3   Results and Discussion

6.3.1   Surface Characterisation as a function of annealing time

The influence of different annealing times at 900°C on the morphology, composition and structure of the thin film surface will be discussed in this section.

6.3.1.1 The variation of surface morphology as a function of annealing time by using SEM

Figure 6.1 shows the surface images following samples being annealed at 900°C for

20,40, 60,70,90 and 120 minutes, respectively. It can be seen that the surface is getting

smoother and exhibits fewer grain boundaries as the annealing time is extended up to

60 minutes. Beyond one hour the film quality becomes worse. Similar to the results

found in Chapter 5 there is an optimum dwell condition at the critical annealing

temperature of 900°C to achieve the best annealing effect. The change in the surface

morphology is strongly related to a change in the composition and structure of the thin

film. EBSD phase images of sp^3 diamond and sp^2 graphite in combination with a grain

size spread look-up table were used to make a more detailed interpretation of the

morphological changes found in SEM images.
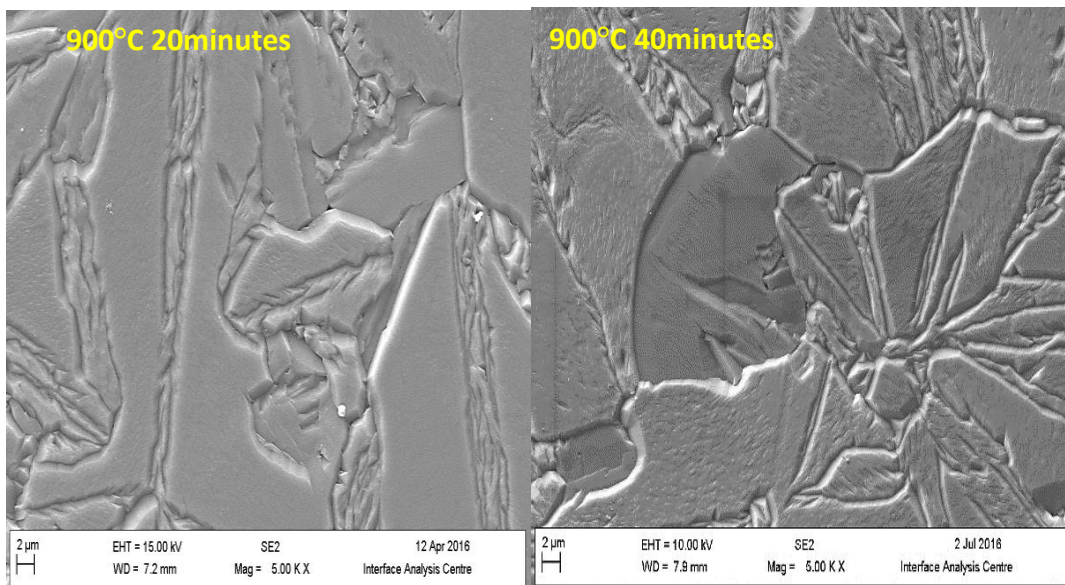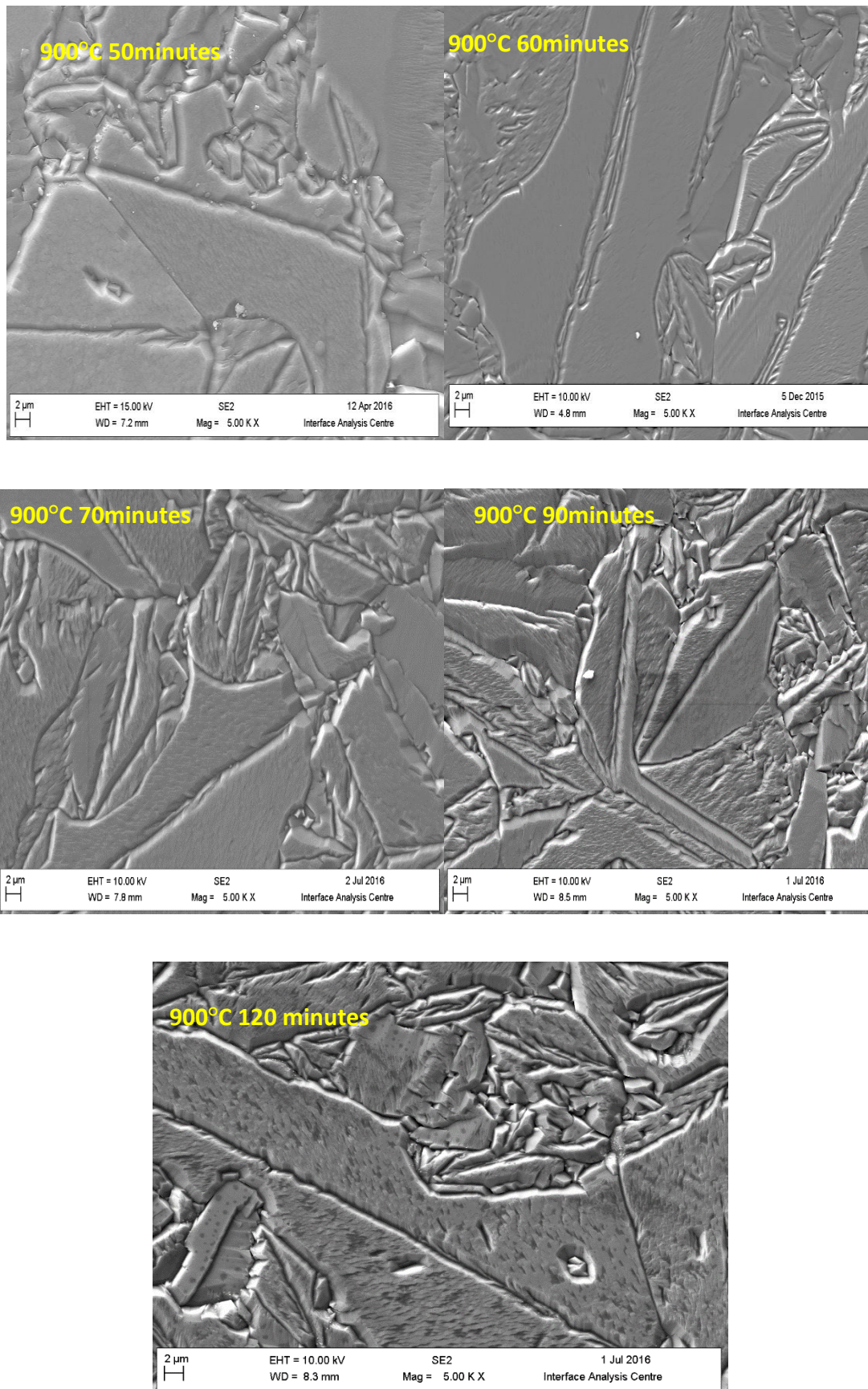
Figure 6.1.*SEM images of surface morphologies of boron-doped diamond thin films as a function of annealing time*

6.3.1.2 The variation of phase composition and grain size as a function of annealing time by using EBSD

Figure *6.2* shows the phase images processed from EBSD data which represents the percentage of graphite (green) and diamond (red) in the scanned area as a function of annealing time. In order to be able to compare the amount of graphite and diamond after different annealing times, the scanned area was set to be 200 μm × 100 μm for each measurement. The amount of graphite present in the whole area (fraction number is shown in the square at the right bottom of images) decreases from 7.8 % after 20 minutes to 2.0% after 60 minutes, and then increases all the way back to 22.8% at 120 minutes. As shown in Chapter 4 Figure 4.10, the majority of the graphite is located along the grain boundaries on the surface grown on the polycrystalline CVD substrate, therefore, the amount of graphite along grain boundaries could be one of the factors that cause the grains to change in size with temperature relative to their dimensions at 900°C. This result also is supported by the grain size chart in **Figure *6.3*** which demonstrated the distribution of grain size over the scanned area.
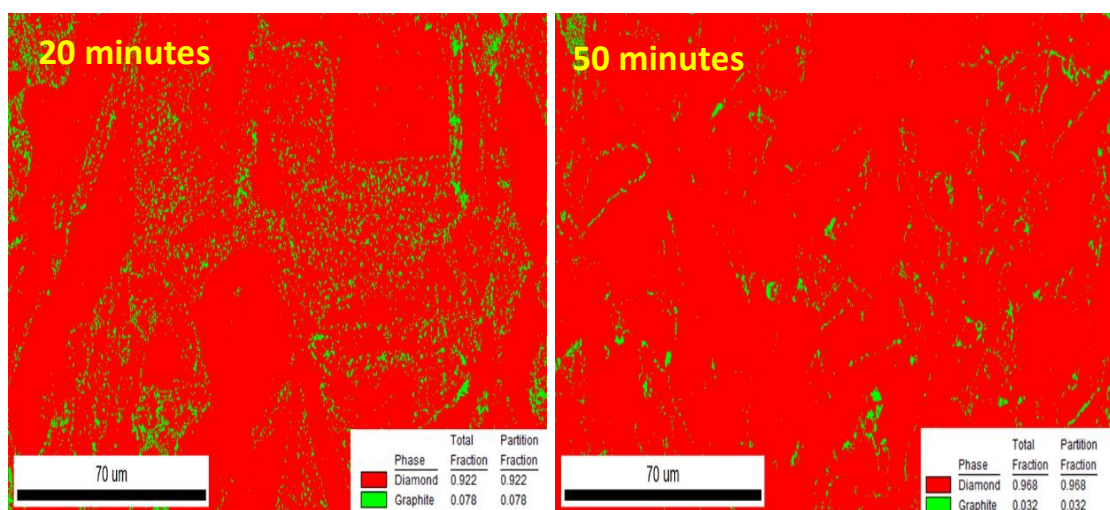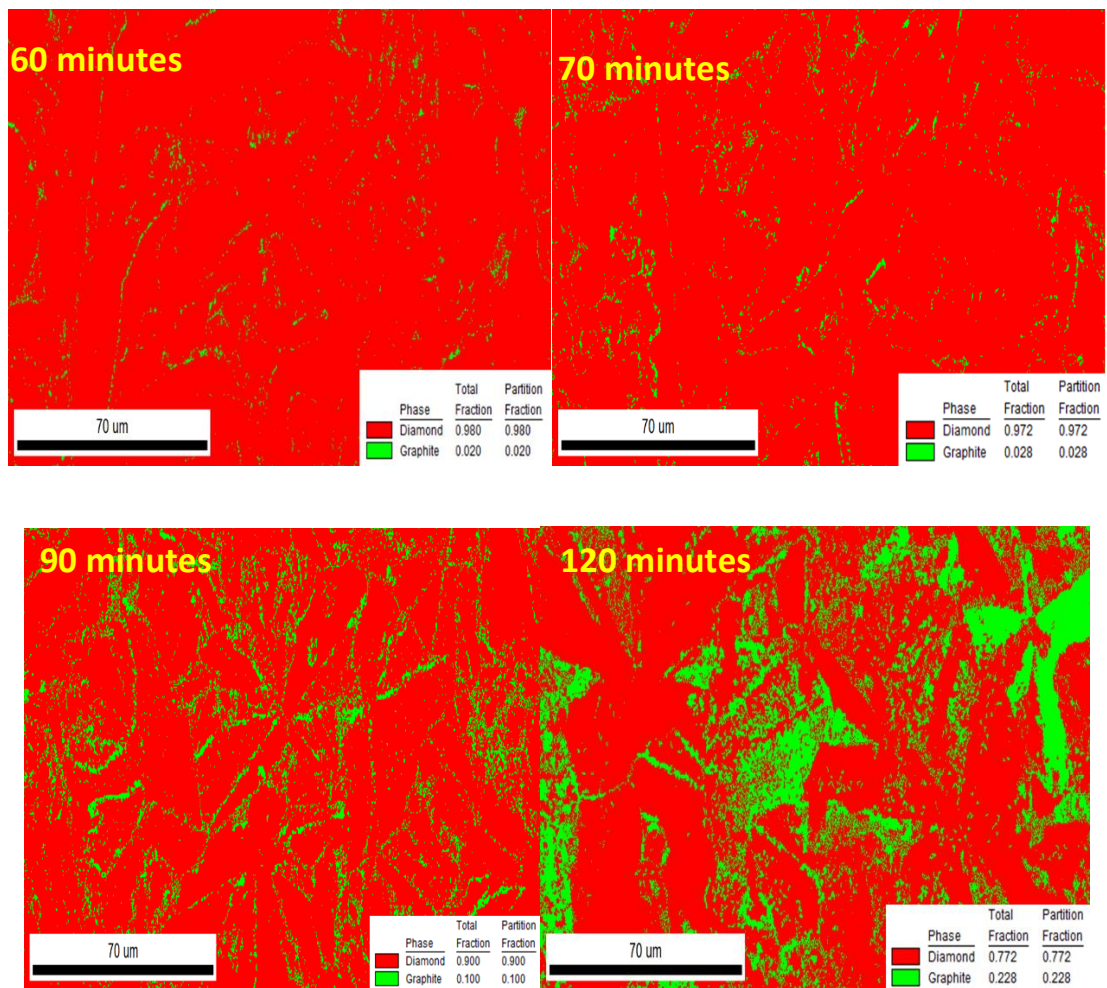
Figure 6.2 *EBSD phase images of the distribution and percentages of crystalline graphite and diamond on the surface as a function of annealing time.*

It can be seen in **Figure *6.3*** that over 70% of the area is comprised of crystals with a grain size located in the range between 12 μm to 38 μm for a 20 minute anneal. For the range of annealing conditions shown, the trend is that the grain size shifts towards to a larger crystal size and the range of sizes narrows, from 15 μm-42 μm for a 50 minute anneal (red bar) to 32 μm-55 μm (cyan bar) for a 60 minute anneal with the maximum value of 42 μm and 55 μm, respectively, which indicates the enlarged crystal size for the annealing times <60 minutes. The height variation of black, red and cyan bars displays the evolution of grain size at different annealing times. The trend is reversed when the annealing time above 60 minutes as observed from the height and

191

location variation of the yellow, blue and purple bars, respectively. The percentage of

area with large crystals (>40 μm) dramatically decreases with the companion of

increasing in the area with relatively smaller crystals (<10 μm), pulling down the

average grain size from 21.93 μm at 70 minutes, 18.66 μm at 90 minutes and 16.37 μm

at 120 minutes. The results obtained in **Figure *6.5*** is in good agreement with SEM

images presented in **Figure *6.1*** and offers further evidence to support the trends

observed for the decreasing amount of graphite before 900°C from the EBSD phase

images in **Figure *6.2***.
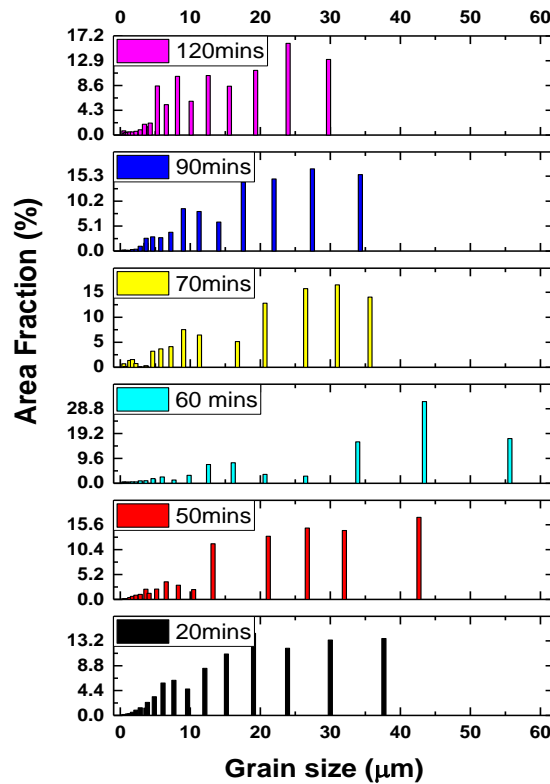
Figure 6.3 *EBSD grain size distribution chart of the as-annealed sample surface at 900 ℃.*

(Colour ranged by the different annealing times in the range from 20 minutes to 120 minutes.
The height of the coloured columns represents the percentage of certain grain size accounted
for in the overall scanned area at a particular time).

In summary, the variation of surface morphology of these BDD thin film is highly time-dependent. The variation in the grain size could be related to the distribution of graphite located in the grain boundaries of the sample film surface. The optimum annealing time of 60 minutes greatly improves the surface morphology as grown BDD films.

6.3.1.3 *The structural and defect change as a function of annealing time by Raman spectroscopy*

Figure 6.4 shows the normalised Raman spectra of the BDD surface as a function of annealing time. In graph A the relatively weak peak at 800 cm^{-1} representing hydrogen-free amorphous carbon[255, 280] gradually decreases until it disappears at an annealing time of 60 minutes which might indicate the in-diffusion of –H over the surface area of the sample leading to an increasing amount of "hydrogenated" carbon (α-C:H). The graphite peak around 1550 cm^{-1} is reduced with increasing annealing time before reaching a minimum at 60 minutes and afterwards increases for times above 60 minutes as shown in Graph B. The variation of α-C and graphite is summarised in **Figure 6.5** by plotting the ratio of sp^2:sp^3 and α-C: sp^3, respectively as a function of annealing time. Interestingly, the disappearance of the α-C signal at times above 60 minutes is accompanied by an increasing graphite content which might indicate the transformation of α-C into graphite, which has been reported for various annealing conditions previously [281-283] and is one of the reasons for the increasing amount of sp^2 detected. Another possible reason is the –H effusion out of the sample surface once the equilibrium time of diffusion is exceeded which leads to the conversion of hydrogen-free carbon into an energetically stable sp^2 carbon structure. This observation is supported by EBSD phase images (**Figure 6.2**).

193

The sp^3 peak located at the 1332.08 cm^{-1} with a tail pointing towards lower wavenumber and nearly straight line shape on its high wavenumber side is observed in both **Figure 6.4** A and B shows the interference effect from the boron impurity band [284]. It is evident that the shape of this peak becomes more asymmetric as the annealing time exceeds 60 minutes, which could be the result of a rearrangement of the quantum energy of the impurity band due to the dissociation of the boron pairing (B$_2$) complex into substitutional boron (B$_s$) which is supported by the SIMS depth profile (**Figure 6.9**) in a later section. Based on the model calculations from Goss (detailed discussion in Chapter 2 Section 2.1.3.2.3) the critical temperature for the thermodynamics equilibrium of dissociation versus bonding of the B$_2$ complex is around 900°C at a boron concentration of 10^{20} cm^{-3} where the binding energy of the B$_2$ complex is zero. The variation in the asymmetry of the sp^3 peak as a function of time could be further experimental evidence suggesting the annealing time is another factor influencing the thermal stability of B$_2$. The Full Width at Half Maximum (FWHM) and the absolute intensity of the sp^3 peak are other indicators that can be used to track the influence of annealing time on the overall defect content of the samples. For annealed samples containing a lower density of defects, a narrower sp^3 peak (lower FWHM value) is observed, along with a higher peak emission intensity. Experimental studies have revealed that the decrease in FWHM and the increase in the intensity of the diamond peak in CVD diamond films is correlated with the density of the dangling bonds [261, 285]. A similar trend has been found in this work, in **Figure 6.6**, which presents the correlation between peak width and emission peak intensity. Specifically, the value of FWHM decreases from 8.6 to 7.9 and then increases to over 10 at an annealing time of 120 minutes, while the absolute intensity of the diamond Raman line barely changed for annealing times less than 50 minutes. However, it becomes over 15 times higher than the previous sample after 60 minutes of annealing, and then, drops back to the lower peak intensity values. It is very clear to see that the highest and narrowest sp^3 peak occurred at 60 minutes which indicated the good quality of the thin film surface and the low level of defects compared to the other annealing times.
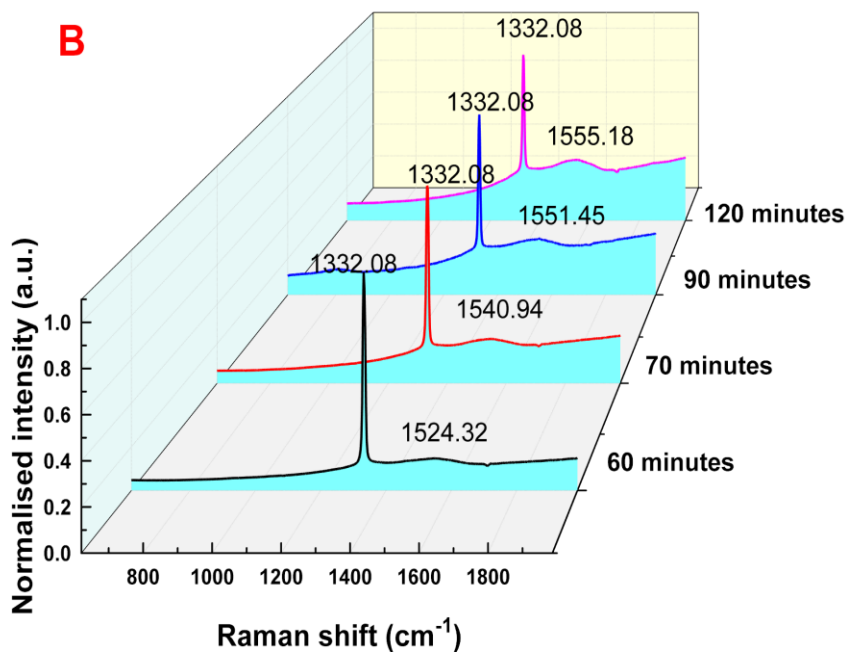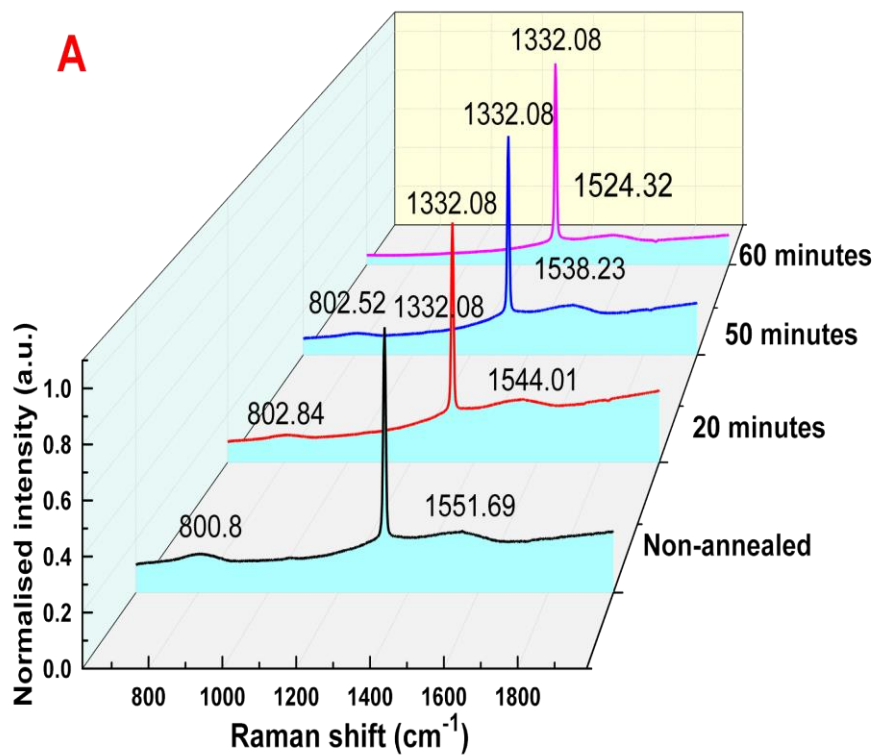
Figure 6.4 *The normalised Raman spectra of the annealed BDD surface as a function of different annealing times. (Graph A: from 20 minutes to 60 minutes; Graph B: from 60 minutes to 120 minutes).*
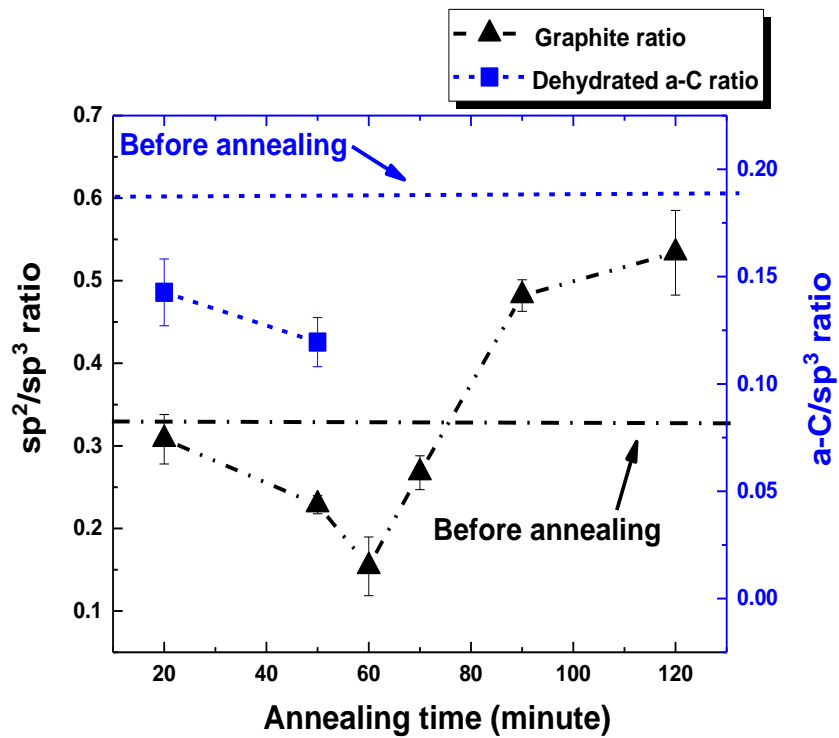
Figure 6.5 *The sp²/sp³ Raman peak ratio (black points) and the a-C/sp³ Raman peak ratio (blue points) as a function of annealing time based on the normalised Raman spectra.*
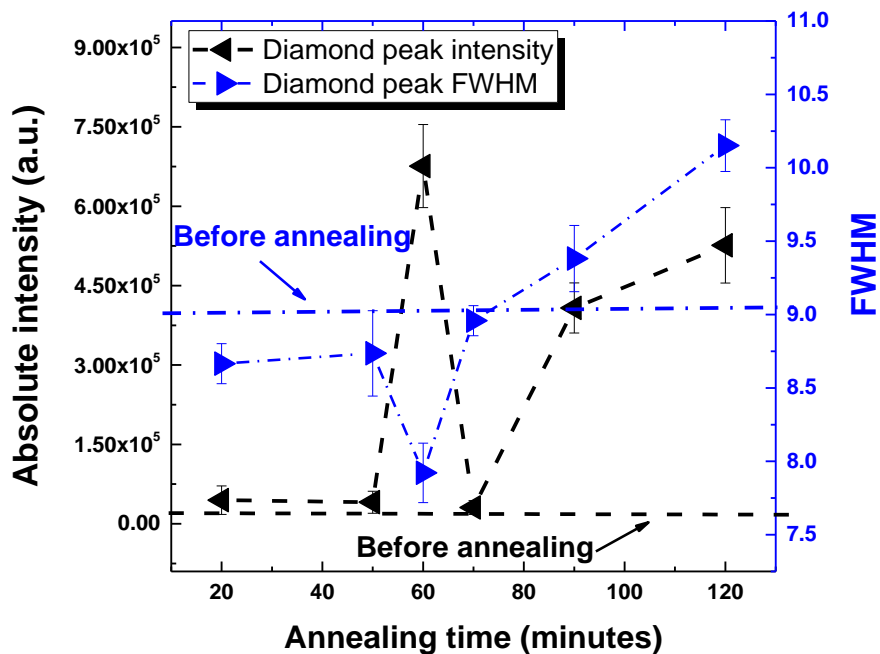
Figure 6.6 *The summary of absolute peak emission intensity and FWHM of the sp³ diamond peak based on the normalised Raman spectra.*

196

In summary, based on the results revealed by SEM with EBSD analysis and Raman spectra, the annealing time is another critical parameter that plays an important role in determining the change in the non-diamond carbon content defect density, and the composition of the sample surface. It is important to find out the influence of various annealing times performed at the annealing temperature of 900°C on the bulk properties.

6.3.2 The influence of annealing time on the bulk properties of BDD films

6.3.2.1 SIMS Mass spectra of BDD thin film

Figure *6.7* is the SIMS mass spectra of the as-annealed sample at 20 minutes obtained under positive SIMS mode. As detailed in Chapter 5, section 5.3.2, BDD films show that hydrocarbons ($-CH_x$) are the most abundant species present in the sample surface. It is hard to tell whether the hydrogen-boron complex ($-BH_x$) also contributes to the mass peak of 12, 13 or 14 as the amount of boron is far less than the carbon content in the CVD diamond. Furthermore, other possible species, such as ^{13}C, N_2 and O_2, are difficult to detect as the concentrations are much lower than the detection limitation of the SIMS when using the CVD growth conditions used in this work. Therefore, the mass spectra provide evidence to show that the hydrogenated carbon is one of the main defects in the BDD films. However, due to a large amount of hydrogen within the films and vacuum base pressure at which SIMS was performed, the concentration of various $-CH_x$ species was not accurately calibrated. The focus of this section is to look at the variation of boron concentration and distribution as a function of annealing time.
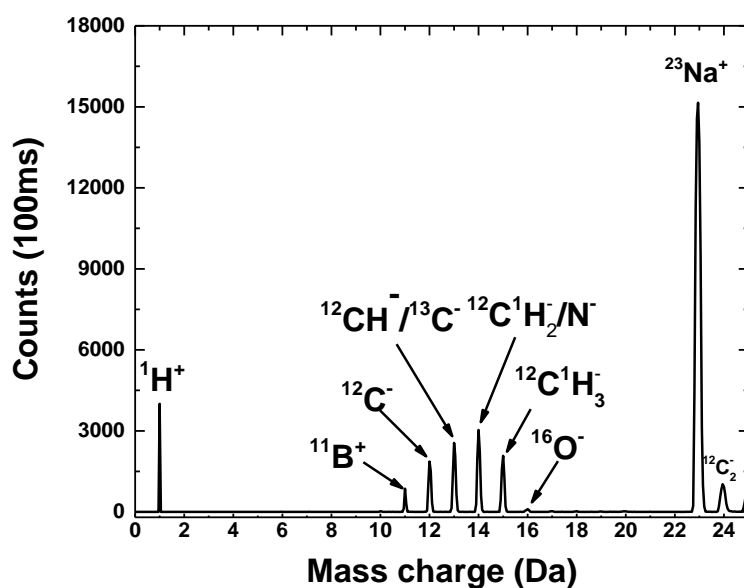
Figure 6.7 *The mass spectrum of the annealed BDD thin film surface under positive SIMS mode.*

6.3.2.2   Boron distribution and concentration as a function of annealing time

Figure 6.8 is the depth profile of boron obtained under different annealing times (colour line) plotted against the depth of the thin film. As it can be seen in this figure, the profile of boron within the layer displays two stages: an evenly distributed plateau from the PCD substrate to around half of the layer thickness which then steadily increases until it is almost double the value at the plateau near the sample surface. One of the interesting features that are shown in **Figure 6.8** is the gradual reduction in the depth of the diamond layer with annealing time up to annealing times of 60 minutes which can be confirmed by the shifted sodium (^{23}Na) peak at the interface between the layer and PCD substrate in **Figure 6.9**.

Based on the results found in Raman spectra (**Figure 6.4**) and EBSD phase images (**Figure 6.2**), the reason for the shrinkage in the doped layer thickness for times less than 60 minutes at 900°C could link to the transformation between non-diamond carbon (a-C

and graphite) and diamond at grain boundaries. Additionally, the interaction between hydrogen and its trapping centres according to the different annealing times might also lead to the "collapse" in a volume of the annealed sample [247].

Another notable feature of the depth profile data presented in **Figure *6.8*** is the variation in the boron concentration and its distribution as the annealing time is increased towards 60 minutes. It seems that the shrinkage in the grown diamond layer "compresses" the boron into a smaller volume. However, the overall boron concentration of annealed samples has no significant increases as a compensation for the shrinking volume with the increasing annealing time, especially the purple line at 60 minutes. Previous experimental studies [271, 286] have found that the diffusion coefficients of boron in diamond are $\sim 3\times10^{-12}$ cm$^2\cdot$s^{-1} at 1400°C and $\sim 2\times10^{-15}$ cm$^2\cdot$s^{-1} at 1000°C, respectively. Based on these reports, it is unlikely that the diffusion of boron within the CVD diamond thin film takes place, and this has been confirmed by SIMS depth profile measurements. Also, for the annealing conditions considered here, it is not possible for boron effusion to occur out of the sample into the diamond substrate. The answer may lie in the thermodynamic processes between bonding and dissociation for the boron pair complexes (B_2), which function as a deep trap for hydrogen. Although the theoretically determined thermodynamic equilibrium point occurs at 900°C, which means boron does not favour either bonding or dissociation, the strong tendency for –H to be trapped during hydrogen diffusion leading to the formation of B_2H_m complexes that hinders B_2 pairs from dissociating temporarily for annealing times less than 60 minutes. The presence of B_2H_m complexes would present a problem in respect of detecting ^{11}B using SIMS. This information would be necessary

in order to establish a complete thermodynamic model of boron related complexes

and hydrogen diffusion at elevated temperatures.
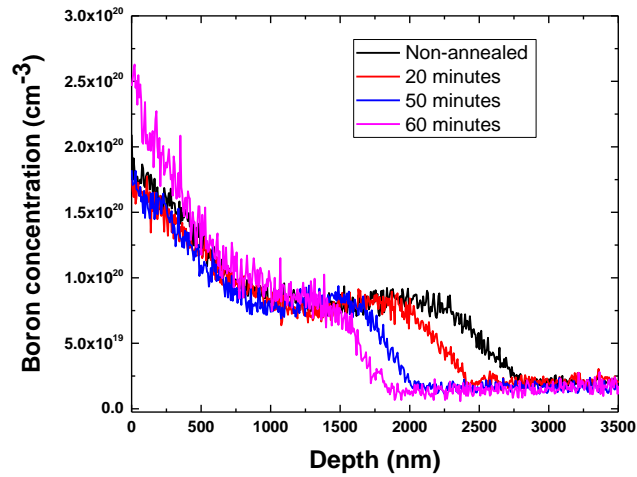
Figure 6.8 *The depth profile of boron (^{11}B) vs the depth of annealed BDD thin film for 20 minutes (red line), 50 minutes (blue line) and 60 minutes (purple line).*
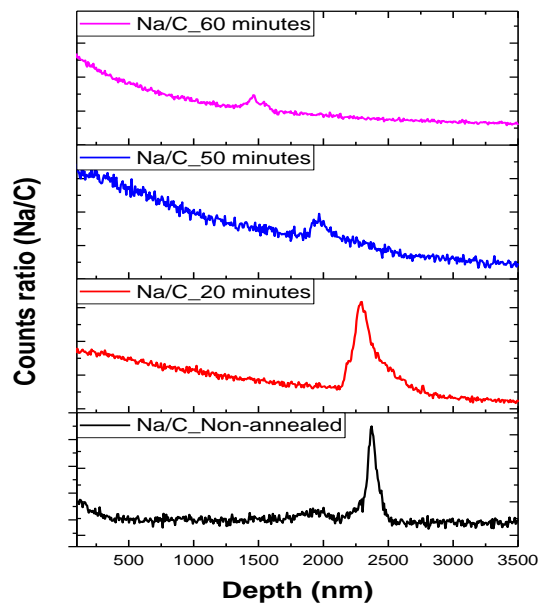
Figure 6.9 *The depth profile of sodium (^{23}Na) counts ratio (^{23}Na/^{12}C) over the depth of annealed BDD thin film for 20 minutes (red line), 50 minutes (blue line) and 60 minutes (purple line).*

Figure *6.10* shows the boron depth profile obtained at various annealing times that exceed 60 minutes. There are two main changes that can be observed: one is the gradual increase in boron concentration (colour online) and slightly altered depth of boron with time. It is apparent that the boron profile becomes progressively higher from the 60 minute anneal to 120 minute anneal which indicates that there is dissociation of hydrogen-boron pairs (B_2H_m) into substitutional dopant (B_s) complexes. This supposition is supported by carrier concentration measurements which will be discussed in section 6.3.3.1. It would appear that the trend revealed by **Figure *6.10*** is also further evidence to support the idea that hydrogen effusion occurs when enough annealing time has been provided for hydrogen to leave the sample. The theoretically predicted increase in substitutional boron concentration with annealing temperature may also be linked to the stronger asymmetric "Fano" effect on the sp^3 Raman peak in **Figure *6.4***.

The overall influence of annealing time on the depth of boron in BDD thin films in comparison with an un-annealed sample has been summarised in ***Figure 6.12*** The variation of thin film depth/thickness as a function of annealing time in comparison with non-annealed ones details the variation of depth as a function of time at 900°C. It can be found in **Figure *6.12*** that annealing times longer than 60 minutes has much less influence on the film depth for its un-annealed samples. In particular, after 120 minutes of annealing, the boron depth of the sample had changed little in comparison with the un-annealed sample. This was confirmed by tracking the location of sodium (Na) peak with annealing temperature as shown in **Figure *6.11***. This phenomenon could be the result of hydrogen loss which plays a key role in the repair of the diamond

lattice. The valley shape behaviour displayed in **Figure *6.12*** indicates that annealing

time plays a very important role in the variation of the depth of as-deposited BDD

films. However, due to the extremely low diffusion coefficient of boron below 1000°C,

the variation of boron depth profile is unlikely to be the reason to cause the thickness

change. However, it may work as an indicator to show that the change in the

configuration of boron related complexes is highly time-dependent.

Figure 6.10 *The depth profile of boron (^{11}B) vs the depth of annealed BDD thin films for 60*
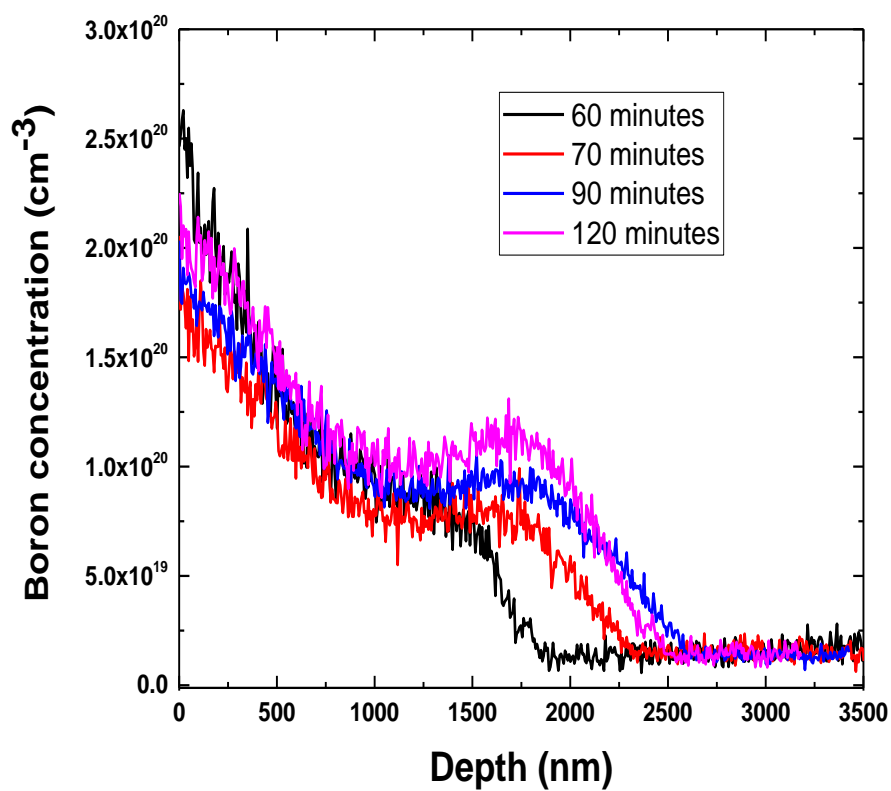*minutes (black line), 70 minutes (red line), 90 minutes (blue line) and 120 minutes (purple line).*
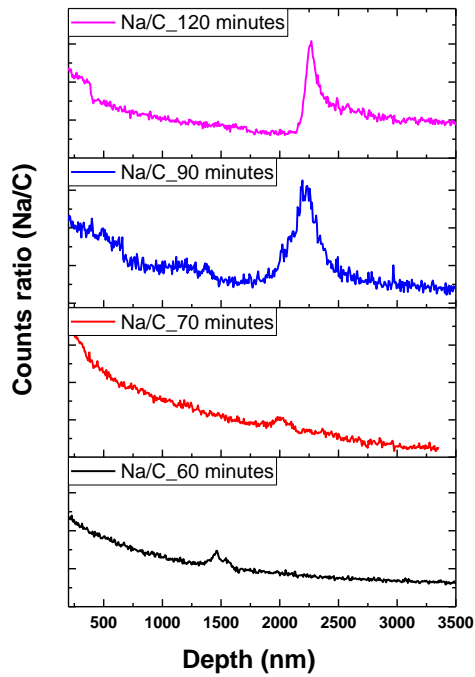
Figure 6.11 *The depth profile of sodium (^{23}Na) ratio (^{23}Na/^{12}C) vs the depth of as-annealed BDD thin films for 60 minutes (black line), 70 minutes (red line),90 minutes (blue line) and 120 minutes (purple line).*
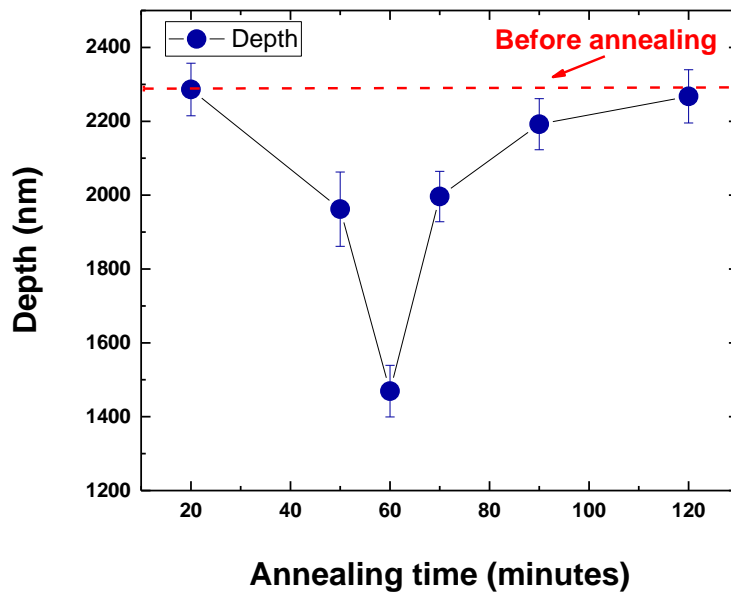
Figure 6.12 *The variation of thin film depth/thickness as a function of annealing time in comparison with non-annealed ones*

In summary, the variation in the boron distribution and its concentration as a function of annealing time at 900°C shows that time is another significant parameter that affects the thermodynamic behaviour of B_2 in heavily BDD thin films. So far, the influence of annealing time on the variations in the surface morphology, microstructure, dopant distribution and concentration within the bulk have been investigated which all play a key role in the electrical properties of as-grown BDD films. It will be discussed in the next section.

6.3.3   The influence of annealing time on the electrical properties of BDD films

6.3.3.1   The variation of carrier concentration of as-annealed BDD films as a function of annealing time

A home-built Hall Effect set up was used in this work to study the electrical properties: carrier concentration (P), mobility (μ) and resistivity ($Þ$) of as-deposited samples. **Figure *6.13*** displays the variation of carrier concentration of the individual as-annealed sample in comparison with a non-annealed one as a function of time. The carrier concentration is generally lower than for the non-annealed ones for annealing times that are less than 90 minutes, which offers evidence for a passivation effect of boron acceptors due to the indiffusion of hydrogen. Specifically, the number density of carriers slightly decreased with increasing annealing time and reached its lowest value of 2.9×10^{16} cm^{-3} after 60 minutes which is nearly three times lower than for the non-annealed sample. Once the annealing time extends beyond 60 minutes, a larger number of carriers contribute to the electrical transport which is in agreement with the SIMS depth profile in **Figure *6.11***. One thing to be noticed is that the carrier concentration at 120 minutes is even higher than in the non-annealed sample, which might be the result of dissociation of B_2 complexes releasing more substitutional

boron. However, no more than 1% of incorporated boron is electrically active as an acceptor according to the SIMS and Hall Effect data indicating a large amount of boron interstitials or aggregates exist in the diamond lattice, which is in the agreement with the previous literature [105, 108, 287]. Therefore, the trend found in carrier concentration as a function of annealing time could be the experimental evidence to support the thermodynamics that boron paring (B_2) is not only temperature dependent but time dependent as well.
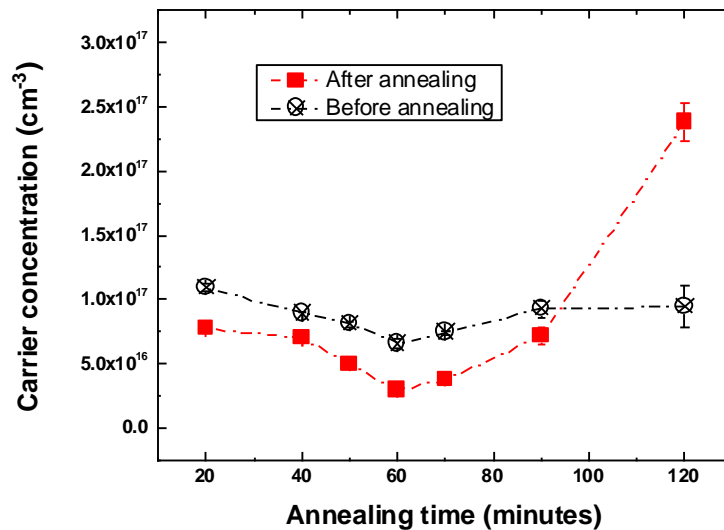
Figure 6.13 *The Hall Effect measured carrier concentrations of annealed BDD thin film(Red solid data point) as a function of annealing time, in comparison with each individual sample before annealing (black hollow data points).*

6.3.3.2   The variation of carrier mobility (μ) of as-annealed BDD films as a function of annealing time

The variation of carrier mobility as a function of annealing time in comparison with the non-annealed material is shown in **Figure 6.14**. The annealed samples generally have a higher carrier mobility than non-annealed samples following various annealing times. This is in agreement with the result that annealing the diamond samples at 900°C improves the mobility of as-grown BDD films as described in Chapter 5. The reverse valley shape found in **Figure *6.15*** in comparison with the carrier concentration

trend displays the defect-scattering effect that the carrier experienced before and after 60 minutes. Specifically, the measured mobility increases with increasing annealing time until 60 minutes and then gradually decreases for annealing times longer than 60 minutes. There are a few reasons causing this phenomenon. One of the main reasons is the reduction in overall number density of defects, such as non-diamond carbon found in the Raman spectra (**Figure *6.4***), the density of grain boundaries obtained from EBSD phase images (**Figure *6.3***), and the ionised substitutional boron from Hall Effect measurements (**Figure *6.13***), which leads to much reduced defect scattering-effect. The data presented in **Figure *6.15*** provides a direct correlation between carrier concentration and mobility as a function of the annealing time. It is also seen that the drop in carrier concentration is the reason that the mobility of holes within the bulk of films is improved.
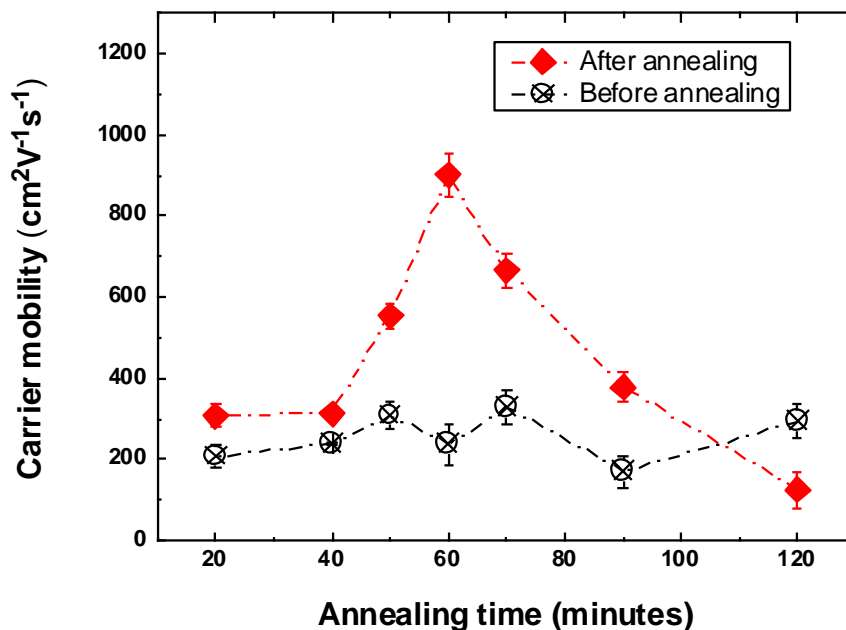

Figure 6.14 The Hall Effect results for the carrier mobility of annealed BDD thin films (red solid data points) as a function of annealing time in comparison with each individual sample before annealing (black hollow data points).
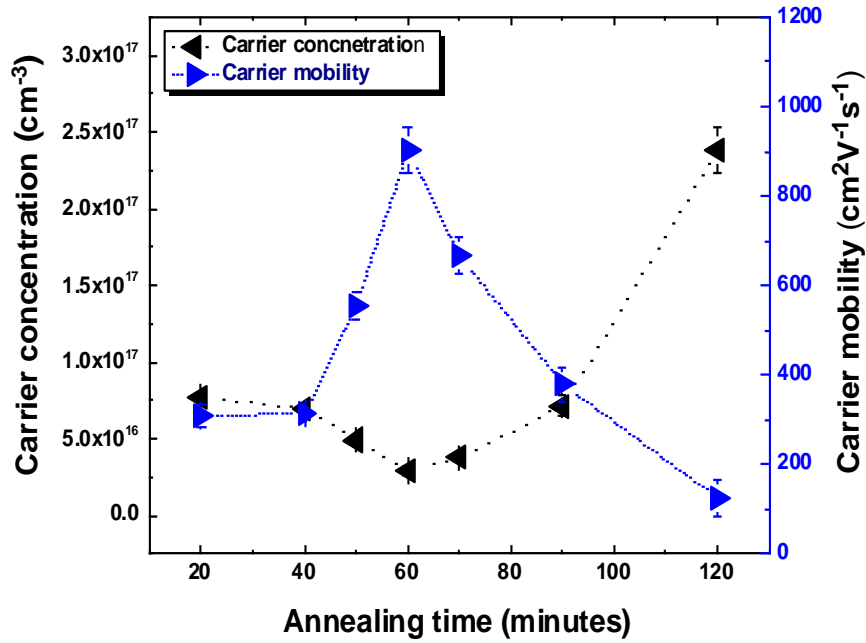
Figure 6.15 *The correlation between carrier concentration (black solid data point) and mobility (blue solid data points) obtained by Hall measurement.*

6.3.3.3 The variation of resistivity of as-annealed BDD films as a function of annealing time

The variation of carrier concentration and mobility are the main factors that influence the conductivity of semiconductor materials [288]. In order to demonstrate the overall influence of annealing on the resistivity of BDD films, the percentage change between the resistivity before and after annealing is calculated using the simple equation below:

$$\rho\% = \frac{\rho_{after} - \rho_{before}}{\rho_{before}} \times 100\% \qquad \text{Equation (6.1)}$$

Where ρ_{after} and ρ_{before} are the resistivity obtained after or before annealing

Figure *6.16* presents the relationship between the results obtained from equation 6.1 and annealing time. The negative value on the Y axis represents the direction of change which means the value of resistivity of annealed samples is lower than non-

annealed samples. It can be seen that the annealing of samples at 900°C for periods

between 20 minutes and 120 minutes always improves the conductivity compared

with the value of conductivity recorded for as-deposited films. Besides the 60-minute

annealing conditions which significantly improved conductivity by around 40%, other

samples generally improved by around 8%-15%. These results demonstrate that a

better quality of BDD film may be achieved for electronic device applications after

annealing at 900°C for 60 minutes. There are several factors that contribute to the

improvement in conductivity of annealed samples. Although the carrier concentration

is slightly lower than non-annealed BDD (**Figure *6.13***) at 900°C due to hydrogen

diffusion, the reduction in ionised acceptors significantly weakens the scattering effect

which is one of the main driving forces that leads to greatly improved carrier mobility.

This result shows that the electrical conductivity of as-grown materials is not only

limited to the amount of carriers activated within the bulk. On the other hand, surface

(section 6.3.1) and bulk analysis (section 6.3.2) indicated that the microstructure of the

host lattice and the state of defect complexes are other major reasons that

significantly affects the conductivity of the BDD thin film samples.

 In summary, the annealing time is a key factor that significantly influences the

electrical properties of as-grown BDD thin films. An annealing time of 60 minutes is the

optimum time that produces a desirable improvement in the quality of BDD films

(boron concentration around 10^{20} cm^{-3}) with the highest value of conductivity and

carrier mobility obtained in the range of annealing time between 20 minutes to 120

minutes at 900°C.
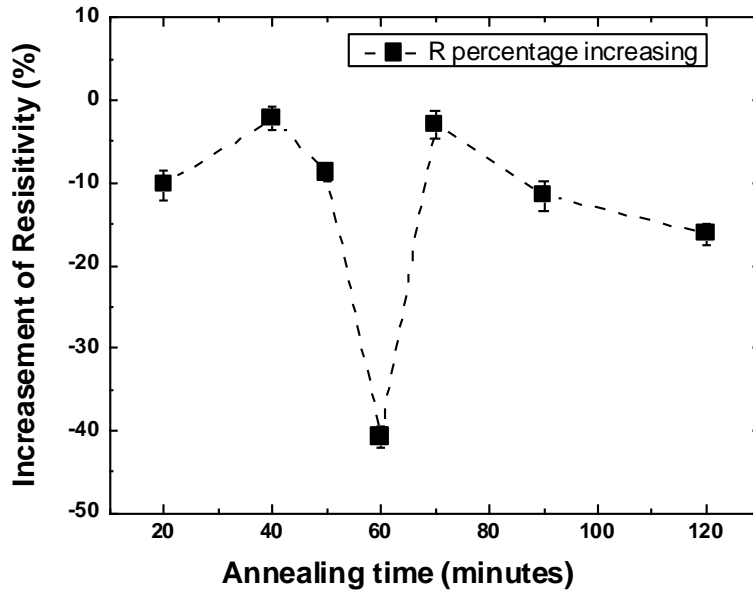
Figure 6.16 *The calculated percentage difference between resistivity before and after annealing condition compared with as-grown BDD samples ($\frac{\rho_{after} - \rho_{before}}{\rho_{before}}$) as a function of annealing time. (Negative values represents the change in resistivity of BDD films is increasing after annealing).*

6.3.3.4 The comparison of electrical properties with previous reports

In order to highlight the annealing effect on the electrical properties of heavily boron-doped diamond, recent review papers [289,290] are used for this purpose. It can be seen from **Figure *6.17*** and ***Figure 6.18*** that the carrier mobility obtained in Section 6.3.3 is the highest value so far for the carrier concentrations > 10^{16} cm^{-3} with the doping concentrations > 10^{20} cm^{-3}. Such improvement in the electrical properties can enlarge the applications of this highly-doped BDD film in the electronic devices.
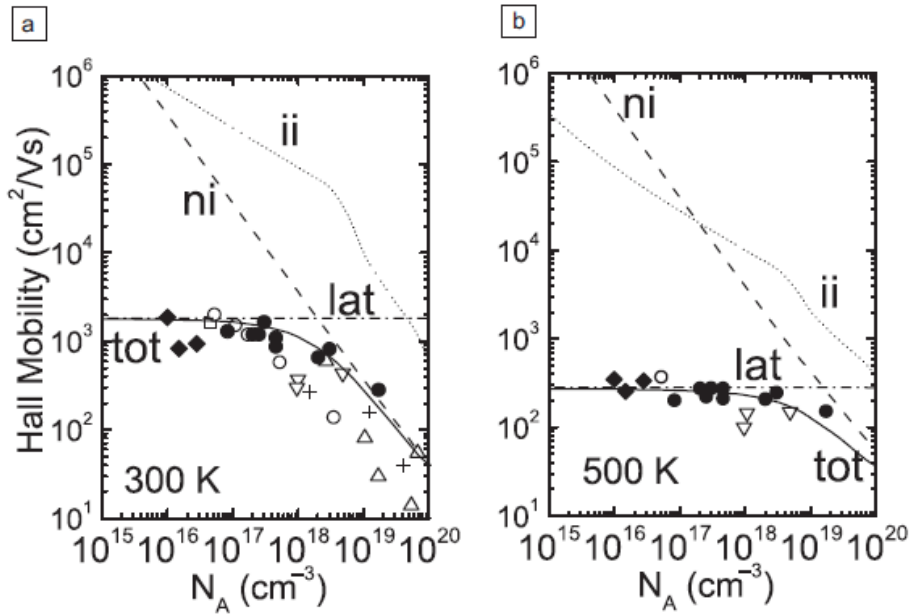
Figure 6.17 *Hall mobility of holes as a function of doping level in homoepitaxial diamond at (a) 300 K and (b) 500 K. The symbols indicate experimental data, and the theoretical contributions of various scattering modes are illustrated by dashed and dotted lines for the lattice (lat, acoustic, and optical phonons): a dotted line for the ionized impurities (ii) mode, and a dashed line for the neutral impurities (ni) mode[289].*
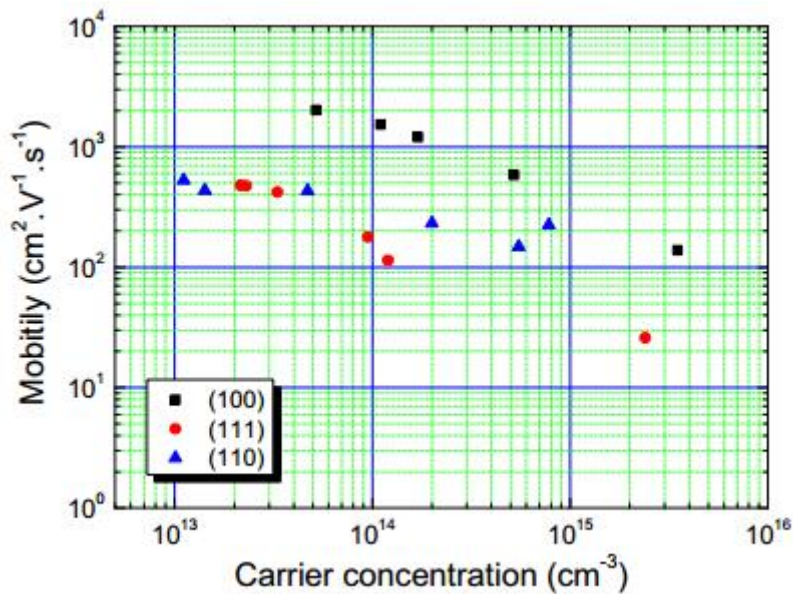
Figure 6.18 *Variation of carrier mobility as a function of the carrier density measured at room temperature by Hall effect using Van der Pauw technique for samples grown on (100) , (110) and (111) (unpublished) oriented substrates[290].*

6.4 Conclusion

The influence of annealing time for periods between 20 minutes to 120 minutes at 900°C on the surface morphology, the structural composition, the dopant distribution and the electrical properties of heavily BDD thin films have been investigated in this Chapter. It has been found that the effect of annealing time on these properties is highly time-dependent which suggests that the diffusion of hydrogen and thermodynamic behaviour of B_2 under each annealing condition could be the main reason for the results obtained. The major discovery found in this work is that a 60 minute anneal at 900°C is the optimum time for enhancing the electrical behaviour of BDD thin films. The main results are summarised below:

1) The surface of the thin BDD layer displayed a smoother morphology with enlarged crystals and a reduced amount of non-diamond carbon for anneal times less than 60 minutes.

2) The shrinkage in the thickness of BDD thin films increased with the annealing time up to 60 minutes.

3) The concentration of boron incorporated into the diamond lattice steadily decreased with annealing time, but after longer than 60 minutes of annealing the concentration started to increase as a result of -H diffusion and thermodynamic equilibrium between the dissociation and bonding of boron (B_2) complexes which function as a deep H trap centre.

4) The carrier mobility increases with increasing annealing time for annealing times less than 60 minutes, which reaches nearly 1000 $cm^2V^{-1}s^{-1}$ and then gradually drops back after 60 minutes with increasing carrier concentration.

In summary, annealing heavily boron doped (boron concentration around 10^{20} cm^{-3}) thin films at 900°C for 60 minutes significantly improves the quality of the films and enhances the electrical performance for potential electronic applications. The overall time- or temperature-depend and behaviour is controlled by the thermodynamics bonding/dissociation behaviour of B_2 pairing which functioned as a deep defect trap centres.

6.5 References

269.   Aziz, M.J., Thermodynamics of diffusion under pressure and stress: Relation to point defect mechanisms. Applied Physics Letters, 1997. 70(21): p. 2810-2812.

270.   Sung, T., G. Popovici, M. A. Prelas , R. G. Wilson and S. K. Loyalka, Boron diffusion into diamond under electric bias. Journal of Materials Research, 1997. 12(05): p. 1169-1171.

271.   Popovici, G., R.G. Wilson, T. Sung, and M.A. Prelas, Diffusion of boron, lithium, oxygen, hydrogen, and nitrogen in type IIa natural diamond. Journal of Applied Physics, 1995. 77(10): p. 5103-5106.

272.   Chevallier, J., D. Ballutaud, B. Theys,F. Jomard,A. Deneuville,E. Gheeraert, and F. Pruvost, Hydrogen in monocrystalline CVD boron doped diamond. Physica Status Solidi (a), 1999. 174(1): p. 73-81.

273.   Williams, B. and J. Glass, Characterization of diamond thin films: Diamond phase identification, surface morphology, and defect structures. Journal of Materials Research, 1989. 4(02): p. 373-384.

274.   Ono, A., T. Baba, H. Funamoto, and A. Nishikawa, Thermal conductivity of diamond films synthesized by microwave plasma CVD. Japanese Journal of Applied Physics, 1986. 25(10A): p. L808.

275.   Prawer, S., D. Jamieson, and R. Kalish, Investigation of carbon near the graphite-diamond-liquid triple point. Physical Review Letters, 1992. 69(20): p. 2991.

213

276.   Stotter, J., Y. Show, S. Wang, and G. Swain, Comparison of the electrical, optical, and electrochemical properties of diamond and indium tin oxide thin-film electrodes. Chemistry of Materials, 2005. 17(19): p. 4880-4888.

277.   Koizumi, S., K. Watanabe, M. Hasegawa, and H. Kanda, Ultraviolet emission from a diamond p-n junction. Science, 2001. 292(5523): p. 1899-1901.

278.   Sung, T., G. Popovici, M. A. Prelas and R. G. Wilson, Boron diffusion coefficient in diamond. in MRS Proceedings. 1995. Cambridge Univ Press.

279.   Saguy, C., et al., Diffusion of hydrogen in undoped, p-type and n-type doped diamonds. Diamond and Related Materials, 2003. 12(3): p. 623-631.

280.   Ferrari, A. and J. Robertson, Resonant Raman spectroscopy of disordered, amorphous, and diamondlike carbon. Physical Review B, 2001. 64(7): p. 075414.

281.   Barreiro, A., et al., Understanding the catalyst-free transformation of amorphous carbon into graphene by current-induced annealing. Scientific Reports, 2013. 3.

282.   Nistor, L., V. Ralchenko, I. Vlasov, A. Khomich, R. Khmelnitskii, P. Potapov, and J. Van Landuyt, Formation of amorphous carbon and graphite in CVD diamond upon annealing: a HREM, EELS, Raman and optical study. Physica Status Solidi (a), 2001. 186(2): p. 207-214.

283.   Casiraghi, C., F. Piazza, A.C. Ferrari, D. Grambole, and J. Robertson, Bonding in hydrogenated diamond-like carbon by Raman spectroscopy. Diamond and Related Materials, 2005. 14(3): p. 1098-1102.

284.   Bustarret, E., E. Gheeraert, and K. Watanabe, Optical and electronic properties of heavily boron‑doped homo‑epitaxial diamond. Physica Status Solidi (a), 2003. 199(1): p. 9-18.

285.   Jia, H., J. Shinar, D.P. Lang, M. Pruski, Nature of the native-defect ESR and hydrogen-dangling-bond centers in thin diamond films. Physical Review B, 1993. 48(23): p. 17595-17598.

286.   Pecková, K., J. Musilová, and J. Barek, Boron-Doped Diamond Film Electrodes—New Tool for Voltammetric Determination of Organic Substances. Critical Reviews in Analytical Chemistry, 2009. 39(3): p. 148-172.

287.   Fujimori, N., H. Nakahata, and T. Imai, Properties of boron-doped epitaxial diamond films. Japanese Journal of Applied Physics, 1990. 29(5R): p. 824.

288.   Lundstrom, M., Fundamentals of carrier transport. 2009: Cambridge University Press.

289.   S Yamasaki, E Gheeraert, Y Koide, Doping and interface of homoepitaxial diamond for electronic applications. Mrs Bulletin, 2014, Cambridge University Press.

290.   Mortet V., Pernot J., et al., Properties of boron-doped epitaxial diamond layers grown on (110) oriented single crystal substrates. Diamond & Related Materials, 53 (2015) 29–34.

Chapter 7   Conclusions and Future work

7.1   Conclusions

In this thesis, heavily boron-doped diamond thin films (BDD) have been fabricated on the polycrystalline diamond substrate surfaces using HFCVD. The influence of boron concentration, substrate surface and thermal annealing on the physical, structural, and electrical properties of BDD films had been investigated with the aim of improving the overall quality and hence enhancing the electrical performance of as-grown samples.

BDD film growth on seeded and non-seeded substrates demonstrate huge differences in the surface morphology of the as-deposited layer. The non-seeded homoepitaxial films display much larger crystal size than the seeded MCD films, with the majority of the crystal orientations lying in [001] and [111] directions. The higher density of grain boundaries within the seeded MCD films demonstrated greater Fano interference on the sp^3 Raman line due to the higher boron concentration incorporated within the bulk than the non-seeded films, which shows evidence of boron clusters or aggregates at the grain boundaries. This result in the lower hole mobility and conductivity of seeded samples than for the homoepitaxial ones at every boron doping level.

Increasing boron concentration doped into the diamond lattice causes several changes described as below:

1) A reduced number of defects, such as grain boundaries and graphite with enlarged crystal surface, has been observed based on the SEM and EBSD phase images on the non-seeded films, especially for boron concentrations above 10^{20} cm^{-3} ; at the same time there is no such significant change observed from MCD films grown on the seeded substrate surface. Thickness measurement from the

216

cross-sectional SEM images shows that the re-nucleation rate of growth also enhanced with the increasing boron content causing a slower growth rate during film deposition.

2) The boron-related band at 1200cm^{-1} in Raman spectra has been found in both homoepitaxial and MCD films at B concentrations above the threshold of the metal-diamond transition (3×10^{20} cm^{-3}) which highly interferes with the electronic energy structure of diamond. The large downshift in the sp^3 Raman peak obtained from seeded MCD films demonstrated that the compressive stress originated from a large amount of boron aggregated at grain boundaries. No large shift in the diamond Raman peak was found in the non-seeded homoepitaxial films at every level of boron doping showing much less stress is created under homoepitaxial growth.

3) The grain boundaries accommodated more clustered/aggregated boron as observed by comparing the results of SEM images and boron SIMS depth profile, and functioned as one of major scattering centre that significantly influence the electrical properties of as-grown BDD films

4) The doping efficiency of boron became very low once the dopant amount exceeded the metal-diamond transition threshold, as the hole concentration decreases with the increasing of boron atoms. The hole mobility of homoepitaxial thin films is nearly 3 times higher than MCD films with the conductivity 2 times lower than MCD ones.

The thermal annealing has significant impact on the physical, electrical and structural properties of as-grown BDD films. It has been found that annealing a

heavily boron-doped layer (10^{20} cm^{-3}) under vacuum at 900°C for 60 mins could

significantly improve the hole mobility from 198 cm^{-1}V^{-1}S^{-1} to 988 cm $^{-1}$V^{-1}s^{-1} with a

40% increase in conductivity. Investigations on the thermal stability of boron pairs

(B$_2$) and defect diffusion under different annealing temperature and time revealed

that a valley "V" shape behaviour of electrical and physical properties of BDD films,

controlled by the thermodynamics bonding and dissociation equilibrium of boron

pairs (B$_2$) which function as a hydrogen deep trap centres forming B$_2$H$_x$ complexes.

The results discussed in Chapter 5 and Chapter 6 could contribute to support and

further complete the thermodynamics modelling of boron complexes.

7.2   Suggestions for Future work

7.2.1   Characterisation

7.2.1.1   EBSD images

Due to the lack of a crystalline boron diffraction pattern data available in the IAC

lab, future work to obtain the EBSD pattern and phase images of crystalline boron-

carbide could provide direct further evidence to explain the location and

orientation of boron under various annealing conditions. Furthermore, It also can

be a useful work to study the diffusion of boron at high temperature (>1400°C)

using EBSD techniques which plays an important role in the electrical properties of

as-grown BDD films.

7.2.1.2   SIMS depth profile

The investigation of the thermal stability of hydrocarbons (CH$_x$) is also an

important area to complete the whole picture of defects mechanism in CVD

diamond [291]. SIMS depth profiling is a useful tool to trace the concentration and

distribution within the bulk of the films. However, there are a few challenges to overcome: one is the precursor gases need to be fully changed with deuterium in order to mark with ^{1}H by the signal collection system of SIMS. Another one is the proper calibration of standard samples which is the key to obtain accurate and reliable results.

7.2.1.3   NanoESCA

   NanoESCA, an Ultra High Vacuum (UHV) Photo Electron Emission Microscopy (PEEM) system, is the state-of-the-art technique for real-space and momentum-space imaging and spectroscopy [292, 293]. This non-destructive technique provides the electronic properties (such as work function) and chemical composition of thin layers of materials. Investigating the influence of thermal annealing on the electrical properties and chemical structure of the as-grown homoepitaxial films in this work in related to the surface morphology such as crystal orientation and grain boundary densities and opens the door for exploring and understanding fundamental knowledge of CVD doping.

7.2.2   Potential applications

   Boron doped diamond materials have been used for energy-related devices, such as thermionic emission [260, 294], Schottky diodes [295, 296], field-effect transistors [297] and electron emitters [298]. However, the intrinsic defects and low efficiency of doping in CVD diamond film limit the performance in its applications. Annealing heavily boron doped thin film under different times and temperatures alters the physical, structural and electrical behaviour of these BDD films. It would be

meaningful to investigate the performance of these as-annealed materials in these devices especially for the BDD films annealed in the vacuum at 900°C for 60 minutes.

7.3 References

291. Messier, R., A.R. Badzian, T. Badzian, K.E. Spear, P. Bachmann and R.Roy, *From diamond-like carbon to diamond coatings.* Thin Solid Films, 1987. **153**(1): p. 1-9.
292. Escher, M., et al., *NanoESCA: a novel energy filter for imaging x-ray photoemission spectroscopy.* Journal of Physics: Condensed Matter, 2005. **17**(16): p. S1329.
293. Escher, M., et al., *NanoESCA: imaging UPS and XPS with high energy resolution.* Journal of Electron Spectroscopy and Related Phenomena, 2005. **144**: p. 1179-1182.
294. Koeck, F.A., *R.J. Nemanich, A. Lazea, and K. Haenen.* Diamond and related materials, 2009. **18**(5): p. 789-791.
295. Chen, Y., M. Ogura, and H. Okushi, *Temperature dependence on current–voltage characteristics of nickel/diamond Schottky diodes on high quality boron-doped homoepitaxial diamond film.* Applied Physics Letters, 2003. **82**(24): p. 4367-4369.
296. Gildenblat, G.S., S.A. Grot, C.W. Hatfield, C.R. Wronski, *High temperature Schottky diodes with boron-doped homoepitaxial diamond base.* Materials Research Bulletin, 1990. **25**(1): p. 129-134.
297. Shiomi, H., Y. Nishibayashi, and N. Fujimori, *Field-effect transistors using boron-doped diamond epitaxial films.* Japanese Journal of Applied Physics, 1989. **28**(12A): p. L2153.
298. Bunshah, R.F., S.R. Jou, and H.J. Doerr, *Diamond thin film electron emitter*. 1997, Google Patents.

Appendix A

EBSD orientation images of heavily boron doped diamond thin film from boron doping

flow rates 0.005 sccm to 0.025 sccm
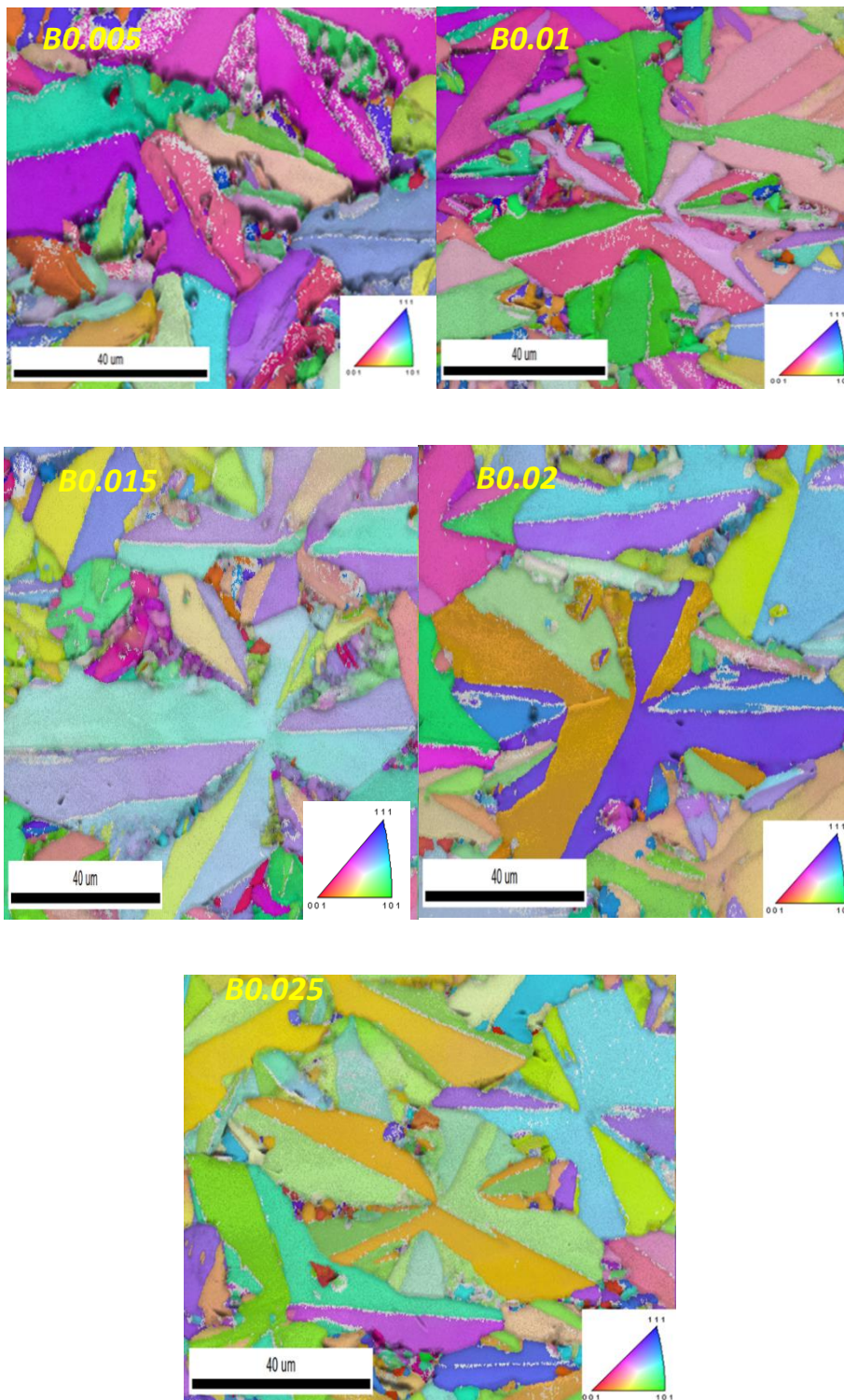
Appendix B

Secondary Ion Mass Spectroscopy (SIMS) calibration of boron implanted diamond samples.

Samples

A polycrystalline CVD diamond sample from Element Six was supplied for measurement of the sensitivity of SIMS to B in diamond. Three samples were implanted:

1. B^+ implanted at 10^{12} cm^{-2} at 50 keV
2. B^+ implanted at 10^{14} cm^{-2} at 50 keV
3. B^+ implanted at 10^{15} cm^{-2} at 50 keV

SIMS depth profiles were performed using a gallium ion beam at 25keV energy and an incident angle of 45°, etching at a magnification of 3000X on the instrument with a beam current of 3.0 nA (measured on a Keithley picoammeter with the beam into a Faraday cup). The relevant ions were monitored during a depth profile; ($^{11}B^+$ and $^{12}C^+$), as a function of time, using the ion counting facility of the SIMS instrument. A "gating" facility was used to reject secondary ions from the sidewalls of the pits. The depth erosion rate 0.28 was nm/s, which was measured by Focused Ion beam, was used in determining the profile depths below.

SIMS Depth Profiles

A typical SIMS depth profile of the 1×15 cm^{-2} implanted sample is shown in Figure 1.

The ratios of B$^+$ to C$^+$ are shown in Figures 2. The depth values have been used
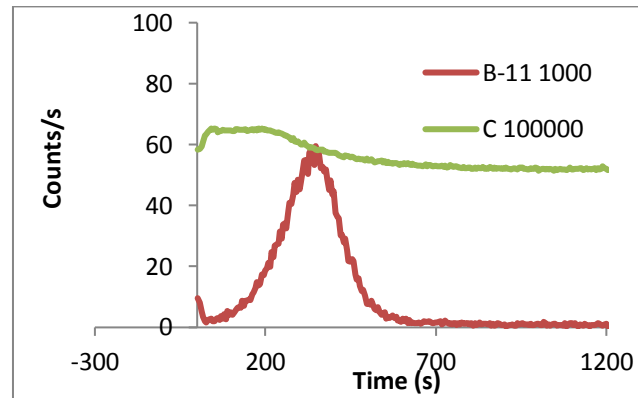
according to the calculation above.

Figure 1. Depth profile of SCD implanted with 1×10^{15} cm^{-2} of both B$^+$ ions. Showing

intensity of ions detected against the etch time
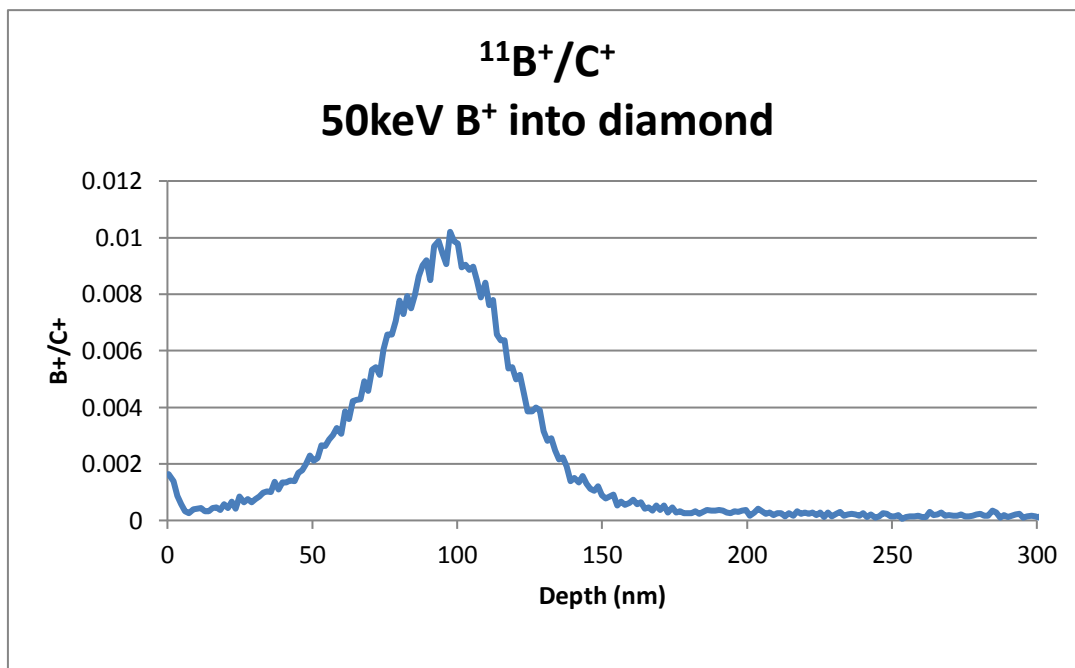
Figure 2. Ratio $^{11}B^+/C^+$

The profile of the B^+ signal is approximately Gaussian, as expected from an implantation of this type.

Concentration Calculations

Gaussian curves were fitted to each profile, using the usual equation:

$$y = \frac{K}{\left(\sqrt{2\pi}\right)\sigma} e^{-\frac{(x-\mu)^2}{2\sigma^2}}$$

where μ is the peak depth, K is a measure of the magnitude (height), and σ is a measure of the Gaussian width. The integral of this form equates to K:

The ratios of B^+/C^+ was used for the fit in Excel. The results are presented in the Table below:

Sample	OFFSET	K	μ (nm)	σ (nm)
B	0	0.57	96	24

These values can be used to calculate the volume concentration of the implanted material with depth.

225

Again assuming the implantation depth profile to be Gaussian, the concentration of

implant material (cm^{-3}), $C(x)$, where x is depth, can be given as:

$$C(x) = \frac{A}{\left(\sqrt{2\pi}\right)\sigma} e^{-\frac{(x-\mu)^2}{2\sigma^2}}$$

where A is the area concentration (i.e. 10^{15} cm$^{-2)}$. We now know σ, so we can calculate

C.

The peak concentration for Boron is therefore:

$$C(x = \mu) = \frac{10^{15}}{(\sqrt{2\pi}) \times 24 \times 10^{-7}} = 1.66 \times 10^{20} cm^{-3}$$
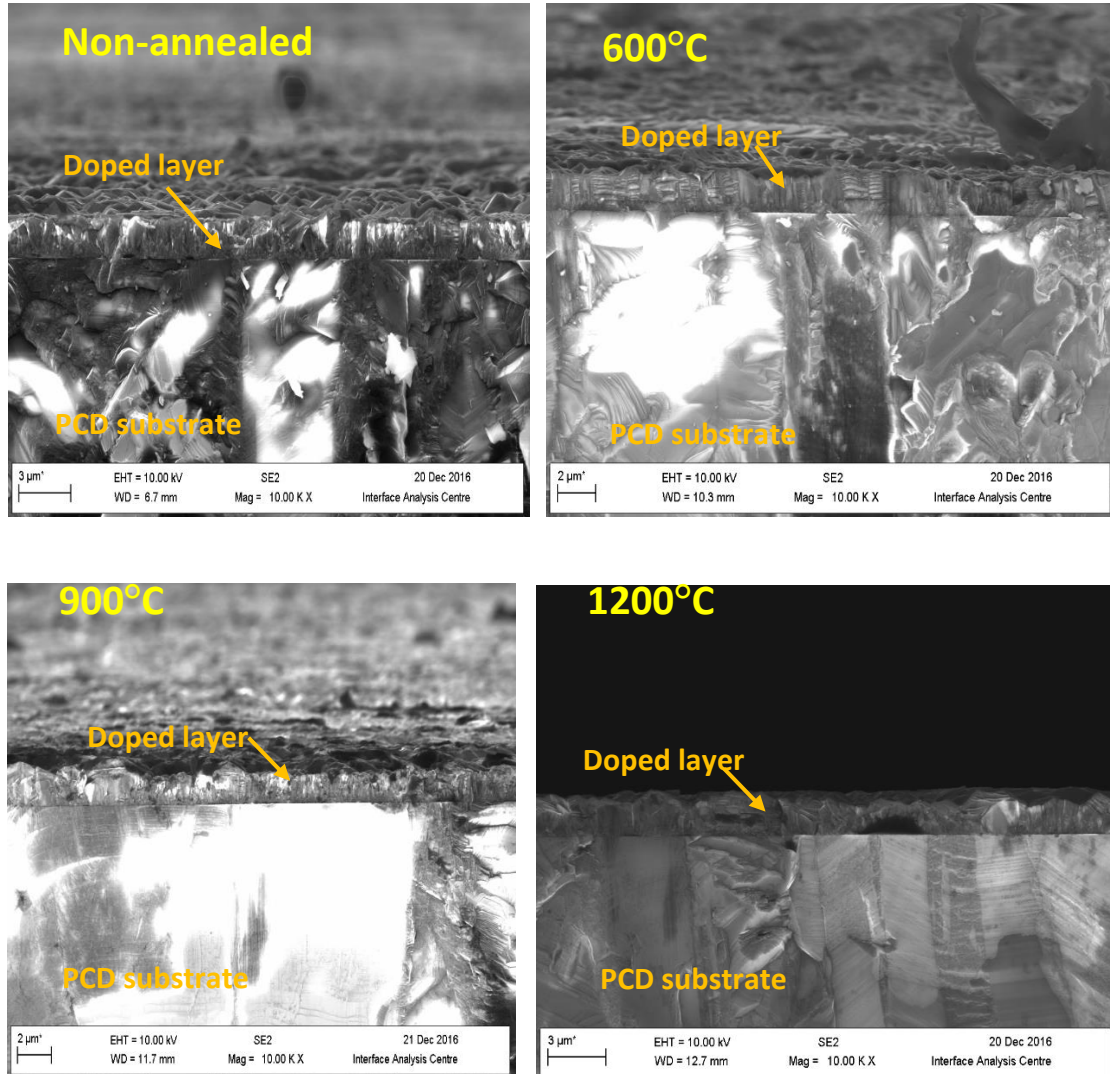
The SIMS sensitivities to the materials can be obtained by using the K values from the

Gaussian fits, and the area concentrations (calculating A/K).

From these results, the following calibration factor is obtained:

B concentration [B] = 1.8 x 10^{22} x (B$^+$/C$^+$ ratio). (cm^{-3})

Appendix C

Cross-sectional SEM images of annealed BDD films grown on the seeded substrate

All four samples were grown under the same deposition condition (1% CH4, B_2H_6 0.005sccm) at the same time. The thickness of as-grown thin film has been measured by using Image J which can be seen in the table below:

Sample	Thickness±SD (μm)
Non-annealed	*2.105±0.15*

|	
600°C	1.925±0.128
900°C	1.326±0.116
1200°C	2.026±0.064

Appendix D

Grain boundary density measurement by using Image J

To obtain the GB density, a black and white 8-bit digital image was converted from SEM coloured images by adjusting the threshold within the limited range in order to define the grain shape and boundary. In this work, the black colour (the intensity is 255 in 8-bit system) is mapped for grains and the white colour (the intensity is 0) is for grain boundaries. Then the ratio of the count of overall white pixel over the sum of counts of chosen image is the density of GBs. The procedure is described below:

SEM images   Binary Black & white images

229
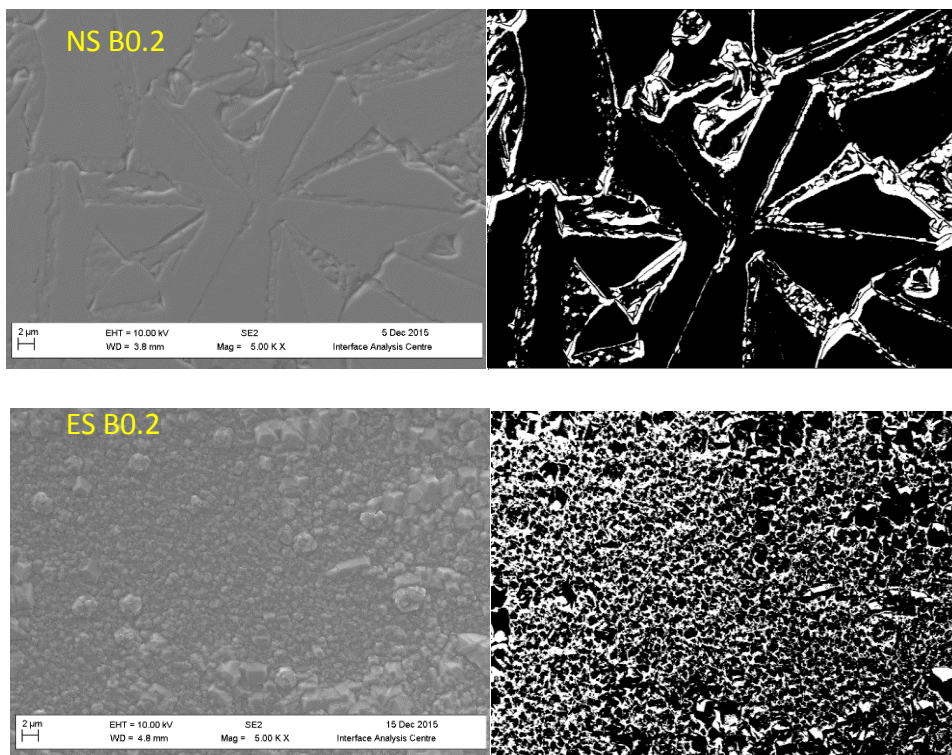
Histogram calculation result

Sample	Value	Count	% Area
	255	682937	81.92
NS 0.2	0	150726	18.08
ES 0.2	255	497734	63.29
	0	**288698**	**36.71**